Fatigue Behaviour of Aluminium Alloy AA2024 to Titanium Alloy Ti6Al4V Friction Stir Lap Welded Joints

Steve Korakan Ales

A thesis submitted to
Auckland University of Technology
in fulfilment of the requirements for the degree of
Doctor of Philosophy (PhD)

2021

School of Engineering, Computer and Mathematical Sciences

ABSTRACT

Friction stir welding (FSW) is a solid-state joining technique which can be used for joining not only similar or dissimilar aluminium alloys but also between aluminium alloys and other high melting temperature alloys. Welding of an aluminium alloy to a high melting temperature alloy with traditional fusion welding processes is not suitable as it results in excessive growth of brittle intermetallics in the weld region. Recent studies by many researchers have provided well-established data showing superior tensile and shear properties of Al to Ti FSL welds in comparison to other welds of aluminium alloys to other high melting temperature alloys made using FSW and tested in static loading. The process parameters have been often used to test the efficiency of FSL welds in order to improve their tensile and shear strength properties of Al to Ti FSL welds. However, thus far, there is a total lack of study on the fatigue properties of Al to Ti alloy welds made using FSW which has prevented Al to Ti FSW to be applied industrially. As a result, the study of fatigue behaviour of Al to Ti friction stir lap welding (FSLW) is important for establishing useful data for its various applications that engineers, designers and manufactures need. Lap weld (FSLW) is another major weld geometry widely used.

Thus, the primary aim of this research was to determine the fatigue properties and investigate the fatigue behaviours of AA2024 to Ti6Al4V alloy welds made using FSLW at wide range of stress amplitudes. The alloys used were aerospace aluminium and titanium alloys and thus the study is particularly relevant for applications in aerospace industry.

Experimentally, fatigue tests have been conducted on welds of AA2024 (A14.5Cu1.4Mg0.5Mn) alloy to Ti6Al4V alloy welds made using FSLW, using a tool with a pin diameter of 6 mm. Pin bottom aimed for touching the Ti6Al4V plate but not penetrating ($d_P \approx 0$) although it was inevitable that pin could also readily penetrate ($d_P > 0$) slightly with the FSLW being position controlled. FSLW experiments were also conducted by placing thermocouples at the weld interface regions so that temperature cycle data during FSLW could be obtained. Two other series of experiments have also been conducted, one refers to using a large pin and the other refers to using an interlayer so that $d_P = 0$ is more certain. For the large pin experiment, a lower rotational speed was required to avoid insufficient stir flow and the top tunnel defects. After FSLW experiments and fatigue tests, microstructures in the weld interface region and on fracture surfaces have been studied in detail. This includes samples tested with crack growing during fatigue testing "frozen" so that the crack growth behaviours relating to the weld structures could be better observed and studied.

It has been found that, for both $d_P \approx 0$ and $d_P > 0$, fatigue limits of the FSL AA2024/Ti6Al4V welds were slightly higher than the fatigue limits of the FSL Al to Al alloy welds reported in literature. Examination of cross sections of samples with crack growth interrupted thus "frozen" during testing and fracture surfaces of the tested samples have demonstrated diffusion welding forming the very thin interface intermetallic layer during FSLW. This thin layer being the major mechanism responsible for the good fatigue strength of the welds. For $d_P > 0$, a significantly larger diffusion AA2024/Ti6Al4V weld distance outside the pin width than that for $d_P \approx 0$ welds have been observed. This was the reason for the fatigue limit of $d_P > 0$ welds being comparable to the fatigue limit of $d_P \approx 0$ welds despite of the mix stir zone (MSZ) in $d_P > 0$ welds being a brittle one due to excessive growth of intermetallics. The different thermomechanical conditions for the different diffusional weld widths will be illustrated.

As the pin diameter was increased from 6 mm to 9 mm the total width of the AA2024/Ti6Al4V FSL weld was also increased for $d_P > 0$. However, it has been found that there was no significant increase in the effective weld width outside the MSZ. The larger pin has also been found to readily penetrate more, having a detrimental effect that the deep MSZ could cause fracture in the Ti6Al4V plate. The effective weld width for $d_P \approx 0$ has also been found not to have increased, compared to that of the weld made using a normal size pin. This is likely due to the result of using a lower pin rotational speed, for avoiding top weld channel defects, so that effective diffusion welding is not enhanced. Thus, the fatigue performance of weld made using large size pin has been found to be comparable to the fatigue performance of the welds made using the normal size pin.

Using an Al interlayer, together with the standard size tool pin, has been found to have provided no benefit for increasing the fatigue strength, for both 8 mm and 10 mm wide interlayer. The reason for this has been found to be the similar diffusion weld width, as the stir flow width and possibly the temperature history are the same with or without the use of interlayer when the pin does not penetrate the bottom Ti6Al4V plate. Analysis of the fracture surfaces have confirmed that the thin interface intermetallic layer having been formed, thus still enabling comparable performance of AA2024 to Ti6Al4V FSL welds made with Al interlayer.

ACKNOWLEDGEMENTS

I wish to record my deep sense of gratitude and profound thanks to my research supervisor Professor Zhan Chen, Department of Mechanical Engineering, Auckland University of Technology, for his keen interest and constant encouragement with my work during all stages, to bring this thesis into fruition.

I would also like to express my sincere gratitude and deep appreciation to Dr. Shamzin Yazdanian, Manukau Institute of Technology, for his enthusiasm and a strong interest in research which have made a deep impression on me for his invaluable advice and guidance in the research. Dr. Yazdanian has effectively acted as an expert supervisor during my Ph.D. study.

Dr. Tim Pasang is my secondary supervisor and is acknowledged for his valuable discussions during the initial stage of this research and encouragement throughout the study.

I express my sincere thanks to technical officers Mr. Ross Jamieson, and Mark Masterton for their invaluable help and support throughout my research. I am also thankful to Mr. Jim Crossen, workshop Manager, Department of Mechanical Engineering, Auckland University of Technology, for his support.

I wish to acknowledge the support and love of my family, my wife, Levica; my son, Londari; and my two daughters, Karen and Karina. Not the least but my last gratitude and appreciation to my mum, Yuwan for her love and continuous prayers throughout my study.

ATTESTATION

I hereby declare that this submission is my own work and that, to the best of my knowledge and belief, it contains no material previously published or written by another person nor material which to a substantial extent has been accepted for the qualification of any other degree or diploma of a university or other institution of higher learning, except where due acknowledgement is made in the acknowledgements.

Name: **Steve Korakan Ales**

Signature:……..

Date: **26/04/2021**

TABLE OF CONTENTS

LIST OF FIGURES

LIST OF TABLES

NOMENCLATURES

Symbol	Meaning	Unit
FSW	Friction Stir Weld	-
FSBW	Friction Stir Butt Weld	-
FSLW	Friction Stir Lap Weld	-
Ø	Diameter	mm
ω	Rotational tool speed	rpm
rpm	Revolution per minute	rev/min
υ	Transverse weld speed	mm/min
$OD_{shoulder}$	Outside shoulder diameter	mm
OD_{pin}	outside pin diameter	mm
D_{Pin}	Pin dimater	mm
L_{pin}	Pin length	mm
Δσ	Stress range	MPa
µm	Micro millimetre	-
σ_{min}	Minimum stress	MPa
σ_{max}	Maximum stress	MPa
Al	Aluminium of any grade	-
Ti	Titanium (Ti6Al4V)	-
R	Stress ratio	F_{min}/F_{max}
IMCs	Intermetallic Compound (s)	Nm (µm)
TWI	The Welding Institute	-
σ_{lap}	Lap shear	MPa
Ref.	Reference	-
A_{eff}	Effective contact area	mm^2
F	Force	kN
Deg.	Degree	°
EWW	Effective weld width	mm
SEM	Scanning electros microscope	-
OD_{pin}	Outside diameter of pin	mm
N/A	Not available	-
d_P	Depth of pin penetration	mm
σ_a	Stress amplitude	MPa
AS	Advancing side	-
RS	Retreating side	-

F_{max}	Maximum force	kN
FS	Friction Stir	-
BM	Base Metal	-
L_{pin}	Length of pin	mm
USW	Ultrasonic Spot weld	-
µFSW	Micro friction Stir Welding	-
σ_{Lap}	Lap shear	MPa (N/mm^2)
SpFW	Spot Friction Welding	-
MSZ	Mixed Stir Zone	-
F_m	Maximum Force	kN
Fm/Ws	Max. Force per sample width	N/mm
P	Penetrated weld sample	-
NP	Non-penetrated weld sample	-
IMCs	Intermetallic compound layer (s)	-
N	Cycle number	(s)
σ_e	Equivalent (Von mises) stress	MPa
σ_A	Applied stress	MPa
T	Temeprature	°C
T_{max}	Maximum temperature	°C
UTS	Ultimate Tensile Strength	MPa

1. INTRODUCTION AND LITERATURE REVIEW

1.1 Friction Stir Welding: A General Background

For many industrial and engineering applications, welding of dissimilar metals is necessary. However, for many dissimilar metal weld couples of large differences in melting points, welds of acceptable strength and toughness are difficult to achieve. This is because, as has been well known and has been well assessed by Kah et al. [1] and in the review by Fang et al. [2] on the various welding techniques for dissimilar metal welding, brittle intermetallic phases in the weld interface region readily form during fusion welding. Thus, solid-state welding is favourable for welding of dissimilar metals as diffusion rate is low in solid-state in comparison to that in a liquid state and the growth of brittle interface intermetallic compounds (IMCs) can be minimized. For this reason, friction stir welding (FSW), which is a solid-state process, has been studied extensively for welding various dissimilar metal couples.

FSW was patented in 1991 by Thomas et al. [3] from The Welding Institute, UK. Since its inception, the process has generated significant interest in research and development activities paving the way for improved friction stir welding (FSW) processes. FSW joint can be accomplished in either a butt joint or a lap joint geometry orientation depending on the nature of weld structure requirements in their applications. During friction stir welding, a tool (non-consumable) is plunged into the joint line to be welded and traverses along the join line. Figure 1-1 illustrates schematically the butt weld FSW. A tool consists of two important features which influence the final weld product and, in this study, a threaded cylindrical pin as shown in Figure 1-1b) was used. The plates to be welded are bolted onto a base plate with respective side supporting plates for firmly clamping the plates together during welding. A large amount of heat is generated locally during welding between the workpiece and the rotating tool which results in plasticization and softening of the materials. The softened materials then flow along with the tool and deposit as it traverses along the joint line. Some materials may flash out if the tool shoulder is plunged deep enough.

Traditional fusion welding of dissimilar alloys particularly with aluminium and other high-temperature materials have always been problematic due to their differences in physical, mechanical, and thermal properties. However, FSW is capable of joining two distinct materials together below their melting temperatures especially with aluminium and its high-temperature counterpart materials. FSW is also utilized in both Butt (see Fig.1-1a) and Lap (see Fig.1-3a) welding geometry configurations to joint aluminium with other high-temperature alloys such as copper, steel, and titanium providing better tensile and shear strength using optimum process conditions compared to strength values of welds made using fusion welding. One of the

parameters in determining high weld strength in FSW butt welding is tool offsetting. A tool offset is generally about 1-2mm to the high-temperature alloy side which can provide high tensile strength for dissimilar FS butt joint as illustrated in Figure 1-1a. This means that ~80 per cent of the pin is rotating and friction stirring mostly on Al side while chipping in ~20 per cent of Cu parts creating what is referred to as mixed stir Zone (MSZ). The MSZ is now the final product responsible for the establishment of the weld joint due to the thermomechanical action of the tool. Figure 1-1b illustrates the final FSW product showing MSZ and an interface at which Al/Ti bonding is formed through interdiffusion of elemental particles.

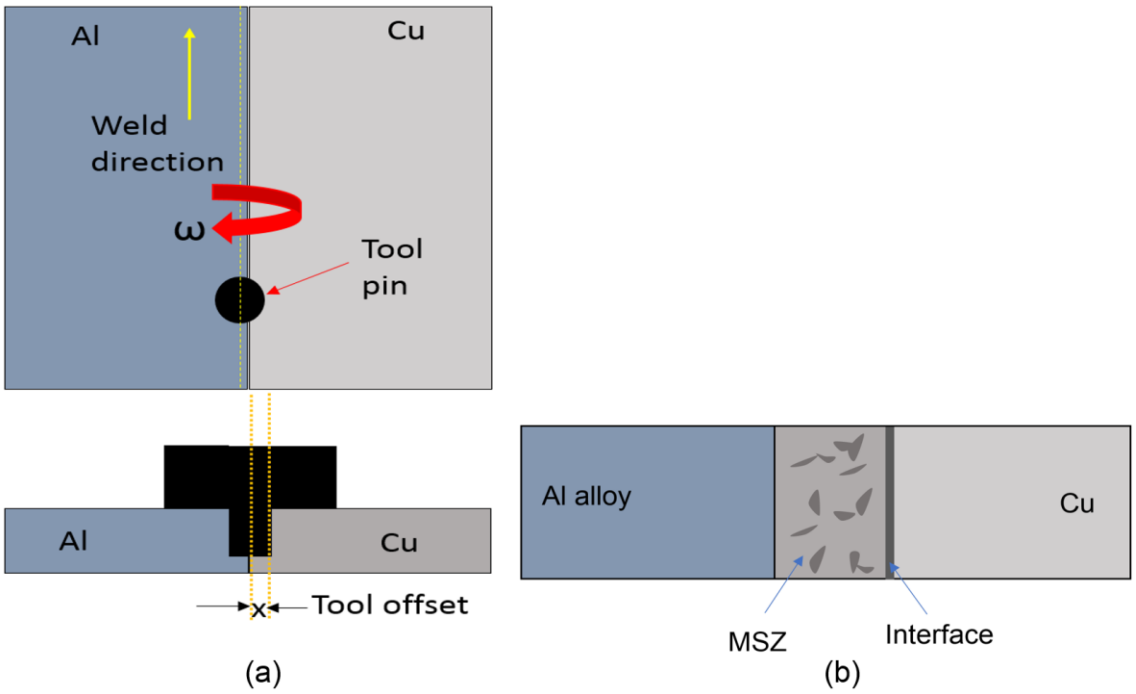

Figure 1-1 Schematic illustration of tool offset in the FSW of a dissimilar joint of aluminum-copper. Tool offset (x) may vary between 0.1-2mm.

Apparently, there are two sides during FSW known as the advancing side (AS) where rotational tool motion and traverse direction are in the same direction whereas the retreating side (RS) is where the rotational tool and traverse direction are in opposite directions as shown in Figure 1-2a. Usually, the tool direction is parallel with the rolled direction of the parent material (see Fig.1-2a). The FS welded region is known as the nugget zone (NZ) because the weld couples are of the same material. The process of NZ formation is fully explained by Chen et al. [4], in their 2008 article on shear flow and NZ formation during FSW of aluminium alloy 5083-0. Figure 1-2b shows the NZ with other major features observed at the weld region are; heat affected zone (HAZ) and thermomechanical affected zone (TMAZ).

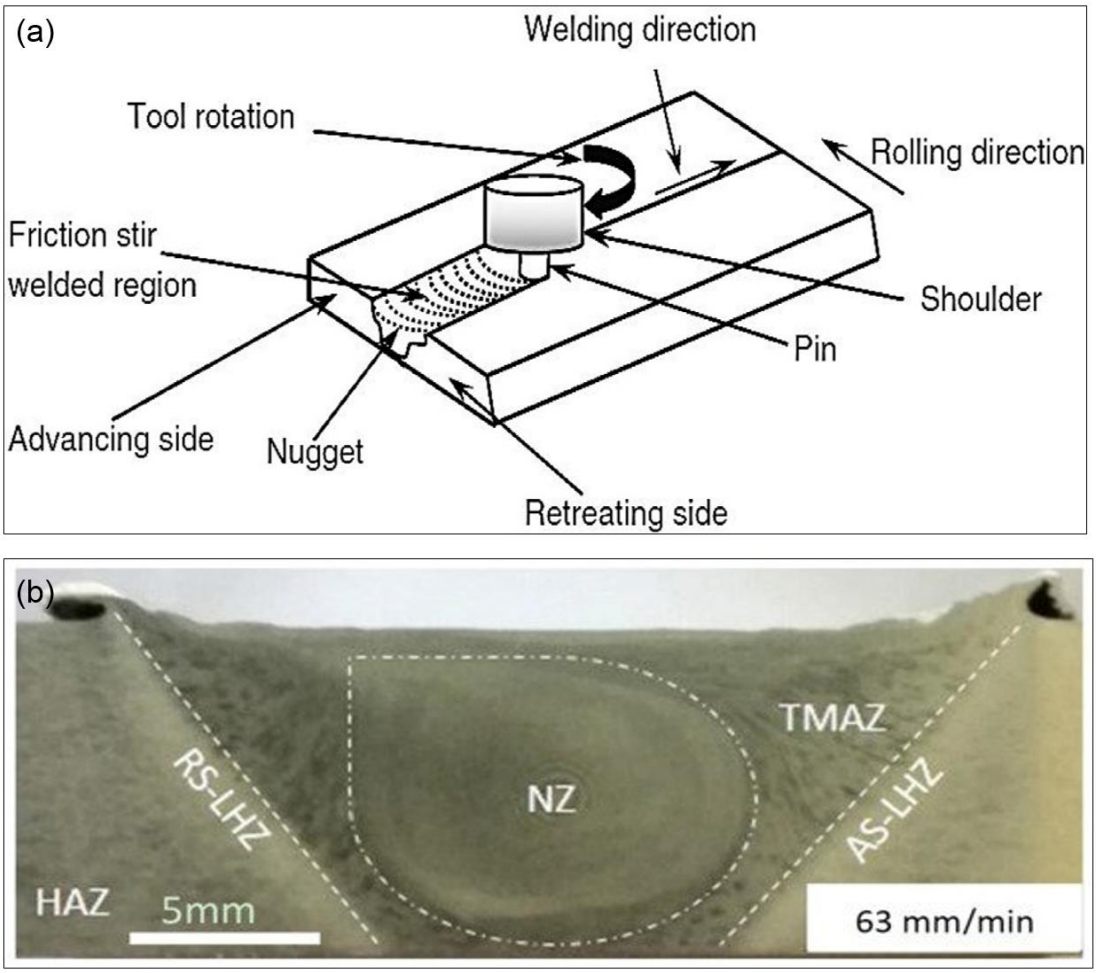

Figure 1-2 (a) Schematic illustration of FSW process of Al to Al butt joint [5], (b) Nugget zone of FSW Al to Al alloy [6].

An FSW lap geometry configuration is illustrated in Figure 1-4a and two different sizes of tools with a threaded cylindrical head as shown in Figure 1-4b. Full too profile (Shoulder diameter, pin diameter and pin length) is presented in experimental section (Chapter 2).

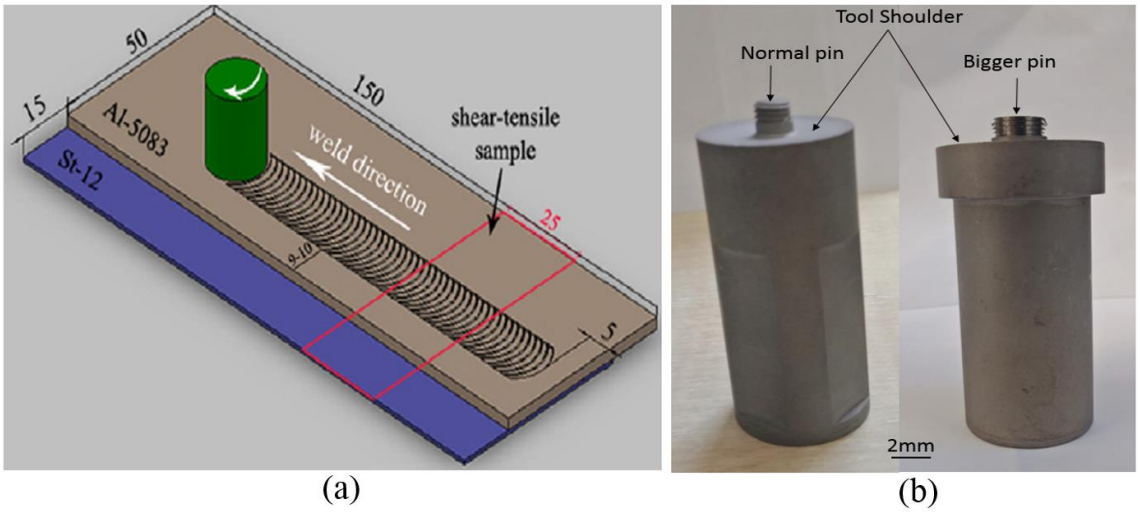

(a) (b)

Figure 1-3 Schematic Illustrations of friction stir lap welding process[7] and (b) two different sizes of actual FSW tools with threaded pins.

There are several advantages of FSW over traditional fusion welding which consumes a large amount of energy. FSW is a solid-state joining process in which materials do not melt but only plasticize below their melting point. Thus, a major advantage of FSW is free from solidification-associated defects like porosity and cracking that may form during fusion welding. For this reason, there is no FSW unweldable aluminium alloys while, for high strength aluminium alloys such as 2xxx and 7xxx alloy, they are not fusion weldable. FSW is environmentally friendly comparing to fusion welding which uses consumable rods and oxyacetylene gas welding. Moreover, due to the rotating pin, generating intense heating and plastic deformation will occur at the stir zone which will have different recrystallized grain structures at the weld zone as illustrated in Figure 1-4. The formation of recrystallized fine grain structures results in high weld strength and fatigue resistance.

The past two decades have seen FSW applications mainly in transport industries; aerospace, military, naval, railway, automotive, and most recently computer industries [7-12]. Aluminum grades such as 2xxx and 7xxx series have been widely used in these industries but, as has been explained, they cannot be welded using fusion welding processes but now their weldability problem has been overcome by using FSW.

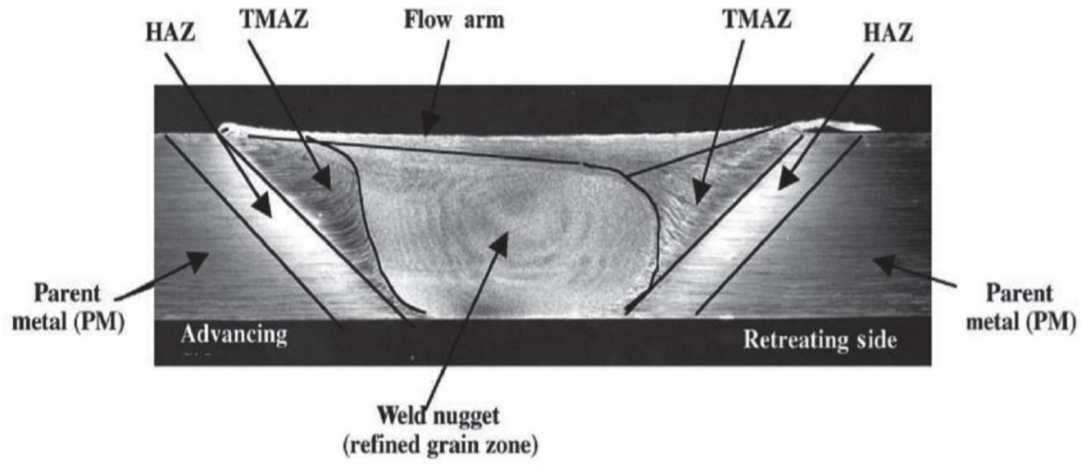

Figure 1-4 Microstructures of the weld zone showing the PM (patent metal), SZ (stir zone), TMAZ (thermomechanical affected zone), and HAZ (heat affected zone) [13].

Aluminium to titanium welding is challenging because of their significant differences in mechanical, chemical, and physical properties such as crystal structure, melting point, thermal expansion, etc. For example, Aluminium and titanium's melting points are 660 °C and 1660 °C respectively, a huge difference of 1000 ^{o}C. This difference leads to great difficulties in joining with fusion welding because aluminium-titanium will form a large intermetallic compound (IMC) which will grow excessively in liquid weld pool during fusion welding and is highly detrimental to the weld's mechanical properties. The excessive growth of the intermetallic compounds, namely Ti_3Al, TiAl, $TiAl_2$, and $TiAl_3$, during fusion welding which is unavoidable. However, the formation of IMC is necessary for the establishment of a weld joint but needed in a small amount

necessary for forming a strong weld strength. Growth of intermetallics in solid state is a slow process as diffusion in solid state is slow. Thus, a solid-state welding process like FSW which is carried out below the solidus temperature line can be used which will retard the formation of large IMCs.

Titanium (Ti6Al4V alloy) is widely used as structural materials in the aerospace industry, for both frame and engine components, and in the chemical and related industries (e.g., condenser tubing for nuclear and fossil-fuel power generation, off-shore oil drilling). This is because of titanium's unique combination of superior (e.g., fatigue) strength-to-weight ratio, high operating temperatures, and corrosion resistance. However, aluminium (2024-T6) on the other hand has specific properties and characteristics useful in many structural applications. It has a low melting point of about 600-degree Celsius, lightweight with a specific weight of 2.7g/cm^3, about a third of that of steel, and has good ductility. The two distinct alloys used in this research will be described in a more detail with their corresponding physical, chemical compositions, and mechanical properties in Chapter 2.

Over the last 15 years, there have been various studies on Al to Ti FSLW and there are well-established data on tensile and shear properties of Al to Ti FSL welds tested under static loading. The quality of FSL weld has most often been evaluated in terms of the process parameters to improve their tensile and shear strength properties. However, one of the most important factors that are always involved in structures in various applications particularly in aerospace industry is the fatigue of materials in service. Fatigue is a form of failure that occurs in structures subjected to dynamic, fluctuating and cyclic stresses [14]. For instance, bridges, machine components, and aircraft experience fatigue loading during their service life. Fatigue damage of mechanical components remains a major cause of failures in engineering structures. For instance, fatigue fracture of titanium alloy turbine engine components is the principal cause of failures in aircraft engines, representing a major threat to the safety and readiness of the aircraft fleet. This can result in essentially unpredictable failures of engine components, particularly turbine blades and disks, due to the premature initiation of fatigue cracks at small defects and their rapid propagation under oscillating loading conditions.

Clearly, fatigue has not been considered to date in their studies on various FSLW of Al to Ti joints. Without fatigue property data and the understanding of fatigue behaviour of the weld structures, engineering applications of the structures subject to cyclic loading cannot not be considered neither. Hence, the study of fatigue behaviour of FSLW of Al to Ti is necessary for establishing useful engineering data for its various areas of applications which are required by engineers, designers, and manufacturers.

Following the above brief introduction to FS Welds, and before detailing the aspects of this thesis, a detailed literature review is presented to describe the relationship between process parameters (ω, ν) and hook formation, fracture behavior, and stress distribution during tensile and tensile and shear testing of FSW dissimilar alloys in butt configuration is presented, in section 1.2. An FSL weld configuration is presented in section 1.3 with a detailed review of the joint formation and the effect of interface microstructure on fracture behavior of Al to Ti FSL welds.

As has been explained, Al-Ti FSW is currently not being used because of lacking engineering data on fatigue properties of FSW Al-Ti alloys. For a better understanding, studies on fatigue of Al/Al FSL welds from literature are presented in section 1.4 as this will provide a comparative basis for judging the fatigue strength values of AA2024 to Ti6Al4V welds made using FSW and fatigue tested and analysed in this study. Finally, following the detailed literature reviews, the scope and sequence of this PhD research will be presented in section 1.5.

1.2 A Brief Overview of Al to other High Melting Point Alloy Friction Stir Butt Welding

An overview of microstructure features in the interface region and tensile properties of the welds of dissimilar metals (Al-to-steel, Mg-to-steel, Al-to-Ti, Al-to-Cu, and Mg-to-Al) made using FSW has been provided by Simar and Avettand-Fènoël [15] in 2016. A major observation in this overview is that interface intermetallics still strongly influence the strength of the weld strength, although the formation and growth of interface intermetallics are in solid-state except during FSW of Mg to Al. Since that 2016 review, a high number of research publications have continued on the subject of that review.

In this section, the review on literature up to date on the research of FSW and FSLW is directed to Al alloy to high melting alloys (Cu, steel and Ti alloys) welding. A detailed review of microstructures of interface region and fracture strength of FSW dissimilar alloys are presented in order of FS butt and followed by FSL welds. Firstly, a detailed review of the microstructure of the interface region and fracture strength of Al to Cu FSW (butt and FSL weld) is given. Then, interface microstructure and fracture strength of Al/Steel FSW (butt and FSL welds) are presented. Finally, interface microstructure and mechanical strength of Al to Ti FSW (butt and FSL welds) are presented. These three interface couples are representatives of FSW of joint couples with large temperature melting point difference joints established by diffusion of atoms at the weld interface. The Al to Ti FSL welds are presented in particular to critically review the work of various researches on the tensile strength of FSL welds and their microstructures. The overall review includes the formation of intermetallic growths and how various studies have improved in terms of mechanical tensile properties of Al to Ti FSL welds by optimizing test parameters and variables.

However, one of the fundamental engineering considerations is the fatigue properties of Al-Ti FSL welds in structures which this review will not present due to lack of data. Therefore, this has become the main study of this research project.

1.2.1 Friction Stir Butt Welding of Al to Cu Alloys

Sare and Cakir[16], in their 2016 article showed that insufficient mixing as shown in Figure 1-5c of Al to Cu during welding was found to have the cause for ineffective joining of the plates and hence having low tensile strength. However, an optimum tensile strength of 100 MPa was reached at 1330 rpm with a 1 mm tool offset position and traverse speed of 20 mm/min. In their experimental setup, the pin offset was only 1 mm towards Al side while the bulk portion of the pin (i.e., 3 mm) on Cu side for the Al to Cu FS butt weld. The microstructures of base materials (Figures 1-5a and 1-5b) and FS welded with an insufficient mixing and a Cu bulk drawn into Al matrix (Figures 1-6c and 1-6d). More pin extrusion of the bulk Cu parts creating more void defects with bulk particles of Cu parts stirred into Al matrix can lead to poor weld strength. Another critical factor that is unavoidable during FS welding is the formation of intermetallic compound (IMC) layers. The presence of IMC layers at the weld zones is revealed with XRD pattern as shown in Figures 1-6.

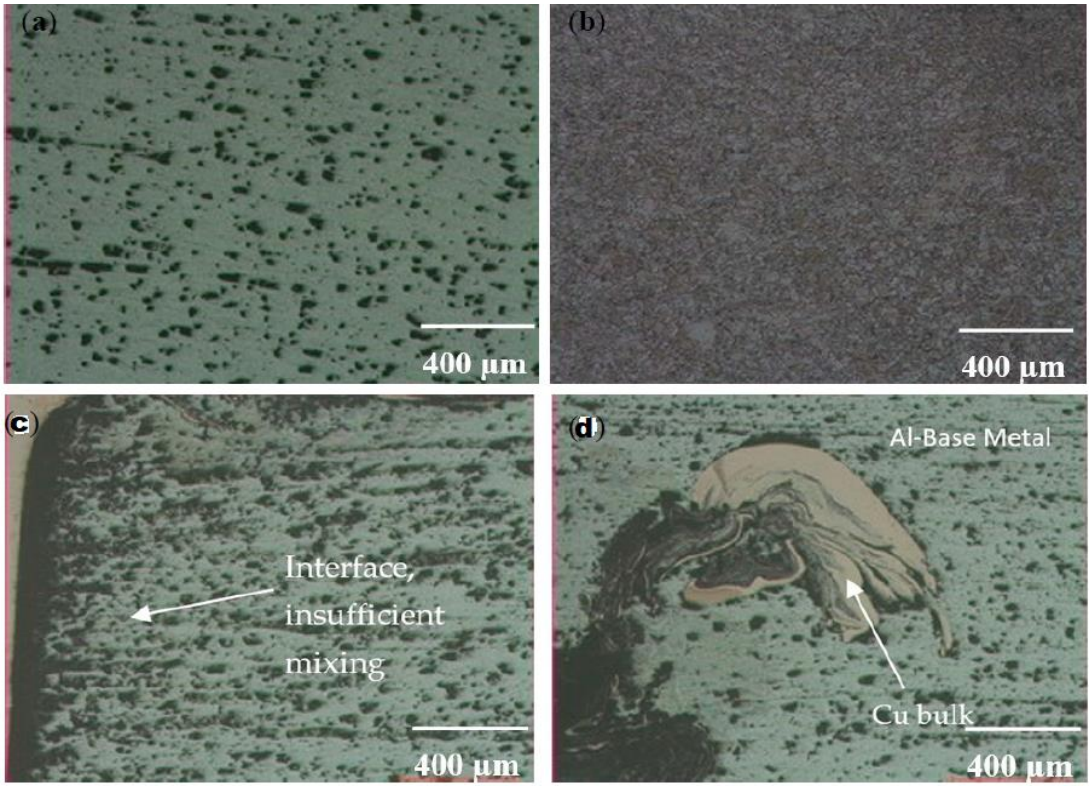

Figure 1-5 Microstructures of base materials (a) Al-1050; (b) Cu and (c) Al side, (d) Nugget Zone for welds done at ω = 630, υ = 50, tool offset = 1 mm specimen [16].

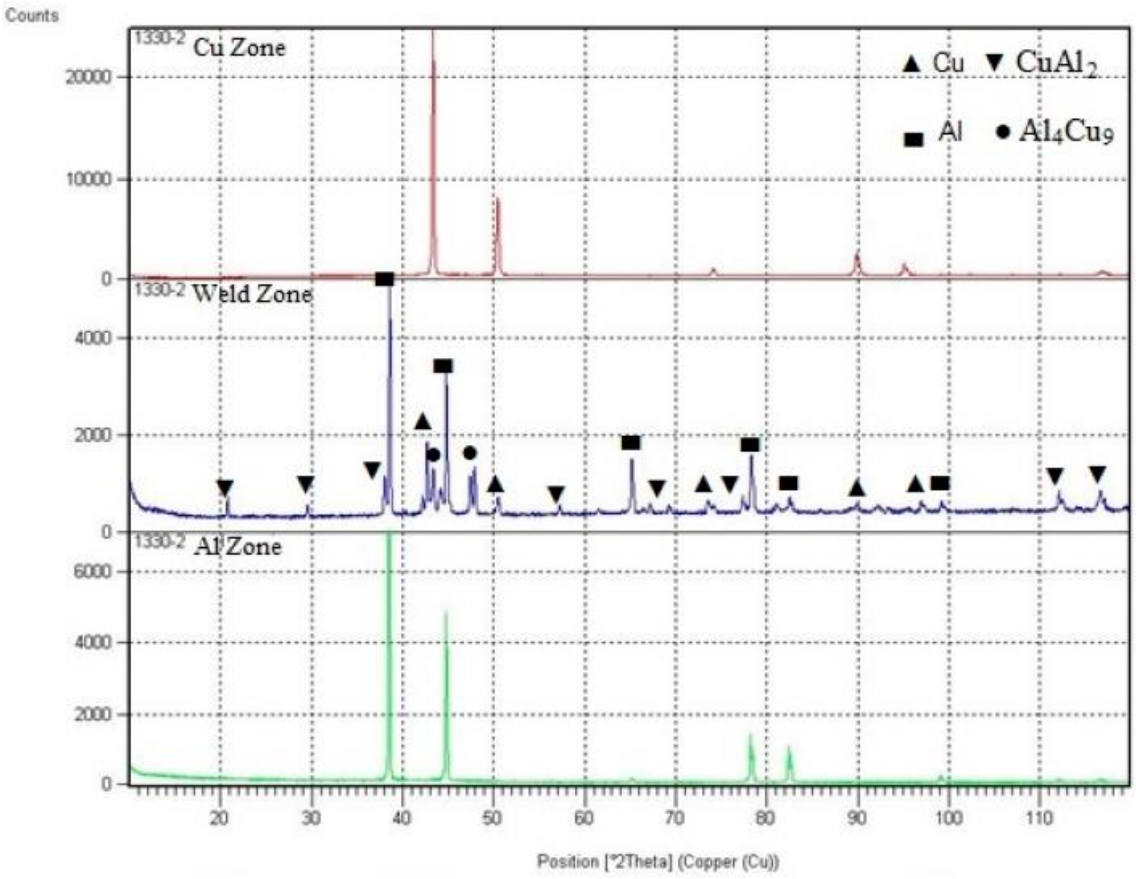

Figure 1-6 X-ray diffraction (XRD) graphs of base materials and weld zone [16].

Shankar et al. [17] have also evaluated the joint strength of Al-Cu FS butt weld relating to welding parameters and pin offset with the formation of IMCs on the material flow and distribution of Cu-Al at the weld interface and examined the effects of these factors on the tensile characteristics of the joint. The tensile strength of 101 and 102 MPa were archived at high rotational tool and weld speed with a reduced IMC layer of 0.3 µm relative to 0.8 µm at the lower tool speed and weld speed. The reduced IMC layer was obtained by increasing the weld travel speed from initial 128 mm/min to 213 mm/min which avoided intense heat enhancement at the Al/Cu interface which will increase IMC growth via diffusion. The intermetallic layer formed at the interface due to interdiffusion at optimum tool and weld speed contributes to a better tensile strength of the joint. The probe offset has a great influence on the weld nugget and MSZ zones. The zero tool offset results in cracks and voids which reduces tensile strength and increases hardness due to large intermetallic particles which become conglomerated at the mix stir zone (MSZ) whereas the tool offset of 1 mm towards the Cu side. Figures 1- 7a to 1-7c shows fracture features from 1 mm tool offset having fine fragments of Cu distributed partially, non-uniform, and uniformly whereas with 0 mm offset are large conglomerated Cu fragments in the stir zone as shown in Figures 1-7d and 1-7e.

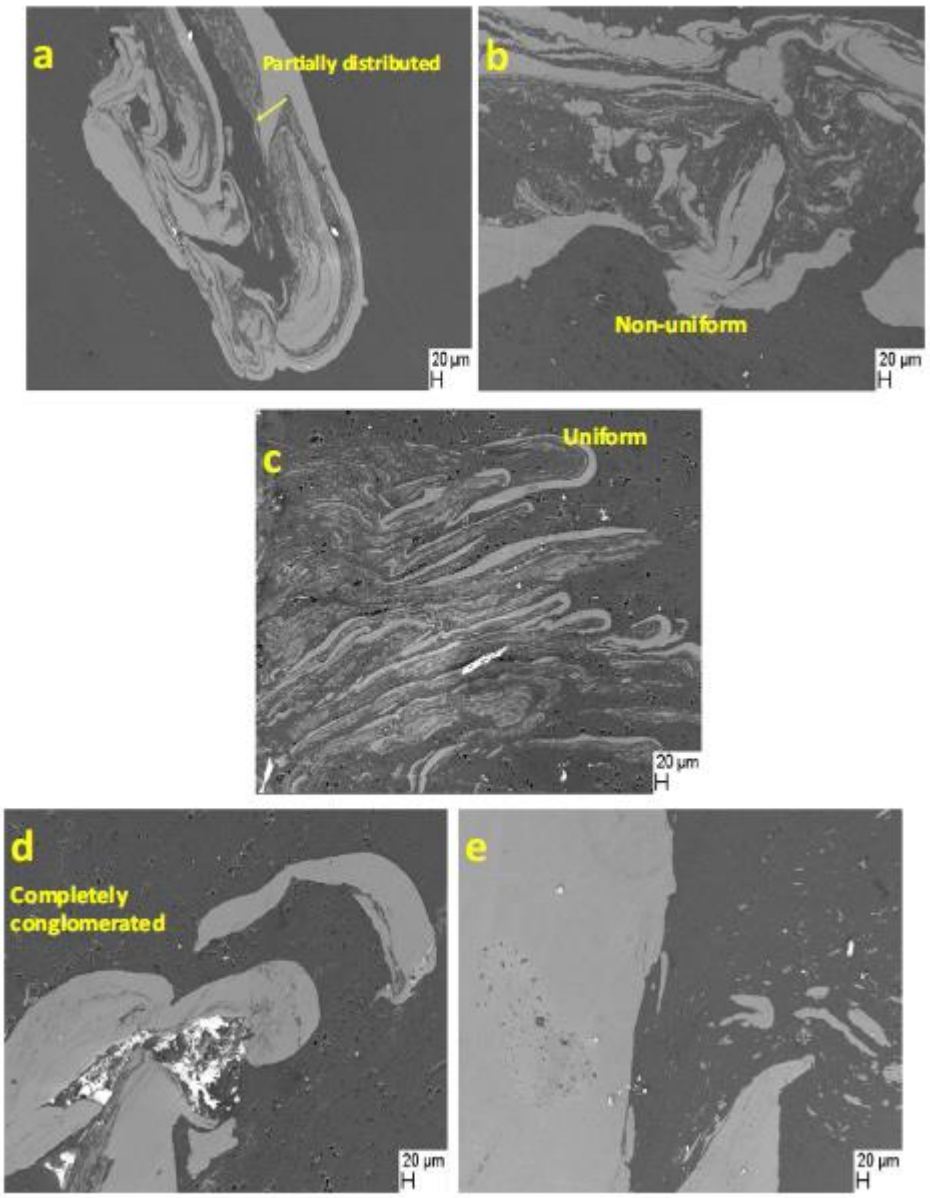

Figure 1-7 Samples prepared at 1 mm offset and at a welding speed of a) 128 mm/min b) 160 mm/min c) 213 mm/min. Samples prepared at 0 mm offset and welding speed of d) 128 mm/min e)160 mm/min [17].

Sachindra and Chattopadhyaya [18], in their 2019 article investigated and achieved 89 MPa tensile strength. This result is comparable with most Al to Cu FSW butt joints in literature. A similar study by Sahu et al. [19] reported that both tensile and hardness tests were performed to evaluate its mechanical properties. The microstructure of the weld zone revealed the existence of lamellar intercalated structure with dispersed Cu particles randomly distributed over the aluminum substrate with predominant flow pattern characterized by onion rings, vortex swirl, and layered structure were observed in the interfacial region as shown in Figure 1-8 labelled with different fracture features.

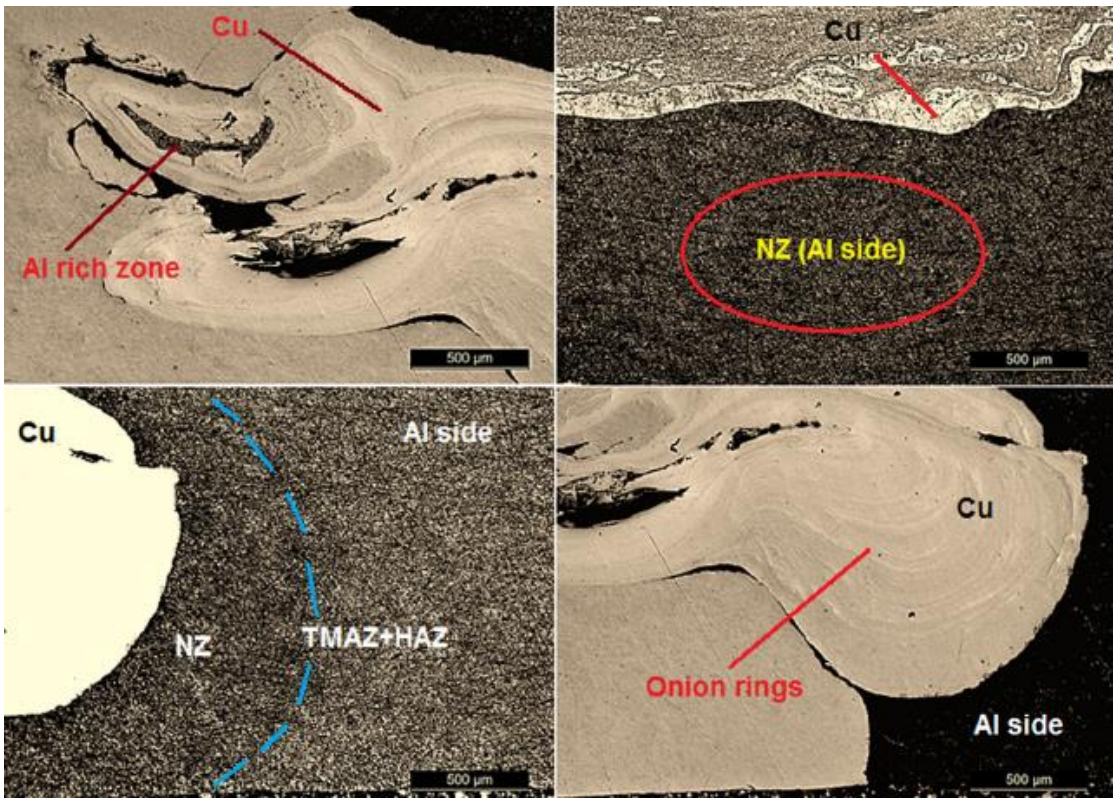

Figure 1-8 Material flow pattern as observed for specimen S1. ω = 1120 rpm, υ =125 mm/min, tool offset = 0 mm [19].

Also, the formation of IMC was observed at the weld interface as revealed by XRD pattern as shown in Figure 1-9 which largely influences the mechanical behaviour at the weld interface. The major IMC being revealed under XRD spectra are ($Al+Al_2Cu$) and ($Al+Al_2Cu+Al_{3.892}Cu_{6.10808}$) With XRD analysis at interfacial region covering equidistance in both AL and Cu substrate. IMCs are integral part of the joint formation. However, access of the intermetallic layer has been reported in literature as detrimental which means an optimum level of it is necessary for a high strength welds under predetermined process parameters such as tool rotation speed (ω), weld speed (υ) and tool offset distance.

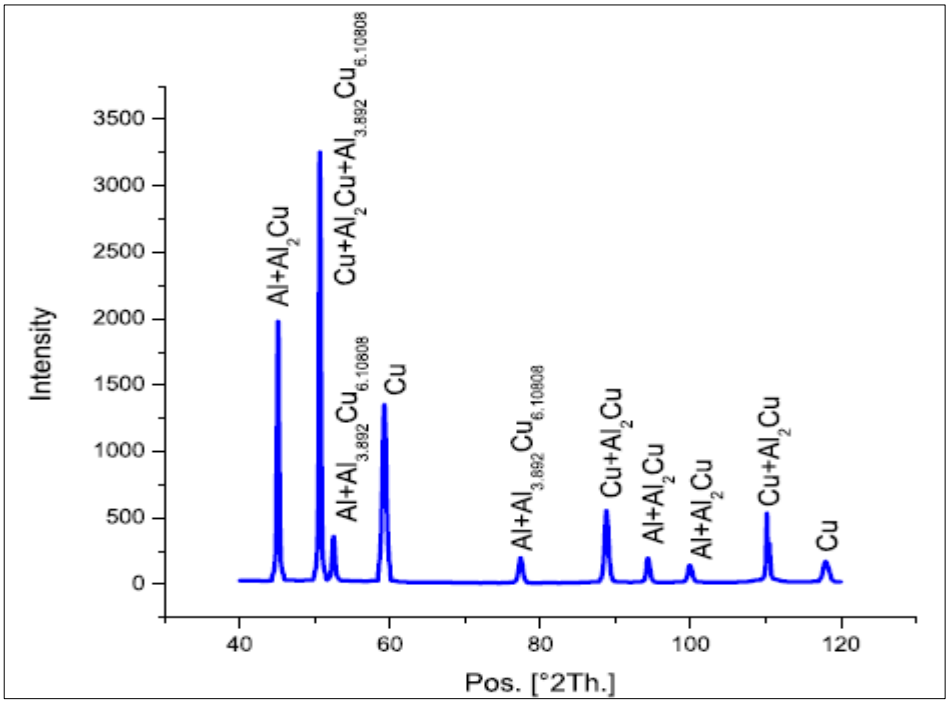

Figure 1-9 XRD spectra taken at the interface between AA6063 and Cu in the friction stir welded specimen S2. ω = 1120 rpm, υ = 100 mm/min, tool offset = 0.95 mm [19].

In addition, the elemental analysis performed between the two alloys at Al-Cu interface on the weld sample revealed the presence of major Al and Cu elements with their minor alloying elements (O, C and Mg) as shown in Figure 1-10. However, elemental analysis only based on the XRD spectra spot analysis so it may not correctly reveal the exactly amount of IMC for the whole weld fracture being examined.

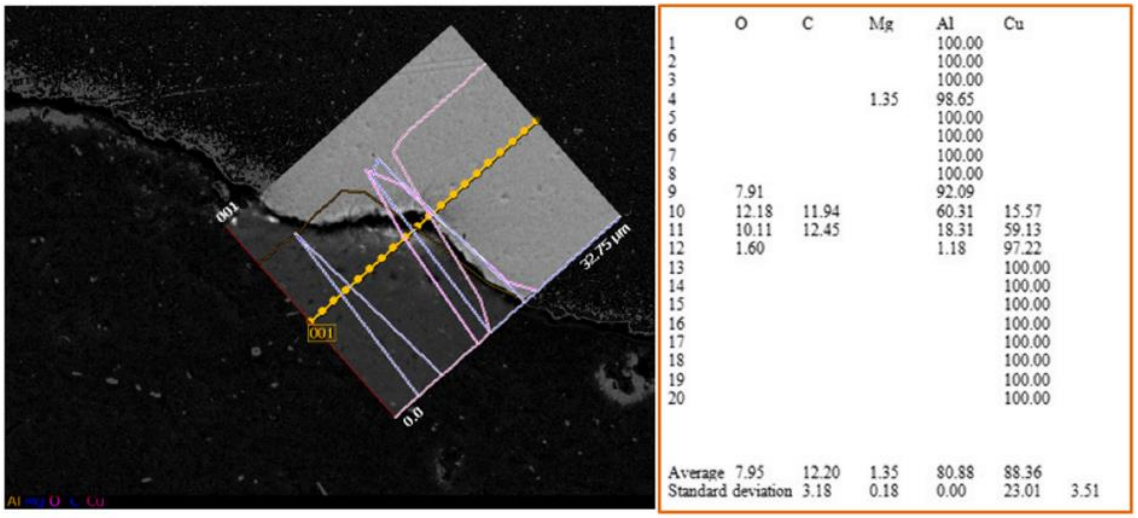

	O	C	Mg	Al	Cu	
1				100.00		
2				100.00		
3				100.00		
4			1.35	98.65		
5				100.00		
6				100.00		
7				100.00		
8				100.00		
9	7.91			92.09		
10	12.18	11.94		60.31	15.57	
11	10.11	12.45		18.31	59.13	
12	1.60			1.18	97.22	
13					100.00	
14					100.00	
15					100.00	
16					100.00	
17					100.00	
18					100.00	
19					100.00	
20					100.00	
Average	7.95	12.20	1.35	80.88	88.36	
Standard deviation	3.18		0.18	0.00	23.01	3.51

Figure 1-10 Elemental analysis (EPMA) made at interface between two dissimilar materials of friction-stir welded specimen S2. ω = 1120 rpm, υ = 100 mm/min, tool offset = 0.95 mm [19].

A recent study by Hou et al. [20], in their 2020 article investigated the heat flow due to the complexity of obtaining accurate data for their weld. Their maximum tensile strength achieved

was 152 MPa which is a good weld strength value. A more recent study by Manohar and Mahadevan [21], in their 2020 article showed that the optimum UTS of 191 MPa and 184 MPa yield strength were achieved. The presence of excessive IMCs was largely avoided in this experimental process and hence resulting in significant improvement in the mechanical strength compared to other works cited here. Figure 1-11 shows parent metals, Cu on the right and Al on the left. Their main aim was to avoid pin penetration by using pin-less tool at Al to Cu interface faying surface because of their very thin (0.8 mm thick) parent metals which may be destroyed completely without forming the joint; however, authors have not clearly described the fact that the weld is formed due to stirring and forging of Cu onto Al as shown in Figure 1-12 and it is difficult to know the total weld width to make a good comparison with others in the literature.

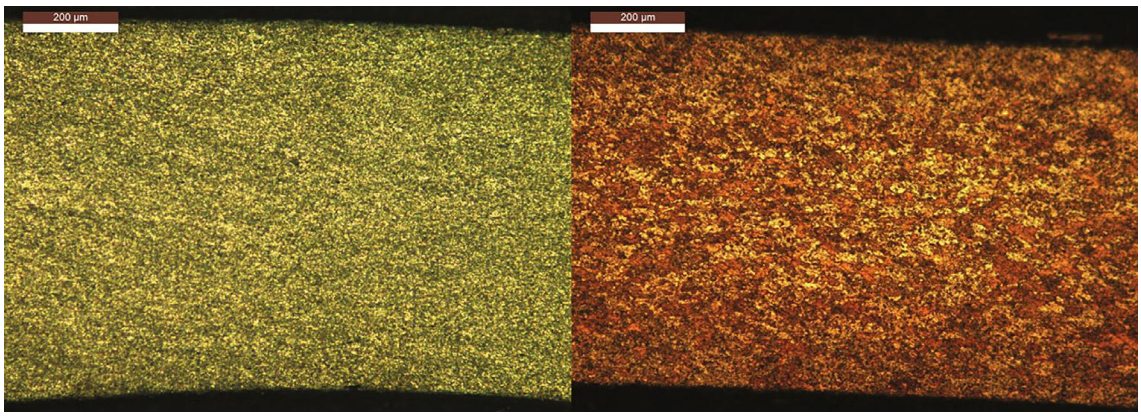

Figure 1-11 Parent metals (6061AA-Left and Pure Cu-Right) observed at 100x magnification and 200 µm resolution [21].

Figure 1-12 shows clearly Cu parts having been drawn into Al side with the pin-less tool from the top surface contact. The pin-less FSW strategy is of course useful because the joint is seen to be formed by two approaches. The first being the joint established due to stirring and forging on the top surfaces of the Al to Cu butt configuration and the second joint is due to the diffusion of elements at the Al-Cu interface during FS welding. Last, the improved mechanical strength is mostly attributed to a reduction in IMC layers as thick IMCs have been reported in the literature [17, 20, 22-25] as having increased in hardness and detrimental for weld strength. Although the paper presents a high-quality work with improved mechanical strength which are comparable to the parent metals, authors have not specifically provided the detailed nature of the pin-less contact at the Al/Cu butt interface in terms of downforce and weld width to achieve such a weld strength almost near to parent metals with their µFSW.

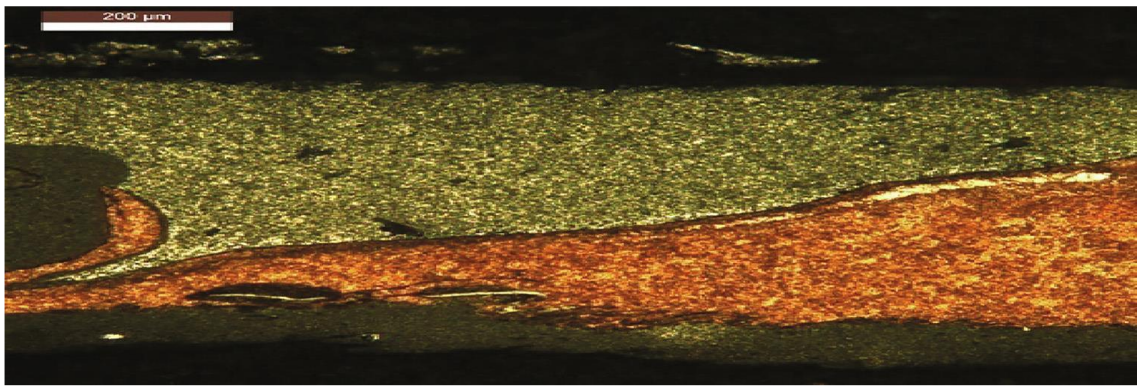

Figure 1-12 WNZ for µFSW-2 observed at 100x magnification and 200 µm resolution [21].

According to Al-Cu binary phase diagram (Figure 1-13) for the Al-Cu system, the feasible intermetallic layers start forming at 300°C and above. Therefore, the formation of IMC layers mainly Al_2Cu phase at Al/Cu interface is considered to provide metallurgical bonding yet it is detrimental in large quantity as it is hard and brittle.

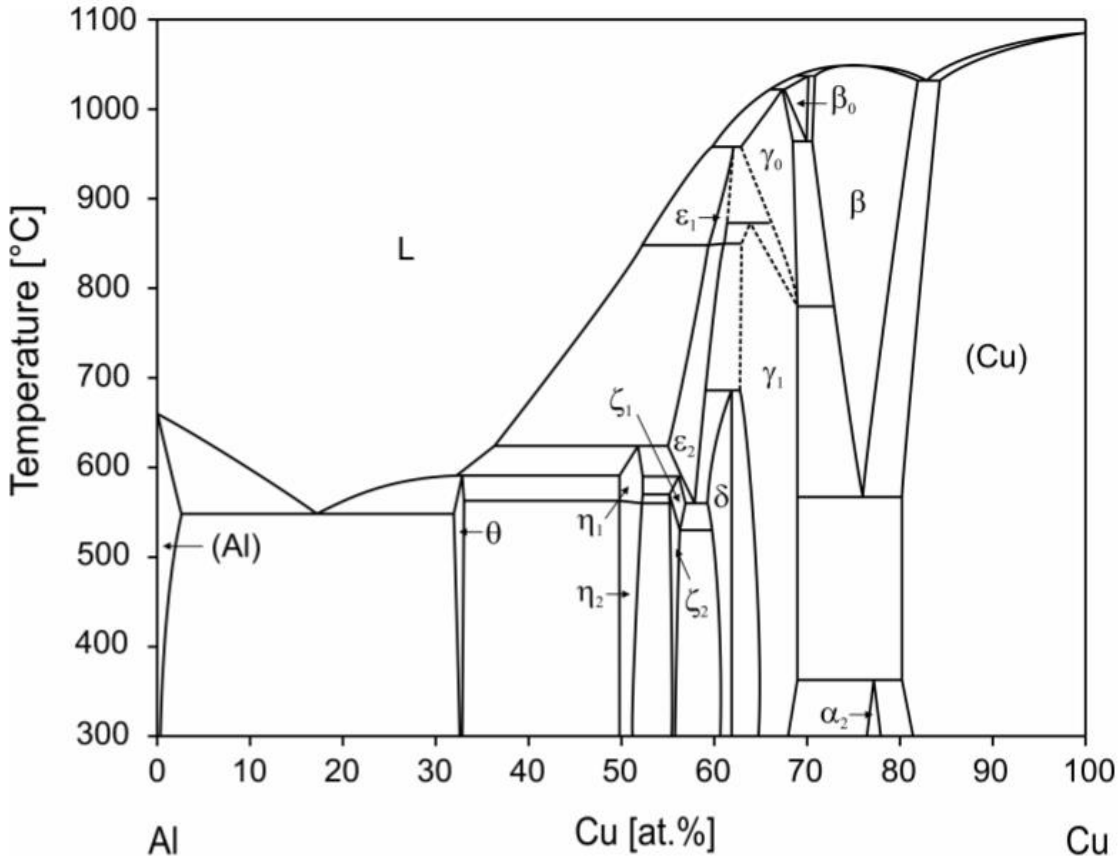

Figure 1-13 The Al-Cu phase diagram showing different level of phases present at various temperature range [26].

The information available in the literature on FS butt welding of Al alloy to Cu is summarized in Table 1-1, including the type of aluminium alloy, FS parameters, tool/pin sizes, Al alloy and Cu thicknesses, tool offset distance marked "X" as shown in Figure1-14, the highest tensile strength of FS weld and the tensile strength of Al alloy before FS, and fracture location during testing. It

should be noted that, in regards to these studies, there has not been a comparative discussion in the literature on which FS condition may have resulted in the best weld strength. How a strength may be regarded as a high weld strength has not been properly defined and explained.

Observing the weld strength values in Table 1-1 may have suggested that the FS condition reported by Manohar et al. [21] has resulted in the highest strength value and thus the best weld. The sample fractured at the interface of the weld. Thus, it may be suggested that 191 MPa is the strength of the weld interface and the strength of MSZ is higher. Base metal strength is 290 MPa and thus a strength higher than 191 MPa in MSZ is reasonable. For the best weld strength value of using 1050 Al alloy at 102 MPa with the sample fractured at MSZ, reported by Celik and Cakir [16], base metal strength is 100 MPa, and thus significantly higher strength in MSZ is not expected. Fracturing in MSZ with 102 MPa tensile strength value is very reasonable. Then how much higher the strength of the weld interface than 102 MPa is however unknown.

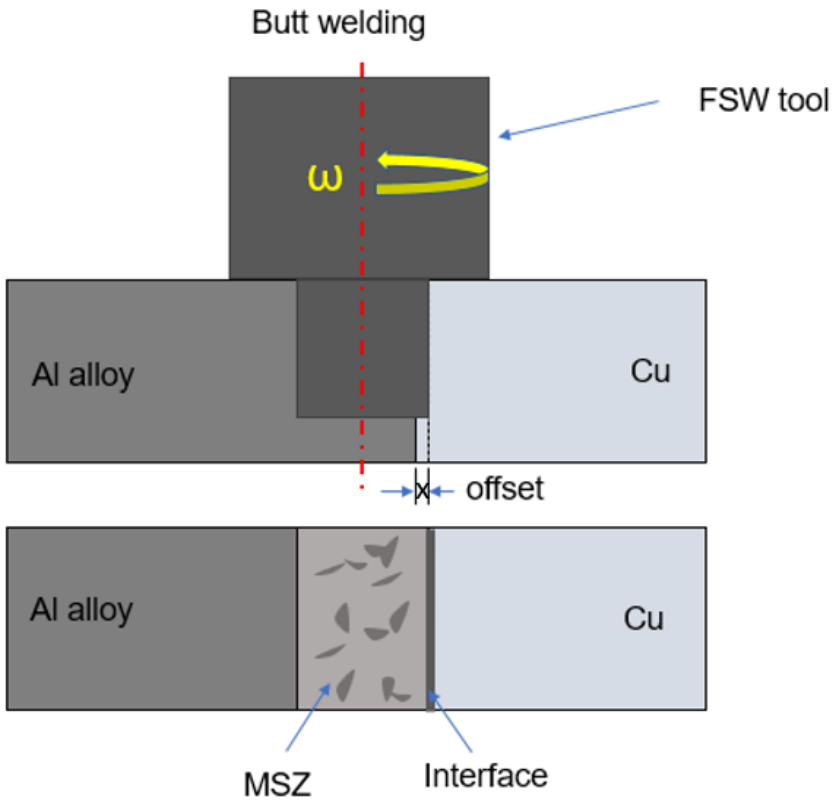

Figure 1-14 Schematic illustration of FS butt weld showing MSZ and weld interface. Tool offset size x is normally between 0.1-2 mm.

The same can be referred to studies by Sahu et al. [19] and Xue et al. [27]. Their base metal strength values are low, although higher than the value of 1050 aluminium alloy. Fracture location in MSZ means the strength of the weld interface is not known. In a comparative sense, the FS condition reported by Manohar and Mahadevan. [21], results in a higher weld strength than that of Sahu et al. [19] and Hou et al. [20], fracturing at the interface. In all other studies of using 1050, 6063, and

1060 aluminium alloys, the strength has been affected by the weak base metal and they thus have provided little information on assessing what FS condition may result in a good Al alloy to Cu weld. This is summarised in Table 1-2. A valid point from these studies listed in Table 1-1 may be that, provided a strong Al alloy is used, the weld strength of the Al alloy to Cu FS butt weld can reach as high as 191 MPa. Despite Ref. [20] with the base Al alloy having the highest strength value of 310 MPa, in all data summarized in the table, and fracturing at the interface as Ref. [21], its strength value is 152 MPa which is low. This difference in in strength values may be due to the effects of their choices of selecting the process parameters.

Table 1-1 Strength and welding parameters of the best friction stir butt welds of Al to Cu.

Base Material Thickness [Ref]	Tool speed (rpm) Travel speed (mm/min) Tilt angle	Pin Profile (mm)	Tool offset (mm)	Specimen Width (mm)	FSW Tensile Strength (Al BM) (MPa)	Fracture location
1050Al/Cu (4mm-4mm) [16]	ω = 1330 v = 20 $\angle$ = 1.5°	$OD_{shoulder}$=18 OD_{pin}=M4 L_{pin} = 3.87	1 Al (3 Cu)	6	**100** (105)	MSZ
1050Al/Cu (6mm-3mm) [17]	ω = 640 v = 213 $\angle$ = 1.45°	$OD_{shoulder}$ = 24 OD_{pin} = 5 L_{pin} = 2.9	1 Cu	22	**102** (105)	MSZ
1050Al/Cu (6mm-6mm) [18]	ω = 1400 v = 63 $\angle$ = 0°	$OD_{shoulder}$ = 28 OD_{pin} = 6 L_{pin} = 5.8	2 Al	5	**88** (105)	MSZ
6063Al/Cu (3mm-3mm) [19]	ω = 1120 v = 100 $\angle$ = 0°	$OD_{shoulder}$ = 18 OD_{pin} = 5 L_{pin} = 2.3	1 Cu	20	**103** (145)	MSZ
6061Al/Cu (3mm-3mm) [20] 2020	ω = 560 v = 32 $\angle$ = 0°	$OD_{shoulder}$=15 OD_{pin} = 5 L_{pin} = 2.7	0.95	8	**152** (310)	Interface
6061-T6/Cu (0.8mm-0.8mm) [21]	ω = 1800 v = 80 $\angle$ = 0.5°	$OD_{shoulder}$ = 15 OD_{pin} = -0 L_{pin} = 0	0	12.5	**191** (290)	Interface
1060/Cu (5mm:5mm) [27]	ω = 600 v = 100 $\angle$ = 0°	$OD_{shoulder}$ = 18 OD_{pin} = 5 L_{pin} = 4.5	0	10	**110** (120)	HAZ

*Notes: If many welds are performed, the welding parameters providing the best strength are reported. v, welding speed/mm min-^{1}; ω, rotational speed/revmin-^{1}; $\angle$, tilt angle; tool offset is reported as the length of insertion of the pin inside the Cu plate; strength is the tensile strength at fracture/(MPa); $OD_{shoulder}$, Outside shoulder diameter; OD_{pin}, Outside pin diameter; L_{pin}, length of pin or pin height.

Table 1-2 Al-Cu FSW Fracture locations and UTS reached.

[Ref.]	Base Metal	Failure location	UTS (MPa)	Interpretation	Comments
[21]	AA6061-Cu (0.8mm:0.8mm)	Interface	191	MSZ>191	MSZ Good
[27]	AA1050-Cu (5mm:5mm)	MSZ	110	Interface>110	Interface Good. How good?

1.2.2 Friction Stir Butt Welding of Al to Steel Alloys

Table 1-3 summarizes the tensile strength values reached in reported papers, each being the highest in the respective paper, as a function of the welding conditions for Al alloy to Steel dissimilar butt welds. The strength values of the welds range from 123 MPa to 211 MPa (Table 1-3, column 6). The tool offsets range from 1 mm to 2 mm towards the Steel plate. A larger tool offset favors a higher heat input, thus more plasticization of steel and can lead to the formation of large intermetallic layers. Weld efficiency is calculated based on the maximum tensile strength of the weld against aluminum alloy base metal. However, where there is no mention of aluminum grade and temper, it is difficult to figure out with insufficient information. However, the quality of the weld can be assessed based on the tensile strength of each weld having the same specimen (weld) width and grade, it is possible to compare weld efficiencies.

Table 1-3 Strength and welding parameters of the best friction stir butt welds of Al to steel.

Base Metals Thickness [Ref.]	Tool speed (RPM) Weld speed (mm/min) Tilt angle	Pin Profile (mm)	Specimen Width (mm)	Tool offset (mm)	Tensile strength (Al BM) (MPa)	Fracture location	Eff. (%) Al (BM)
AA5052H32/ Steel (3mm-3mm) [28]	ω = 500 v = 45 $\angle$ = 1.5°	$OD_{shoulder}$ =- OD_{pin} = 4 L_{pin} = 2.7	6	2 Fe	**188** (207)	SZ Al side	91√
AlSi5/ Steel (1.5mm-1.5mm) [29]	ω = 1600 v = 80 $\angle$ = 0°	$OD_{shoulder}$ = 13 OD_{pin} = 5 L_{pin} = 1.5	10	1 Fe	**207** (259)	SZ Al side	80√

AA6181-T4/Steel (mm3-3mm) [30]	ω = 600 v = 00 $\angle$ = 3°	$OD_{shoulder}$ = 25 OD_{pin} = 2.5 L_{pin} = 2.7	6	0.5 Fe	**123** (267)	SZ	46
Al (99.5wt) & AlSi5/ Fe DC01 2mm-2mm [31]	ω = 400 v = 300 $\angle$ = 0°	$OD_{shoulder}$ = 13 OD_{pin} = 6.5 L_{pin} = 2	5	0	**71.6** (95)	SZ	60√
					115 (120)	SZ	77√
AA5083/Fee SS400 2mm-2mm [32]	ω = 250 v = 25 $\angle$ = 0°	$OD_{shoulder}$ = 15 OD_{pin} = 2 L_{pin} = 1.9	40	0.2	**240** (275)	Interface	86√

*Notes: If many welds are performed, the welding parameters providing the best strength are reported. v, welding speed/mm min-^{1}; ω, rotational speed/revmin-^{1}, offset is reported as the length of insertion of the pin inside the Fe plate; strength is the tensile strength at fracture/(MPa); $OD_{shoulder}$, Outside shoulder diameter; OD_{pin}, Outside pin diameter; L_{pin}, length of pin or pin height.

Friction stir butt welding is one of the methods of solid-state joining processes in FSW that can be conducted between two similar or dissimilar alloys. A rotating tool pin made of high steel H13 is plunged into the base metal faying interface as shown in Figure 1-15. The rotational tool and the weld traverse speed are predetermined before applying FS butt weld. For welds involving FS butt welds of the same alloy, the tool pin is positioned in the centre of the weld. However, with FS butt weld involving high melting point alloys, a small amount of tool offset is allowed on parent metal of the high-temperature side as shown in Figure 1-15 (1.9 mm tool axis offset from the faying surface), the rolling direction of plates are positioned in parallel with the direction of the rotating tool for smooth flow of plasticized materials.

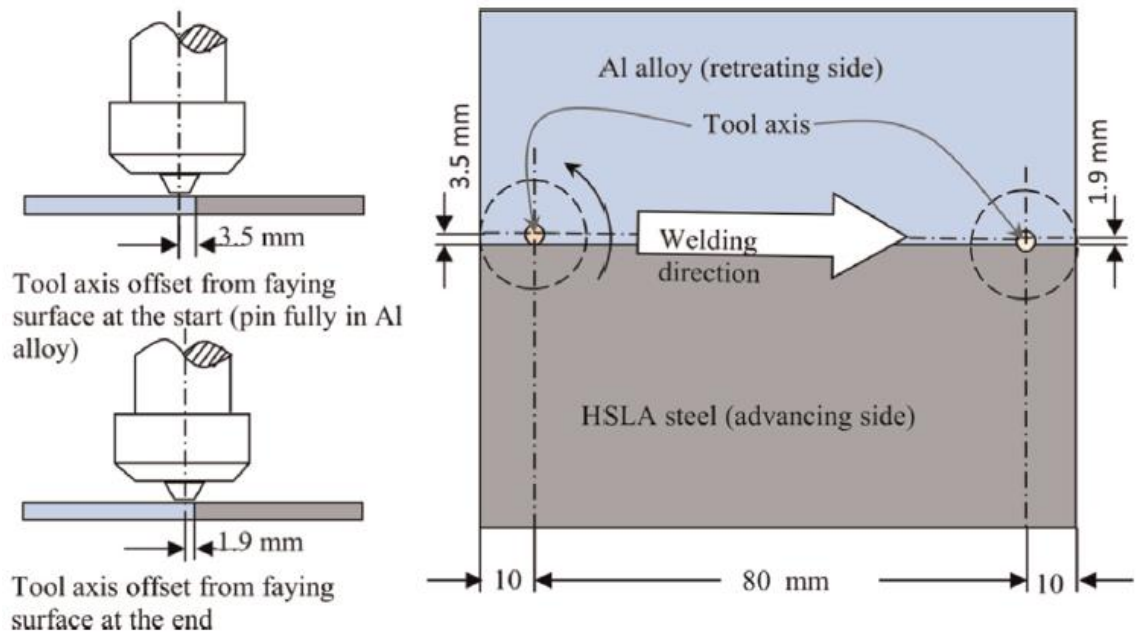

Figure 1-15 Schematics of tool axis offset used for tool T1 [28].

Coelho et al. [29], in their 2012 article showed that the mechanical strength and their relationships to the microstructure of a FS butt welded Al to Steel (HSS). The comparative study done was to find the difference in the joint efficiency between two grades of HSS (DP600 and HC260LA) and AA6181-T4 alloy while maintaining the same welding parameters. They found that the ultimate tensile strength was equal to 80% of the Al BM for both HSS FSW materials. Similarly, Kundu et al. [30], their 2013 article studied the microstructure and mechanical strength of Al to steel FS butt weld on the characteristics of interfacial microstructure and strength properties of the joint but by varying the tool rotational speeds. They discovered that a maximum tensile strength of 123 MPa (86% of Al BM) at the rotational tool and transverse weld speed of 600 RPM and 100 mm/min respectively. Ramachandran et al. [28], in their 2015 article investigated the effect of tool axis offset and geometry of tool pin profile on the characteristics of the dissimilar FS butt weld. They noticed that the highest joint strength was obtained with TC pin profile at 10° taper angle is 188 MPa with 2 mm tool probe offset towards Al side. Since the tool offset is more on the steel side, so more Fe scraps would be expected and thick IMCs would be present in the MSZ. Anaman et al. [33], in their 2019 article showed that major IMC layers at the weld interface at the top and bottom layers were mainly composed of $FeAl_3$ and Fe_2Al_5, respectively. Authors have extensively supplied sufficient data and discussions on the formations of IMCs and it is also shown in Figure 1-16 that at the interface where the large amount of IMC layer has a corresponding high hardness which is detrimental for mechanical strength. However, it is inevitable that the large number of IMCs at the interface is critical and optimum process conditions should be considered to reduce the formation of thick IMC layers and hence improve its mechanical strength.

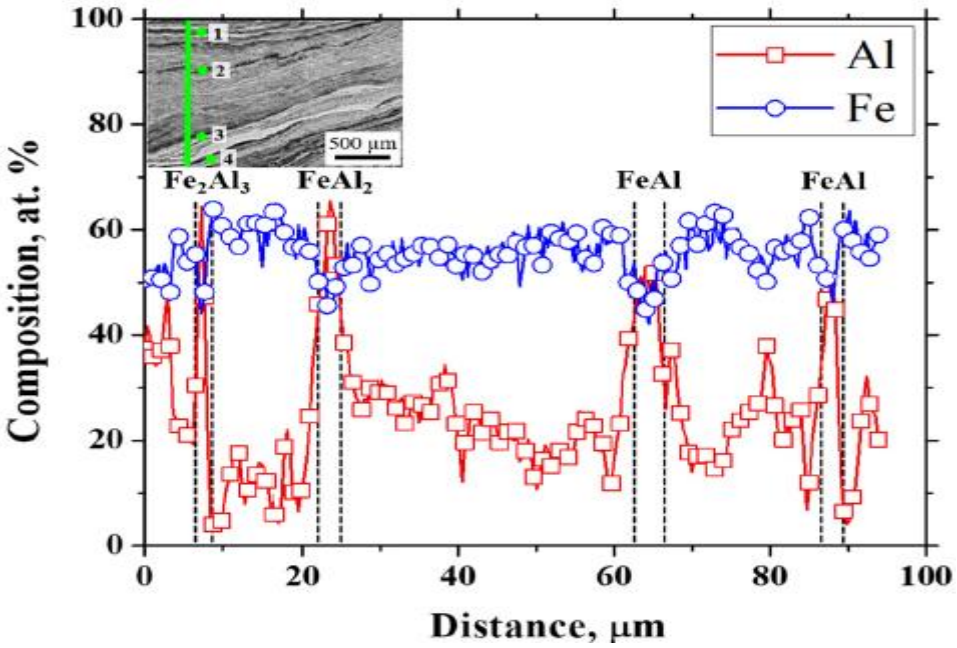

Figure 1-16 Variations of Al and Fe elements in the mixed layer with an EDS line scan where the green line is marked in the inset as illustrated in the upper left corner [33].

A binary Fe-Al phase diagram reveals the phase forming base temperature of 400°C as shown in Figure 1-17) which is 100°C higher than the Al-Cu system and requires more activation energy to initiate intermetallic growths.

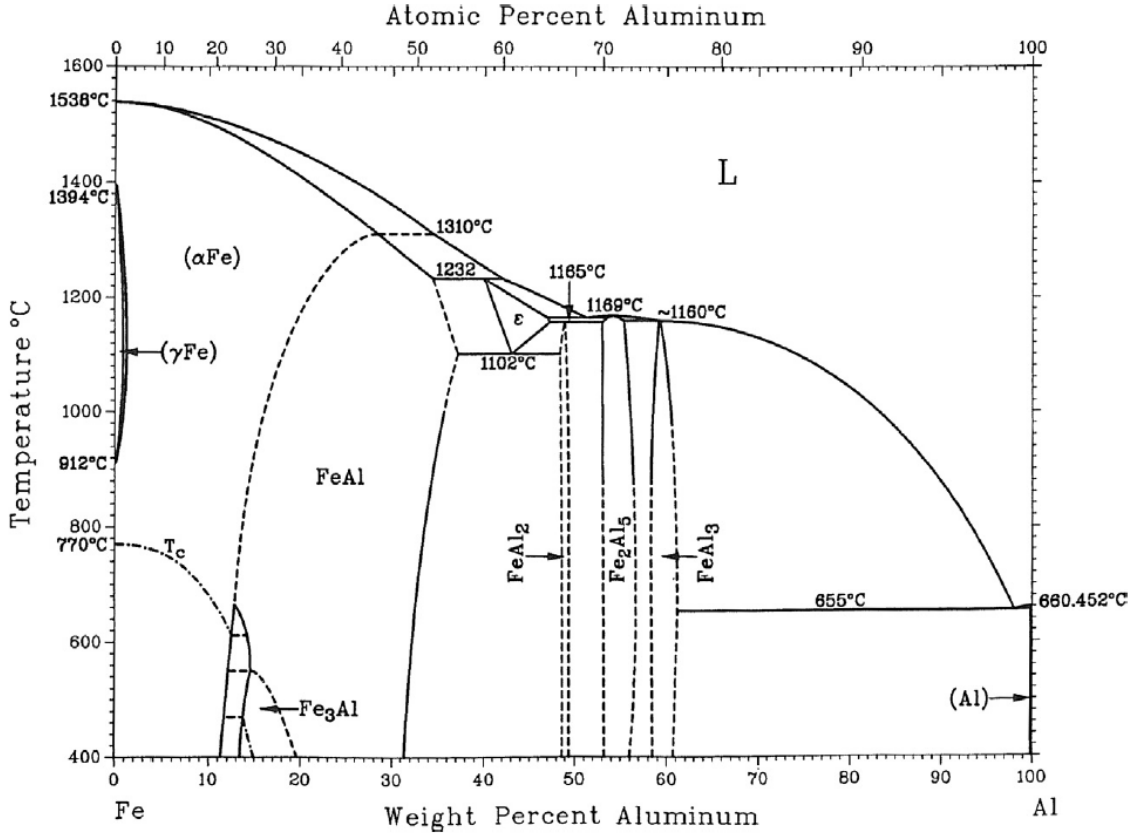

Figure 1-17 Fe–Al binary phase diagram displaying different phases present at various range of temperatures [34].

The various studies on FS butt welds of Al to Steel available in literature have been gathered and presented in Table 1-3. The various process parameters such as tool speed, weld speed, tool tilt angle, and amount of pin offset to the high strength alloy side of the faying have been identified. The offset being zero is when the rotating thrusting pin is just touching the high-temperature alloy side at the faying interface while the whole pin is on Al side as shown in Figure 1-18. Besides, the base metal thicknesses, specimen width, and fracture locations for each weld have also been identified and shown. The best tensile strength of the welds is identified as having 240 MPa [32] and fractured at the interface and the others, Ref. [9-12] fractured at the SZ. This implies that the joint at the interface is strong. However, in Ref. [32], fracture occurred at the interface and yet the tensile strength is comparatively high (240 MPa). This high tensile strength is attributed to its parent metal, Al5083 aluminium which has 275MPa. It should also be noted that the weld efficiency cannot be used as a basis for weld strength comparison with others to say it is either best or poor because each weld strength depends on its base metal and optimum process conditions selected.

In FS butt welding, pin offset was an important part of welds involving dissimilar Al to other high-temperature alloys. Pin offset at zero by Springer et al. [31], means the pin insertion and downward thrust during welding is when the edge of the pin is not overlaying but just touching the top surface of the high-temperature alloy side as shown in Figure 1-18, between Al and steel. However, from the literature gathered, there is no critique on why applying the same pin offset conditions may have also resulted in different strength values. Examining the strength values of the parent Al alloys have different strengths and this could be the major contributor factor despite the selection of optimized parameters for their respective tests. It can be noted from Tables 1-3 that selecting high-strength Al alloy is advisable for high strength structural requirements.

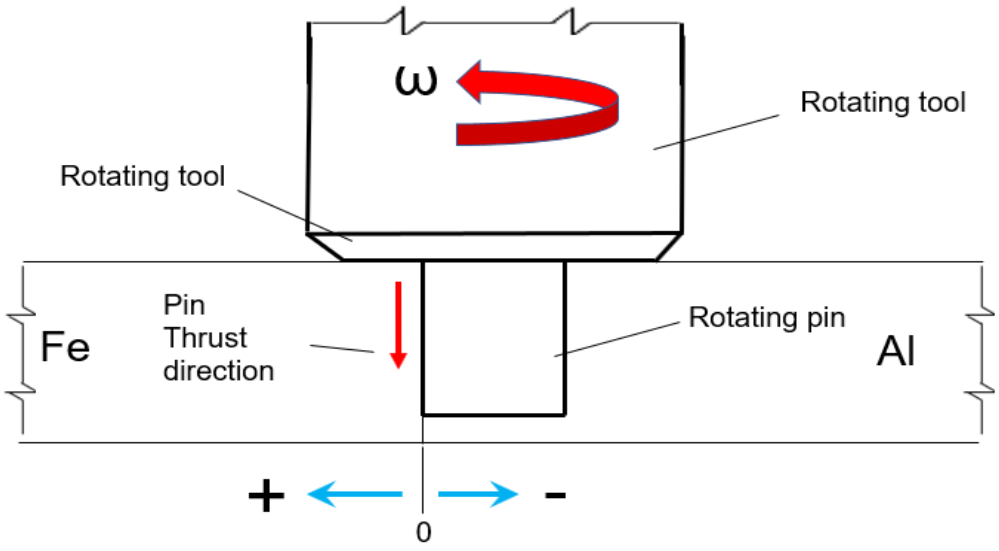

Figure 1-18 Schematic view of the cross-section perpendicular to the weld interface explaining the pin position and the coordinate.

A point illustrated from Table 1-3, as explained above, is that strength of the FS butt weld is as good as its base metal aluminium alloy provided the optimum process parameters were utilized. Note however, the aluminium alloy is in a softened state after FSW as heat during FSW has resulted in the aluminium alloy having lost the effect of either age hardening or work hardening. However, in comparison with the FS butt weld of Al-Cu, Al-Fe FS butt weld performance is stronger. Also, a valid point from these studies may be that, provided a sufficiently strong Al alloy is used, the weld strength of the Al alloy to Steel FS butt weld can reach 240 M Pa, stronger than Al-Cu FS butt welds (191 MPa).

1.2.3 Friction Stir Butt Welding of Al-to-Ti Alloys

There have been various studies on Al to Ti FS butt welds as summarized in Table 1-4 [36-42], providing the best tensile strength reached in the reported papers as a function of welding conditions for Al to Ti dissimilar butt welds. The papers mainly focus on the effect of process parameters on the microstructures and mechanical strength of the welds. Strengths values ranging from 88 to 348 MPa have been reached. Note UTS being 348 MPa is a high strength value considering it is stronger than the strength of peak aged hardened 6xxx alloys.

Figure 1-19 shows an Al-Ti binary phase diagram which shows the various possible intermetallics that may form and growth during FSW of Al to Ti. However, phase diagram does not provide information on the kinetics of formation and growth. As has been explained, formation of intermetallic(s) is often necessary for a metallurgical weld, but excessive growth of the brittle intermetallic(s) results in the weld being brittle and thus low strength. Achieving a high strength value in the Al to Ti weld mean there is an absence of a thick intermetallic layer and the thin intermetallic layer present is not very brittle. This is consistent with Ti-Al alumide is structure material particularly used at high temperature applications.

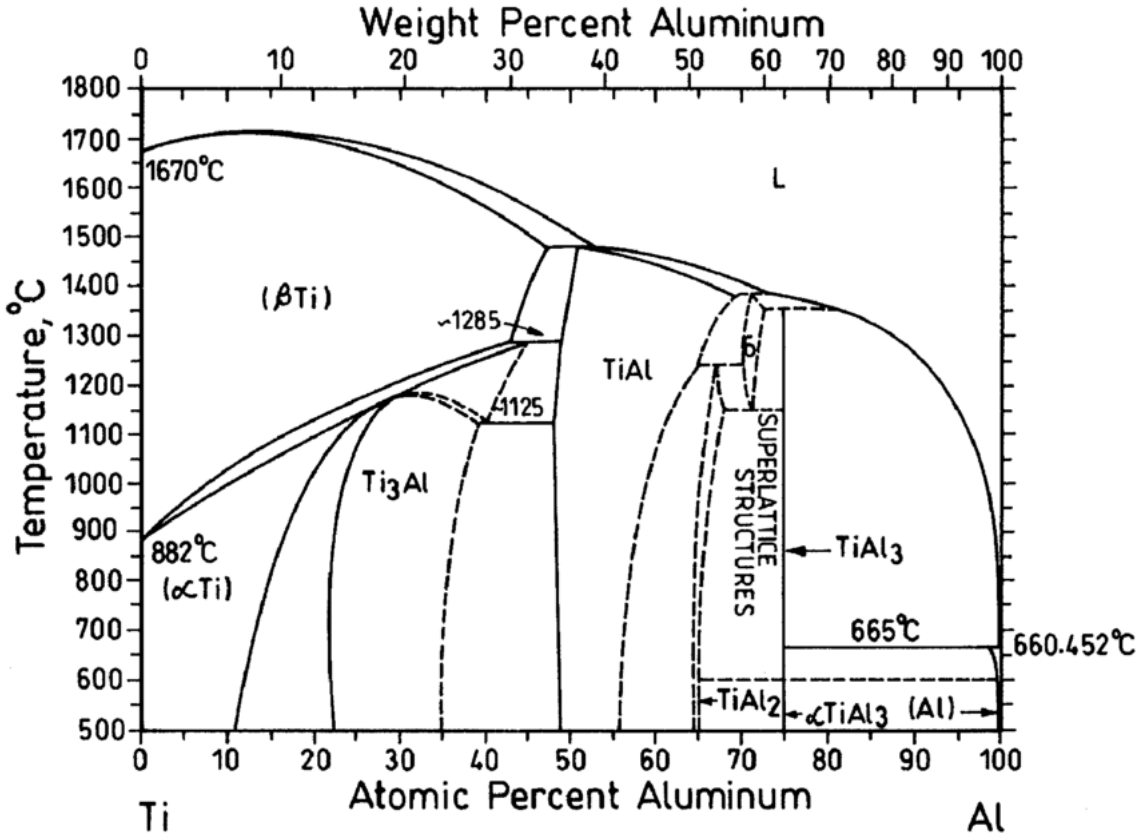

Figure 1-19 Binary Ti-Al phase Diagram with different phases present at various temperature ranges [35].

Dressler et al. [36], in their 2009 article showed that at the Al-Ti interface, two types of bonding can be observed. First, Figure 1-20a shows the fracture surface on the Ti side used for EDX analysis that reveals 90% Al (light blue EDX color) is high on the fractured Al surface while the rest of the spots still show the presence of sufficient Al. This implies that the joint formed at the Al-Ti interface is through diffusion. Second, although the authors do not discuss further, the pin was mostly shifted towards Al side except a few millimetres in order to avoid pin erosion, wear and overheating . However, authors do not provide the pin length and how much was plungged into the parent metals. The high tensile strength value of 348 MPa was possble at Al-Ti interface bonding as a result of avoiding pin wear and hence may have reduced IMC layer. Figure 1-20b shows a larger magnification of (a) reveals that Al particles bonded to the Ti side show the welding connection is very strong with large dimples on the fracture surface.

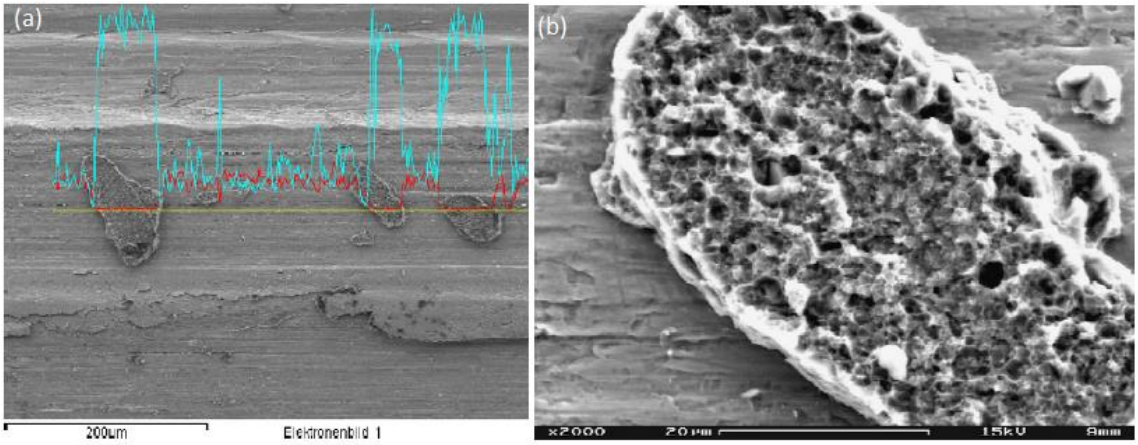

Figure 1-20 Fracture surface (titanium side) with adhesive aluminium spots; EDX colors: red (dark) →titanium, blue (light) →aluminium. (For interpretation of the references to color in this figure legend, the reader is referred to the web version of the article) [36].

Chen and Liu [37], in their 2011 article showed that the tensile strength of the FSW butt joint is maximum when ω = 950 rpm and υ = 118 mm/min achieving a tensile strength of 131 MPa. However, when ω = 750 rpm and υ = 118 or 150 mm/min, the interface joining of Al to Ti is poor giving low weld strength. Figures 1-21a-1-21e shows macroscopic morphology of the FS butt weld features with their corresponding pair of ω and υ.

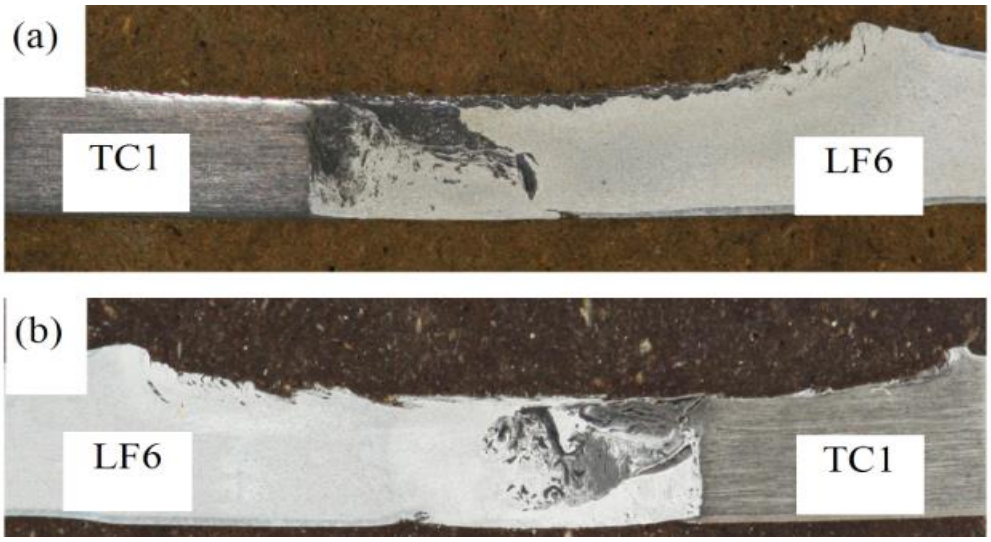

Figure 1-21 The macroscopic morphology of cross section of butt joint: (a) ω = 750 rev/min, v = 118 mm/min; (b) ω = 750 rev/min, υ = 150mm/min; (c) ω = 950 rev/min, υ = 118 mm/min; (d) ω = 950 rev/min, υ = 150 mm/min [37].

Figure 2-1 cont.

Song et al. [38], in their 2014 article showed that the probe offset distance has a great influence on the microstructures and mechanical properties of the joint i.e., an optimum amount of pin offset is necessary to form high strength butt welds as large tool offset has resulted in the formation of thick IMC layers while non-penetration resulted in even no bonding. Figure 1-22a to1-22c shows the SEM micrograph of each of the pairs of ω and υ. The corresponding optimum tensile strength is at a tool offset of 0.9 mm and ω = 1000 rpm as shown in Figure 1-23d while Figures 1-23a to 1-23c and 1-23e are lower.

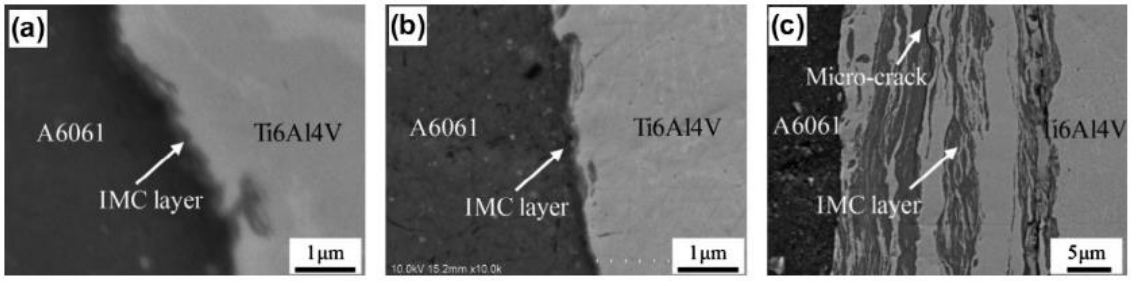

Figure 1-22 Back-scattered electron images of interfacial microstructure of joints at 1000 rpm with various probe offset distances: (a) 0.6 mm, (b) 0.9 mm and (c) 1.2 mm [38].

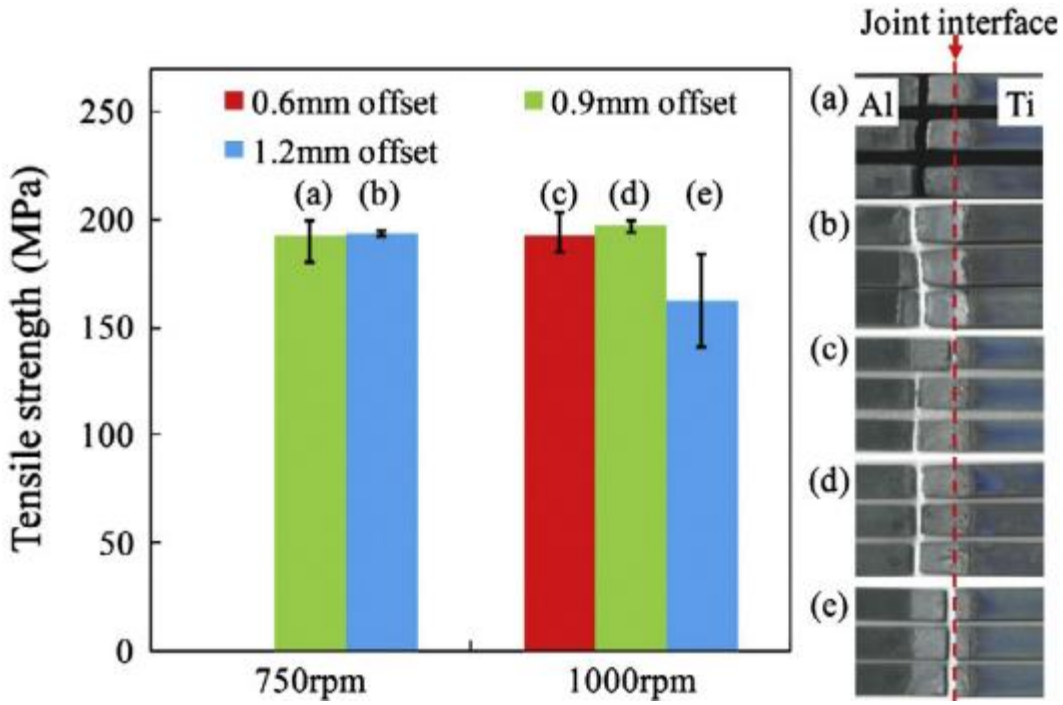

Figure 1-23 Tensile strength and the top surface of specimens after tensile test [38].

Zhang et al. [39], in their 2014 article, showed that more than 92% of mechanical strength can be achieved with diffusion type bonding. Wu et al. [40], in their 2015 article, showed that 68% of the tensile strength can be achieved with the combination of the right parameters (Table 1-4, column 6). A study by Chen et al. [41], in their 2018 article showed that 83% tensile strength was achieved with optimum process parameters (Table 1-4, column 3). Moreover, Choi et al. [42], in their 2018 article showed that high rotational tool and weld speed resulted in the formation of a large amount of IMC layers which show a low tensile strength (Table 1-4 column 6).

Observing Table 1-4, the various process parameters, different grades of aluminium alloy and fracture locations have been widely explored. One would easily notice from Table 1-4 that base Al alloy have different tensile strength values ranging from industrial aluminium pure grade with 90 MPa to as high as 483MPa for aerospace-grade Al alloy like AA2024. Therefore, the tensile strength is also dependent on the strength of the base material. While looking at the same grade Al alloy between Ref. [36] and Ref. [41] their tensile strength does not differ very much after they have gone through different levels of heat treatments. High strength Al alloy FSW to Ti alloy has been observed in providing the best tensile strength in comparison with Cu and steel base metal counterparts.

An important point from these studies may be that, provided a strong Al alloy is used, the weld strength of the Al alloy to Ti FS butt weld can reach 348 MPa which is considerably stronger than Al-Fe and Al-Cu butt welds. The strong Al to Ti welds suggests that during FSW excessive growth of brittle intermetallics at interface region can be avoid under an appropriate FSW

condition. To further summarise, of all the strength data of butt welds made by FSW , the highest strength value is 348 MPa for welds of AA2024-T3 to Ti6Al4V from Dressler et al.[36]. Their study shows fracture occurring in the interface region of the welds, although detailed microstructure examination was not conducted. The strength value at 348 MPa for the interface region should be considered high as this value is higher than the ultimate tensile strength values of the commonly used 6061-T6 and work-hardened 5083 aluminium alloys. Later, in the work of Wu et al. [40] on butt FSW of AA6061 to Ti6Al4V, the best strength of the welds is 215 MPa with fracture occurring away from interface region and in the Al6061 side. This is consistent with the work of Dressler et al. that the interface region is strong when FSW is conducted in a proper condition. In Wu et al.'s study, a thin $TiAl_3$ was identified at the interface between Al6061 and Ti6Al4V. More recently, Choi et al.'s [42] analysis on the interface region between Ti and Al in welds made using butt FSW has revealed the presence of $TiAl_3$, TiAl and Ti_3Al in the interface thin layer.

Table 1-4 Strength and welding parameters of the best friction stir butt welds of Al to Ti.

Base Metals Thickness [Ref.]	Tool speed (RPM) Weld speed (mm/min) Tilt angle	Pin Profile (mm)	Test Width (mm)	Tool offset (mm)	FSW Tensile Strength (Al BM) (MPa)	Frac-ture loca-tion	Eff. (%) Al (BM)
AA2024-T3/ TiAl6V4 (2mm-2mm) [36]	ω = 800 v = 80 $\angle = 0^\circ$	$OD_{shoulder}$ = 18 OD_{pin} = 6 L_{pin} = -	12.5	0	348 (480)	Inter-face	73
AA LF6/ Ti TC1 (2mm-2mm) [37]	ω = 950 v = 118 $\angle = 2^\circ$	$OD_{shoulder}$ = 15 OD_{pin} = 5 L_{pin} = 1.85	12.5	0.5 Ti	131 (320)	Inter-face	41
6061Al/ Ti6Al4V (2mm-2mm) [38]	ω = 1000 v = 120 $\angle = 3^\circ$	$OD_{shoulder}$ = 15 OD_{pin} = 6 L_{pin} = 1.9	12.5	0-1.2 Ti	190 (310)	HAZ Al	61
Al-6Mg / Ti6Al4V (4mm-2mm) [39]	ω = 1200 v = 60 $\angle = 0^\circ$	$OD_{shoulder}$ =- OD_{pin} =- L_{pin} = 2.2	22	2 Ti	292 (295)	Al side	90
AA6061/ Ti6Al4V	ω = 750 v = 280	$OD_{shoulder}$ = 15	10	1.2 Ti	215		68

(2mm-2mm) [40]	∠ = 3°	OD_{pin} = 6 L_{pin} = 1.9			(310)	Inter-face	
AA2024/ Ti6Al4V (3mm-3mm) [41]	ω = 700 v = 60 ∠ = 0°	$OD_{shoulder}$ = 18 OD_{pin} = 6 L_{pin} = 2.5	12.5	2.5 Ti	347 (483)	MSZ √ (Al rich)	83√
Pure Al/Pure Ti (2mm-2mm) [42]	Ω = 800 v = 100 ∠ = 3°	$OD_{shoulder}$ = 12 OD_{pin} = 4 L_{pin} = 1.9	6	0.2 Ti	88 (90)	Inter-face	98

*Notes: If many welds are performed, the welding parameters providing the best strength are reported. v, welding speed/mm min-^{1}; ω, rotational speed/revmin-^{1}; ∠, tilt angle; tool offset is reported as the length of insertion of the pin inside the Ti plate; strength is the tensile strength at fracture/(MPa); $OD_{shoulder}$, Outside shoulder diameter; OD_{pin}, Outside pin diameter; L_{pin}, length of pin or pin height.

1.3 Review on Friction Stir Lap Welding of Al to High Melting Point Alloys

In this section, a thorough review of FSW on Al to Cu FSL weld is presented first, then followed by Al to Steel FSL weld. Finally, Al to Ti FSL weld is presented first by looking into various aspects of their process parameters, mechanical performance characteristics, and microstructural features.

Tensile-shear testing of lap (σ_{lap}) welds is a common testing method and the strength can be taken as the maximum load divided by the sample width (F_m/W_s). FSLW conditions (ω, ν and in dimensions), maximum achieved σ_{Lap} and Fm/Ws (N/mm) for Al/Cu FSL welds are given in Table 1.5.

The mechanical performance of FSL welds under static loading is normally determined using tensile shear testing methods. Schematic illustrations of tensile shear testing is shown in Figure 1-24a as a non-penetrated FSL weld and Figure 1-24b with a pin penetrated to the bottom plate. The schematic is presented here that will be useful when reviewing various literature presented in this section.

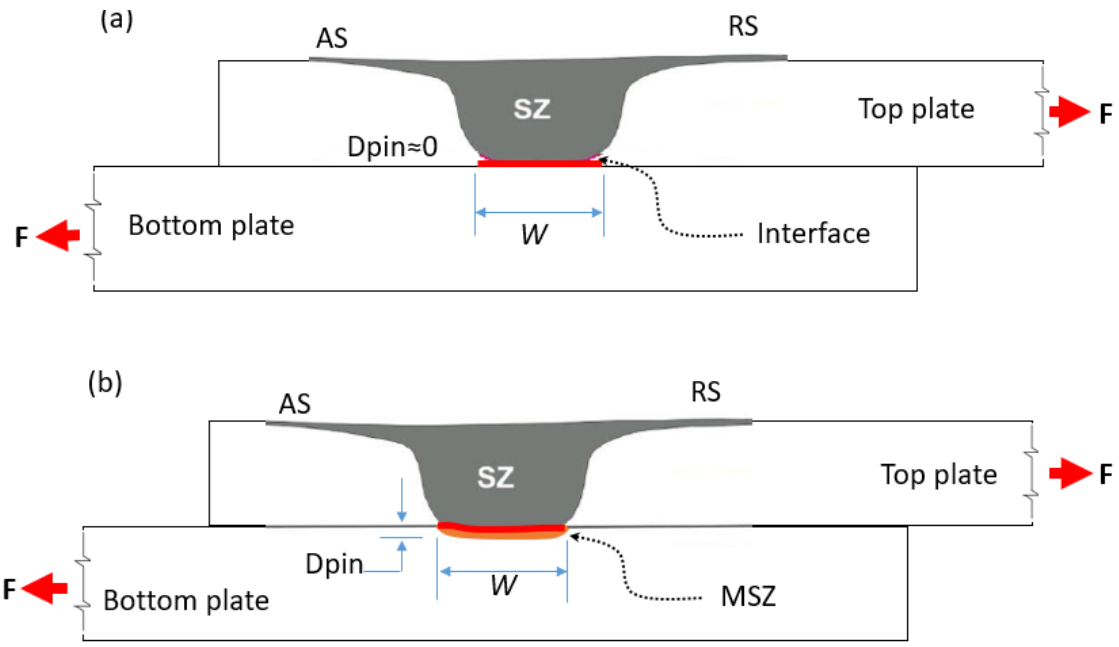

Figure 1-24 Schematic illustration of tensile shear testing: (a) advancing loading configuration and (b) retreating loading configuration.

1.3.1 Friction Stir Lap Welding of Al to Cu alloys

Table 1-5 is a summary of Al-Cu FSL welds with process parameters including ω, υ, tilt angle, base metal thickness, pin profiles (tool shoulder diameter, pin diameter, pin length, and shape). Also, F_m/W_s is important in FSL weld that determines the weld strength of a test specimen.

Firouzdor and Kou evaluated [39] mechanical properties of thin 1.6mm thick 6061 to a commercially available pure Cu were FSL welded with top lap modified as butt weld configuration before welding. They found that the modified AA6061/Cu FSL weld has improved tensile strength value five to nine times higher in ductility. However, relatively at high weld travel speed (υ), modified FSW could not provide better strength as a result channel formation.

In a study by Gopal et al. [43] they achieved a 25.64 MPa (4000 N / 26 mm = 154 N/mm). Choudhury et al. [44], reported having 111.41MPa (specimen size not specified). Recently, Guan et al. [45], evaluated the structural property characteristics of Al-Cu at high rotational speed without pin penetration into low Cu sheet. Their failure strength at the Al-Cu interface was 250 N/mm (3000 N / 12 mm).

It was observed that FSL welds of dissimilar alloys have no defined methods of testing used in FSL weld testing currently available. Each specimen width (W_s) of FSL welds in Table 1-5 (column 5) 26mm, 18 mm, 12 mm, 6 mm, etc. shows that researchers have determined their choice of Ws during specimen preparation. They must have either borrowed from existing standard testing methods such as ASTM D5868 used for lap shear adhesion test for fibre reinforced plastics

done under specific conditions. Therefore, there is not yet a standard test available for Al alloy to other high strength materials for lap welds for dissimilar materials of various thicknesses for FSW.

Figure 1-25 shows a diagram of joints ultimate tensile stresses from the lap shear test results [46]. In their tests, their samples of 3 mm aluminium alloy lapping to Cu all failed in the aluminium alloy side. FSW heat results in annealing of the welded alloys and FSW has also resulted in a slight thinning of the top aluminium alloy plate. Furthermore, stress concentration during tensile-shear testing, as will be shown in the simulation of this study, results in local stress level in the lap ends more the three times the remote applied stress level. The result reaching 205 MPa remote stress applied to a 3 mm plate lap weld so failure occur could be very questionable. And thus a Al to Cu FSL weld could support a tensile-shear value of 511 N/mm is highly questionable.

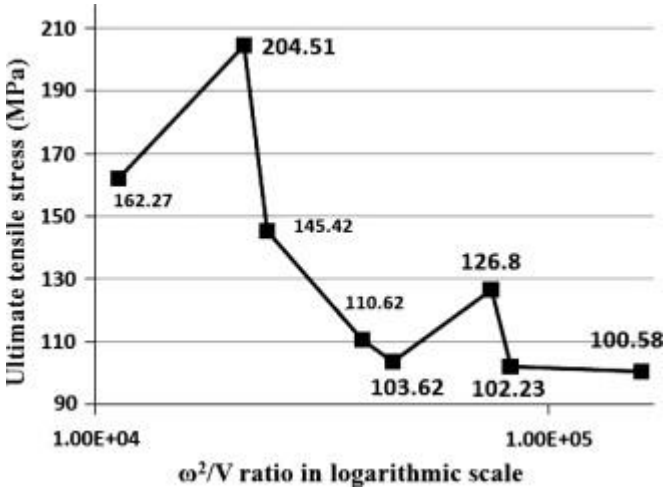

Figure 1-25 Diagram of the maximum fracture loads from the lap shear test results ordered by magnitude of ω^2/υ values [46].

As can be seen from the discussion above, studies on Al to Cu FSLW from literature have been viewed insufficiently clear. A difficulty of evaluating tensile-shear strength of the lap weld region has been the failure inside aluminium alloy due to the use of the insufficiently thick aluminium alloy. Furthermore, not providing the full sample size of tensile-shear testing has resulted in difficulty in estimating the load required to shear fracture the lap weld, making it difficult to make comparison to strength values from other studies.

Table 1-5 Summary of the FSLW conditions with maximum σ_{Lap} achieved for Al-Cu dissimilar welds (data collected from literature).

Base Metals Thickness [Ref.]	Tool speed (RMP) Weld speed (mm/min) Tilt angle	Pin Profile (mm)	Fracture strength for base metal (Al & Cu) (MPa)	F_m/W_s (N/mm)	Fraction location

AA5083/Cu (2.5mm-3mm)[46]	ω = 600 - 1550 v = 15 - 32	$OD_{shoulder}$ = 19.1 OD_{pin} = 5 L_{pin} = 4.5	350 210	9203/18 =511	Al
AA6061T6/Cu (1.6mm/1.6mm) [47]	ω = 1400 v = 127 $\angle = 3^{\circ}$	$OD_{shoulder}$ = 10 OD_{pin} = 4 L_{pin} = 1.6	280 250	2200/12 =183	Cu side
AA3003/Cu (3mm-3mm) [43]	ω = 1500 v = 70 $\angle = 0^{\circ}$	$OD_{shoulder}$ = 16 OD_{pin} = 4 L_{pin}= 5.7	200 210	4000/26 ≈ 154	Cu side
AA6061-T6/Cu (3mm-3mm) [44]	ω = 800 v = 20	$OD_{shoulder}$ = 20 OD_{pin} = 3.5 L_{pin} = 5.7	290 210	No information on sample width	Interface
AA6061-T3/Cu (3mm-3mm) [45]	ω = 2500 v = 25	$OD_{shoulder}$ = 12 OD_{pin} =- L_{pin} = 2.85	290 210	3000/12 =250	Interface

*Notes: If many welds are performed, the welding parameters providing the best strength are reported. v, welding speed/mm min^{-1}; ω, rotational speed/revmin^{-1}; $\angle$, tilt angle; strength is the tensile strength at fracture/(MPa); $OD_{shoulder}$, Outside shoulder diameter; OD_{pin}, Outside pin diameter; L_{pin}, length of pin or pin height; F_m = Maximum failure load; W_s = specimen width.

1.3.2 Friction Stir Lap Welding of Aluminium to Steel Alloys

Tool positioning is basically a careful administering of downforce to achieving a desired amount of pin penetration ($d_P > 0$) or non-penetration ($d_P \approx 0$) whichever is preferred, both are of course equally responsible for establishment of FSW. However, the weld strength in either condition may vary depending on the welding parameters considered for their FSW. Figure 1-26 illustrates two tool positioning situations. In both cases, there is always uncertainty because the tool position is just based on manual control of downforce while carefully monitoring the variations in numerical values of force, torque and temperature on the LowStir laptop. Chen et al. [48], in their 2013 article showed the effects of tool positioning on the joint interface microstructure and facture strength of Fe-Al FSL weld. They show that F_m/W_s is not affected by pin penetration because as the pin penetration is reduced to about zero but when greater than zero the MSZ remains. The small amount of pin penetration (0.1 mm) with no defects has been shown to produce F_m/W_s = 310N/mm which agrees with others [49-52, 53], and as shown in Figure 1-27a. This suggest that

once the pin has penetrated to form a MSZ, as long as the weld is free of cavilties and pores, the MSZ will behave the same under tensile shear loading and fracture at the same load level.

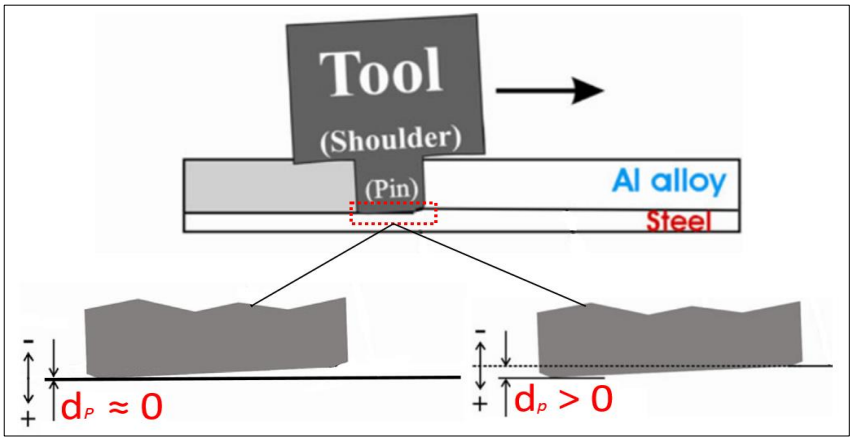

Figure 1-26 Schematic illustration of friction stir lap welding (FSLW) of Al to Steel having pin penetrated to the steel ($d_P > 0$) and non-penetrated ($d_P \approx 0$) [48].

However, in Figure 1-27b with $d_P = -0.5$, intermetallic outbursts are seen. Furthermore, in Figure 1-27c, an intermetallic layer without MZS was formed when $d_P \approx 0$ giving the highest weld joint strength of 435/N/mm. This suggests that, with a thin layer of intermetallic layer without MSZ, the lap weld is strong. This interface layer has formed is the result of diffusion welding, as the pin has not penetrated steel and no friction stir of the steel bottom plate has taken place. Furthermore, it is quite understandable that if the pin was removed from the Al-Fe interface further towards Al, diffusion welding is not complete and there will not be a complete joint forming.

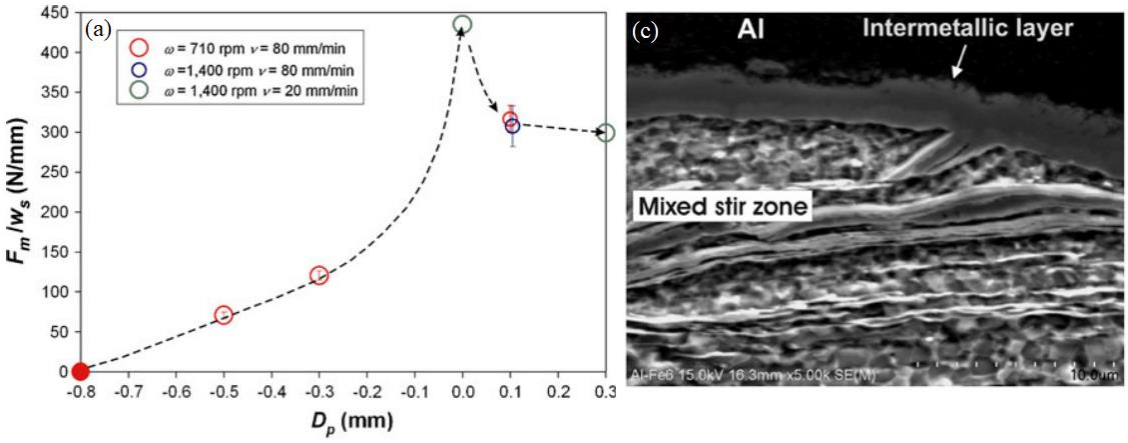

Figure 1-27 Tensile-shear testing data of welds made using various conditions: (a) F_m/W_s data plotted as a function of d_P with ω and υ values as indicated (the error bars represent one standard deviation), (b) selected tensile-shear test curves with ω, υ, and d_P values as indicated, (c) SEM micrograph taken in the interface region of Al and mixed stir zone, (d) a sample taken with a $D_{Pin} = 0.1$ [48].

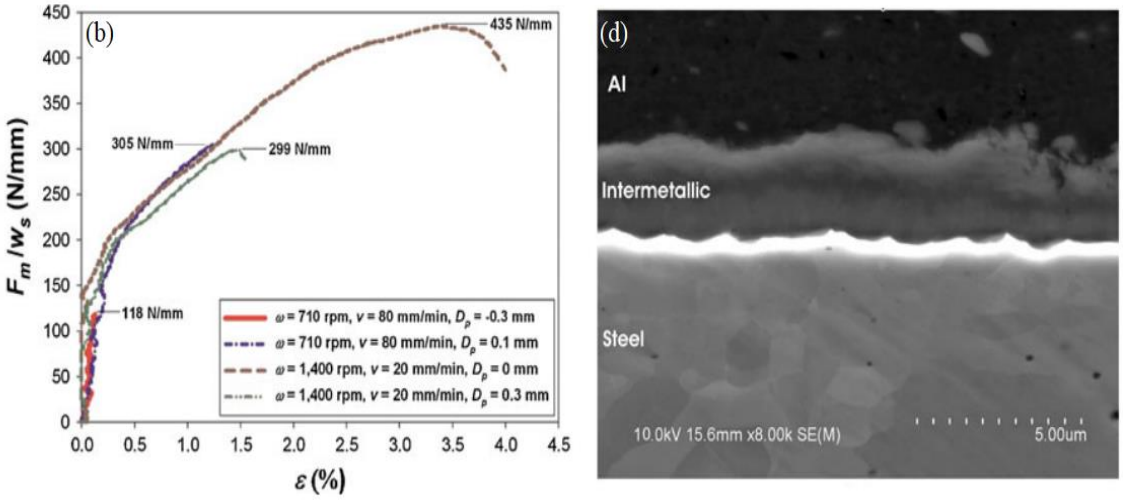

Figure 1-27 cont.

Movahedi et al. [49], their 2013 article studied the effect of annealing treatment of Fe-Al FSL weld and showed that annealing temperature 350°C was better than that at 300°C or 400°C. They further concluded that a thin intermetallic layer at the weld interface has a higher impact on the improvement of the joint strength which is evident when at 350°C, IMC thickness is 0.35µm and above 350°C higher IMC thickness. Also, a thin IMC layer is seen at less time with lower temperature (see Fig. 1-28a, 1-28b) whereas IMC thickness growth is more at higher temperature and duration (see Fig. 1-29c, 1-29d). Figure 1-29 further shows the relationship between annealing duration and joint strength at three different temperatures. Figure 1-29a shows that 120 min annealing time at 35 ^{0}C gives a high fracture strength whereas Figure 1-29b shows a high failure load just in 45min at 400 ^{0}C. This suggests that a good relationship can be established between the annealing temperature, duration, and IMC thickness leading to high weld strength joints.

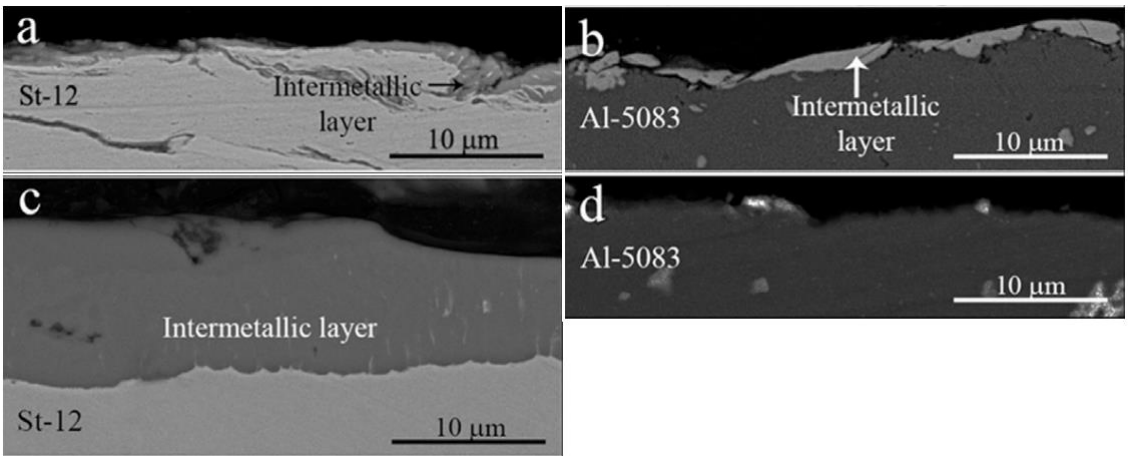

Figure 1-28 SEM/BSE images of the fracture paths for the samples annealed at: (a and b) 400 °C, 60 min and (c and d) 400 °C, 180 min [49].

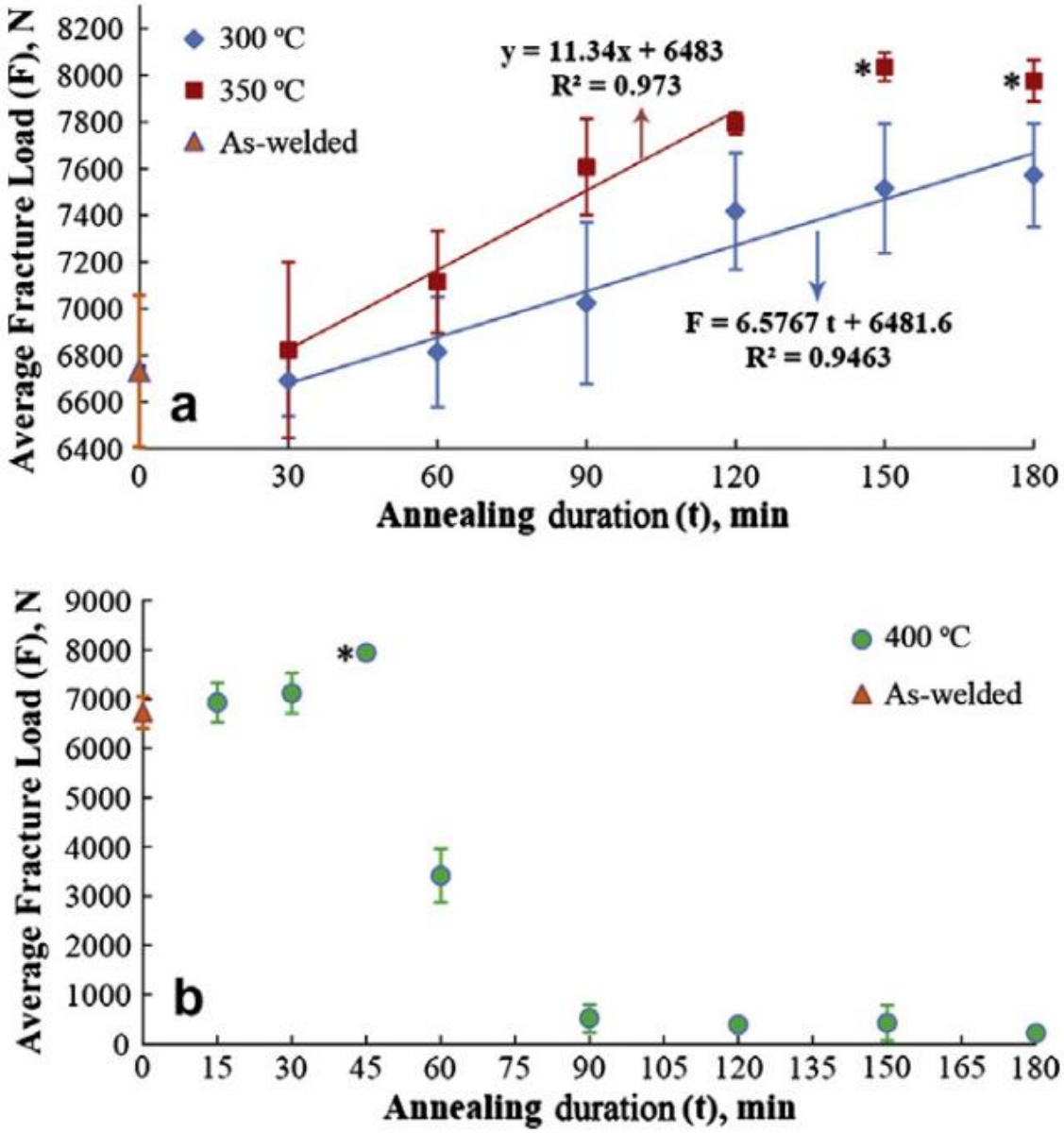

Figure 1-29 Average fracture loads vs. annealing duration at annealing temperatures of (a) 300 and 350 °C, (b) 400 °C (*: fracture from St-12 base sheet) [49].

Helal et al. [50], in their 2019 article evaluated the microstructure and mechanical properties of Al/steel (low carbon). Their maximum failure load was 3.611kN which was achieved by varying tool penetration onto the bottom plate while at a constant ω and varying υ between 50-400mm/min to minimize the formation of IMC layers. A more recent study conducted by Zhou et al. [51], using friction surface assisted friction stir lap welding (FSaFSLW) in their 2020 article reported that a defect-free, highly refined, and equiaxed grain structure was found in the interlayer without stirring the bottom steel part and claim that IMC formation in the conventional weld is replaced by Fe content ~10at.%. However, the ultimate lap shear failure load is 2.8 kN. This result is quite lower than other conventional FSL welds of Fe-Al.

Other studies have also indicated that the presence of thick IMC layer decreases the mechanical strength of the FSL weld Al-to-Steel joints [52, 53], however, a careful selection of process

parameters can minimize the intermetallic growth layers. Figure 1-30 shows the SEM images for welds made using FSLW of Al5083-to-ST12 with various υ but the same ω. It can be seen that the formation of the IMC layer gradually develops as the υ decreases (see Fig.1-30a, 1-30c). Helal et al. [50, 53] showed that combinations of higher ω and a lower υ result in the formation of a thick IMC layer at the interface. In other words, an optimum level of a joint can be achieved at a certain ω and υ to avoid insufficient weld or formation of a thick IMC layer which can reduce weld strength. In Figure 1-31, the graph shows the relationships between υ, $\sigma_{Lap,}$ and IMC thickness layer at various ω. It can be seen that the highest fracture load achieved among the five tests done with ω, υ, and IMC thickness are 2600 rev/min, 200 mm/min, and 2.8 µm respectively. It is seen that IMC between 2.5 - 3 µm is required for a high weld strength.

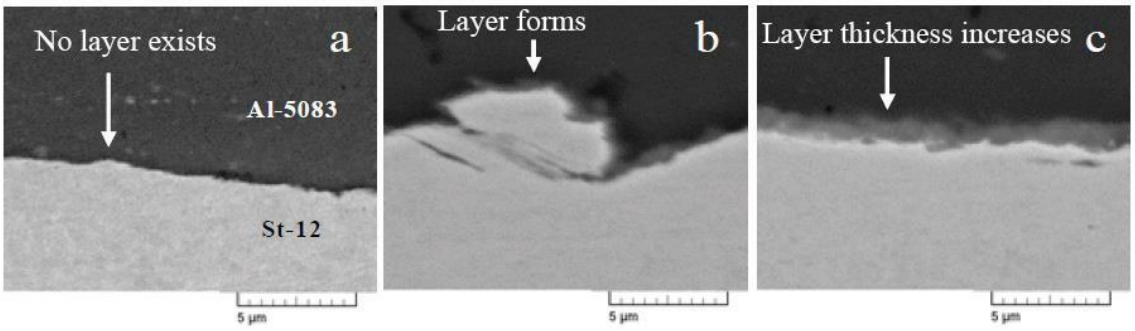

Figure 1-30 SEM images of diffusion layer at the interface: (a) 750 rpm, 23 cm/min, (b) 750 rpm, 19 cm/min (c) 750 rpm, 15 cm/min [52].

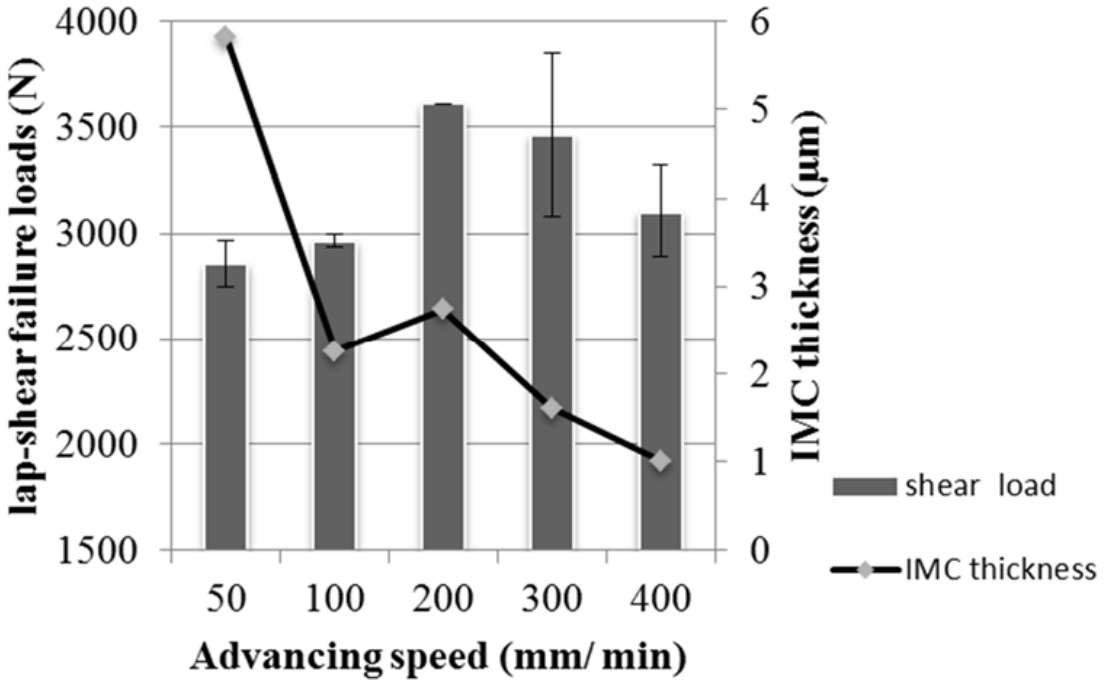

Figure 1-31 Relationship between advancing speeds, shear load and intermetallic compound (IMC) thickness [54].

Table 1-6 summarizes the best process parameters selected including tool tilt angle (∠), tool rotational speed (ω), weld speed (υ), parent metal thickness, pin profiles (shoulder diameter, pin

length, and pin size), and fracture location (interface or BM) for Al-Steel FSL welds. A significant part of Table 1-6 is the IMC thickness of the FSL welds presented. The following pieces of literature [46, 49, 51-53] have not presented the corresponding temperature at which the IMC thickness was achieved. According to Chen et al. [48] and Movahedi et al. [49], however, it is clear that IMC thickness presented with their corresponding peak temperatures, ω, and υ, IMC thickness is 2.5 µm and 7.8 µm, respectively. It is obvious that at low ω, υ and temperature the IMC thickness is high [49]. Comparatively, according to Chen et al. [48], the best tensile shear strength achieved was 435N/mm (≈ 218 MPa) and fractured at the interface as a result of controlling the pin penetration by just touching ($d_P \approx 0$) to reduce IMC thickness. Therefore, a thin IMC layer was seen to provide high tensile shear strength of FSL welds.

Table 1-6 Summary of the FSLW conditions with maximum σ_{Lap} achieved for Al-Steel dissimilar welds (data collected from literature).

Base Metals (Thickness) [Ref.]	FS Param-eters (rpm, mm/min tilt ∠)	Pin Profile (mm)	Fracture strength (Al & Cu)	Max. σ_{lap} (Al & Fe) (MPa)	F_m/W_s (N/mm)	Fraction loca-tion	IMC (µm) Temp.
AA6060-T5 /Steel (6mm-2mm) [48]	ω = 1400 v = 20 ∠ = 2.5°	$OD_{shoulder}$ = 25 OD_{pin} = 6 L_{pin} = 4.5	160 550	117 340	6960/16 = 435*	Interface	40 2.5 (544 °C)
AA5083/Steel (St-12) (3mm-1mm) [49]	ω = 750 v = 23 ∠ = 2.5°	$OD_{shoulder}$ = 16 OD_{pin} = 3-4.5 L_{pin} = 3	350 550	275 340	7000/25 = 280*	Steel	- 7.8 (400 °C)
AA6061-T6/Steel (3mm-0.8mm) [50]	ω = 1200 v = 50, 100-400 ∠ = 5°	$OD_{shoulder}$ = 20 OD_{pin} = 5 L_{pin} =-	290 550	207 340	3611/10 = 361*	Steel	- 2 -
AA6061/ Steel (2mm-2mm) [51]	ω = 1000 v = 100 ∠ = 3°	$OD_{shoulder}$ = - OD_{pin} =- L_{pin} = 2	290 550	124 340	2800/20 = 140	Interface	Diffusion layer

AA5754/ Steel 2.1mm-3mm [55]	ω = 1800 v = 16 & 45 $\angle = 0^{\circ}$	$OD_{shoulder}$ = 12 OD_{pin} = -4 L_{pin} = 1.9	270 550	220 340	1471/10 = 147	Interface	- ≈2-3 -

*Notes: If many welds are performed, the welding parameters providing the best strength are reported. v, welding speed/mm min-^{1}; ω, rotational speed/revmin-^{1}; $\angle$, tilt angle; strength is the tensile strength at fracture/(MPa); $OD_{shoulder}$, Outside shoulder diameter; OD_{pin}, Outside pin diameter; L_{pin}, length of pin or pin height; F_m = Maximum failure load; W_s = specimen width.

1.3.3 Friction Stir Lap Welding of Aluminium to Titanium Alloys

Study on FSLW of Al to Ti has been extensive and in this section, Al to Ti FSL welds are presented with a wide range of strength values. Their significant differences in mechanical strengths are discussed. This section is particularly relevant to the present thesis work, as the review will demonstrate the superior static strength of the welds in comparison to welds of Al to Cu and Al to steel and to show that study on fatigue behaviour of the welds is highly necessary.

Following the studies demonstrating excellent FS welds of Al to Ti alloys, early studies on Al to Ti FSL welds conducted by Chen and Nakata et al. [56], in their 2009 article showed that transient phase $TiAl_3$ forms by Al-Ti diffusion-reaction at the joining interface and concluded that the presence of $TiAl_3$ is largely dependent on the welding speed υ (heat input).

Figure 1-32 presents the micrographs of their welds. It can be seen that when the pin penetrated the bottom plate (Ti) (see Fig. 1-32a, and 1-32b), Ti pieces were being drawn into the Al matrix by the stirring effect of the rotating pin. Moreover, large voids formed on the titanium side is because of the large Ti pieces being drawn out by pin and insufficient flow of materials into the gaps left behind creating void defects which are opposed to what the authors described as micromechanical bonding because of the stirring effect of pin forcing the Al pieces into cavities of Ti surface. However, when the pin did not penetrate the Ti plate (as indicated in Fig. 1-32d and 1-32e) the joint exhibited a high σ_{Lap} (Lap shear) value of 469 N/mm. In comparison to tensile-shear strength values of Al to Cu and Al to steel FSL welds reported and discussed in the last two sections (1.3.1 and 1.3.2), this value (469 N/mm) can be regarded a high strength value. All the samples failed at the weld interface as shown in Figures 1-32c and 1-32f. The high σ_{Lap} value of 649 N/mm indicates that a strong bonding is formed at the Al to Ti FSL weld interface without penetrating much on the titanium plate.

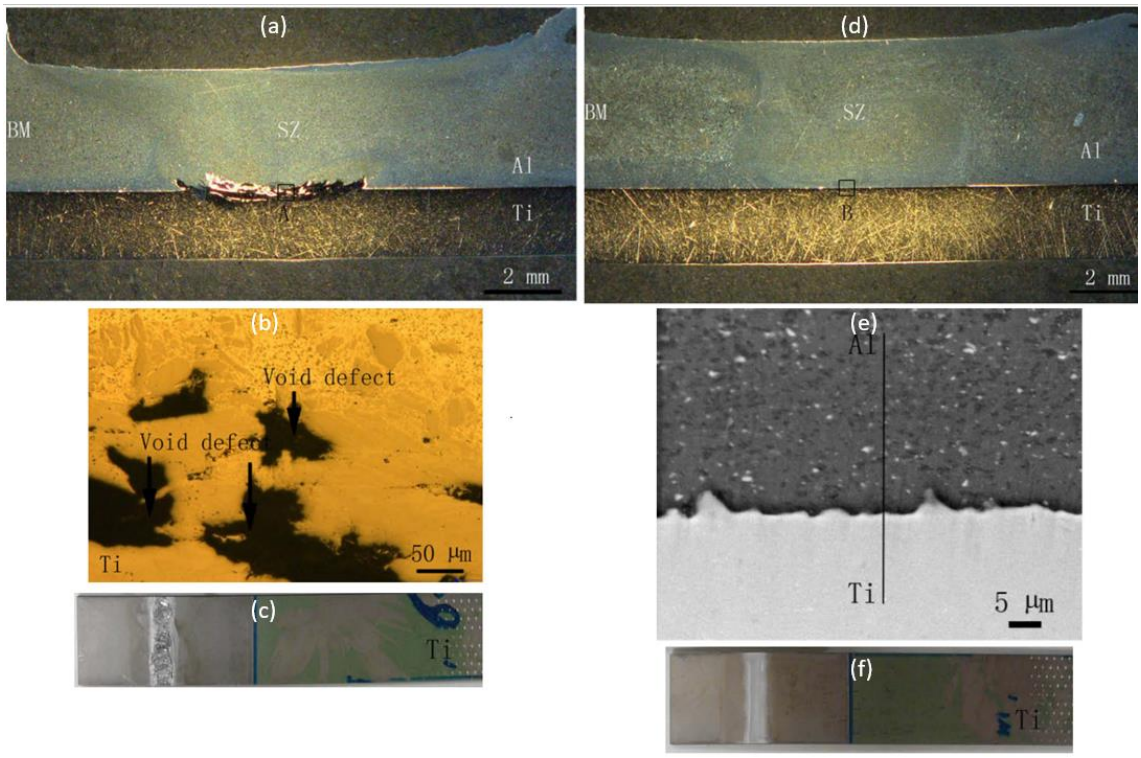

Figure 1-32 Macro/microstructure of Al to Ti FSL welds made using ω = 1500 rpm and: ν = 60 mm/min, (a) macrograph (b) microstructure of interface region (c) image of fractured tensile shear tested specimen. ν = 90 mm/min: (d) macrograph (e) SEM image of interface region (c) image of fractured tensile shear tested specimen [56].

Chen and Nakata [56] further suggested that the $AlTi_3$ intermetallic compound layer formed at the interface region based on XRD patterns as shown in Figure 1-33 were obtained from the fracture surfaces of the samples tested. However, this suggestion may be untrue because there is no visible size of the IMC layer can be seen on the SEM micrograph in Figure 1-32e.

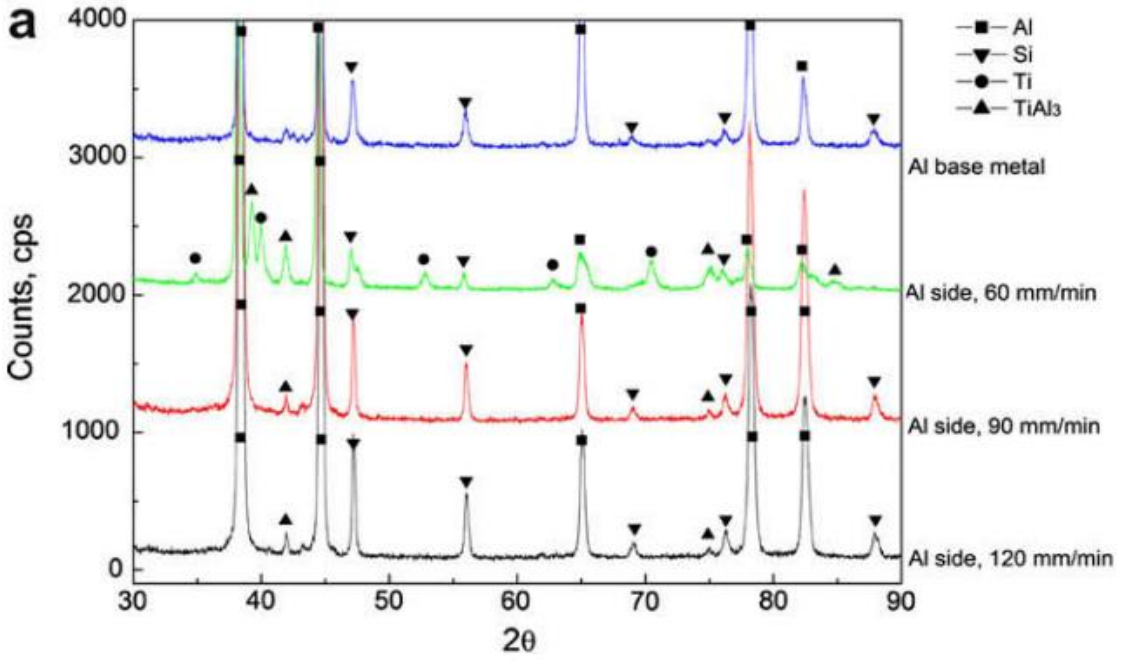

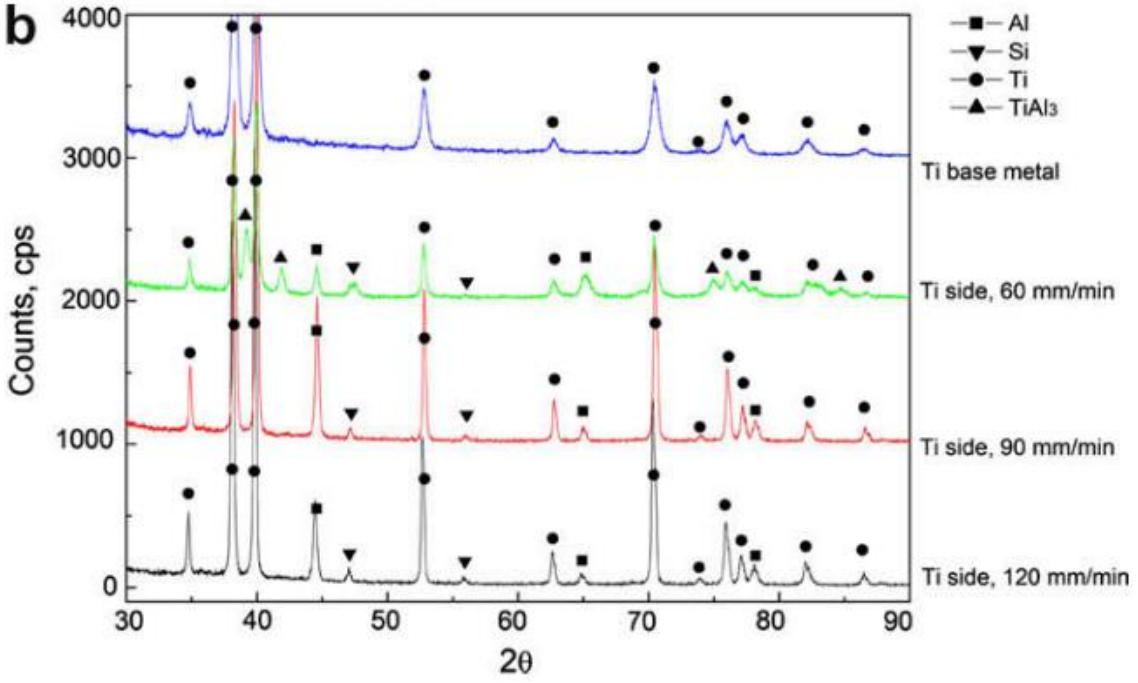

Figure 1-33 XRD spectrums from different fracture surfaces: (a) from Al sides and (b) from Ti sides [56].

Figure 1-34 is a schematic illustration of pin penetration condition ($D_{Pin} > 0$) of a Al/Ti FSL weld with letter *h* in the figure representing an arbitrary value usually between 0.1-1.5 mm. Chen et al. [57], conducted Al to Ti FSL weld with a pin penetration condition as shown in Figures 1-35a and 1-35c. In their article showed that failure load decreased with an increase in welding speed while maintaining ω = 1500 rpm. At υ = 60 mm/min, a failure load of 2.8 kN (Table 1.7, column 6) was achieved. They further observed that a groove-like crack occurred at the interface when weld speed was increased to 150 mm/min. This feature could be the presence of a large amount of IMC layer at the weld interface due to an increase in heat input by the actions of both welding speed and rotational tool speed when the pin was forced into the bottom plate (Ti side). The resulting fracture load is a low σ_{lap} value of 1.9 kN. Several microcracks can be seen in the interface regions of the weld (see Fig. 1-35b, and 1-35d). All their FSL test samples fractured at the interface and their maximum σ_{lap} value reached 224 N/mm (2800N/12.5 mm) which is comparatively much lower than the σ_{lap} value (469N/mm) reported by Chen and Nakata [56]. The reason for this may be the discontinuity/cavities observed in the MSZ.

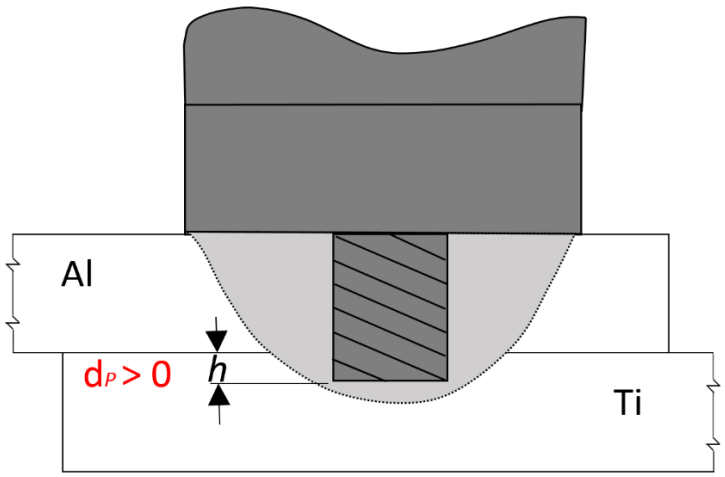

Figure 1-34 Schematic illustration of a pin penetration condition ($d_P > 0$) for a FSL weld. The letter *h* represents the size of pin penetration height.

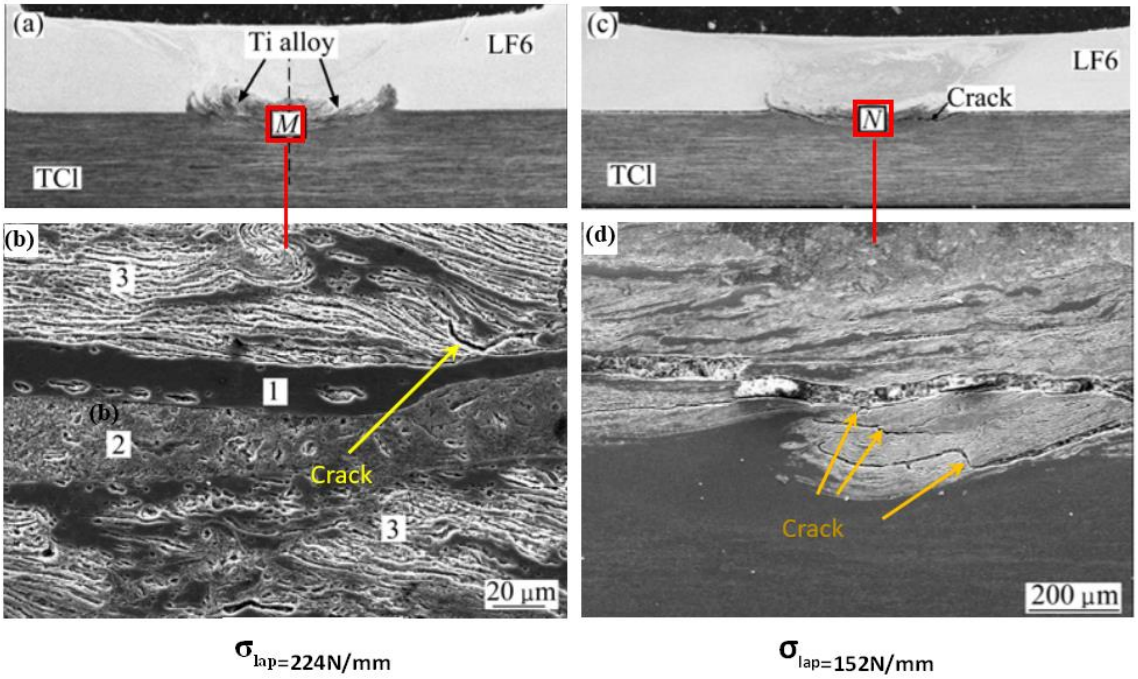

Figure 1-35 Macro/microstructure of Al to Ti FSL welds made using ω = 1500 rpm and υ = 60 mm/min, (a) macrograph, (b) microstructure of interface region. υ = 150 mm/min, (c) macrograph, (d) microstructure of interface region [57].

Wei et al. [58], also conducted Al to Ti FSL weld with a pin penetration condition in which they have reported that a dark region with a swirl-like structure was observed as shown in as a mixed region in Figure 1-36a but is clearly shown in Figure 1-36c at the interface region and further concluded that the failure load was approximately equal to the parent metal 1060Al. However, this cannot be a good comparison with literature while their test sample width is 10 mm which is significantly smaller than most FSL weld sample widths that can provide sufficient weld. The high rotational tool speed, weld speed, and pin extrusion of Ti parts forming a large amount of mixed stir could be the reason for having a significantly low failure load.

The FSL welded test samples fractured both at the interface and top plate (Al) on the retreating side as shown in Figures 1-36b and 1-36e at 150 N/mm and 191 N/mm, respectively.

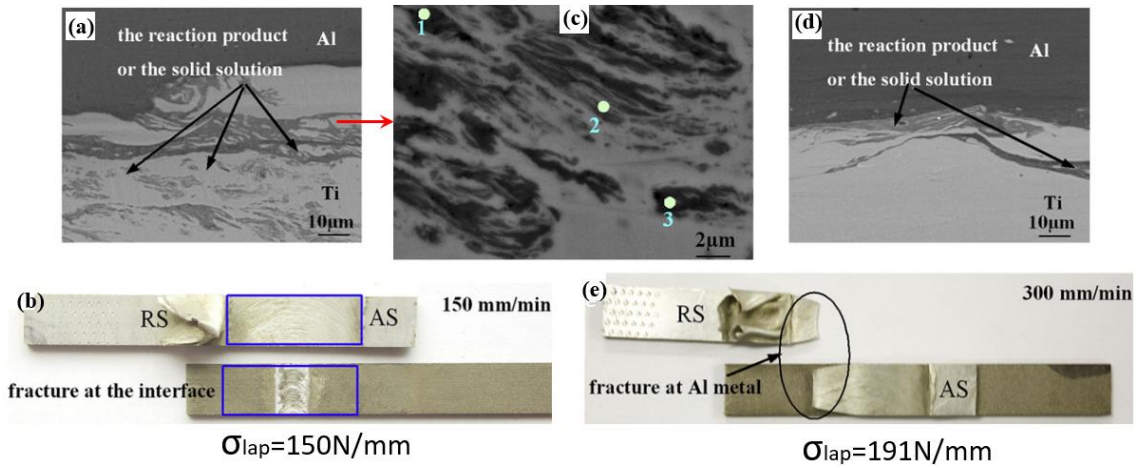

Figure 1-36 Typical micro-morphologies of the joining interfaces at welding speeds of (a) 150 mm/min, (b) 300 mm/min welds made using ω = 950 rpm [58].

According to studies by Chen and Yazdanian [59], their 2015 article showed that non-penetrated ($d_P \approx 0$) but tool pin tip just close to touching Ti side did result in a high tensile shear load of 11248 N (11248/16= 703 N/mm) (See Table 1.7, column 6). They concluded that the very strong FSL weld is the result of the IMC layer being very thin (< 250 nm) due to the very slow growth kinetics of IMC at the Al-Ti interface. They further stated that even though the pin penetrated ($d_P > 0$) a bit, the weld strength would still be regarded high because a crack path would go through tough bridges of αTi at the weld interface. It is obvious that too much pin extrusion coupled with high tool rotation and weld speed is a regime for poor weld strength but not necessarily low. Figures 1-37a and 1-37b shows the comparison of two welds both having a mixture of $d_P \approx 0$ and $d_P > 0$ with their corresponding weld strengths (W_s/mm). In both cases, the penetrated weld shows sufficient weld strength of more than 630 N/mm. It can be noted that, since d_P is manually controlled during FSLW, a precise d_P cannot be established to achieved $d_P = 0$. Figure 1-38a shows a $d_P \approx 0.7$ mm sample fractured at the interface reaching a failure load at 8400 N (8400N/16mm = 525 N/mm) as indicated on the right with the load-extension graph. although non-penetrated ($d_P \approx 0$) sample shows some levels of strength higher than penetrated ($d_P > 0$) samples with the highest load reached is 11248 N (11248/16=703 N/mm) in the experiment (W2-SP7) being high as shown in Figure 1-38b on the right with load-extension graph, the weld strength varies a little and this is shown with SEM image in Figure 1-39 displaying a mixture of brittle fracture and dimples in the fractured surface. Figure 1-40 shows the SEM image further displaying ductile fracture of Al6060 dominant in Figure 1-37b.

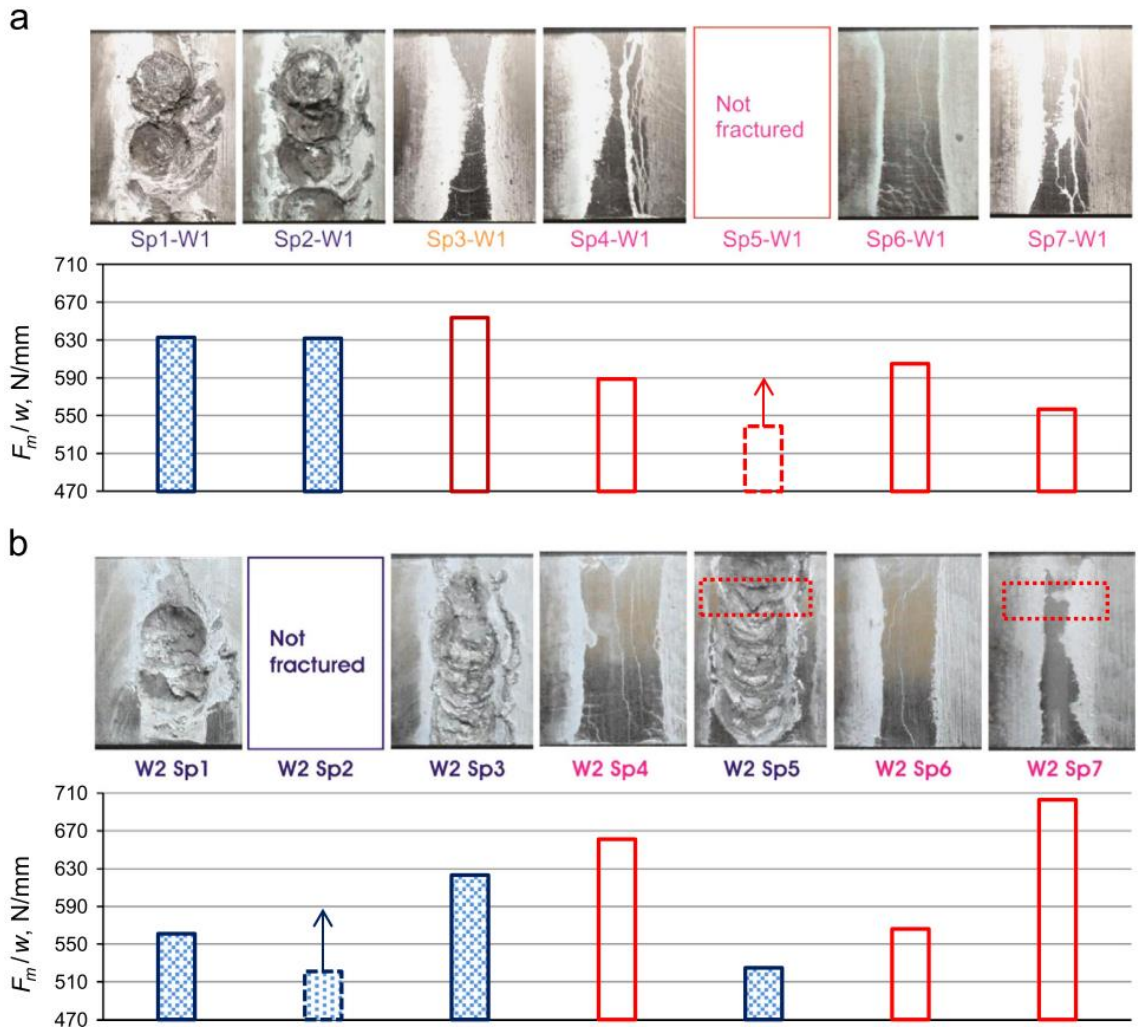

Figure 1-37 Experimental values of Fm/w plotted with sampling locations together with images of the fracture surface of the broken sample from each location (on Ti64 side), (a) experiment 1, and (b) experiment 2. In (b), areas marked red in the photos are shown at higher magnification by SEM images in Figures 1-39 and 1-40 [59].

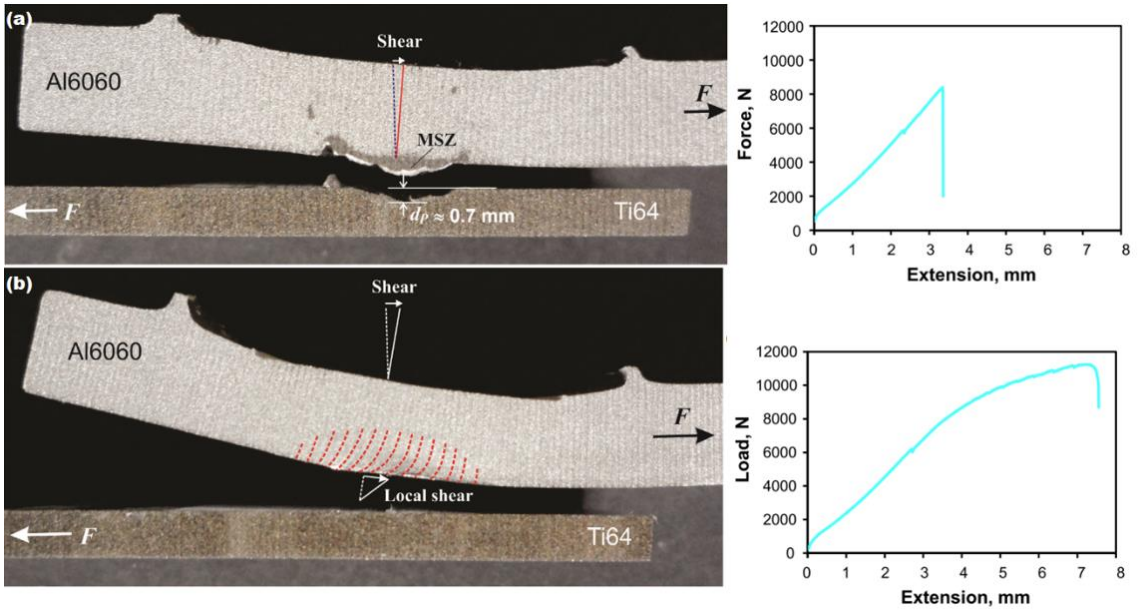

Figure 1-38 Images of tensile-shear tested samples (a) Sp5-W2 sample with a low degree of shear indicated and (b) Sp7-W2 sample showing severe local shear and bending, and (c)

load-extensive curves for the two tests: left curve for Sp5-W2 sample and right curve for Sp7-W2 [59].

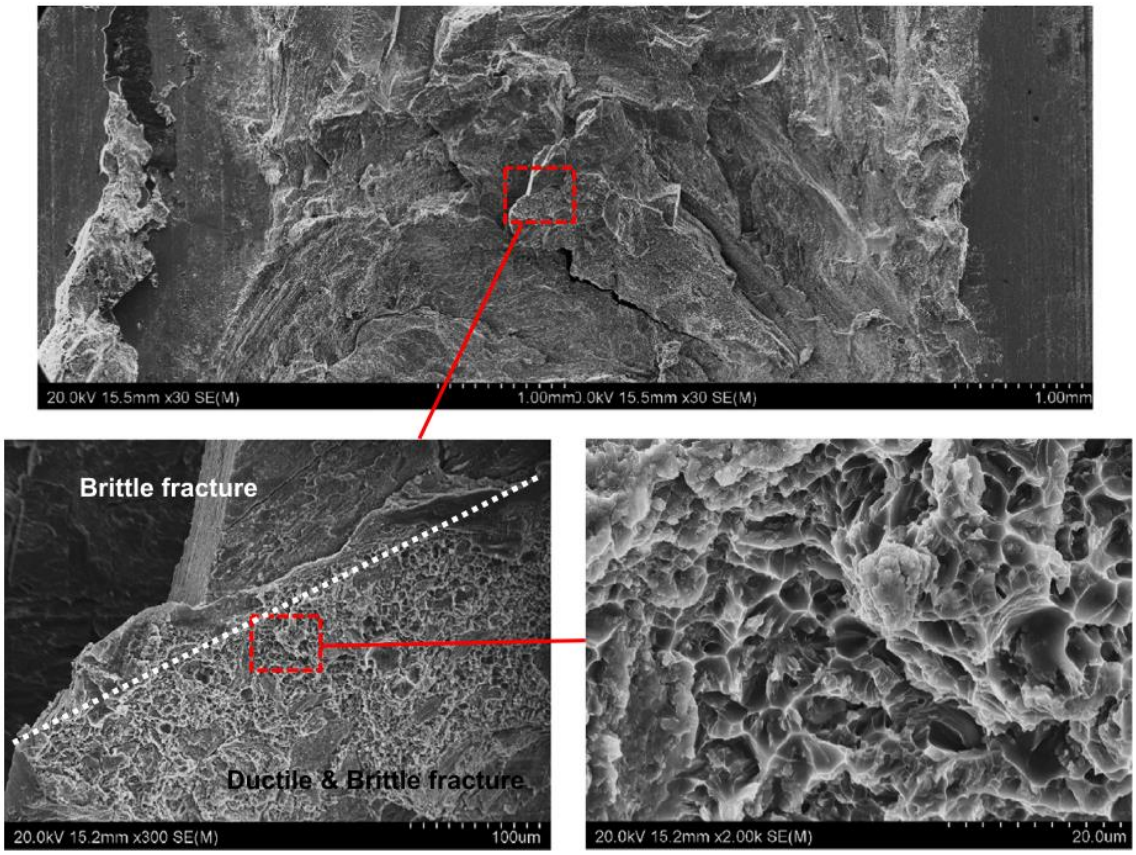

Figure 1-39 SEM fractographs of tensile-shear tested Sp5-W2 sample, taking in the area as indicated in Figure 1-32b, displaying brittle fracture quite dominant but also mixed with dimples in the fractured surface [59].

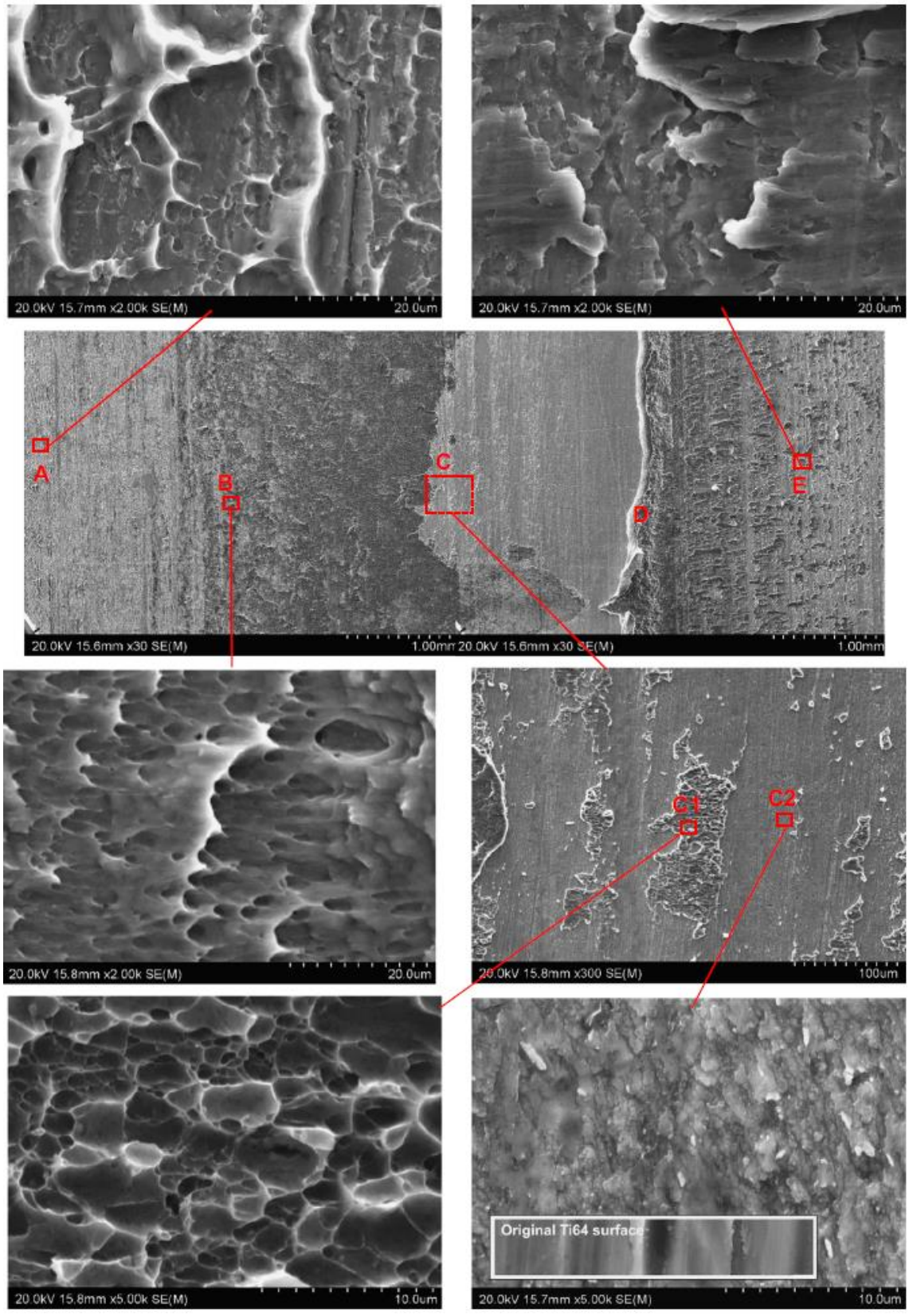

Figure 1-40 SEM fractography of tensile-shear tested Sp7-W2 sample, taking in the area as indicated in Figure 1-35b, displaying ductile fracture of Al6060 dominant [59].

Bo et al.[60] , their 2016 article showed that post-anneal treatment at 400 - 600 °C for 1hour duration can generate a relatively homogenized diffusion-dissolution layer of a multi-island-shaped dual-phase structure at the Al to Ti interface and improves the bonding strength. The

failure load of 8500 N (8500 N/10 mm = 850 N/mm) in their work is high above average compared to others in Table 1-7. The high strength weld may be attributed to post-anneal treatment as has been explained and comparably high with reference literature cited (Table 1.7, column 6). Figure 1-41a reveals a thin IMC layer which when magnified (see Fig. 1-41b) shows laminated microstructure coupled with post-annealing treatment which may be why the strength is exceptionally high. The second spot (c) in Figure 1-41 as enlarged Figure 1-41c and again enlarged as spot (d) in Figure 1-41d shows laminated interface layer providing strong weld strength.

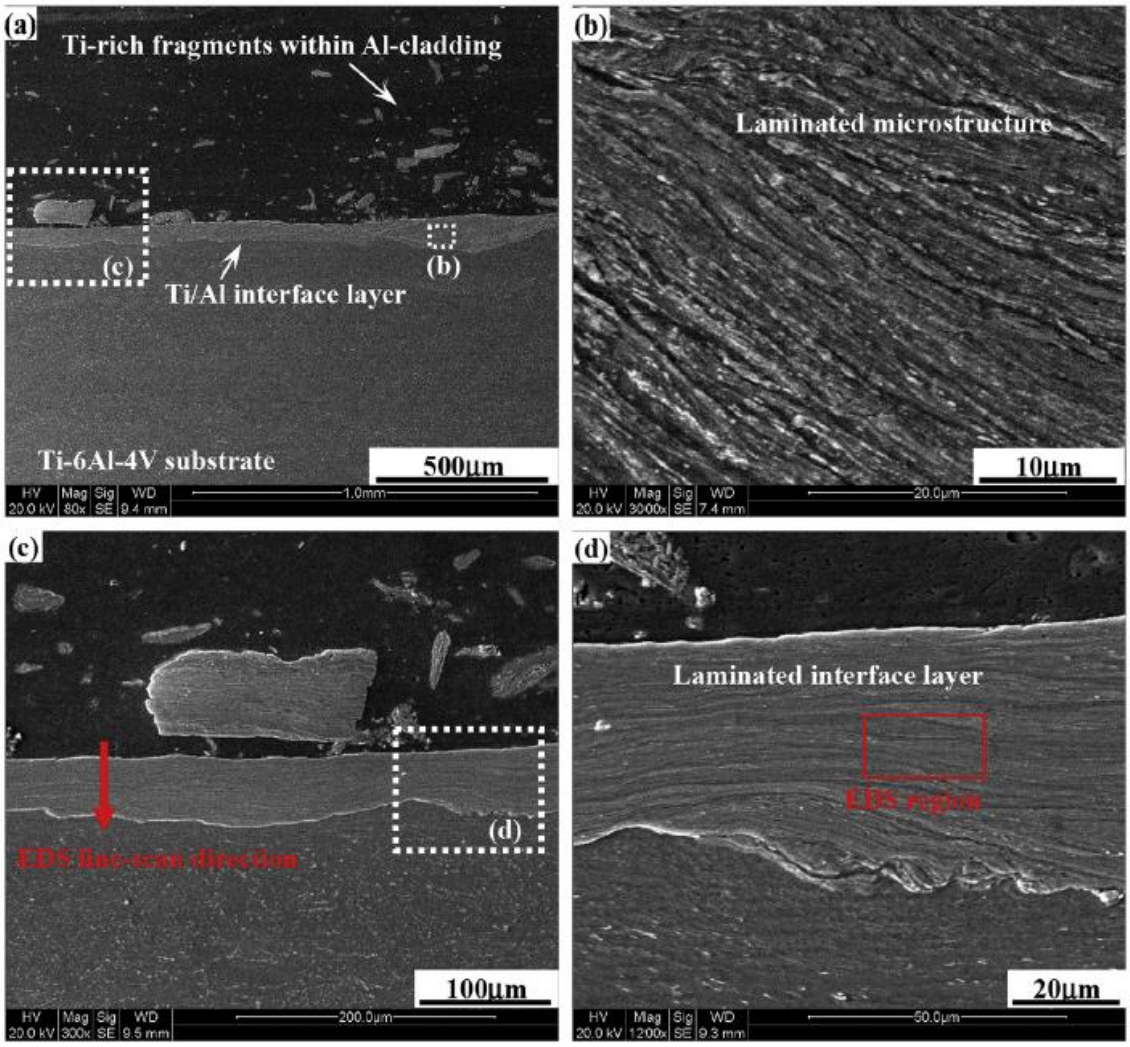

Figure 1-41 SEM images of FSLW fabricated Al to TiAl64V interface layer structures using different *d* values, when other processing parameters are invariable: (a) *d* ¼ 0 mm; (b) *d* ¼ 0.05 mm; (c) the enlargement in (b); (d) *d* ¼ 0.15 mm; (e) *d* ¼ 0.2 mm; (f) the enlargement in (e) [60].

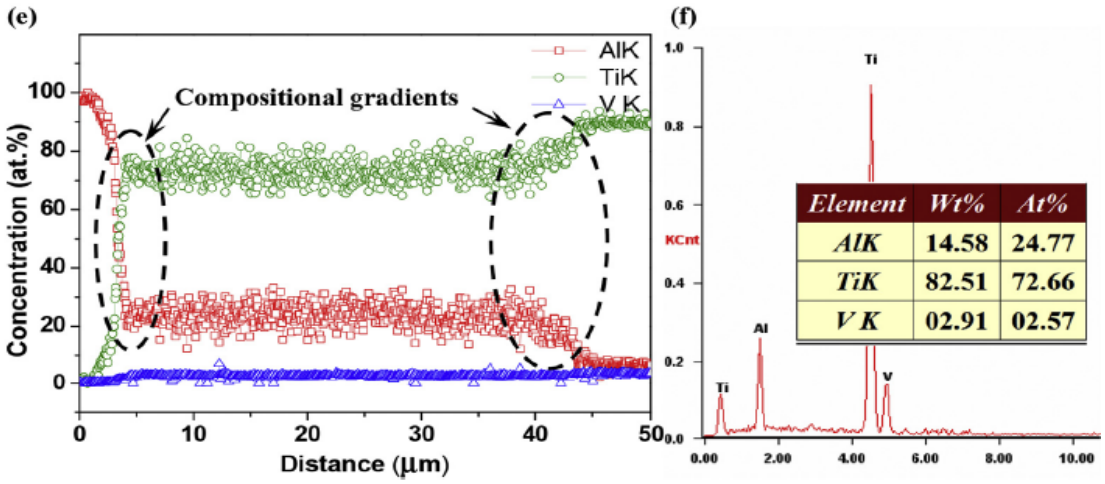

Fig. 4-1 cont.

Recognizing the high strength Al to Ti welds made by FSLW when $d_P \approx 0$ and the issues of tool wear and excessive growth of brittle intermetallic when $d_P > 0$, Huang et al. [61] experimented a novel FSLW technique. In their 2017 article they showed that Ti-Al surface coating was performed before running the hybrid friction stir lap welding (FS-HFSW) as shown in Figure 1-42a *(*Al friction surfacing) and FSL welding as shown in Figure 1-42b. Their high shear tensile strength was attributed to combined contributions of metallurgical reactions of nanoscale $TiAl_3$, IMCs, and mechanical interlocking of Al to Ti interface and Al/Al-coating interface.

Figure 1-43a shows various shear failure loads with different welding parameters with the highest failure load being12.2 kN (12200 N / 20 mm = 610 N/mm). The two main failure zones are HAZ where the highest failure load occurred while the rest failed at the interface zone as shown in Figure 1-43b, 1-43c, and 1-43d show nanoscale $TiAl_3$ and Al to Ti inter-locking respectively, which are responsible for the excellent weld strength. Tool abrasions were avoided as pin plunged only between Al-coating/Al-plate interfaces as shown in Figure 1-42b (superimposed). It can be generally concluded that a high strength Al to Ti FSL is possible with control precession of pin plunge at the Al to Ti interface. This FS-HFS welding process conforms with previous studies [59] avoiding pin penetration ($d_P \approx 0$) onto the bottom (Ti side) plate giving a similar result.

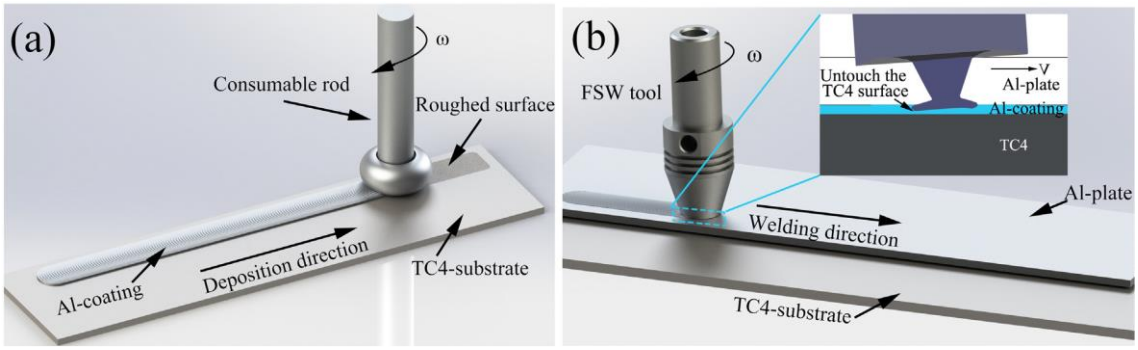

Figure 1-42 The FS-HFSW process: (a) friction surfacing; (b) friction stir lap welding [61].

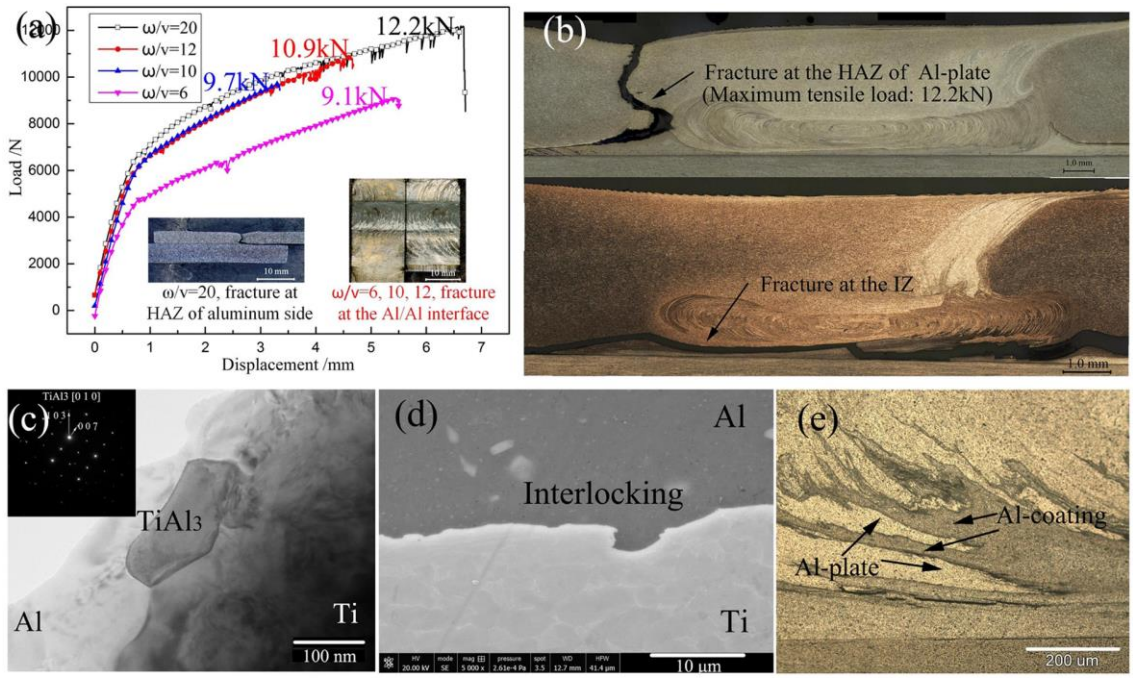

Figure 1-43 (a) Force-displacement curves at different parameters; (b) two kinds of fracture modes; the interfacial behavior of (c) nanoscale $TiAl_3$ IMCs layer (d) inter-locking, and (e) materials mixing at the Al-coating/Al-plate interface [61].

Yue et al. [62], in their 2018 article showed that using a low rotating tool speed of 300 rpm and 30mm/min weld speed was able to achieve a defect-free weld with a maximum weld strength of 7667.1 N (7667.1 N/20 mm = 383 N/mm) while high tool speed formed voids at the lap interface which is comparable to results obtained from others in the literature. However, at the low temperature, hook defect has been identified which at high rotational tool speeds ranging from 900 - 1400 rpm barely forms hooking as it was reported in most literature involving high temperature alloys. In Figure 1-44; a) no hook is observed but a void is seen at the interface at the rotation tool speed of 1200 rpm, b) both a hook and void are formed at 800 rpm, c) hooks have been formed at both ends at 500 rpm and, c) a large hook was formed at right end of the weld interface at 300 rpm.

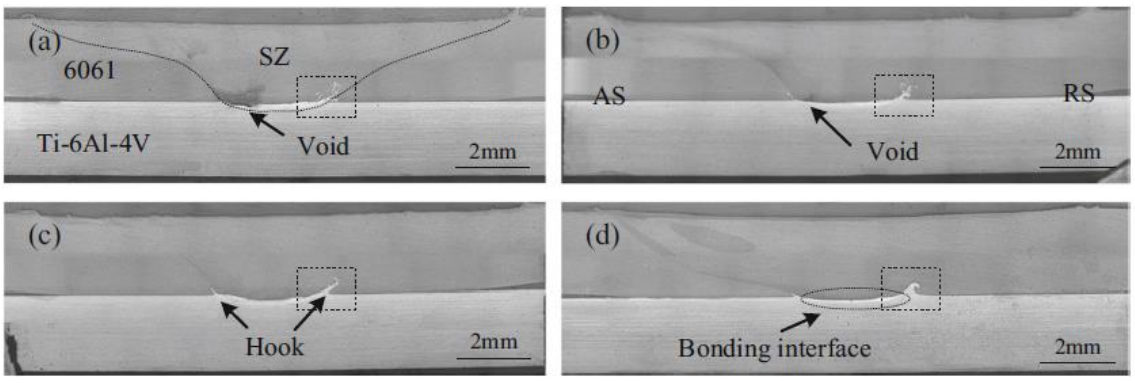

Figure 1-44 Cross sections of the lap joints using different rotating speeds: a) 1200 rpm, b) 800 rpm, C) 500 rpm and d) 300 rpm [62].

Figures 1-45a and 1-45b show further hook defects at ω = 500 rpm and ω = 800 rpm, respectively. Despite the formation of the hook being detrimental in weld joint strength particularly in aluminum and other low temperature alloys, a very interesting phenomenon involving FSL welds of Al to Ti is that failure is not common in the hook region.

(a) (b)

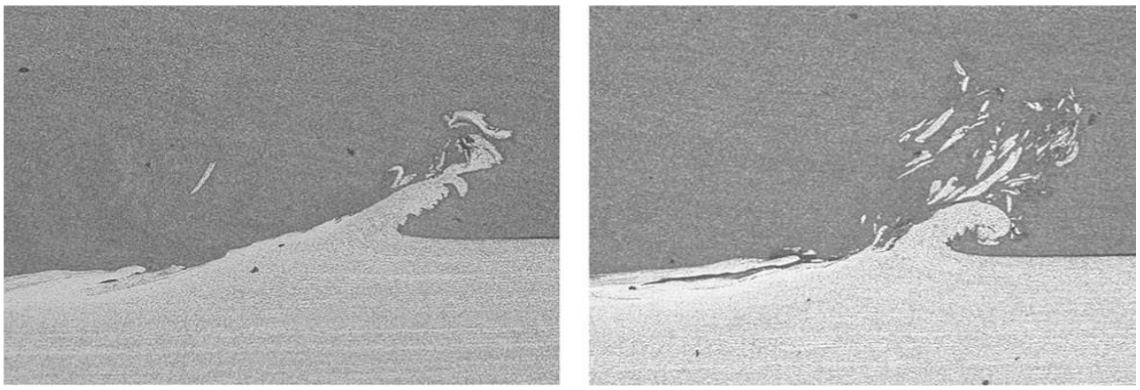

Figure 1-45 The broken Ti alloy above the hook at two different rotational tool speeds: a) 500 rpm, b) 800 rpm [62].

There have been several studies [63-67], on the influence of ω on the microstructure and mechanical properties. Zhao et al. [64], in their 2019 article investigated the interfacial microstructure with different pin profiles to see the relationships between interfacial microstructure, mechanical properties, and fracture mechanism. They showed that interfacial microstructures and mechanical properties are remarkably affected by the probe length. Possible phases were seen concerning pin probe length starting the first phase Ti and $TiAl_3$ formed due to lower activation energy. The maximum shear strength of 147.5 MPa (≈ 430 N/mm) was obtained with 3.1 mm probe length. However, this strength value is still low in comparison with other literature because its pin width is 3mm (almost specimen width of 3.3 mm) which is much lower than most FSL weld specimen width for sound comparison of weld strength.

A series of studies done on microstructure and mechanical properties evaluation using different welding parameters in fabricating Al-Ti FSL weld [51-62] have shown an average shear strength of ~480 N/mm. However, articles presented by Chen and Yazdanian [59] and Huang et al. [61], have significantly shown high weld strength values of 703 N/mm and 610 N/mm, respectively. The above high strength values are in fact due to their improvements in conventional method of FSW approach aiming at avoiding pin penetration ($d_P > 0$) at the weld interface which proved high strength FSL welds production.

Chen and Yazdanian [59] and Huang et al. [61] have used almost a similar approach in achieving their high strength FSL welds by avoiding pin penetration onto the bottom plate. However, Li et al. [60] have achieved the highest strength value of 850 N/mm with conventional FSLW compared to all FSL welds in the cited pieces of literature [56-59, 62-67]. The resulting strength may be that

from several contributing factors like thin parent metals, small specimen width (Ws), and post-annealing treatment. However, the authors have not sufficiently provided as to how much depth of pin penetration was allowed because of the intricate nature of the thin (2 mm thick) Al parent metal as a top sheet. Therefore, there are still certain details missing from their work to acertain their readers of their important research.

It should be noted that IMC thickness in Al to Ti FSL welds by many in literature (see Table 7, column 7) have been reported to be ≤ 7.5 µm. However, without an IMC layer, no joint is expected but there is no clear understanding of how IMC layer be optimized to produce a high strength weld joint. IMC ($TiAl_3$) was the main interaction layer presence at the Al to Ti interface as schematically shown in Figure 1-46 in all Al/Ti FSL welds. However, Li et al. [60] reported IMC layer of 45 µm which is quite high among literature available and its shear lap strength is 850 N/mm. However, the weld has been post annealed where pure Al base metal can reach as high as 690 MPa in tensile strength from only around 90 MPa.

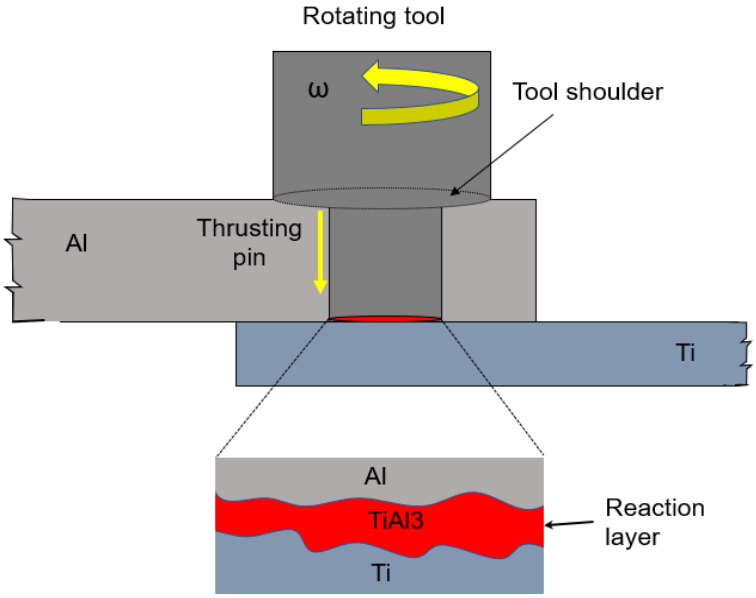

Figure 1-46 Schematic illustration showing intermetallic reaction layer formation during FSL welding.

Observing weld strength in terms of F_m/W_s, with different parent material thickness, alloy grade, and more importantly the specimen width (W_s), there is no common specification used in these articles. It appears that specimen specifications have been borrowed from elsewhere and others have been decided by the authors of the article.

Also, there is not enough attention given by various literature on the importance of weld width (W_s). Weld width (W_s) is one of the important factors that play a significant role in the overall strength of the weld and should be considered to properly compare the overall strength of the weld with other similar published papers because currently, FSLW tests are not standardized.

A known high strength Al alloy currently available in the industry is AA2024 (480-550MPa) and the FS butt welds by Dressler et al. [36] and Chen et al. [41], involving two different tempered AA2024 alloys were presented earlier (see Table 1-4). However, there is a lack of information on AA2024/Ti FS lap welds of dissimilar joints in the literature. However, FS butt welds of AA204-T3/Ti6Al4V [36] and AA2024/Ti6Al4V [41] may be sufficient to deduce its weld strength based on the parent Al alloy. In comparison with all the base Al alloys reviewed in this chapter, AA2024 has the highest tensile and shear strength.

A valid point from these studies may be that, provided a strong Al alloy is used, the weld strength of the Al alloy to Ti FS lap weld can reach from 703N/mm - 850N/mm which are considerably higher than steel. Al to Ti FSL welds were stronger than the other two high-temperature alloys, namely Steel and Cu FSL welds.

Table 1-7 Summary of the collected data from literature on FSLW conditions with maximum σ_{Lap} achieved for Al to Ti FSL welds

Base Metals Thickness Ref.	FS Parameters (rpm, mm/min, tilt ∠)	Pin Profile (mm)	Fracture strength (Al & Cu) (MPa)	Max. σ_{lap} (Al &Ti) (MPa)	Force per unit width F_m/W_s (N/mm)	IMC thickness
AA-ADC12/ Ti6Al4V [56] (4mm-2mm)	ω = 1500 v = 60 ∠ = 3°	$OD_{shoulder}$ = 15 OD_{pin} = 5 L_{pin} = 3.9	310 862	245 760	9400N/20 = 470	≤ 5 µm
AA LF6/ Ti6Al4V [57] (2mm-2mm)	ω = 1500 v = 60 ∠ = 2°	$OD_{shoulder}$ = 15 OD_{pin} = 4 L_{pin} = 2.1	862	760	2800/12.5 = 224	
AA1060/Ti6Al4V [58] (3mm-3mm)	ω = 950 v = 300 ∠ = 0°	$OD_{shoulder}$ = 25 OD_{pin} = 6 L_{pin} =	69 862	69 760	1910/10 = 191	
AA6060/ Ti6Al4V [59] (6mm-2.5mm)	ω = 1400 v = 20 ∠ = 2.5	$OD_{shoulder}$ = 25 OD_{pin} = 6 L_{pin} = 5.2	160 862	117 760	11248/16 = 703 (NP)	≤ 250 nm

Pure Al to Ti6Al4V [60] (2mm-3mm)	ω = 1200 v = 60 $\angle$ = 3°	$OD_{shoulder}$ = 15 OD_{pin} = 6 L_{pin} = 2	90 862	75 760	8500/10 = 850	45 µm
AA6082-T6/ Ti6Al4V [61] (3mm-3mm)	ω = 1800 v = 90 $\angle$ = 3°	$OD_{shoulder}$ =- OD_{pin} = 8	150 862	85 760	12200/20 =610 (NP-int.)	< 250 nm
AA6061-T6/Ti6Al4V [62] (2.7mm-2.5mm)	ω = 1200 v = 30 $\angle$ = 2.5°	$OD_{shoulder}$ = 15 OD_{pin} = 4-7 L_{pin} = 2.7	290 862	207 760	7667.1/20 = 383	6 µm
6061Al/ Ti6Al4V [63] (3mm-2mm)	ω = 1000 v = 100 $\angle$ = 3°	$OD_{shoulder}$ = 12 OD_{pin} =- Probe = 3.1	290 862	207 760	8985/20 = 449	-----
AA6061/Ti6Al4V [64] (3mm-2mm)	ω = 1000 v = 100 $\angle$ = 3°	$OD_{shoulder}$ =- OD_{pin} =- L_{pin} = 2.9	290 862	207 760	1418/3.3 ≈ 430	
AA6061/Ti6Al4V [65] (3mm-2mm)	ω = 1000 v = 100 $\angle$ = 3°	$OD_{shoulder}$ = 12 OD_{pin} = 3 L_{pin} = 3.1	290 862	207 760	4500/10 = 450	7.5 µm
AA6061/Ti6Al4V [66] (3mm-2mm)	ω = 1000 v = 80 $\angle$ = 3°	$OD_{shoulder}$ = 12 OD_{pin} = 3 L_{pin} = 3.1	290 862	207 760	4026/10 ≈ 403	<5µm
AA6061/Ti6Al4V [67] (3mm-2mm)	ω = 1400 v = 60 $\angle$ = 3°	$OD_{shoulder}$ = 2 OD_{pin} = 3 L_{pin} = 3.1	290 862	207 760	1412.67/3.1 ≈ 455	< 5 µm

*Note that if many welds were performed, the welding parameters providing the best strength have been presented: v, welding speed/mm min^{-1}; ω, rotational speed/revmin^{-1}; $\angle$, tilt angle; strength is the tensile strength at fracture/(MPa); $OD_{shoulder}$, Outside shoulder diameter; OD_{pin}, Outside pin diameter; L_{pin}, length of pin or pin height; F_m = Maximum failure load; W_s = specimen width.

1.4 Brief Review on Fatigue of Aluminium-to-Aluminium Welds made using Friction Stir Welding

Searching through the open literature, no research on fatigue properties and behaviour of Al to Ti welds made either by FSW or FSLW have been conducted. Furthermore, it appears there has not been fatigue study of Al to Cu or to steel welds made using FSW or FSLW. As will be reported and discussed (in Chapter 3), fatigue properties of Al to Ti welds made in this study will be compared to Al to Al welds made using FSLW. Thus, in this section, similar and dissimilar Al-to-Al FSL welds are discussed from static to cyclic loading conditions. A further discussion on the FSL weld deficiencies such as hooking and cold lap defects which are detrimental to joint integrity and mechanical performance will be discussed.

1.4.1 Cyclic Stresses

Figure 1-47 shows cyclic loading parameters in a repeated cyclic stress cycle. Each of the parameter is briefly discussed below:

The stress amplitude alternates about a mean stress σ_m, defined as the average of the maximum and minimum stresses in the cycle, or

$$\sigma_m = (\sigma_{max} + \sigma_{min})/ 2 \quad (1)$$

Furthermore, the range of stress is just the difference between σ_{max} and σ_{min}, namely

$$\sigma_r = \sigma_{max} - \sigma_{min} \quad (2)$$

Stress amplitude σ_a is just one half of this range of stress, or

$$\sigma_a = \sigma_r/2 = (\sigma_{max} - \sigma_{min})/ 2 \quad (3)$$

Finally,the stress ratio R is just the ratio of minimum and maximum stress amplitudes:

$$R= \sigma_{min} / \sigma_{max} \quad (4)$$

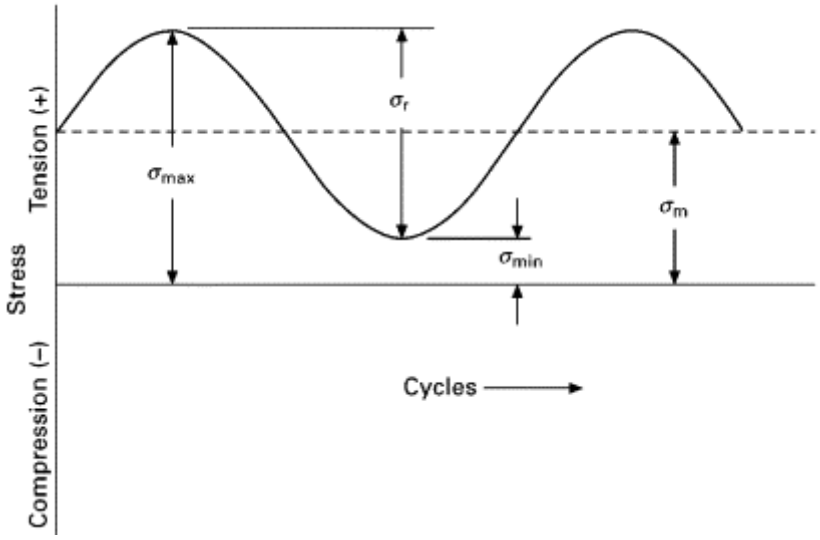

Figure 1-47 Fatigue stress profile for a repeated stress cycling with cyclic loading parameters [68].

1.4.2 S-N Curve

Figure 1-48 shows the S-N curve which presents three important information regarding a material experiencing a cyclic loading condition. Fatigue strength is defined as the stress level at which failure will occur for some specified number of cycles (E.g., 10^7 cycles). Another important parameter that characterizes a material's fatigue behaviour is fatigue life is the number of cycles to cause failure at a specified stress level. Fatigue limit or sometimes called endurance limit is the stress level at which failure will not occur for indefinite number of cycles. Porous alloys such as steel and titanium have fatigue limits about 35-60 per cent of their tensile strength [69].

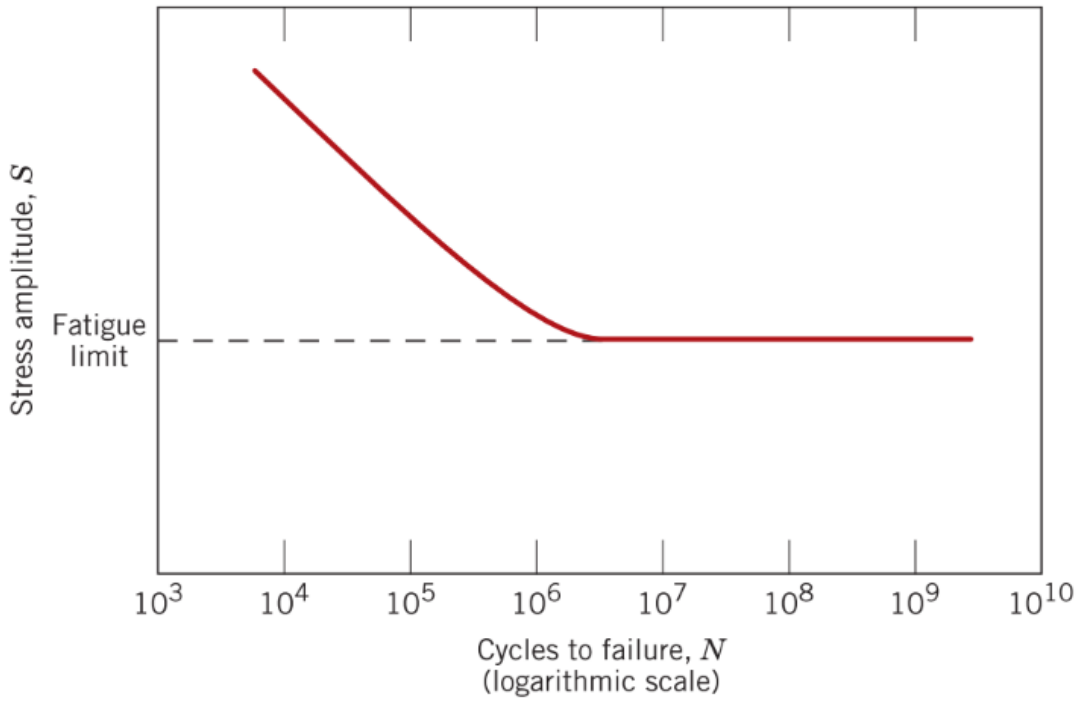

Figure 1-48 Stress amplitude (S) versus logarithm of the number of cycles to fatigue failure (*N*) for (a) a material that displays a fatigue limit [69].

Table 1-8 is a summary providing fatigue life of both similar and dissimilar FSL welds of aluminium to aluminium alloys, maximum stress amplitude (MPa), fracture strength of the parent alloy (MPa), pin profiles (mm) (shoulder diameter, pin length and diameter) and FS parameters (rotational tool speed, weld speed and tool tilt angle). However, one common issue shared in these reported articles [70-73] is that the authors have not provided their fatigue strength values in terms FSLW which depends on the size of the specimen width. Therefore, given the stress amplitude in MPa, applied load in force per unit (F_m/W_s) can be easily determined with known specimen thickness and weld width (pin tip diameter). Table 1-8, column 6 presents the calculated F_s/W_s values.

Table 1- 8 Summary of the fatigue life cycle for Al-Al FSL welds (data collected from literature).

Base Metals [Ref.]	FSPara-meters	Pin size (mm)	Fracture strength (Al & Al) (MPa)	Max. σ_{lap} Amp. (MPa)	F_m/W_s (N/mm)	Cycle Number (*N*)
AA2024-T3/ AA2024-T3 (1.6 - 1.6)mm [70]	ω = 1400 *v* = 400 ∠ = 2°	$OD_{shoulder}$ =- OD_{pin} =- L_{pin} =-	440	27	864/20 = 43	1X 10^7
AA2024-T3/ AA2024-T3 (1.6 - 1.6) mm [71]	ω = 1400 *v* = 400 ∠ = 2.5°	$OD_{shoulder}$ =- OD_{pin} =- L_{pin} =-	440	25	800/20 = 40	1 x 10^7
AA5754-T6/AA6082-H111 (5 - 5) mm [72]	ω = 1400 *v* = 400 ∠ =-	$OD_{shoulder}$ =- OD_{pin} =- L_{pin} =-	270 280	15	1200/16 =75	2 x 10^6
AA5754/ AA6082 (2 – 2) mm [73]	ω = 1000 *v* = 400 ∠ = 2°	$OD_{shoulder}$ = 16 OD_{pin} = -5 L_{pin}=-	270 280	20	600/15 =40	2 x 10^6

*Provided are the stress amplitude, fatigue strength in terms of FSLW strength can be calculated with specimen thickness and weld with (N/mm). If many welds were performed in a single article, the welding parameters providing the best strength is presented. *v*, welding speed/mm min^{-1}; ω, rotational speed/$revmin^{-1}$; ∠, tilt angle; strength is the tensile strength at fracture/(MPa); $OD_{shoulder}$, Outside shoulder diameter; OD_{pin}, Outside pin diameter; L_{pin}, length of pin or pin height; F_m = Maximum failure load; W_s = specimen width.

Fersini and Pirondi [70, 71], in their 2007 and 2008 articles reported two different procedures of fatigue tests conducted with stress ratio, R = 0.1; three simulated and one experimental numerical results have been discussed. Figure 1-49 on the bottom right shows the blue dotted marker which does not indicate on the legend and is misleading. The experimental procedure shows a slightly better result than the simulated models used. However, in Figure 1-50 is the comparison of the experiment and numerical modelled results without initial overload. Out of the three models used, the experimental result is still slightly higher than the predicted fatigue t results.

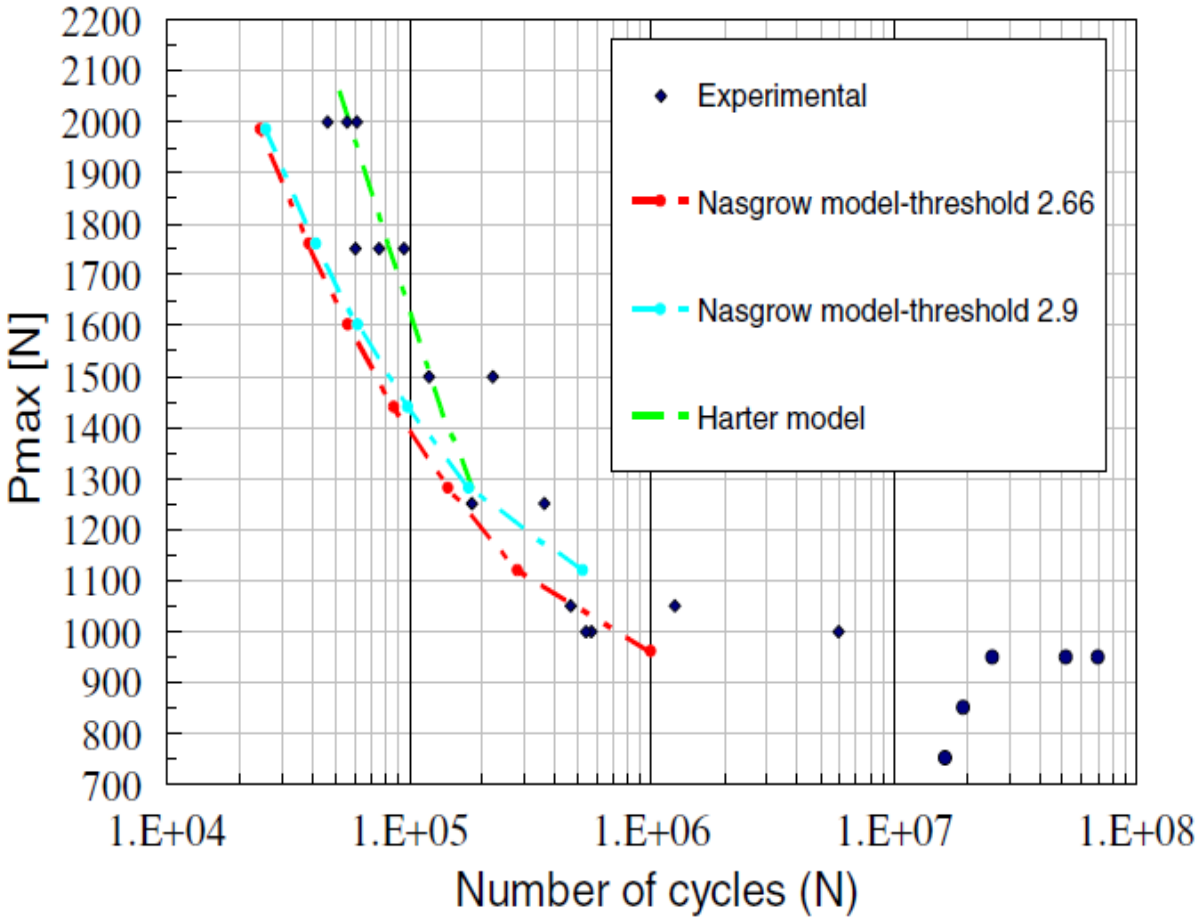

Figure 1-49 Load (N) against number of cycles (N); a comparison between experimental and three numerical results [70].

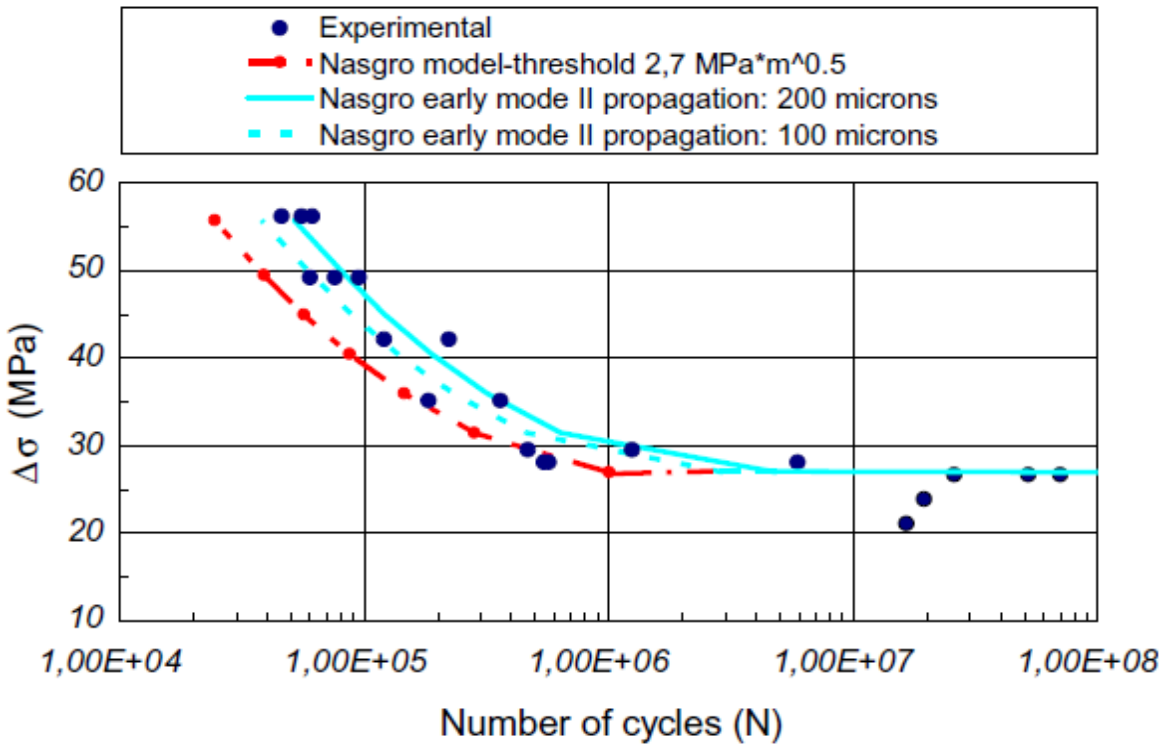

Figure 1-50 Experimental and predicted fatigue lives without initial overload [71] expressed as stress amplitude against the number of cycles.

Xu et al. [72], in their 2012 article investigated the microstructure and fatigue properties of Al to AL FSL weld joints using single pass welding (SPW) and double pass welding (DPW) to compare their fatigue strengths and the effects of hooking defects while applying different fatigue stress ratios R (σ_{min} / σ_{max}) set to 0.1 and 0.5 for SPW and 0.1 and 0.3 for DPW. Their main objective was to provide general fatigue assessment because of lack of statical data on Al to Al FSW being seldom in publications. They conclude that existence of hook defects mainly at TMAZ region in FSW lap weld joints which reduced the effective sheet thickness (EWT) hence induce extreme stress concentration at the site. They have also reported that DPW could not improve the fatigue strength compared to SPW due to severity of its hooking defects and reduction in EWT leading to final reduction in fatigue strength. Figure 1-51 clearly shows under *S-N* curve, DPW for both R = 0.1 and R = 0.5 have less significance in the overall fatigue performance of FSW lap joint. However, for SPW, R = 0.1 and R= 0.3 do show some level of difference in their fatigue data. For SPW R = 0.5, the data points are just falling similar to DPW R = 0.1 and DPW R = 0.3.

It is quite obvious that at high stress ratio, the fatigue life is lowered and is evident in the data obtained for SPW R = 0.1 and R = 0.5 as shown in their corresponding *S-N* curve. However, authors have not provided any other explanation as to why using the two different stress ratios for the SPW resulted in such a huge margin. It was observed that the authors have conducted their fatigue tests at stress amplitude of 17 MPa (1360 N/16mm = 85 N/mm) for SPW R = 0.1 and 30 MPa (2400 N/16 mm = 150 N/mm) for R = 0.5. It is quite obvious that at high stress ratio and stress amplitude, the fatigue data is expected to be at low fatigue low. However, using different

stress ratios with different stress amplitude is not possible to compare the strength of the FSW lap joints for the same weld. The test parameters must be the same in order to compare the variations in their fatigue performance.

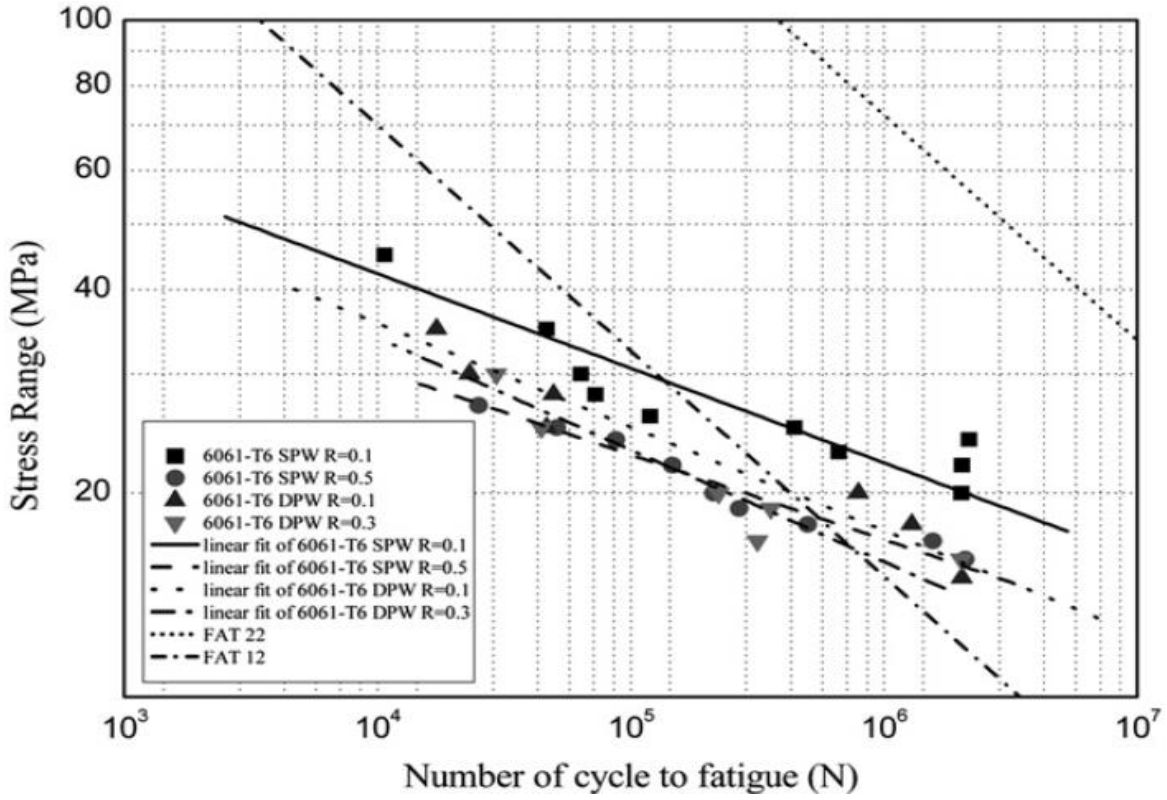

Figure 1-51 Stress amplitude against the number of cycles; S–N curves under different conditions of stress ratio *R*, SPW and DPW [72].

Figure 1-52 shows a common SPW joint fatigue fracture surface. There are several zones in fatigue fractography, including fatigue crack initiation, propagation, and the final fracture zone. As shown in Figure 52a, the fracture has several crack initiations from the bottom of the top plate, which corresponds to the hooking spot. The fracture surface can be divided into two parts as the distance from the bottom surface increases: the propagation area is much smoother, with some fatigue strips on the surface; the final fracture area is relatively denser, with visible ductile fracture and tearing ridge patterns. Besides that, several oval traces have been discovered. There are some brittle fracture features in the propagation, as well as some secondary cracks as shown in Figure 1-52b. At higher magnifications, fatigue striations can be seen clearly shown in Figure 1-52c, with the light horizontal lines indicating the progression of a crack across the part with each period. The ductile cracking associated with several deep hole style dimples can be found in the final fracture region, as shown in Figure 1-52d.

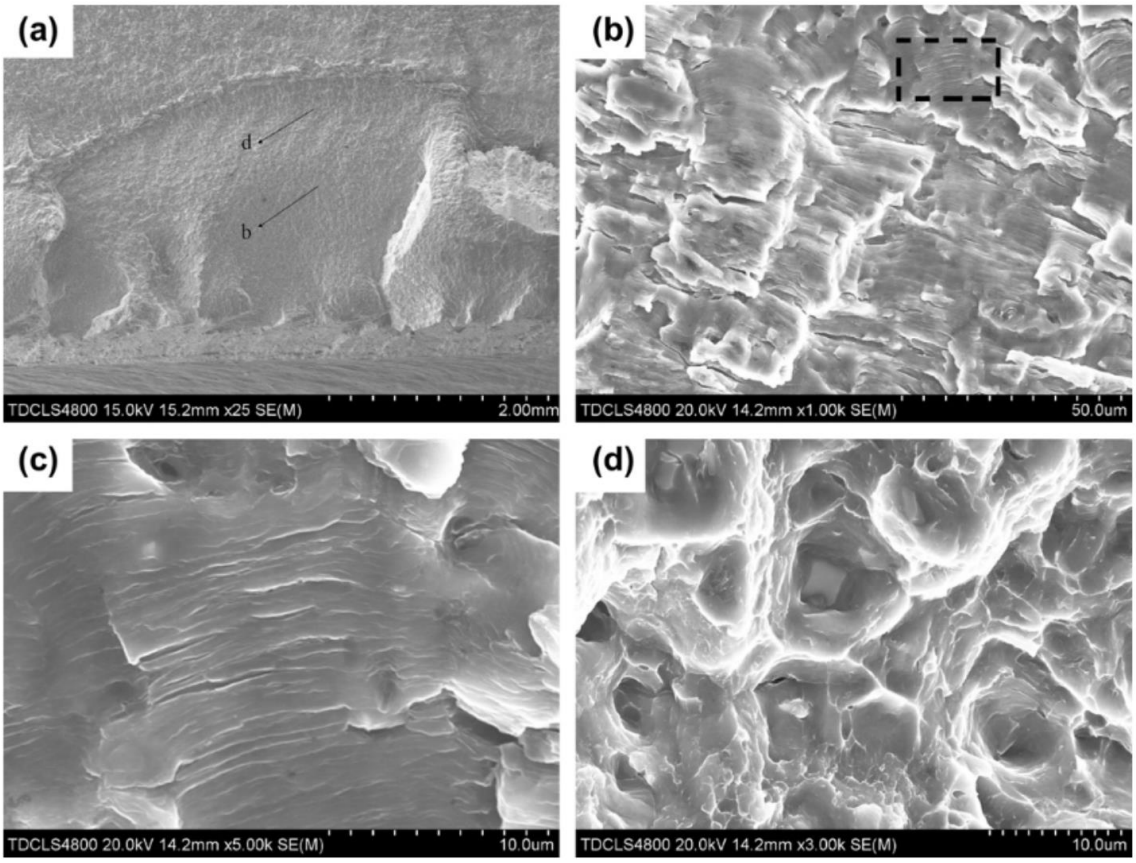

Figure 1-52 SEM images of fatigue fracture surfaces of the SPW specimen tested at 17 MPa stress amplitude (R = 0.5): (a) overall view of the fracture surface at a lower magnification, (b) the fatigue crack propagation zone, (c) fatigue striations at a higher magnification of the dashed box in (b), (d) the final fracture region [72].

Figure 53 depicts a standard DPW joint fatigue fracture surface. As shown in Figure 1-53a, the fracture has several crack initiations from the bottom of the upper plate corresponding to the hooking site, but the location of crack initiation is more than SPW joints, which is one cause for the poor fatigue properties. The intergranular cracking along the weak grain boundaries as shown in Figure 1-53b and 1-53c showed that the initiation sites were in the NZ and that the fracture pattern was crystallographic. The fatigue striations as shown in Figure 53d and 1-53e are also common in crack propagation, although this region has more secondary cracks, causing the fatigue property to deteriorate. On the final fracture area, shallow-hole shaped dimples were observed as shown in Figure 53f.

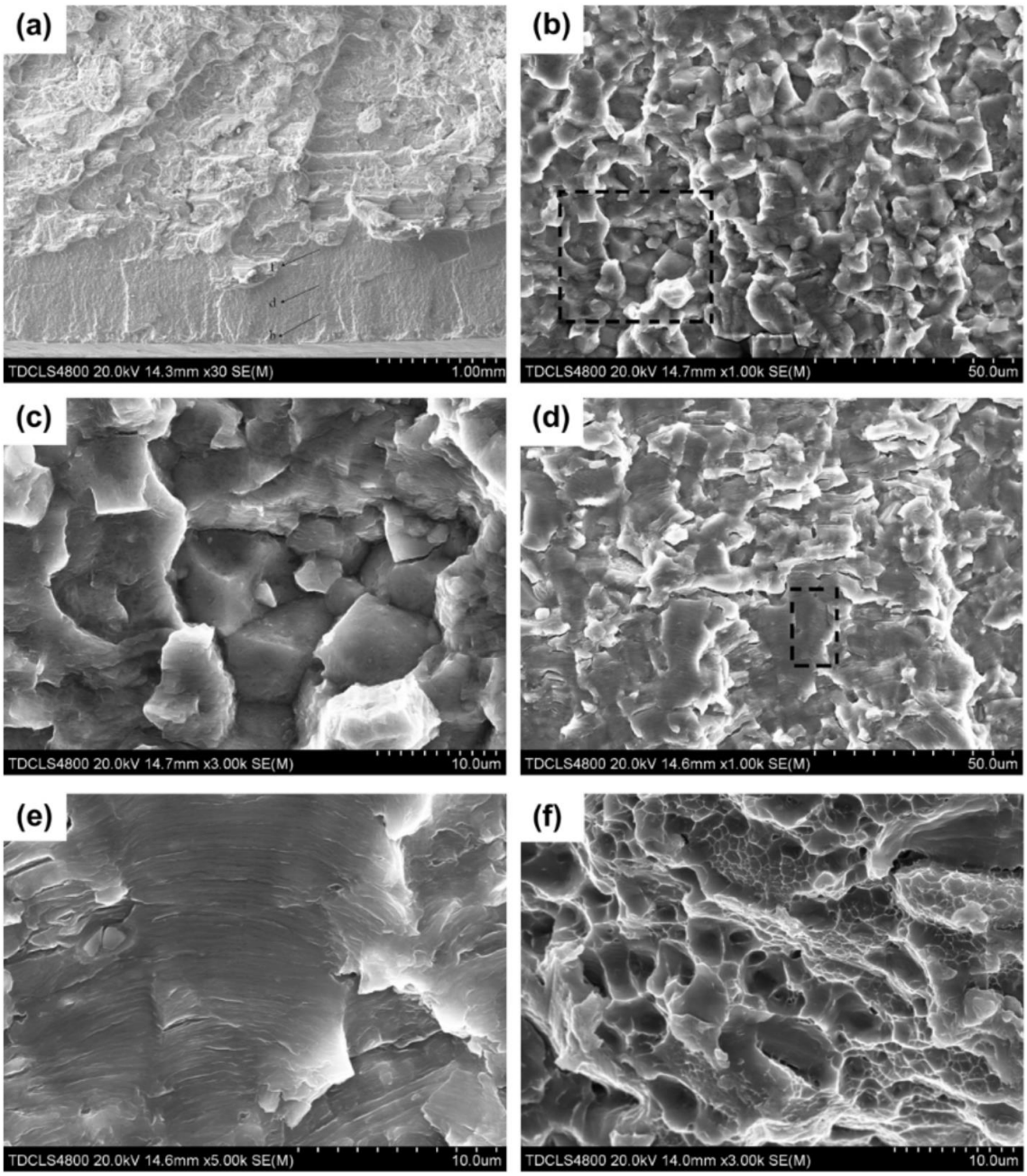

Figure 1-53 SEM images of fatigue fracture surfaces of the DPW specimen tested at 30 MPa stress amplitude (R = 0.3): (a) overall view of the fracture surface at a lower magnification, (b) magnified view near initiation, (c) intergranular cracking along the weak grain boundaries of equiaxed grains, (d) the fatigue crack propagation zone,(e) fatigue striations at a higher magnification of the dashed box in (d), (f) the final fracture region [72].

Infante et al. [73], in their 2016 article reported that Al/Al FSL welds present two major welding defects which mostly affect both tensile and fatigue strength. First, hooking is a major problem that weakens the weld strength on FSL welds of aluminium alloys. A hook feature is shown in Figure 1-54 which is common in Al/Al FSL welds. Second, kissing bond defect is another contributing factor in reducing the mechanical strength of the Al/Al FSL welds.

They further showed that with a stress ratio of 0.1 and stress range from 15 MPa (480 N/20mm = 24 N/mm) and 25 MPa (800 N/16 mm = 50 N/mm), fatigue life falls between 10^4 and 10^5 cycles for AA5754/AA6082 FSL welds while AA6082/AA6082 FSL welds can undergo the same number of cycles at cyclic stress amplitudes from 25 MPa (50 N/mm) - 75 MPa (2400 N/16mm = 150 N/mm) as shown in Figure 1-55 with two different S-N curves for a similar and a dissimilar FSL weld aluminium alloy. Figure 1-56a shows a micrograph of a similar (AA6082–AA6082) joint displaying NZ. Figure 1-56b shows hook formation in the dissimilar joints while Figure 1-56c is a typical laminar flow of dissimilar Al material flow.

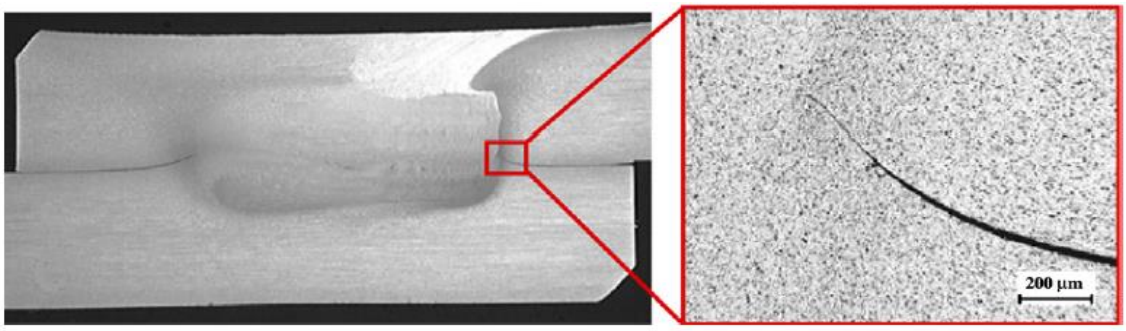

Figure 1-54 Example of overlap weld section and material hooking defect [71].

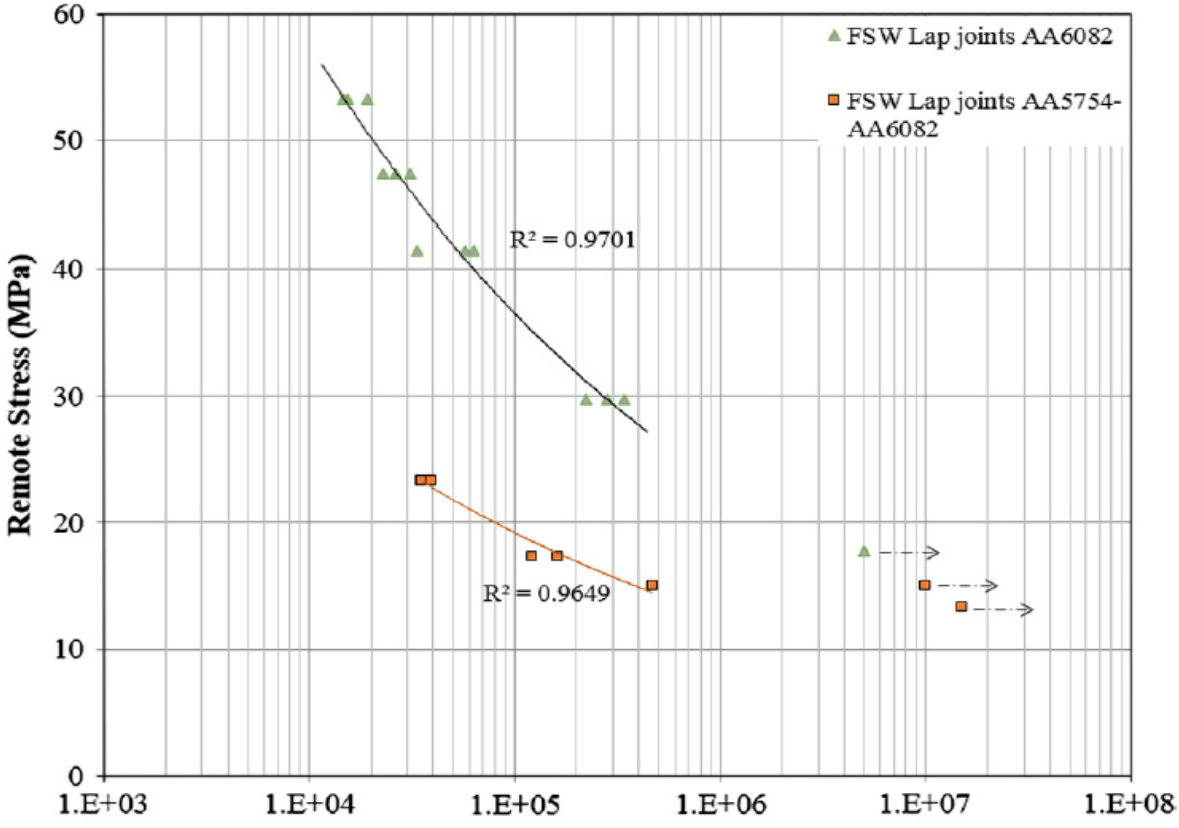

Figure 1-55 Remote stress against number of cycles, S–N curves at R = 0.1 for dissimilar and similar joints [73].

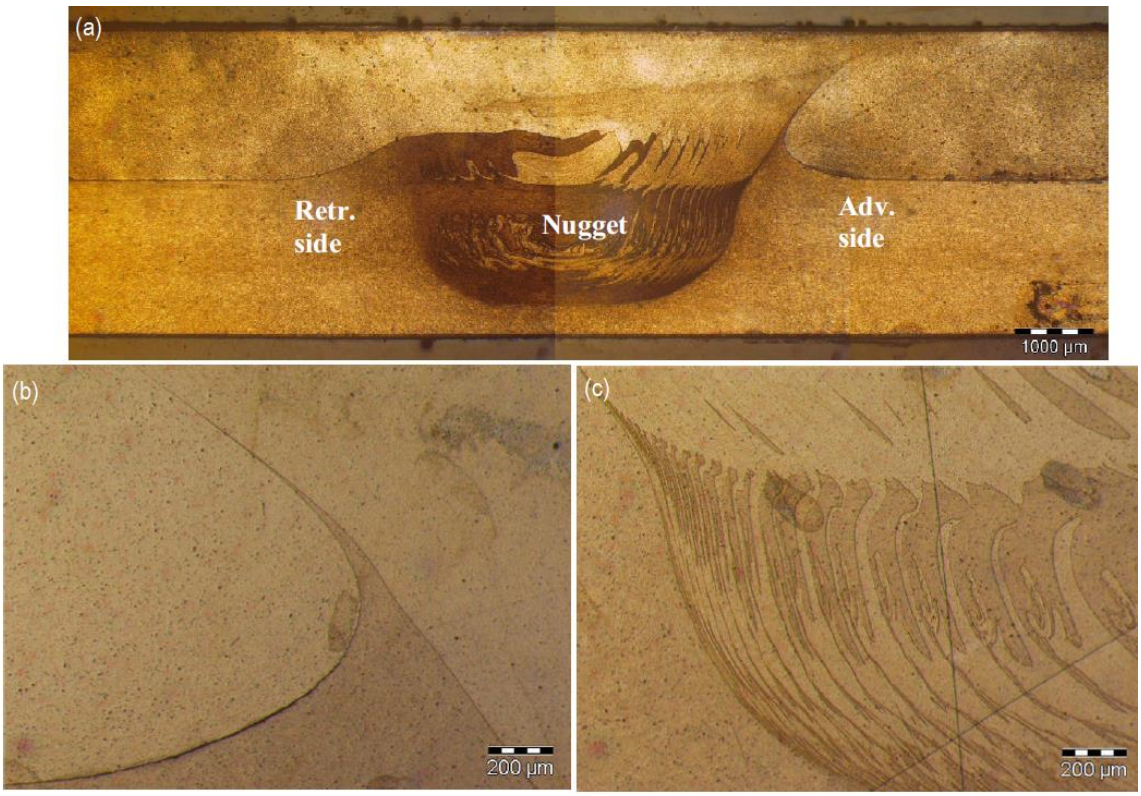

Figure 1-56 (a) Micrograph of the similar material joint (AA6082–AA6082), (b) Hook defect of the dissimilar joint (AA5754–AA6082) and (c) Closer look of the left side edge of the nugget (AA5754–AA6082) [73].

A valid point from these studies [70-73] may be that, provided a strong Al alloy is used, the weld strength of the Al alloys FS lap weld can reach more than 10^7 cycles at shear strength of 20 MPa (600 N/15 mm = 40 N/mm) – 27 MPa (810 N/15 mm = 54 N/mm). This means that in Al to Al FSLW geometry, only low stress amplitudes can be used. However, the fatigue strength of Al FSLW to dissimilar high-temperature alloys may perform far better than Al-Al FSLW alloys because shear strength in terms of FSLW Al to high-temperature alloys such as Al to Ti FSL welds can reach as high as 703N/mm [59] to 850N/mm [60].

1.5 Scope of this Research

1.5.1 Summary of Literature and Knowledge Gaps Identified

On FSW of dissimilar metals, with a focus on the Al to Ti alloy couple, the above review of the relevant literature has shown the following:

- Extensive studies have been reported on FSW of Al alloy to high melting temperature alloys (Cu, steels, and Ti alloys) in both butt and lap weld geometries. There is however little work on the fatigue of welds made by FSLW of Al alloy to other high melting temperature alloys. Study on fatigue properties of Al to Cu FSL welds may not be significant as the welds may not find their industrial applications. Study on the fatigue of Al to steel FSL welds has rarely been reported and this is likely the result of low static strength of the welds and the welds are limited in structural applications. Thus, interest in their fatigue properties is also limited.
- Many studies have shown the excellent static tensile-shear strength of Al to Ti FSL welds, which, comparatively, are considerably higher than those of Al to Cu and Al to steel FSL welds. Furthermore, strength values of Al-to-Ti FSL welds are comparable to strength values of Al to Al FSL welds. Thus, potentially, Al to Ti FSLW can be applied widely in industry where weld strength is an important consideration. However, an important consideration of welds in structures, particularly for transportation applications, is their fatigue properties. Despite this important consideration, no published studies have been reported on fatigue properties and behaviours of welds made using FSLW of Ti to Al alloys.
- The excellent static strength of Al to Ti FSL weld has been attributed to the extremely slow growth of the Ti-Al interface intermetallic, avoiding the presence of a thick and brittle intermetallic layer. However, for Al to Ti FSL welds made with a pin having penetrated to the Ti bottom plate to result in the forming of a brittle mix zone, welds are still high in static strength. There thus appears an insufficient understanding of how diffusion welding during FS in lap geometry contributes to the effective welding outside of the pin bottom area, which in turn contributes to the high static strength obtained.
- To avoid pin penetration, pre-deposition of Al is a solution but FS deposition appears to be too thin. On the other hand, a cold spray may not be significantly different from simply laying an Al thin sheet. Also, there has been uncertainty on how tolerant the condition can be regarding the distance between the pin bottom and Ti surface where friction stir heat is sufficient for efficient diffusion welding of the Al to Ti lap couple.

1.5.2 Research Questions and Outline of the Thesis

Based on the gaps identified and explained above, the following research questions are asked and are necessary to be answered for FSLW of Al to Ti to be considered whether it is suitable for application in situations where fatigue loading is a critical consideration:

1. What is the fatigue strength of Al to Ti FSL welds and how do their strength values compare to fatigue strength values of Al to Al FSL welds?
2. How does the important position control parameter, pin penetration or non-penetration, affect the fatigue strength values?
3. What is the diffusion welding portion outside the pin width that may form and contribute to the high fatigue strength and how does the corresponding thermal condition difference due to the two different pin penetration conditions contribute to the different degrees of diffusion welding?
4. How does increasing the pin diameter, which should increase both FS heat and weld area, contribute to the increase in fatigue strength?
5. How do the fatigue strength value of Al to Ti FSL welds made by simply laying of an Al thin sheet as an interlayer, rather than FS deposition and cold spray, compared with the values of normally made Al to Ti FSL welds?
6. How do the different widths of interlayer affect the weld width which in turn may affect fatigue strength?

In the next chapter (Chapter 2), experimental procedures are described and explained. Research results and discussion will be presented in Chapter 3 for answering questions 1 to 3, in Chapter 4 for answering question 4, and in Chapter 5 for answering questions 5 and 6. Conclusions will be given in Chapter 6.

2. EXPERIMENTAL PROCEDURES

Three series of FSLW experiments of welding AA2024 and Ti6Al4V alloys are conducted, series of using normal pin, series of using large size pin and series of using Al interlayer. The experiments in series 1 and series 2 included non-pin penetration and pin having slightly penetrated due to the uncertainty of the vertical position using the commonly and practical use of positioning control. After welding, the welds were fatigue tested under tensile-shear loading with a wide range of loads and R = 0.1. Extensive cross sectional metallographic examination on the welded interface regions, particularly on tested samples in which crack growth was "frozen", and fractographic examination on fracture surfaces was conducted. Finite element analysis (FEA) to reveal the stress distribution in the weld region, under a static loading, was also conducted. The details of these experiments, testing, analysis and examination and simulation are presented below in this chapter.

2.1 FSLW of AA2024-to-Ti6Al4V alloys

2.1.1 FSLW Experiment Outline

Table 2-1 summarises the materials and workpiece dimensions used in the major series followed by the two other series in this research. In series 1 (major series) a normal pin with a diameter of 6 mm was used. In series two, a large pin with a diameter of 9 mm was used. In series 3, a normal pin was also used, but in this series, an interlayer of aluminium was used so that non-penetration of the pin to the bottom Ti6Al4V could be more certain. The choice of aluminium alloy top plate with 5 mm being 2.5 times the titanium alloy bottom of 2 mm was for the purpose of aiming for fracture along the Al alloy to Ti alloy weld interface region during fatigue test. Thus, fatigue strength of the weld interface region could be determined. The total thickness being 7 mm was however due to the limitation of the maximum sample clamping width being 7 mm in the sample grips of the fatigue testing machine.

Table 2-1 Summary of material types, workpiece dimension, and pin diameter used in FSLW experimental series

No.	Series	FSLW Couple	Top plate thickness (mm)	Bottom plate thickness (mm)	Plate Dimensions (mm)
1	Normal	AA2024-Ti-6Al-4V	5	2	100 x 240
2	Big pin	AA2024-Ti-6Al-4V	5	2	100 x 240
3	Al interlayer	AA2024-T6 AA1100 Ti-6Al-4V	5	2 = 0.5 + 1.5	100 x 240 8 x 240 100 x 240

As has already been explained, important consideration of FSLW of Al to Ti is for aerospace industry. Thus, aerospace Al alloy (AA2024-T6) and Ti alloy (Ti6Al4V) were used in this study. Table 2.2 shows the mechanical properties of the three alloys used in this experiment. AA110 being used as an Al interlayer in the experiment series 3 as in Table 2-1.

Table 2- 2 Mechanical properties of Alloys used for the series of experiments.

Alloy	UTS (MPa)	Yield Strength (MPa)	Young's Modulus (GPa)	Shear Strength (MPa)	Ref.
AA2024	450	360	73	283	[74]
Ti-6Al-4V	905	890	110	760	[75]
AA1100	125	105	68	-	[76]

Table 2-3 shows the nominal chemical compositions of these alloys for all the three FSLW series. For series three, industrial pure aluminium was used and impurity levels of the alloy are also listed in Table 2-3.

Table 2- 3 Nominal chemical composition of materials used in FSL weld experiments.

Alloy	Al%	Cu	Zn%	Si%	Mg%	V%	Fe%	Mn%	C%	Ti%
AA2024T6	Bal	3.85	0.2	0.45	1.22	-	0.45	0.76	-	0.02
TiAl64V	6.2	-	-	-	-	4.3	0.19	0.02	0.02	Bal
AA1100	Bal	0.05	0.1	0.46	-	-	0.48	0.05	-	-

For series three, the Al interlayer was inserted into a 0.5×8 mm or 0.5×10 mm machined groove in the Ti6Al4V bottom plate at the interface region. The thin AA1100 alloy was mechanically inserted into the groove as the interlayer, while the AA2024 overlapped with Ti6AlV4 before FSLW, as schematically illustrated in Figure 2-1. During FSLW, the pin bottom was more readily located in the Al interlayer without penetrating into the bottom Ti6Al4V plate.

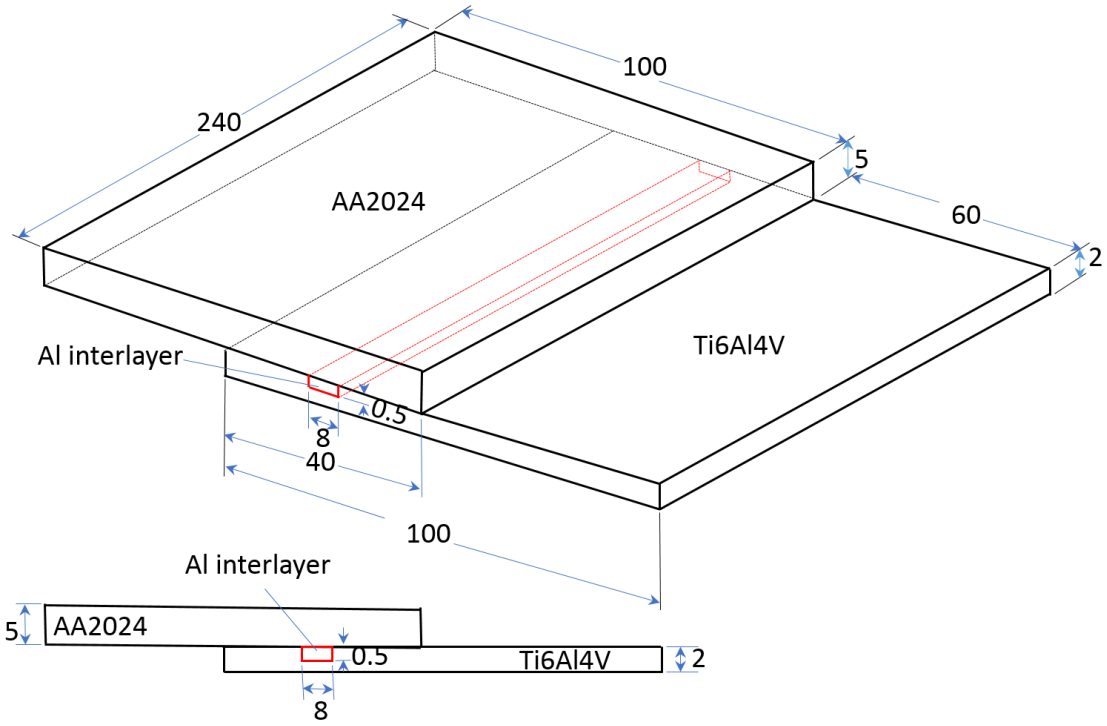

Figure 2-1 Experimental series 3 with Al interlayer inserted into a rectangular groove machined on the 2mm Ti6Al4V. The plate set up is illustration on the top while the wire cut FSLW fatigue test specimen is shown at the bottom.

2.1.2 Clamping System of Retrofitted FSW Machine

All of the FSLW experiments were performed on a retrofitted milling machine. Rotation and linear speed were regulated using phase increments. Each experiment used a bolted clamping system (as shown in Figure 2-2) to prevent plates from thermally expanding and thus lift up, which can happen under normal FSLW conditions. A support plate was below the top plate (the same thickness as the bottom plate). This support plate is referred to as the "lower support plate" in Figure 2-2. A support plate (the same thickness as the top plate) was inserted above the bottom plate. In Figure 2-2, this support plate is referred to as the "upper support plate," and its purpose was to aid in the alignment and stabilization of the lapping plates during FSLW. The lapping plates were clamped to the backing plate (25 mm carbon steel plate) with 5 regular M4 x 0.7 bolts because the tendency of bulking (due to thermal expansion) is higher in the centre of the plates. During the tests, the tool was also tilted 2.5° from the usual direction of the plate towards the trailing side of the tool to improve weld integration. In Figure 2-3, a schematic cross-sectional view of the experimental configuration is shown with precise measurements, including the base support plate, upper plate, low plate and spacer on each plate for stabilization.

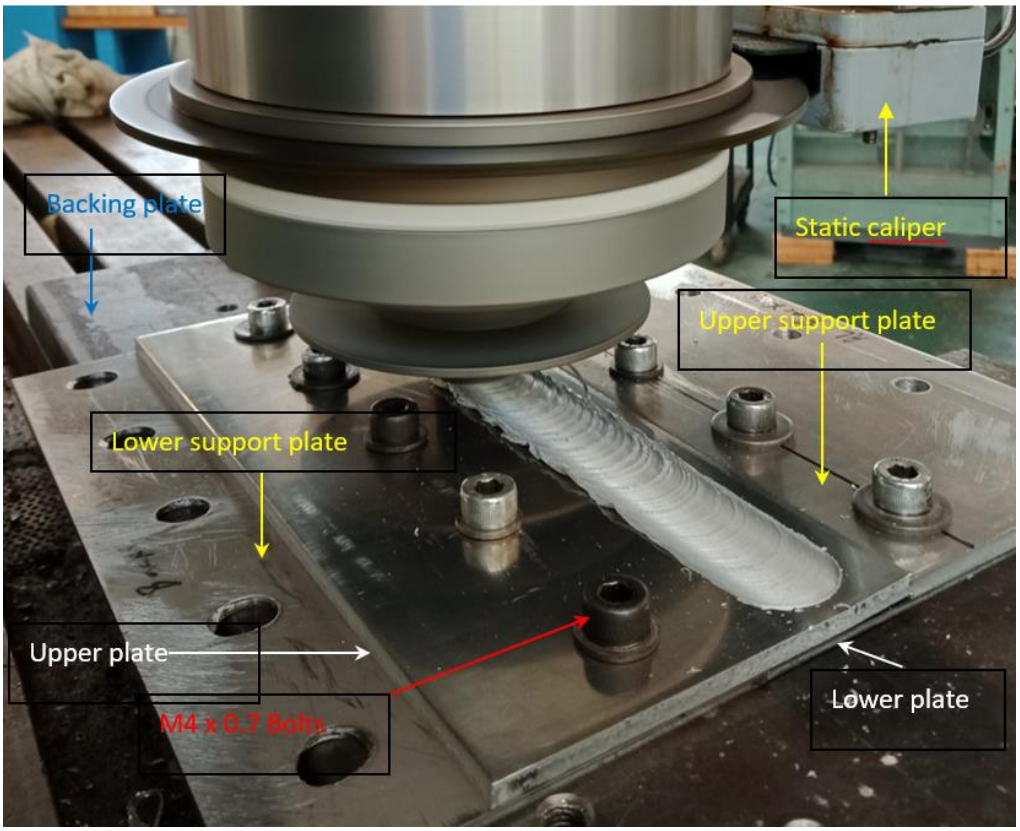

Figure 2-2 A retrofitted milling machine used for FSLW experiments. Bolted clamping system was used to restrain the plates during FSLW. A LowStir™ unit was installed to monitor the forces during experiments.

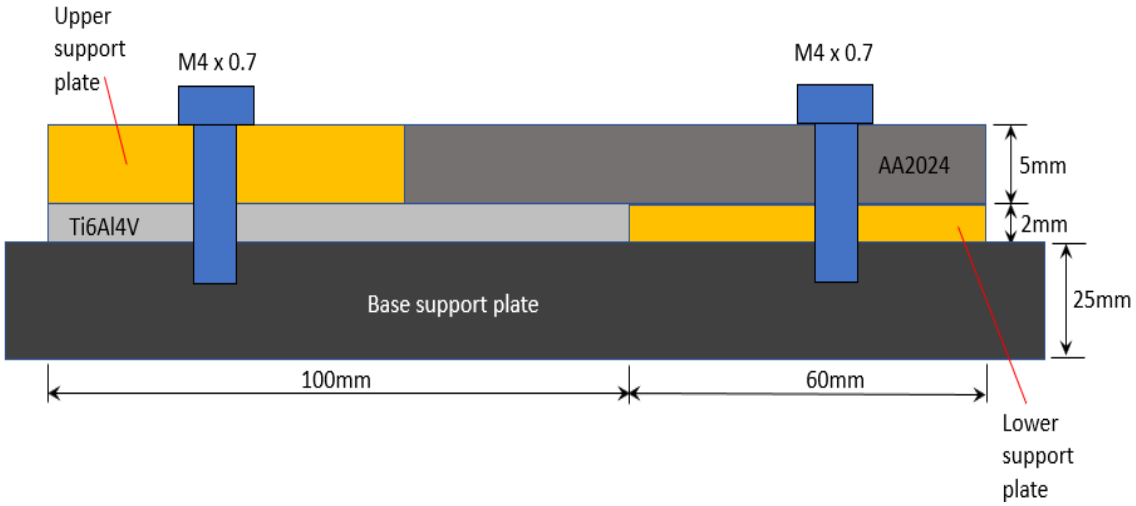

Figure 2-3 Schematic illustrations of clamped plates with the base plate dimensions with spacers (support plates) at each end bolted onto the base support plate.

A Lowstir unit was attached to the milling machine and is used when the down force needed to be monitored. During the experiments of monitoring temperatures under the condition of either pin penetration or non-penetration, as will be explained in a later section, the Lowstir unit was used. A laptop PC running Interface is used to display the information gathered by the Lowstir computer to the user in a simple and straightforward manner; a sample display screen format is shown in Figure 2-4. The instrument panel shows numerical values of forces and torque in real time, as well as the temperature of the device electronics and (if desired) the tool temperature.

Real-time event indicators may also be added to the framework, allowing for comparisons between process conditions/stages and captured data. The main monitor screen includes buttons for starting and stopping data recording. An automatic trigger facility is also available for starting data recording. The current captured data values for the weld in progress are also shown, showing if they are within the appropriate range for satisfactory welding. The display also has a multi-graph feature that allows the user to choose which sensor values are shown.

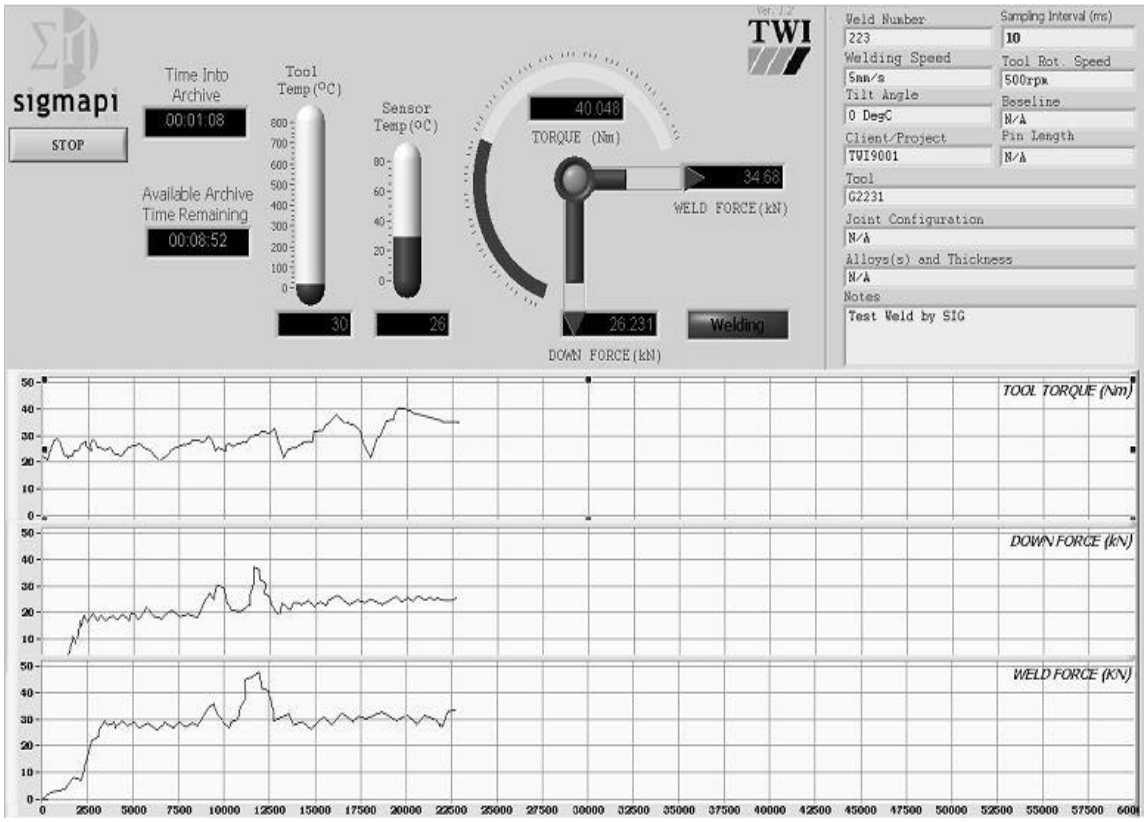

Figure 2-4 Example display screen showing the screen format displaying major parameters; Down force (kN), tilt angle, tool torque (N) and temperature [77].

2.1.3 Tool Preparation

Tool specifications with a pin diameter of 6 mm, pin length of 5.2 mm and a shoulder diameter of 25 mm was used for the FSL welds of experiment series one and series three. However, 9 mm pin diameter and 30 mm shoulder were used for experiment series two. A normal pin drawing is represented schematically in Figure 2-5a. The tool was redesigned to have a 9 mm pin diameter and 30 mm shoulder while maintaining the same pin length as shown in Figure 2-5b. The reason behind the larger pin consideration was to see the effect of the pin size to make a concrete comparative study while maintaining the standard specimen width of 20 mm and 160 mm length in all FSL welds samples produced. The full specifications for the normal and big pin are given in Figure 2-5a and Figure 2-5. The photo images of the tools are shown in Figure 2-5c. The normal pin was used for experiment series 1 and series 3 while the big pin was used in series 2 as outlined in Table 2-3.

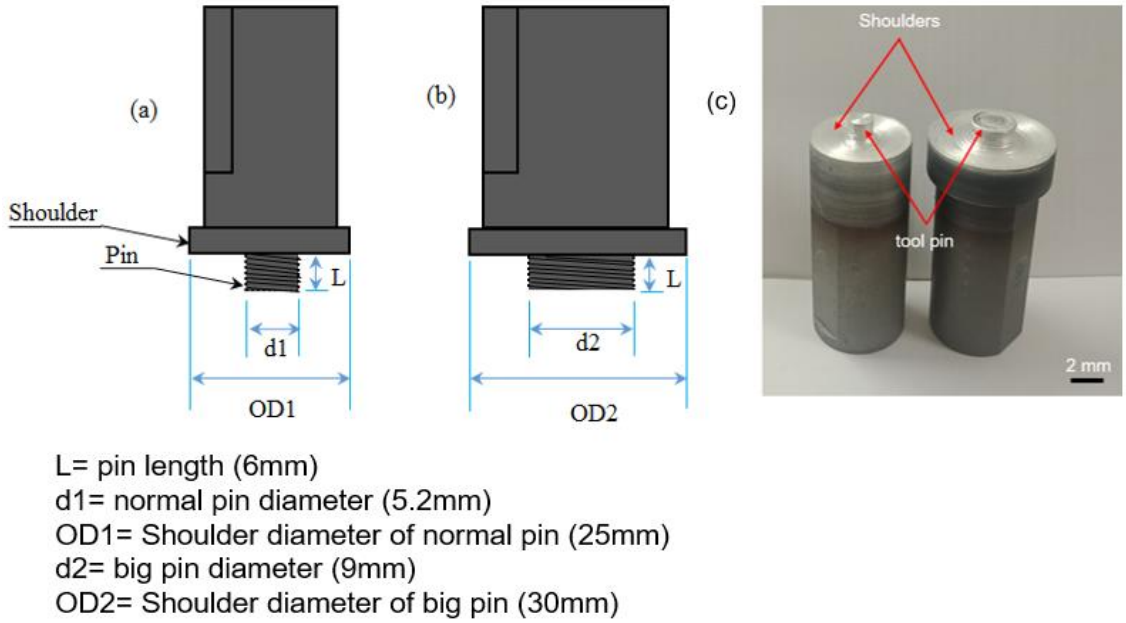

Figure 2-5 schematics of Pin Profiles: (a) threaded normal pin, (b) threaded larger pin, and (c) Photo image of normal pin (left) and big pin (right).

H13 tool steel bars were CNC machined into two different sizes (see Fig.2-5) of the tools used in this research. Heat treatment was carried out after the tools were made under the following two conditions: a) Austenitizing for one hour at 1050 °C and then water quenching, b) Tempering for one hour at 600 °C and then air cooling. For each set of experiments, tools with different pin lengths and shoulder diameters were used, and Table 2-4 summarises the main measurements of the tools used. Since the workpiece materials were in a similar thickness range, a cylindrical tool pin with the same $D_{shoulder}$ and d_{pin} was used in series 1 experiments (indicated in Table 2-4). The $D_{shoulder}$ and pin size were increased in series 2 experiments to see the effect of pin size and thus the effective weld distance. It should be noted that the tool rotation direction was kept constant during all of the tests, ensuring that the threaded pins rotated clockwise.

Table 2-4 Details of the tools used in FSL weld experiments with FSW couples.

No.	Series	FSW Couple	L_{pin} (mm)	d_{pin} (mm)	$D_{shoulder}$ (mm)	Pitch (mm)	Thread (mm)
1	Normal	AA2024-T6/Ti6AlV4	5.2	6	25	1	0.6
2	Big pin	AA2024-T6/Ti6Al4V	5.2	9	30	1	0.6
3	Al Interlayer	AA2024T6/AA1100/Ti6Al4V	5.2	6	25	1	0.6

2.1.4 Selection of FSLW Conditions

Table 2-4 shows the summary of FSL welds conditions including rotation tool speed (ω), weld speed (υ), and tilt angle (∠). A detailed pin profile (pin diameter, pin length, and shoulder diameter). The condition for Series 1 FSLW experiments was based on the work of Chen and Yazdanian [59] in their 2015 article. They demonstrated the use of condition allows high static strength values to be obtained for both non pin penetration ($d_P = 0$) and slight pin penetration ($d_P > 0$).

Figure 2-6 (a-c) shows weld surface features of a big pin in comparison with a normal pin (see Figure 2-6d). A long weld discontinuity along the weld direction due to material pull out was seen when using a big pin with a high rotational speed of 1400 rpm as shown in Figure 2-6a. Also, a very rough material flow was seen forming with the big pin as seen in Figure 2-6b providing poor weld quality and strength compared to a normal pin. High rotational tool speed with big pin causing interruption on material flow resulting in huge voids as shown in Figure 2-6c. Therefore, appropriate action was taken to curb this issue. The rotational welding speed was lowered and set to 1000 rpm while maintaining υ at 20 mm/min which resulted in a good weld as shown in Figure 2-6c. However, with a normal pin, the weld surface is perfectly flashed and weld continuity maintained throughout as shown in Figure 2-6d. This is the reason for changing of tool rotational speed from 1400 rpm to 1000 rpm as shown in Table 2-5.

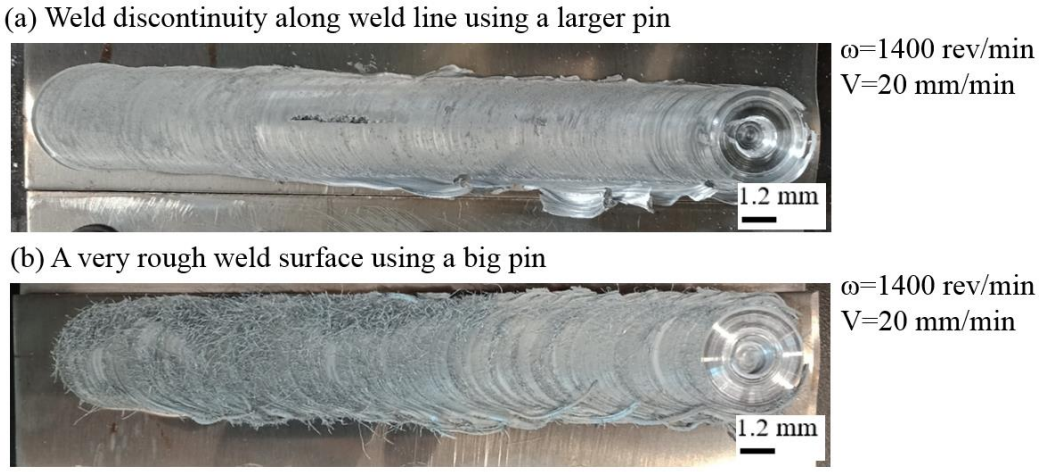

Figure 2-6 Comparison of FSL weld surface features at various ω and υ combinations for normal and larger pin.

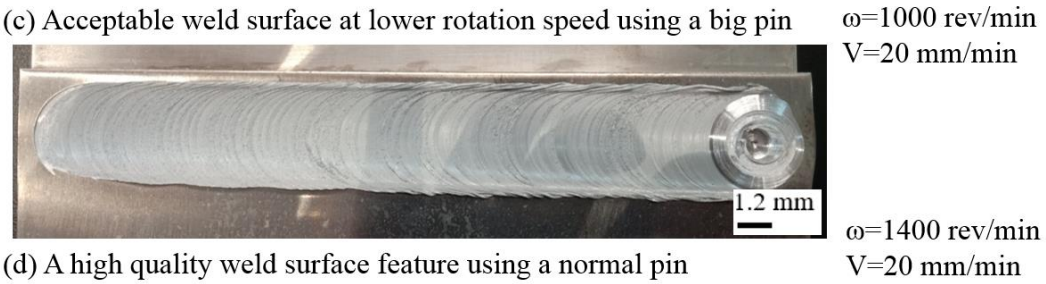

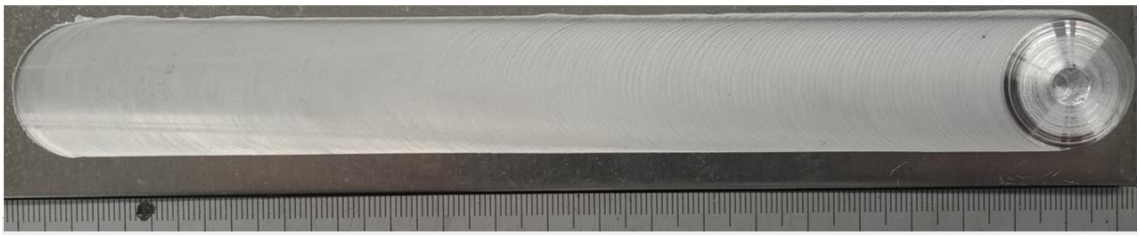

Figure 2-6 cont.

Friction surfacing aided FSW is a method of applying Al layer onto the surface of the bottom base plate by using a Al as a tool before actual FSW is conducted. Figure 2-7 shows some unsuccessful Al friction surface layer deposition. Several failed attempts with Al surfaced friction welding in which the Al friction surfacing tool was unable to establish sufficient Al layer onto the Ti groove surface. Therefore, we proposed using Al interlayer of 240 mm x 8 mm x 0.5 mm thin sheet instead of surface friction deposition which failed. A rectangular groove was machined to fit thin Al of the size of the groove. The Al interlayer was forced to fit into the rectangular groove to perfectly fit before clamping the top plate (AA2024-T6) and run the welding. Figure 2-8 shows a schematic illustration of the cross-sectional view of Al interlayer with AA2024/Ti6Al4V lapping.

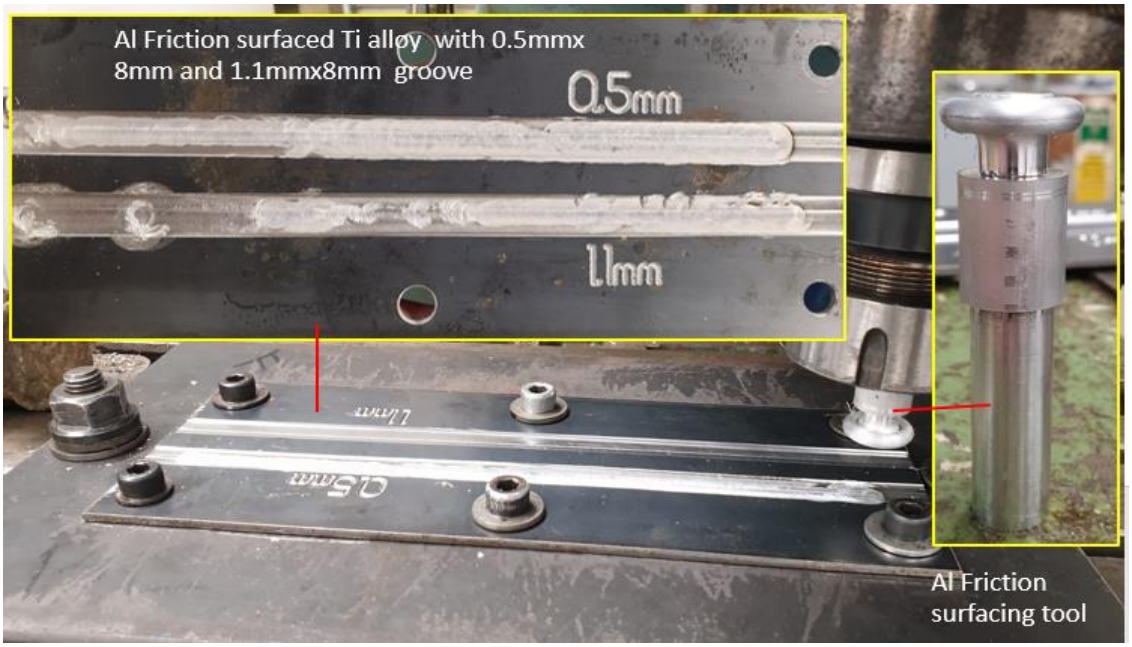

Figure 2-7 Photo showing Al interlayer deposition on rectangular groove TiAl64V surface.

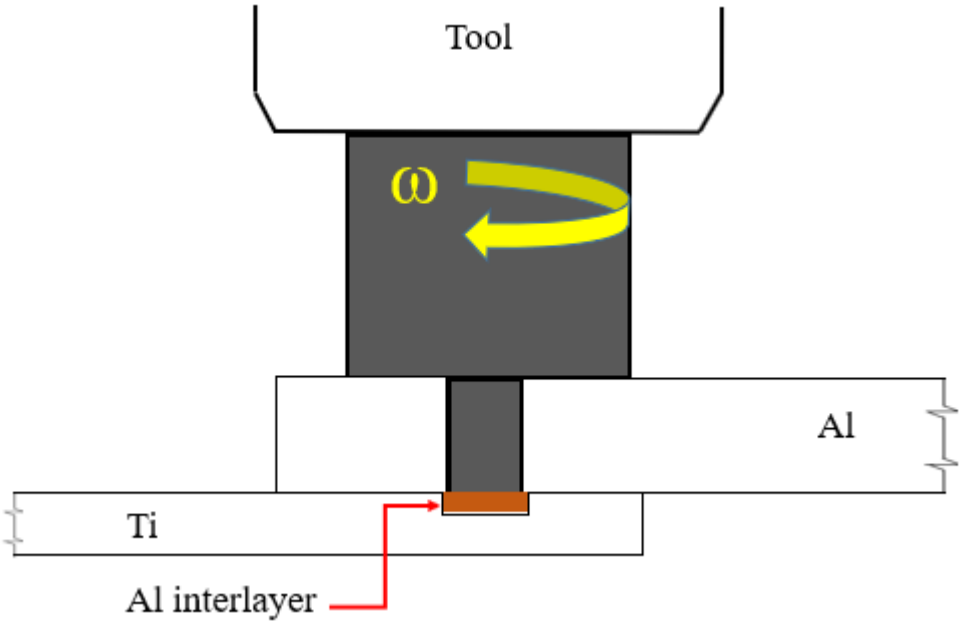

Figure 2-8 Schematic illustration of cross-section of Al interlayer insert while tool pin being plunged in without touching the bottom Ti plate.

Table 2-5 FSL weld parameters

No.	Series	FSLW couple	Tool Profile (mm)	FS Parameters
1	Normal pin	AA2024-T6-TiAl64V	$D_{shoulder}$ = 25 L_{pin} = 5.2 D_{pin} = 6	ω = 1400 rpm υ = 20 mm/min ∠ = 2.5°
2	Big pin	AA2024-T6-TiAl64V	$D_{shoulder}$ = 30 L_{pin} = 5.2 D_{pin} = 9	ω = 1000 rpm υ = 20 mm/min ∠ = 2.5°
3	Al interlayer	AA2024-AA100-Ti6Al4V	$D_{shoulder}$ = 25 L_{pin} = 5.2 D_{pin} = 6	ω = 1400 rpm υ = 20 mm/min ∠ = 2.5°

2.1.5 Temperature Monitoring

Temperature measurement at weld interface was conducted for condition of $d_P = 0$ and $d_P > 0$. The temperature range was measured using a K-type thermocouple (0.5 mm diameter) in the range which could measure from -200° to 1250°C. All temperature measurement experiments used the USB DAQ model TC-08 with 8 channel thermocouple inputs with miniature connectors, K supported type, Picolog Data Logging Software, and USB cable. To fit the twisted thermocouple wires, narrow grooves with a depth of 0.5 mm were milled into the bottom plate (using a small milling cutter), as shown in Figure 2-9a. The sampling interval was 0.02 seconds and the measurement frequency at 50 HZ. Figure 2-9b demonstrates the positioning of thermocouple wires aimed at measuring temperature at the lapping interface of top and bottom plates.

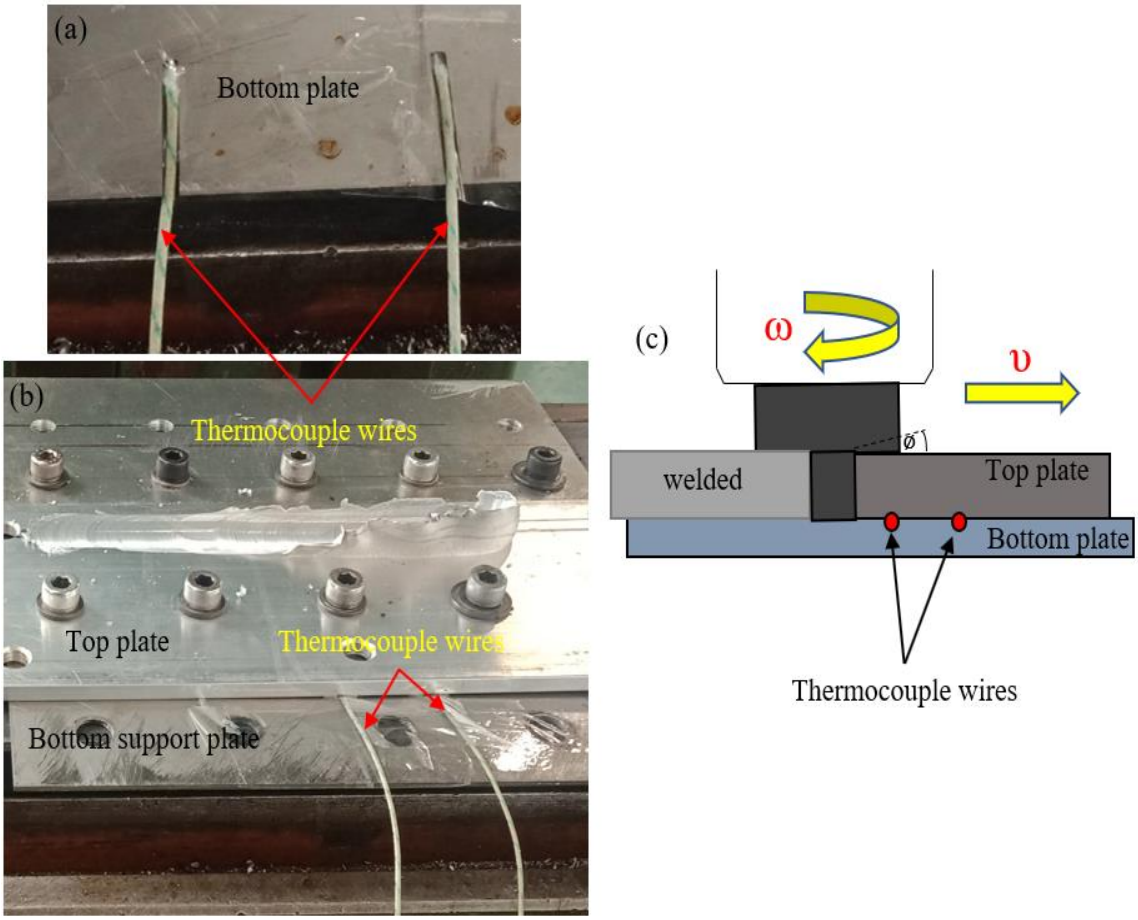

Figure 2-9 (a) Image showing thermocouple wires placed at each narrow groove made on the bottom plate before FSLW, (b) image after FSLW, and (c) schematic diagram of thermocouple positions during FSLW.

The downforce (F_z) monitor was used for controlling pin penetration onto the lower plate using a software monitor displayed on a laptop in which the instrument panel displays the real-time numerical values of forces, torque, and the tool temperature. The capture of the weld in progress can be displayed and controlled to achieve the desired and acceptable welding (see Figure 2-2, example screen format). Each thermocouple may register a different level of temperature if the downforce is varied. Figure 2-10 shows the thermocouple 1 (first location) did not work well, as the thermocouple junction with a few mm behind was not insulated. When the tool was lowered, thermocouple 2 surged in temperature up to 650 °C when F_Z was at its maximum at 3.8 kN and lowered while maintaining F_Z.

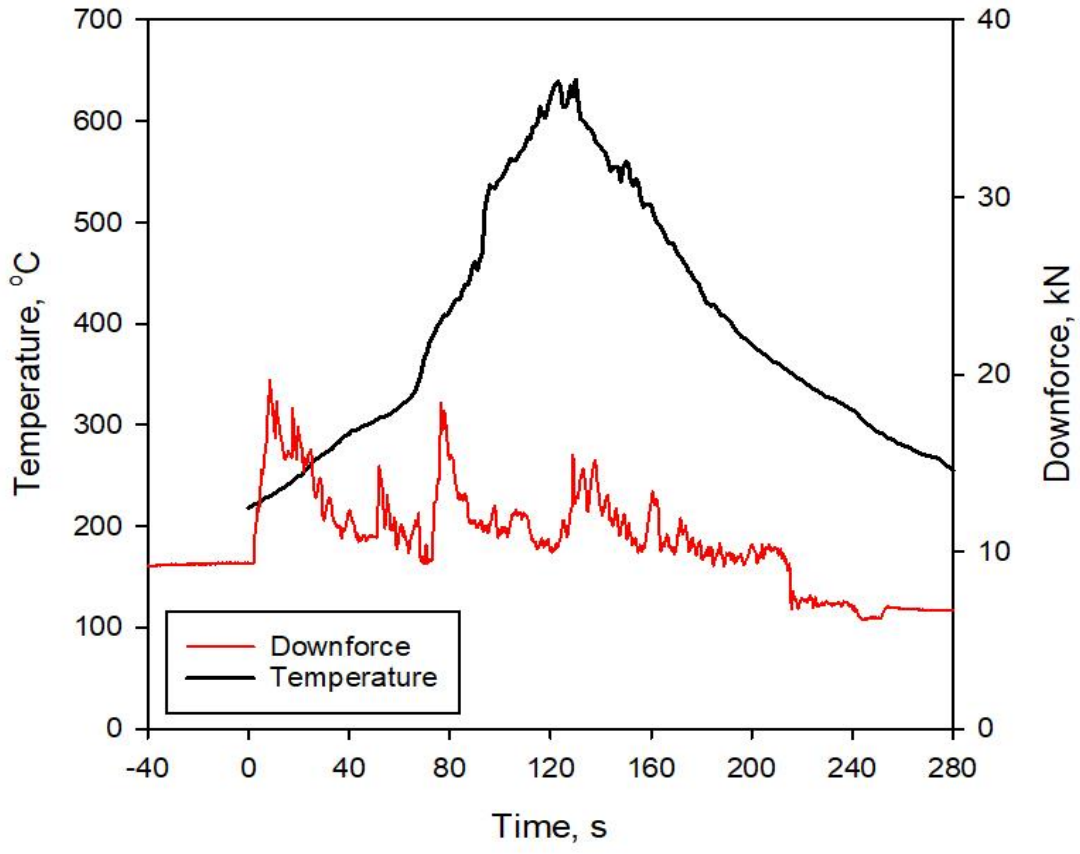

Figure 2-10 Synchronization of downforce, temperature vs time (s).

2.2 Fatigue Testing of the Lap Welds

In this section, a detailed description is presented on fatigue testing. The fatigue test machine set up and how fatigue data were collected using the fatigue parameters and variables is presented. The parameters were set on a station manager Multipurpose Elite software. The test parameters and variables were entered in the fatigue testing module MTS TestSuite™ Multipurpose Elite Software.

2.2.1 Specimen Preparation

FSL AA2025-toTi6Al4V welds were sectioned into fatigue test samples using an electron discharging machine (EDM) for a smooth cutting without placing any stress on the weld. Figure 2-10 shows an FSL weld plate, as an example, marked according to size before cutting. Each specimen from the weld was numbered for easy identification during testing. Three sections in the weld were cut out for preparing metallographic samples as numbers 1, 2, and 3 (see Figure 2-11). Figure 2-12 shows a schematic illustration of the standard fatigue test specimen used in this study with full specifications. Spacers of 10 mm x 20 mm were also cut using EDM for keeping the specimen in alignment during fatigue testing.

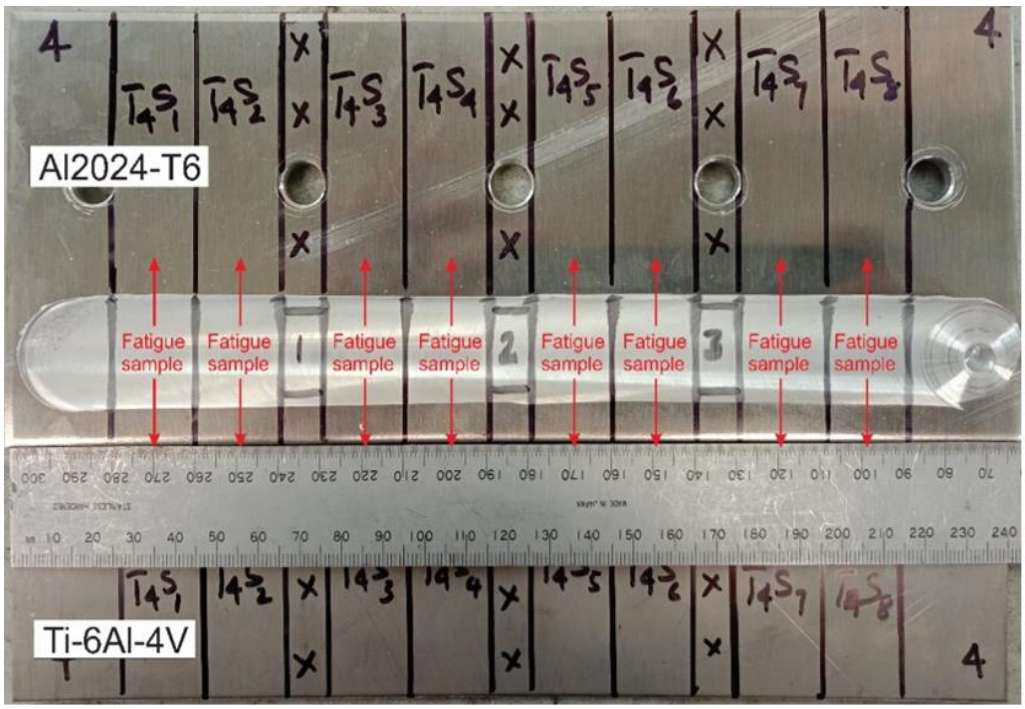

Figure 2-11 Illustration of a welded plate pre-marked with fatigue samples to be sectioned off for fatigue testing.

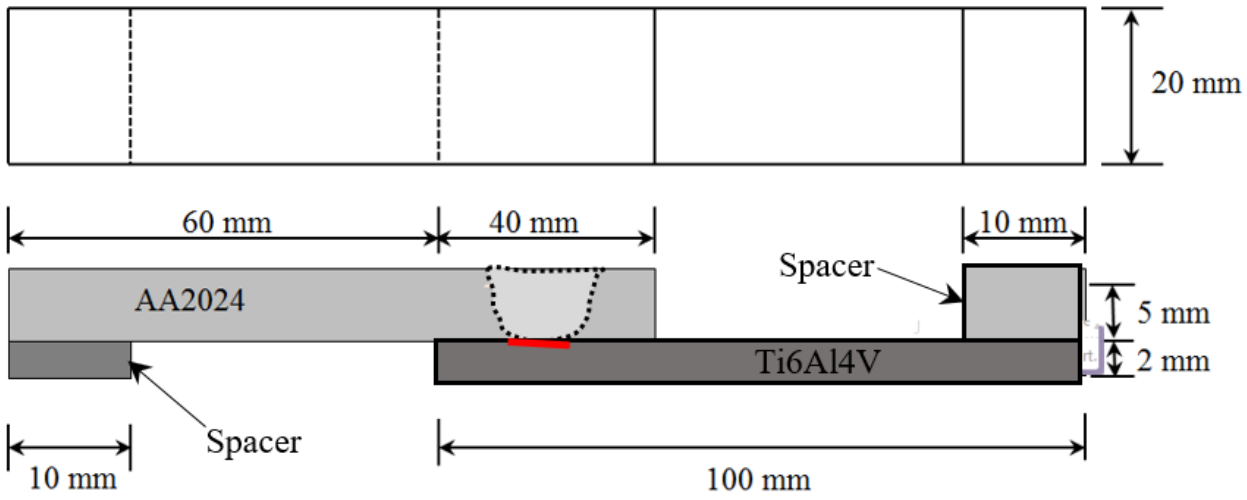

Figure 2-12 Schematic illustration of fatigue test specimen with AA2024 and Ti6Al4V with spacers at both support ends.

2.2.2 Fatigue Testing Machine and Specimen Gripping Systems

An MTS 25 kN capacity servo-hydraulic universal testing machine was used to perform fatigue testing of the FSL welds. Figure 2-13 shows the fatigue testing machine with specimen placed in the top and bottom holders gripped as shown in the exploded view of Figure 2-13 (right)-the fatigue test specimen inserted in the grips of the testing rig. The specimen grips of the top and the bottom jaws can only accommodate a maximum thickness of 7.2 mm. Therefore, 5 mm (2 mm spacer) thickness AA2024 was considered as top plate and bottom plate as 2 mm (5 mm spacer) which pave way for ease of specimen preparation and insertion in the jaws for the fatigue testing

(see Figure 2-12). Therefore, fracture on the top plate could not be prevented with the 5 mm AA2024 as the top plate.

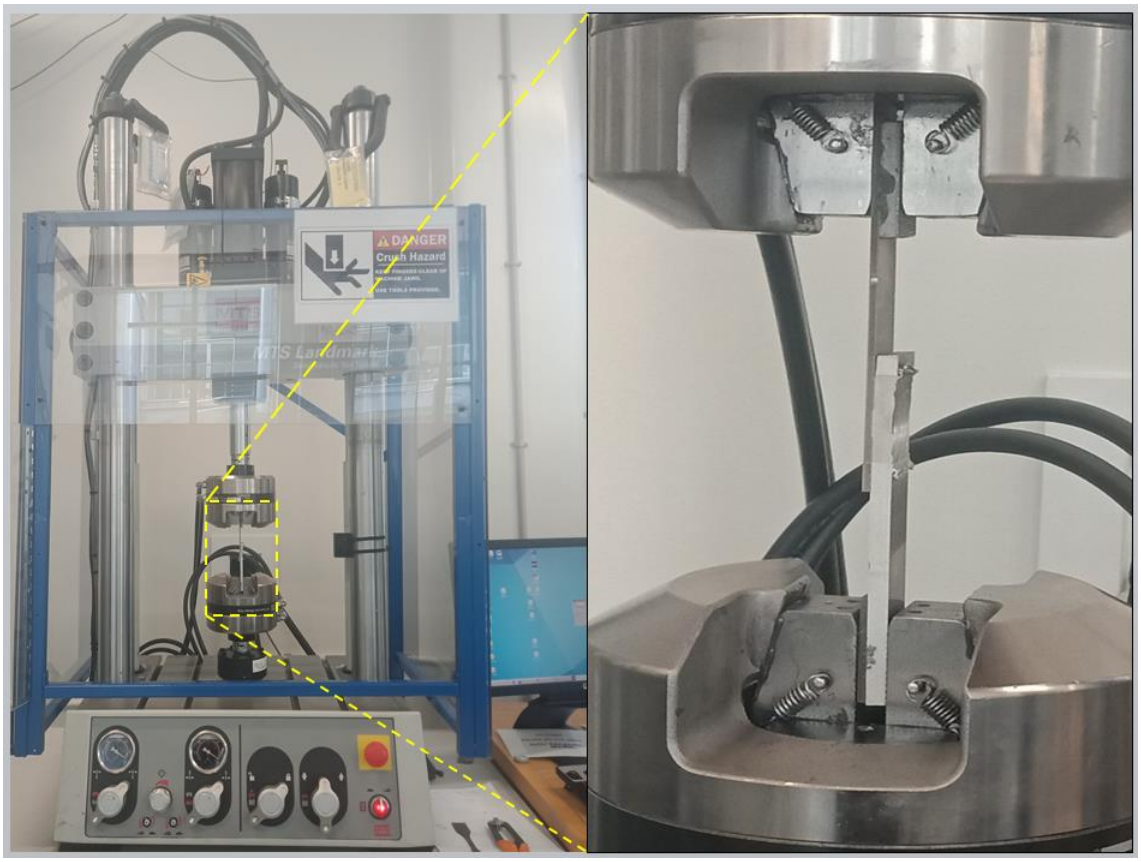

Figure 2-13 Servo Hydraulic Universal Testing Machine (a), FSL weld fatigue test specimen insert with a superimposed view on the right.

2.2.3 Selection of Fatigue Test Conditions and Data Logging

Table 2.6 shows a summary of preliminary set parameters and variables. A range of fatigue testing was conducted with loads ranging from 3 kN - 10 kN using many fatigue test specimens. A fluctuating stress cycle having a stress ratio $R = F_{min}/F_{Max} = 0.1$ was adopted in this experiment. Load frequency was set 20 Hz throughout the fatigue experiments. The rest of the test parameters were selected according to the test requirements.

Table 2-6 Pre-Test fatigue test parameters and variables

Name	**Value**	**Unit**
Total cycles	1000000000	Cycles
Frequency	20	Hz
Peak-Valley Change detectors after Segments	1000	Count
Cycle increment	100000000	Cycles
Force Maximum Command	N/A	kN
Force Minimum Command	N/A	kN
Force Peak Valley Tolerance Parameter	10	%
Force Peak Valley Sensitivity Parameter	10	%
Displacement Peak Valley Tolerance Parameter	90	%
Displacement Peak Valley Sensitivity Parameter	10	%

Running a test on an MTS Landmark load frame system typically requires the use of the following two software programs:

(a) MTS Flex Test (Series 793) Controller Software

The MTS FlexTest controller software is mainly used by operators to set up the station for testing. Although MTS FlexTest software includes many applications, this manual focuses on how to use the Station Manager software to set limits, view sensor data, and maneuver the actuator for specimen installation. The main purpose of the Station Manager application is to set up your station for a test. The following are the main tasks that must be completed in order to prepare the station for the Example HCF Test:

(i) Opening a Station
(ii) Using the Main Window to Open Other Windows
(iii) Setting Limits
(iv) Setting up meters
(v) Setting up a scope
(vi) Applying power to the station
(vii) Moving the actuator for specimen installation
(viii) Setting turning parameters

For this experiment, the three parameters entered in the station manager are the target setpoint or mean load, amplitude, and frequency as shown in Figure 2-14. The target set point and stress amplitude are determined first using equation the expressions $\sigma_m = (\sigma_{max} + \sigma_{min})/2$ and $\sigma_a = (\sigma_{max} - \sigma_{min})/2$, respectively. The results are entered into the station manager application before running the test. The required frequency (20Hz) is selected from the preset values from the application.

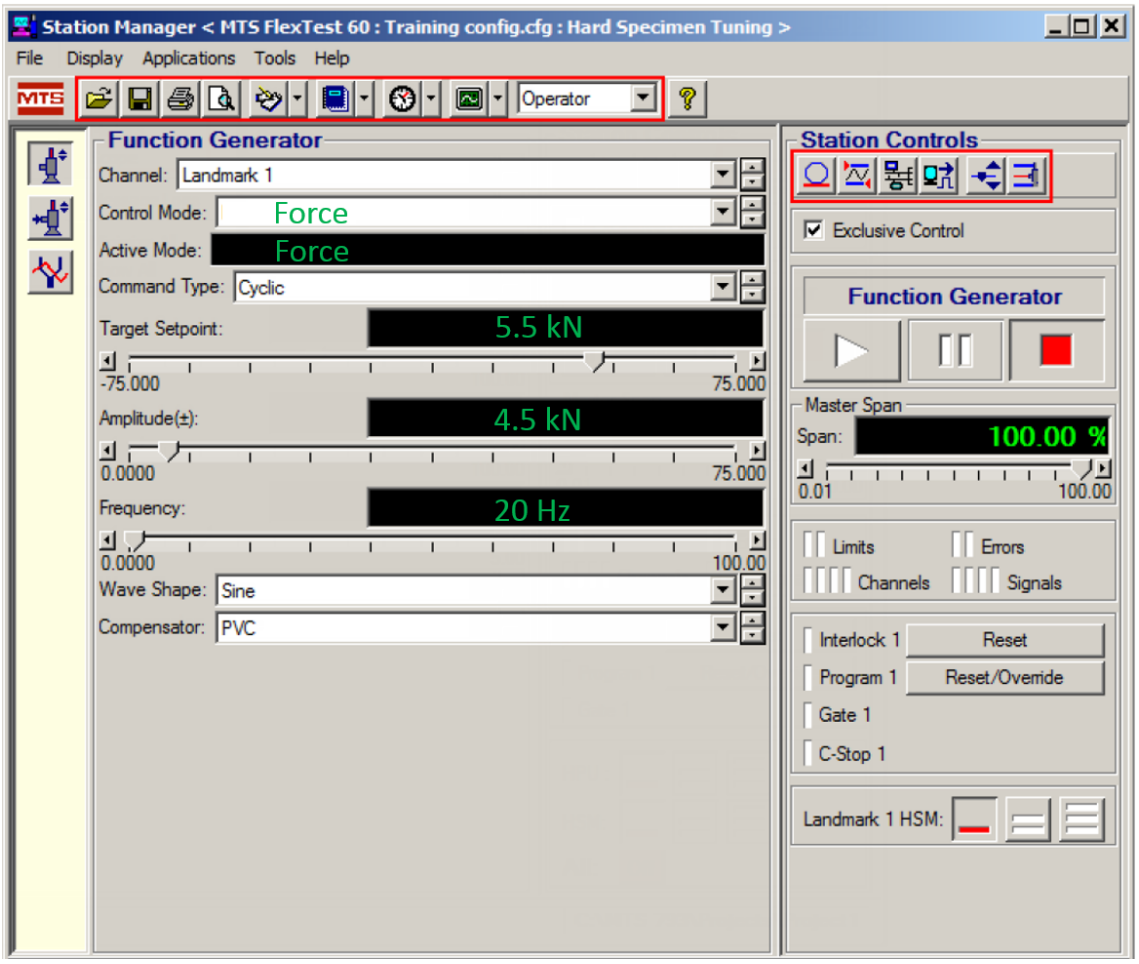

Figure 2-14 A sample station manage window displaying three important parameters; the target set point (average), amplitude and frequency [78].

(b) MTS TestSuite Test Software - MTS Multipurpose (MP) Express Application

The MTS Multipurpose Express application is a light form of the MTS Multipurpose Elite application, tailored to test operators. MTS TestSuite MP Express is mainly used by operators to run tests and produce reports.

(i) Selecting a Test
(ii) Setting Test Parameters
(iii) Running a Test
(iv) Generating a Report

The high cycle fatigue (HCF) results are produced on excel sheets easy for a plot. Figure 2-15 shows a sample report generated for a typical HCF.

MTS

HIGH-CYCLE FATIGUE LOAD-TEST REPORT

Project Information		Specimen Description	
Name of the Project	Project 1	Geometry Type	Generic
Name of the Test	2019-06-18 AUT HCF Zhan-Steve		
Name of the Test Run	Steve-T7S77kN		
User Name	MTS		
Specimen Name	Specimen 17		

Load-Test Control Parameters		Test Results Summary	
Force Maximum Command	7000.0 N	Completed Cycles	6272 cycles
Force Minimum Command	700.0 N		
Frequency	20.0 Hz		

Test History Chart (Peak-Valley Load versus Cycles)

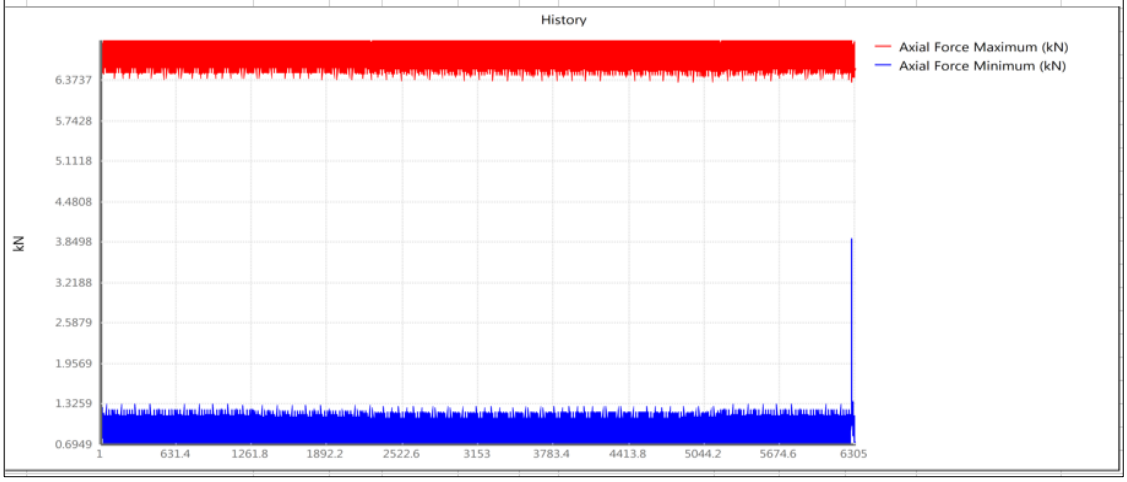

Figure 2-15 Sample fatigue test report exported as an excel file with a n applied load of 7kN recording 6272 cycles.

2.3 Metallographic and Fractographic Analysis

2.3.1 Sample Preparation

First, metallographic samples, as indicated in Figure 2-10 samples 1-3, were sectioned from FSLW samples using wire cut using an electro-discharge machine (EDM). Each EDM cut sample was fed into the hot mounting chamber followed by a spoon full PolyFast carbon filler resin compound. The hot mounting chamber was closed and power switched on during which the sample and the compound were heated simultaneously. The sample was set for 6 minutes for hot mounting and followed by automatic cooling. Then plane grinding was done with 80 - 500 grit paper followed by 1200 - 2400 grid paper for fine grinding. Then followed by diamond polishing to achieve fast material removal and best planeness. A more resilient polishing cloth of 1µm was used to obtain a chip size approaching zero giving a mirror-like surface. Finally, a nitric acid solution was used for the etching of the samples. A 10 per cent nitric acid solution was used. The

pipette was used to scoop nitric acid solution and dipped it onto the polished metallographic sample. Time increments were for 5 - 10 seconds and rinsed with tap water. The sample was again cleaned with alcohol and dried using electric hair drier.

For fractography examination, fatigue-tested fractured samples were cut into a sizable dimension of 25 mm x 20 mm for ease of mounting. The specimen is placed in an ultrasonic cleaner for a few seconds to clean. Then the sample is dried using a hair drier ready for mounting into a sample holder for SEM imaging.

An optical microscope (Moticam 1000, China) with a 5x - 100x lens zooming capability was used to analyze the welded section microstructure. The specimens were cut using a sawing process with cooling water attached to keep the cutting zone cool and prevent grain refining. For successful edge preservation, the sectioned specimens were mounted with thermosetting resin. An automated device with a SiC abrasive layer was used to grind mounted samples. A number of abrasive sheets with grit sizes ranging from 80 to 2000 were used to grind the specimens. Diamond fine abrasives were also used to polish, followed by colloidal alumina paste. Finally, the surface of the specimen was washed with distilled water and etched with Kroll's reagent (100 mL water, 2 mL hydrofluoric acid, and 4 mL nitric acid). All micrograph images were taken under polarized light. Figure 2-16a shows the sample specimen prepared for optical microscopic analysis for a standard weld, and Figure 2-16b shows the sample specimen prepared for an Al interlayer AA2024/Ti6Al4V FSLW with a groove on the Ti6Al4V side.

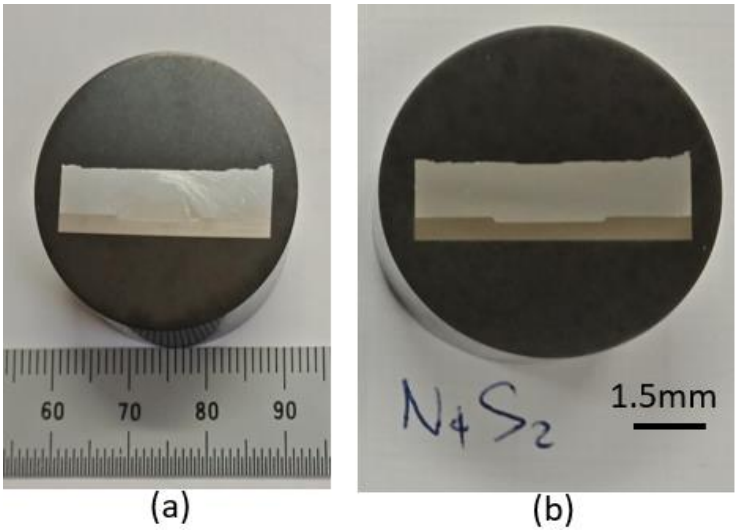

Figure 2-16 Metallographic specimen: (a) for a standard weld, (b) for an Al aided interlayer.

2.3.2 Scanning Electron Microscopy

An electron microscope that uses a beam of high-energy electrons rather than light waves to photograph a sample is known as a scanning electron microscope (SEM). Electrons interact with the atoms in the sample to generate signals that provide information about the sample's surface

topography, structure, and other properties including electrical conductivity. It features ultra-high-resolution imaging (1.0 nm/15kV; 1.6 nm/1kV) and magnifications up to 800, 000 times. High-resolution imaging of fine surface structures and beam-sensitive samples is possible with low electron beam energy options. Using both mapping and spot analysis modes, imaging can be combined with elemental analysis (EDS) to provide information on sample composition. The entire setup of the SU-70 SEM equipment used in this analysis is shown in Figure 2-17.

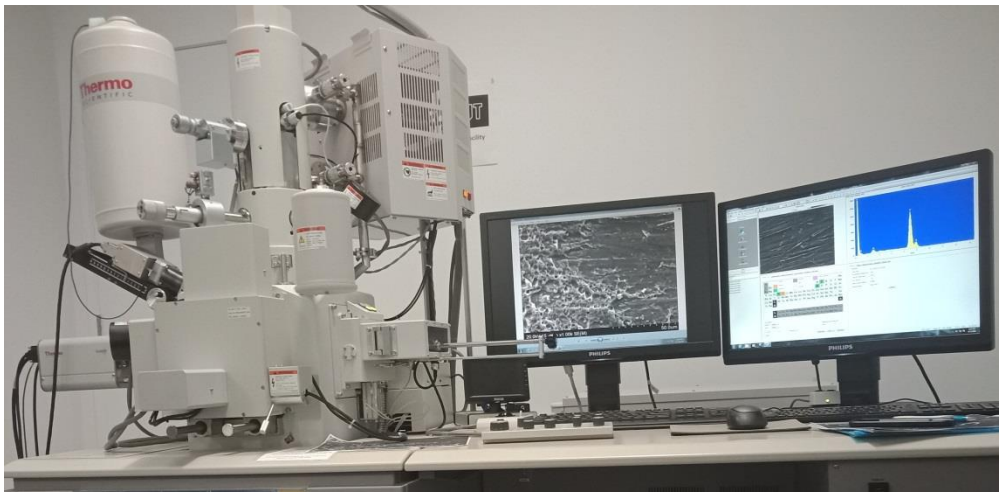

Figure 2-17 Hitachi SU-70 Scanning Electron Microscope with two monitors for SEM (left) and EDS spectra (right).

There are several procedures involved in using the SEM as it is necessary as a minor err may result in the damage of the high-tech equipment. However, basic operational procedures are outlined and they are as follows:

a) Caution on specimen preparation

When swapping specimens, clean gloves were used. It was better to avoid holding the specimen or specimen stub with your bare hand. To avoid out-gassing, the smallest amount of double-sided adhesive tape was used to bind the specimen to the stub. Conductive paste and resin were allowed to dry before inserting the specimen in the chamber.

b) Adjustment of specimen height

As shown in figure 2-17, put the specimen stub on the specimen holder and set the height using the specimen height gauge. Figure 2-18 shows a schematic specimen setup before SEM imaging.

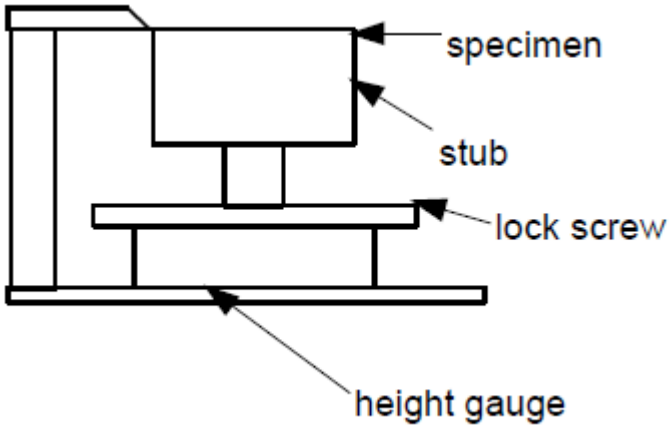

Figure 2-18 Schematic illustrations of specimen set up for SEM on specimen holder [79]

To attach the specimen to the specimen stub, a carefully prepared specimen was put on the specimen stub with the aid of a conductive paste. As shown in Figure 2-18, the polished metallographic and fractographic specimens for x-ray analysis were then fixed to the specimen stub using carbon paste. Figure 2-19a displays a metallographic sample for cross-section weld analysis before mounting on the stub, while Figure 2-19b shows a fractographic weld sample already fixed on the stub and ready to be mounted onto the specimen holder.

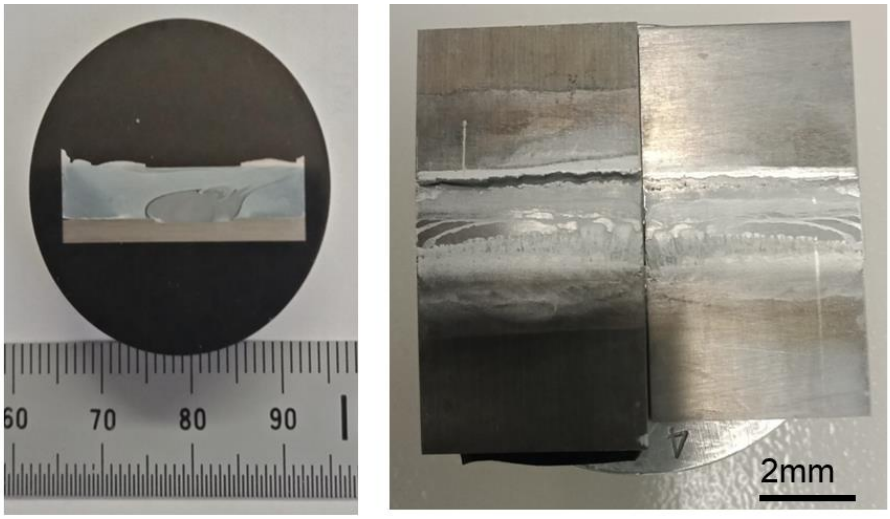

Figure 2-19 Samples prepared for SEM images: (a) Metallographic sample for cross-sectional viewing and (b) fractographic sample for fracture surfaces

c) How to set specimen in place

A carefully prepared specimen was placed on the specimen stub with a conductive paste to fix the specimen on the specimen stub. The polished specimen for the x-ray analysis is then fixed to the specimen stub using carbon paste.

d) At the end of the use

Turning High Voltage off

- Closed opening dialogue window and data saved.
- The HV Off button was turned on the control panel

The following steps were taken to set the stage at the specimen exchange position
Taking out a specimen:

1. Pressed the OPEN button on the specimen exchange chamber. Once the exchange was evacuated and then, the gate valve opened.
2. Turned the knob of the specimen exchange rod clockwise so as the unlock mark came upwards.
3. Inserted the rod straight and plugged the two spring pins at the end of the rod into holes of the specimen holder.
4. Turned the knob counter clockwise so as the lock mark came upwards to hook on the specimen holder.
5. Looking in the chamber and confirming that the specimen holder came out with the rod, pulled out the rod completely.
6. Pressed on the air button on the specimen exchange chamber. The gate valve closed and the air was introduced into the specimen exchange chamber. The buzzer sounded after 15 seconds to inform the completion of the air introduction.
7. Opened the exchange chamber door. Turned the knob clockwise and removed the specimen holder from the rod.
8. Closed the exchange chamber door with the EVAC button. The chamber was evacuated to the specified vacuum.

2.4 Stress Distribution Simulation

The ANSYS^{TM} software is commonly used in the structural and mechanical engineering fields to solve complex problems. It is possible to configure and automate solutions for structural dynamics problems, as well as utilize them to evaluate various design scenarios, using the suite's finite element analysis (FEA) solvers. As a result, Ansys is used across industries to assist engineers in improving product designs and lowering physical testing costs.

2.4.1 FEA Procedures using ANSYS

One of the most commonly used computational methods for evaluating stress and strain in complex structures is finite element analysis (FEA). It is based on the concept of breaking down a complex structure into smaller components known as elements. As a consequence, the first step in any finite element simulation is to use a set of finite elements to discretize the structure's actual geometry. The shared nodes bind the finite elements, which each constitute a distinct portion of the physical structure. The mesh is a set of nodes and finite elements, and the mesh density is the number of elements used in a particular mesh. The solver (computer) assembles the elements at

nodes to form an approximate system of differential equations for the entire structure, then solves the systems of equations involving unknown quantities at the nodes after defining the action of physical quantities on each element (material dependent) (e.g. displacement). After that, the solver returns to the selected elements and uses them to measure the desired quantities (such as stress and strains).

ANSYS models were created using the academic software Ansys to evaluate the stress distribution during tensile shear testing of FSL welds in the current research. Ansys is divided into stages, each of which describes a different aspect of the modelling process. We construct the model as we go through the steps, and Ansys generates an input file that will be sent to the ANSYS solver for review. The following are brief examples of modelling steps and modules:

(i) Engineering Data

Physical and mechanical properties of materials (such as yield strength and elastic modulus) are defined and assigned to parts' regions.

(ii) Model Geometry

The geometry of individual parts is sketched out.

(iii) Model Meshing

The type and size of elements for different regions of the component are chosen to create a finite element mesh.

(iv) Applying boundary conditions and loading

The applied loads and boundary conditions are described in this process. Since load and boundary conditions are step-dependent, we must identify which analysis steps they are active in.

(v) Analysis Setup

Steps for analysis are developed and configured. Then, for each step, output requests (such as stress and strain variables) are defined.

(vi) Solve

The job is submitted for review after all of the tasks involved in defining a model have been completed. Ansys produces an input file that represents the model before conducting analysis on the contents of that file. The Ansys solver computes variable values (such as stress and strains) and then writes them on output databases.

(vii) Results visualization

This module displays finite element models and their output, such as stress contours, in a graphical format.

The key user interface appears when you launch ANSYS Workbench, as shown in Figure 2-20. We will see a wide variety of Research Systems available in the main Toolbox menu, based on the modelling applications. In addition, as shown in Figure 2-20, the static Structural Analysis

System has been highlighted since it was used in this project. In the project schematic graphical pane, the corresponding workflow is shown. As shown in Figure 2-20, each phase of the workflow is completed in turn, and a checkmark appears when the data, such as Engineering data, Geometry, and Model, is agreeable to ANSYS Workbench.

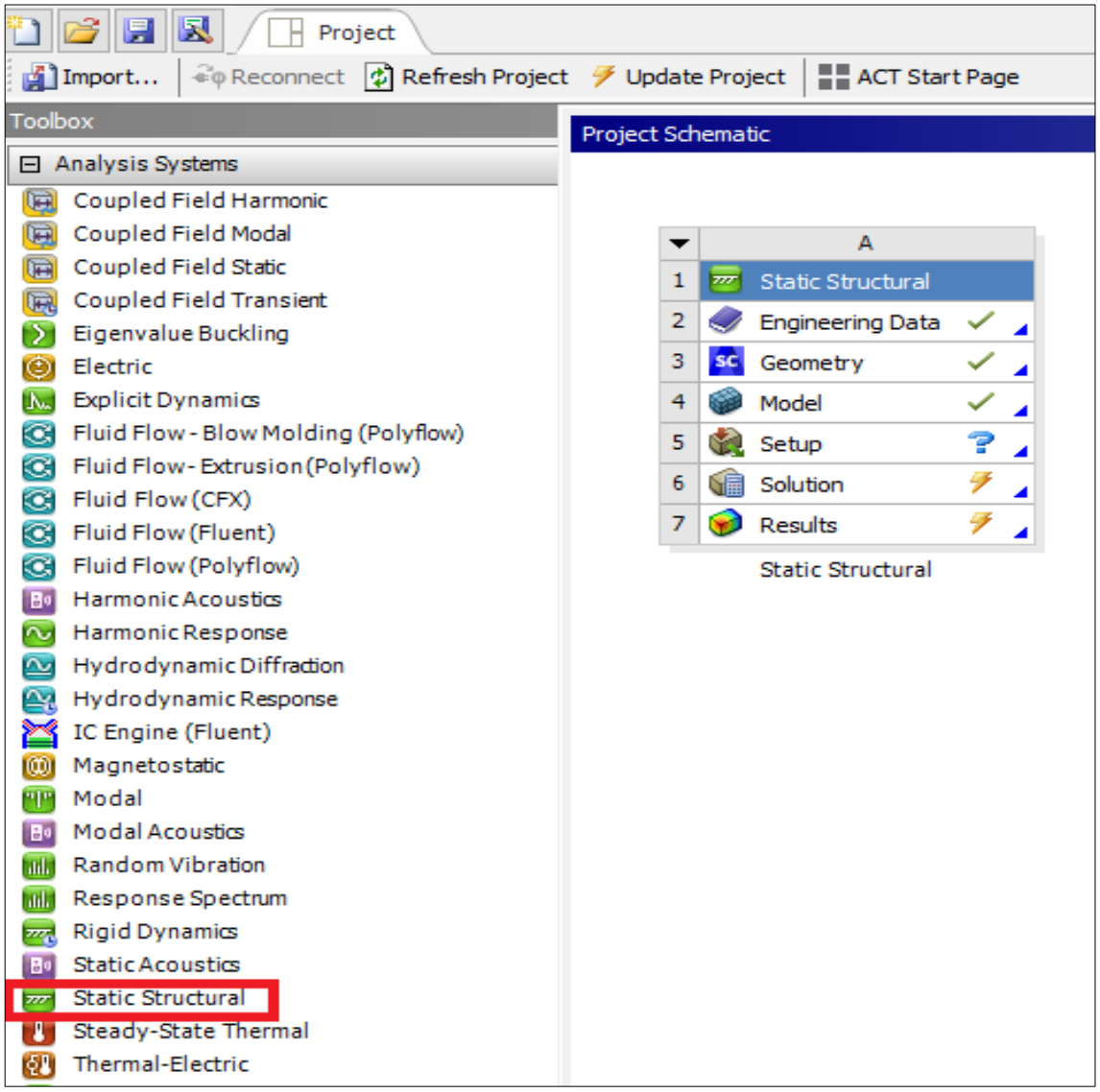

Figure 2-20 Workbench Interface with Static Structural workflow selected and highlighted and top right with project schematic.

All mechanical properties of materials used in the model, such as Young's modulus, Poisson's ratio, yield stress, and so on, are described in the Engineering Data module. (Fig. 2-21)

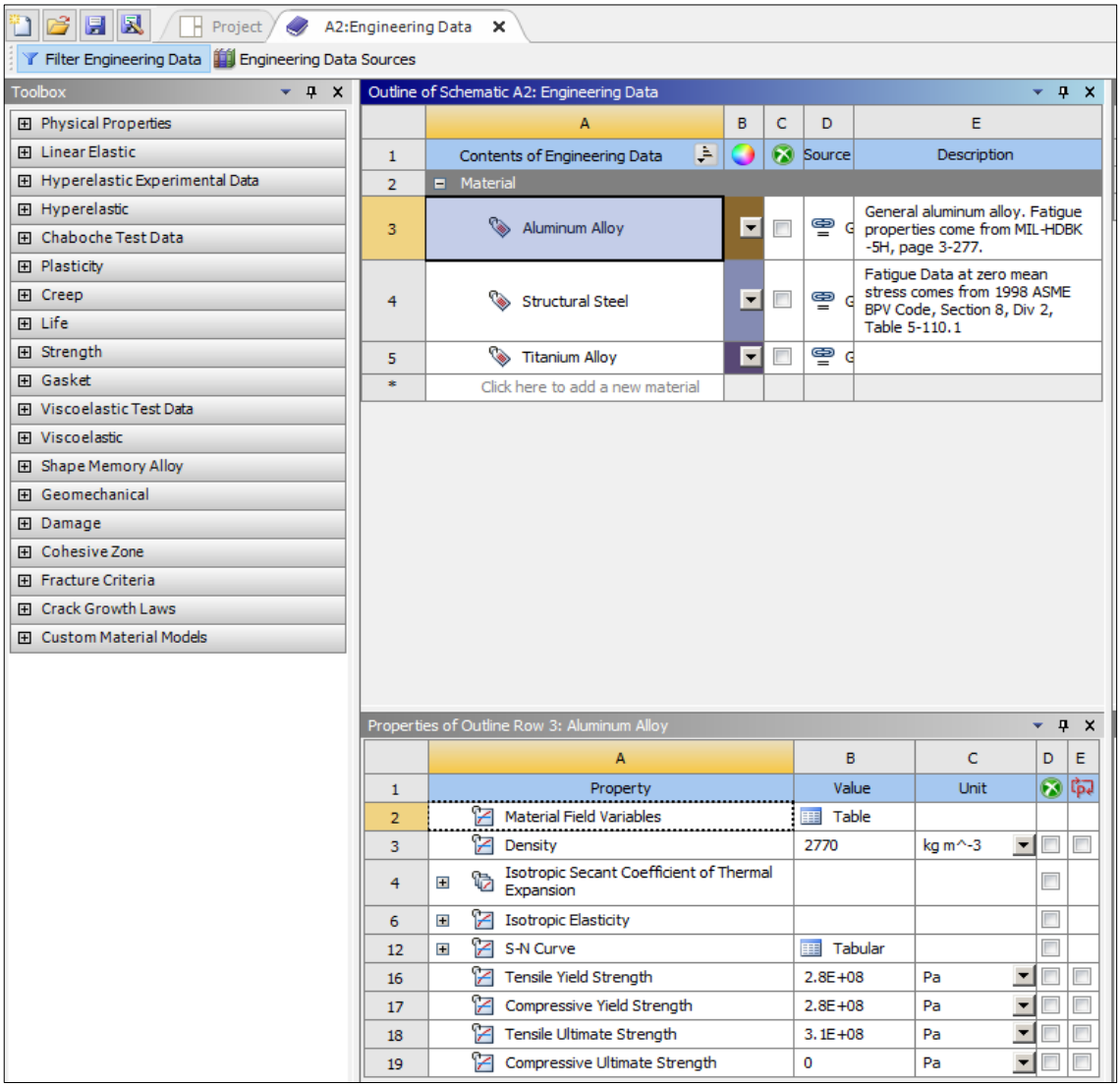

Figure 2-21 Engineering data module with an in-built material property.

The geometry that underpins the finite element analysis (FEA) model is described next in the workflow. Geometry can be imported as a SolidWorks component or drawn in a separate window that, when double-clicked, launches the SpaceClaim computer aided design (CAD) modelling tool (see Figure 2-19). SpaceClaim is a sophisticated Direct CAD modelling tool that allows for component setup and quick redesign. The latter method should be used to modify existing geometry, while SpaceClaim should be used to construct geometry from scratch, according to the ANSYS documentation.

Meshing, or the discretization of the model into smaller elements and nodes, is the next step after forming geometry. After meshing, the model geometry is shown in Figure 2-22b. The loading path and constraints applied in the model are shown in Figures 2-22a and 2-22b. To mimic the loading arrangement, the test piece in the model was restrained similarly to the experimental situation (20 mm duration contact grip) and a tensile load was applied on the opposite side, again in accordance with experimental conditions.

Figure 2-22b also shows static loading (F) corresponding to applied stress. Quite fine meshing has been used to achieve a reliable stress value in areas of the lapping ends separated by a lapping distance (W_{Lap}), as shown in Figure 2-22c. Mesh inspection was then implemented to ensure that the mesh components were not improperly distorted.

The material behaviour of linear elastic material was used to model loading conditions. The linear elastic model is used to describe materials that react to small strains in the material, have proportional stress and strain activity, and return to their original shape after loading and unloading on the same path (elastic).

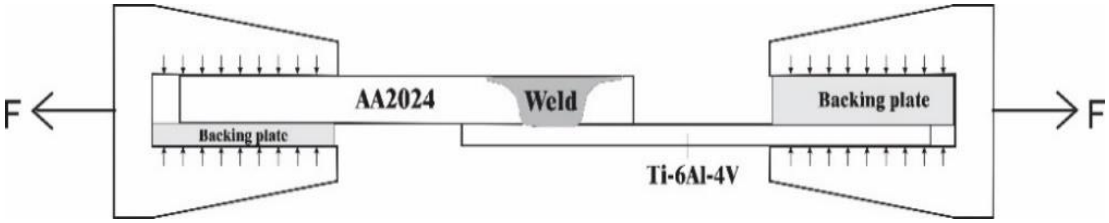

(a)

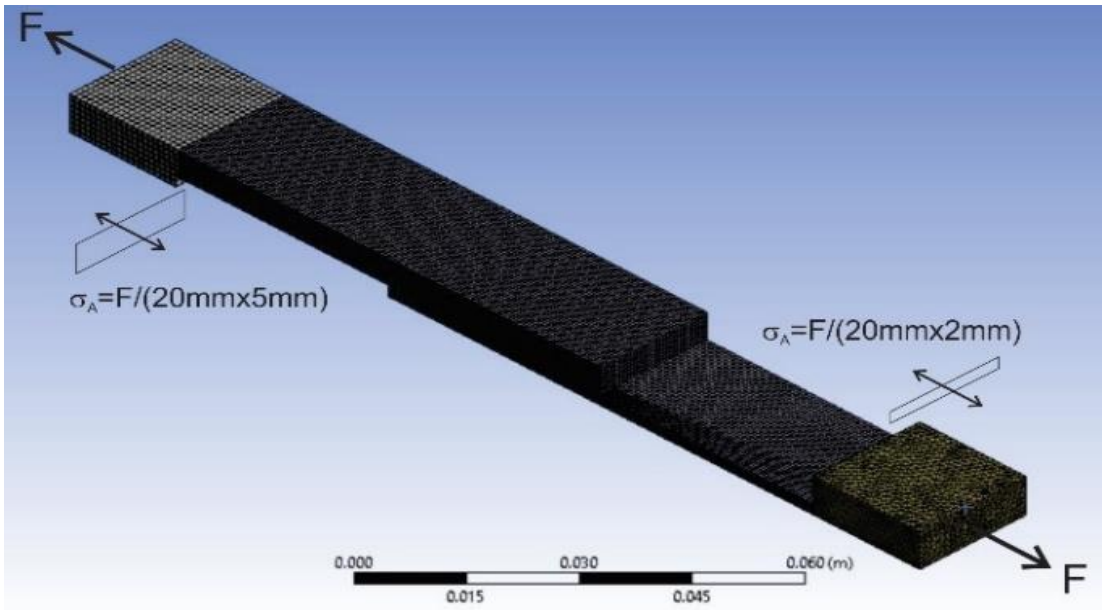

(b)

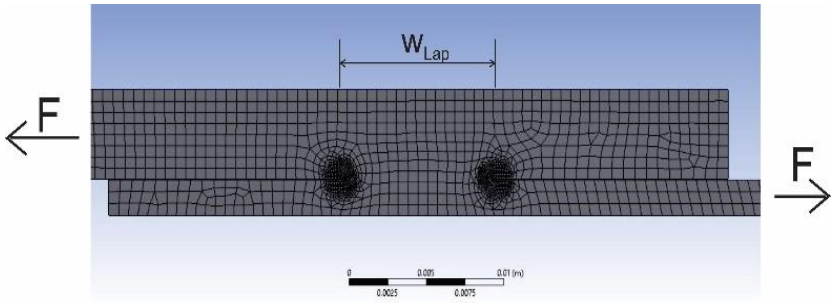

(c)

Figure 2-22 Illustration of meshing for simulation of stress distribution during static loading of a lap joint, (a) schematic of testing, (b) mesh of the whole sample including backing/supporting plates, and (c) finer meshing in the lapping ends.

After completing the model geometry and defining all boundary conditions, the model is ready for analysis and is sent to solver. Later the simulation results can be viewed in the results module. Figure 2-23 shows a sample equivalent stress (von mises) distribution in lap weld geometry after applying remote stress of 40 MPa.

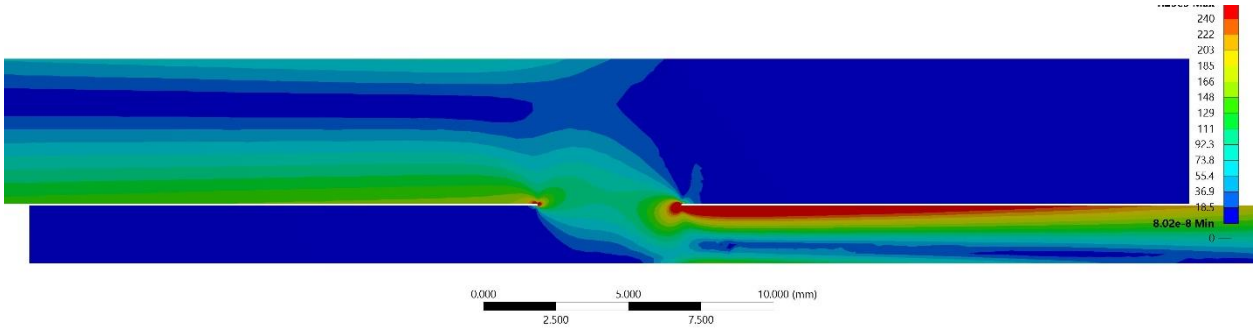

Figure 2-23 Equivalent stress distribution at 40 MPa (4 kN) with high stress concentration at the bottom plate due to the thinned bottom plate.

3. FRICTION STIR LAP WELDING USING NORMAL PIN

In the first and main part of this thesis research, a series of welds were made by FSLW of an aerospace aluminium alloy (AA2024-T6) and Ti6Al4V alloy using a normal pin. Fatigue testing of the series of welds was conducted with a range of applied load so fatigue limit with cycle number up to 10^7 could be determined. The welds are characterized by two different interface structures depending on whether the pin has penetrated to the bottom plate. These are (a) thin interface intermetallic and (b) interface regions of a mix stir zone of intermetallic and Ti6Al4V [59]. Microstructure analysis and examination of fracture surface were followed to reveal how the interface structures affecting the fatigue life of the welds. The details of the results and discussion of the results are present in this chapter below.

3.2 S-N data, Fracture Path and Fatigue Strength

Fatigue data in the form of F_{Max} (left axis) plotted against cycle number (N) are shown in Fig. 3-1. As has already been explained, a fatigue test sample can be a $d_P \approx 0$ (pin non-penetrating, NP) sample or $d_P > 0$ (pin penetrating, P) sample. It can also be partially NP and partially P (thus x %P). Thus, for each data point, pin penetration information is also stated in Figure 3-1. In the low cycle fatigue range, up to ~2×10^4, scatters of the data are relatively high but N appears to increase as F_{Max} decreases. In static tensile-shear testing of Al to Ti welds made using FSLW, the scatter has also been found high having overall $\Delta F_{Max}/F_{Max\text{-}avg} \approx 30\%$ [59] . In the higher fatigue cycle range (> 2×10^4 cycles), as can be viewed in Figure 3-1, scatters are low. The overall fatigue limit expressed as F_{max} for the 20 mm width samples is seen to be ~3.5 kN.

The significance of the fatigue limit determined in Figure 3-1 will be discussed by comparing it to fatigue limit of Al to Al welds made using FSLW. This is because, as has been explained in literature review in Chapter 1 (1.4), there is no information on fatigue study of FSL Al to Ti welds in open literature. For this, strength and fracture path need to be explained. First, fatigue strength data in the form of maximum applied stress (σ_{Max}) verses N are also plotted in Figure 3-1, as this form of strength is also used in literature. The value of σ_{Max} is taken as F_{Max}/A_{AA2024} where A_{AA2024} is the cross-sectional area of the AA2024 plate. As nominally $A_{AA2024} = 0.02\ m \times 0.005\ m = 1\times10^{-4}\ m^2$ and $\sigma_{Max} = F_{Max}/A_{AA2024} = F_{Max}\ (kN/1\times10^{-4}\ m^2) = 10F_{Max}$, for F_{Max} in kN and σ_{Max} in MPa, the conversion is by a factor of 10. Second, the discussion will also be aided by the schematic drawings in Figure 3-2. For the AA2024 to Ti6Al4V welds tested in this study, as have been noted in Figure 3-1, fracture can either be along the AA2024/Ti6Al4V interface (path 1) or in AA2024 (path 2). Fracture path is indicated for each tested sample in Figure 3-1. As has been explained in Chapter 2 (2.1.1), the use of a thicker AA2024 plate is for a higher chance of fracturing along the AA2024/Ti6Al4V interface so that fatigue strength of the AA2024/Ti6Al4V lap welds can be determined.

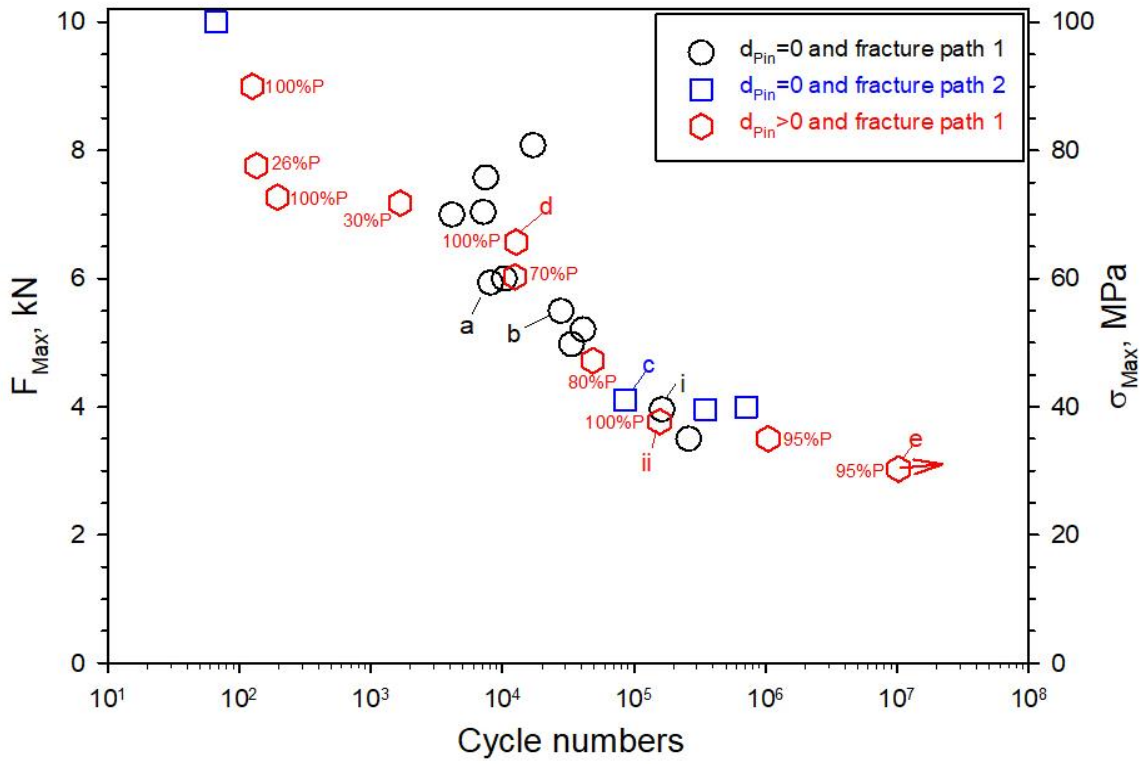

Figure 3-1 Maximum load and stress plotted against the fatigue cycle number. Pin penetration condition and fracture path are indicated. For $d_P > 0$ samples, area % of $d_P > 0$ is indicated. Samples each marked with one of a, b, c, d, e or i, ii are reference letters or numbers for later figures.

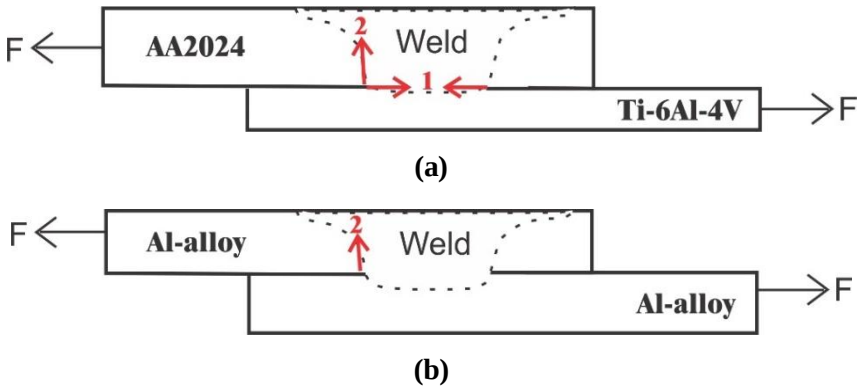

Figure 3-2 Illustrations of (a) AA2024-to-Ti6Al4V weld with thicker top plate and (b) Al-to-Al weld with equal top and bottom plate thickness. Fracture path 1 and path 2 are indicated by arrows.

To explain the fracture paths, photographs of selective tested samples with either fracture path 1 or path 2 are shown in Figure 3-3 (“a” to “e”). A non-tested sample (Fig. 3-3f) is also shown. The top plate in each sample is AA2024 and the bottom is Ti6Al4V. The left side of the AA2024 and the right side of Ti6Al4V are the loading sides for the tested samples, as has already been illustrated in Figure 3-2. The corresponding fatigue data, “a” to “e”, are marked in Figure 3-1. The images in Figure 3-3 have been taken in a manner that the loading side of the AA2024 plate and the Ti6Al4V plate of the tested samples are placed in parallel. Thus, the uplifting of the unloading side of AA2024 can suggest qualitatively the extent of bending (plastic deformation)

during fatigue testing. Figure 3-3f shows a non-tested sample and, from this image, the retreating side of the friction stirred AA2024 has already been slightly uplifted due to the slightly distortion as on the retreating site of the top AA2024 plate there was no clamping during FSLW.

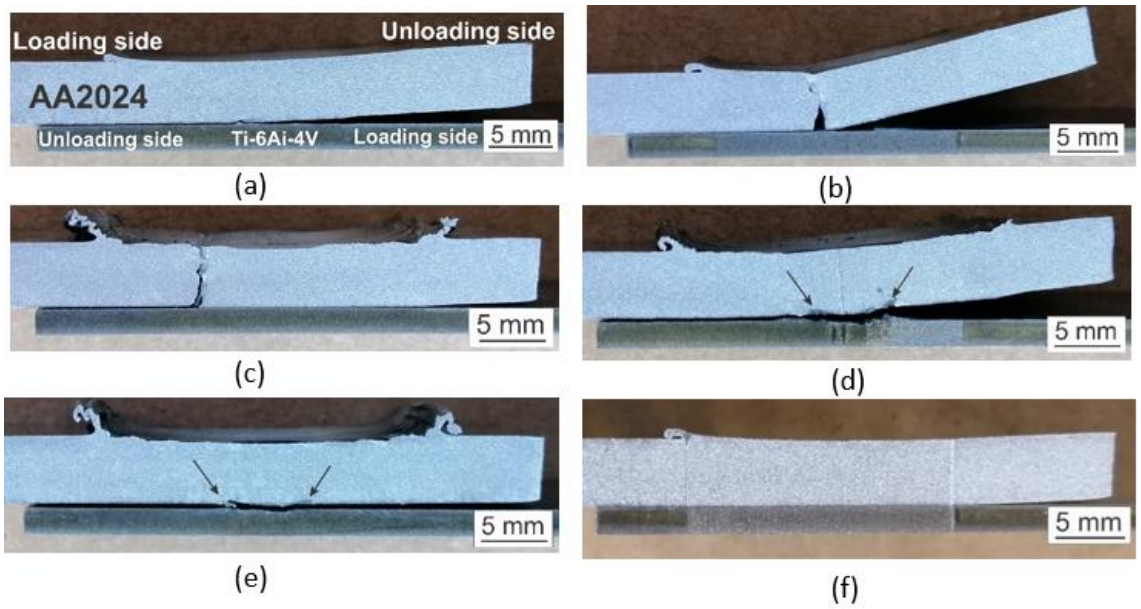

Figure 3-3 Images of tested samples fractured (a) along the interface in the NP sample marked "a", (b) along the interface with extensive cracking having occurred in AA2024 in the NP sample marked "b" , (c) in AA2024 in the NP sample marked "c", (d) along the interface region in the P sample marked "d", and (e) along the interface region in the P sample marked "e", respectively, in Figure 3-1, and image (f) of a non-tested sample. Note: Arrows pointed to the outflow of Ti-Al material in (d) and (e)

Figure 3-3a shows a NP (non-penetrating, $d_P \approx 0$) sample having fractured along the interface (path 1) after 8,100 cycles at σ_{Max} = 60 MPa. By comparing Figure 3-3a to Figure 3-3f, as it is evident that at this loading, the AA2024 part of the welded sample has deformed (bent) slightly before the total fracture. The sample in Figure 3-3b is also a NP sample with fracture path 1, but extensive cracking in the AA2024 nugget region has occurred (incomplete fracture path 2). The sample in Figure 3-3c is fracture path 2 where a complete fracture has taken place in the AA2024 nugget region instead of fracturing along the weld interface region. Four tested samples have fractured in AA2024 nugget, meaning fracture path 2, and they are all NP samples.

The tested sample in Figure 3-3d (fractured after 12,620 cycles) is similar to the one in Figure 3-3a in that both samples fractured along the weld interface region (path 1) with AA2024 clearly bent. The sample in Figure 3-3d is however a P (penetrating, $d_P > 0$) sample and in both sides of the bottom and penetrated region, Ti-Al (and intermetallic) mixture due to the mix flow associated with pin penetration during FSLW can be identified. It appears that the slightly higher σ_{Max} condition for the sample in Figure 3-3d has caused more bending than the sample in Figure 3-3a. The sample in Figure 3-3e is also a (mainly) P sample tested at σ_{Max} = 30 MPa but the test stopped (runout) after 10,247,760 cycles. For this test of low load and long fatigue life, deformation-

bending of the sample is not apparent. Comparing Figure 3-3c to Figure 3-3f, at a higher load with σ_{Max} = 41 MPa, bending is still not apparent.

The appreciable deformation in samples tested with $\sigma_{Max} \geq 60$ MPa (Figure 3-3a and Figure 3-3d), little deformation observed in samples tested with $\sigma_{Max} \leq 41$ MPa (Figure 3-3c and Figure 3-3e) are discussed further. The discussion is aided using the simulated stress distributions shown in Figure 3-4, for static loading. In Figure 3-4a, equivalent (von-Misses) stress (σ_e) distribution around the weld location is shown for an applied load of 4 kN equivalent to σ_A = 40 MPa in the remote location of the AA2024 side. Stress is highly non-uniform for the lapping geometry. Stress is higher on Ti6Al4V side as the load is supported by a thinner section. A clear feature is the high stress concentration in the lapping locations/ends of the weld. Towards the unloaded side, the stress sharply reduces to zero.

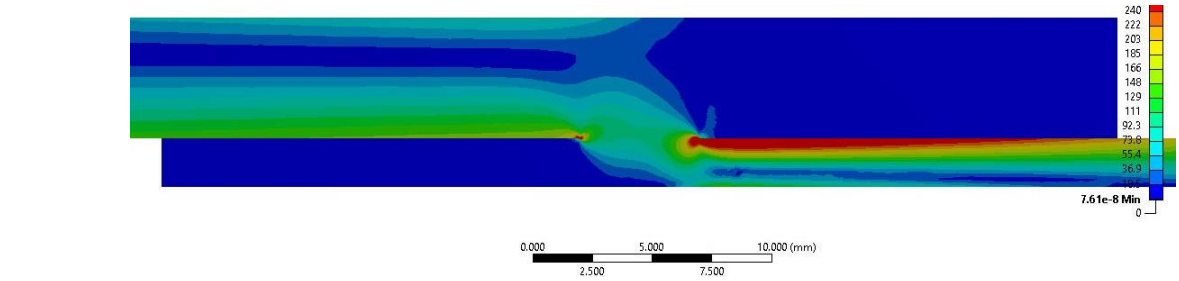

(a)

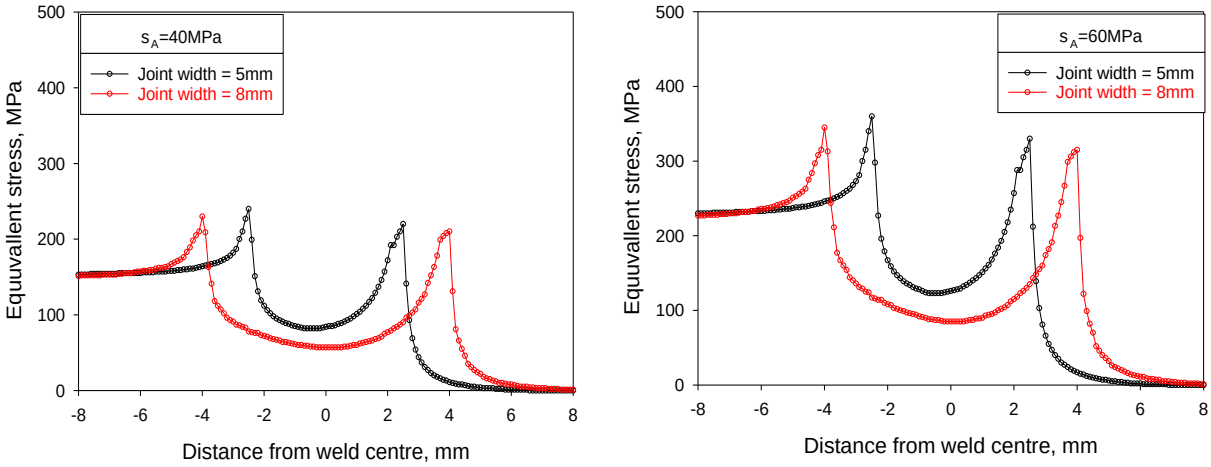

(b)

Figure 3-4 Simulated stress distribution showing stress concentrations in both sides of the lap weld, (a) von-Misses stress distribution based on 4 kN applied load, and (b) data plotted vs. distance on the AA2024 side of the lapping location with σ_A on AA2024 side being 40 MPa (left) and 60 MPa (right).

In Figure 3-4b, σ_e along the bottom of the AA2024 plate of the weld including outside and inside of the lap weld are shown for W_{Lap} of 5 mm and 8 mm, with two applied loads (left and right graph corresponding to σ_A = 40 MPa and σ_A = 60 MPa, respectively). At ~ 1 mm away from the lapping end σ_e is about 3 times the applied (remote) stress. Approaching the lapping end where weld starts, σ_e sharply increases. Moving inside the weld zone, σ_e decreases sharply before

increasing sharply again towards the other end of the weld. After the weld, σ_e decreases sharply to zero. The reason for examining conditions of two W_{Lap} values is for the consideration of the effective weld width. The diameter of the pin considering the root of the thread is 5 mm but the outside diameter is 6 mm. As will be shown, the effective weld width is larger than the pin diameter. Thus, a lapping width of 8 mm is also considered. As shown in Figure 3-4, increasing the width of weld reduces the maximum σ_e slightly.

Zhang et al. [80, 81] conducted a series of tensile property evaluation on friction stir welds of AA2024 alloy plate and found $\sigma_{0.2} \approx$ 275-305 MPa. For the present work of applying 4 kN (σ_A = 40 MPa) during fatigue testing, simulation (left of Figure 3-4b) indicates that the maximum σ_e reaches 240 MPa and 220 MPa in the left side and right side of the stress concentration location, respectively, meaning $\sigma_{e\text{-}Max} \approx 240$ MPa $< \sigma_{0.2}$. This explains that the sample tested at 4 kN and shown in Figure 3-3c, in comparison to Figure 3-3f shows little bending (deformation) after testing. Sample in Figure 3-3a suggests the sample slightly bent for applying 6 kN (σ_A = 60 MPa), consistent with the prediction in Figure 3-3b (right) that $\sigma_{e\text{-}Max} \approx 360$ MPa $> \sigma_{0.2}$ and $\sigma_{e\text{-}Max} \approx 330$ MPa $> \sigma_{0.2}$ on the left side and right side, respectively.

Comparison of the current fatigue limit to fatigue limit of Al to Al welds made using FSLW from literature, summarized in Table 3-1, can now be made. Data from Fersini and Pirondi's study [70]] based on welds of 1.6 mm thick AA2024 to AA2024 sheet marked using FSLW shows that the fatigue limit (their stress range converted to σ_{Max}, knowing R = 0.1) is ~ 28 MPa with fracture path 2 (fracture paths shown in Fig. 3-2). Braga et al. [82] show $\sigma_{Max} \approx$ 30 MPa (run out at 2×10^6 cycles) with fracture path 2, for FSL welds made using 1.6 mm thick AA2024 to AA2024 sheet and with R = 0.1. Infante et al. [73] tested 2 mm thick Al6082 to Al6082 FSL welds using R = 0.1 and their σ_{Max} (runout at 5×10^6 cycles) is ~ 20 MPa with fracture path 2. Thus, using thin sheets for FSLW, the fatigue limit is $\sigma_{Max} \leq$ 30 MPa with fracture path 2.

Table 3- 1 Fatigue strength values from various studies on Al to Al FSL welds

From	Plate alloy & thickness (mm)	Fatigue strength value at N, MPa	Fracture path
Fersini & Pirondi [70]	AA2024, 1.6	~ 28	2
Braga et al. [79]	AA2024, 1.6	30	2
Yang et al. [72]	AA6061, 5	15	2
Infante et al. [73]	AA5754, 2 AA6082, 2	11 20	2 2

Only Xu et al. [72] have made FSL welds using thicker plate, with thickness 5 mm. Using R = 0.1, their maximum value of σ_{Max} for Al6061 to Al6061 welds is ~26 MPa (runout at ~2.3×10^6

cycles) with fracture path 2. In our current study, the top plate is 5 mm. As shown in Figure 3-1, with fracture path 2, fatigue limit expressed as σ_{Max} should be slightly less than 40 MPa as, when $\sigma_A \approx$ 40MPa was applied, three samples failed between (0.9 - 7)$\times 10^6$ cycles. The fatigue limit can thus be regarded as ~35 MPa for samples with fracture path 2. The higher fatigue limit than those reported in literature is reasonable as for Al to Al FSLW, using either thin sheets of a thicker plate, hooking assisting path 2 fracture affecting fatigue strength may be unavoidable.

As has been indicated, the use of 5mm top AA2024 plate is for avoiding fracture path 2 dominant so as to focus more on the AA2024/Ti6Al4V interface region. The meaning of F_{max} = 3.5 kN as a fatigue limit for lap welds based on using 5 mm Al alloy plate is further discussed with reference to fracture path 1. A F_{Max} = 3.5 kN and thus σ_{Max} = 35 MPa in lap weld geometry, as has been shown, may result in a stress concentration at the lapping end to increase the stress by ~ 6 folds to > 200 MPa. For welds using an Al-alloy sheet for example 2mm in thickness, for F_{Max} = 3.5 kN to cause fracture path 1 along the AA2024/Ti6Al4V interface region, the Al-alloy plate needed to support an applied stress of 88 MPa. In the lapping ends where stress concentrates, stress may be well above 500 MPa. Al-alloys in the weld region can only support stress many times less without failure. Thus, the AA2024/Ti6Al4V interface region in the present FSL welds being able to support F_{Max} = 3.5 kN to 1×10^7cyles without failure with fracture path 1 can be viewed strong. This also suggests that the AA2024/Ti6Al4V interface region in the FSL welds can readily support fatigue loading without failure as excessively thick plates are not normally used in lap weld designs.

3.3 Features of Welds and Fatigue Fracture

As has been explained in Experimental Procedures, three tests were interrupted before final failure. The cross-section of the first test interrupted sample is shown in Figure 3-5. The sample is a NP sample tested at mid-high loading at 6 kN for 10, 560 cycles and this cycle number should be one for the sample to be near a complete fracture according to Figure 3-1. Figure 3-5a displays the typical weld nugget zone (NZ) and thermomechanical affected zone (TMAZ). Above NZ is the shoulder flow zone. The mid-height width of NZ is 9.1 mm and in the bottom adjoining Ti6Al4V is 8.1 mm. For this NP sample without pin penetrating and thus without a mix stir flow, welding between AA2024 and Ti6Al4V is through diffusion at high temperature and under the downward force during FSLW. As has been demonstrated for an experiment [59] similar to the current NP FSLW condition, a thin interface intermetallic layer formed and thus the alloy couple was diffusion welded, which was responsible for a high tensile-shear strength to be obtained. The

thin intermetallic layer between the aluminium alloy and titanium alloy during FSLW of Al-to-Ti has been structurally identified [61].

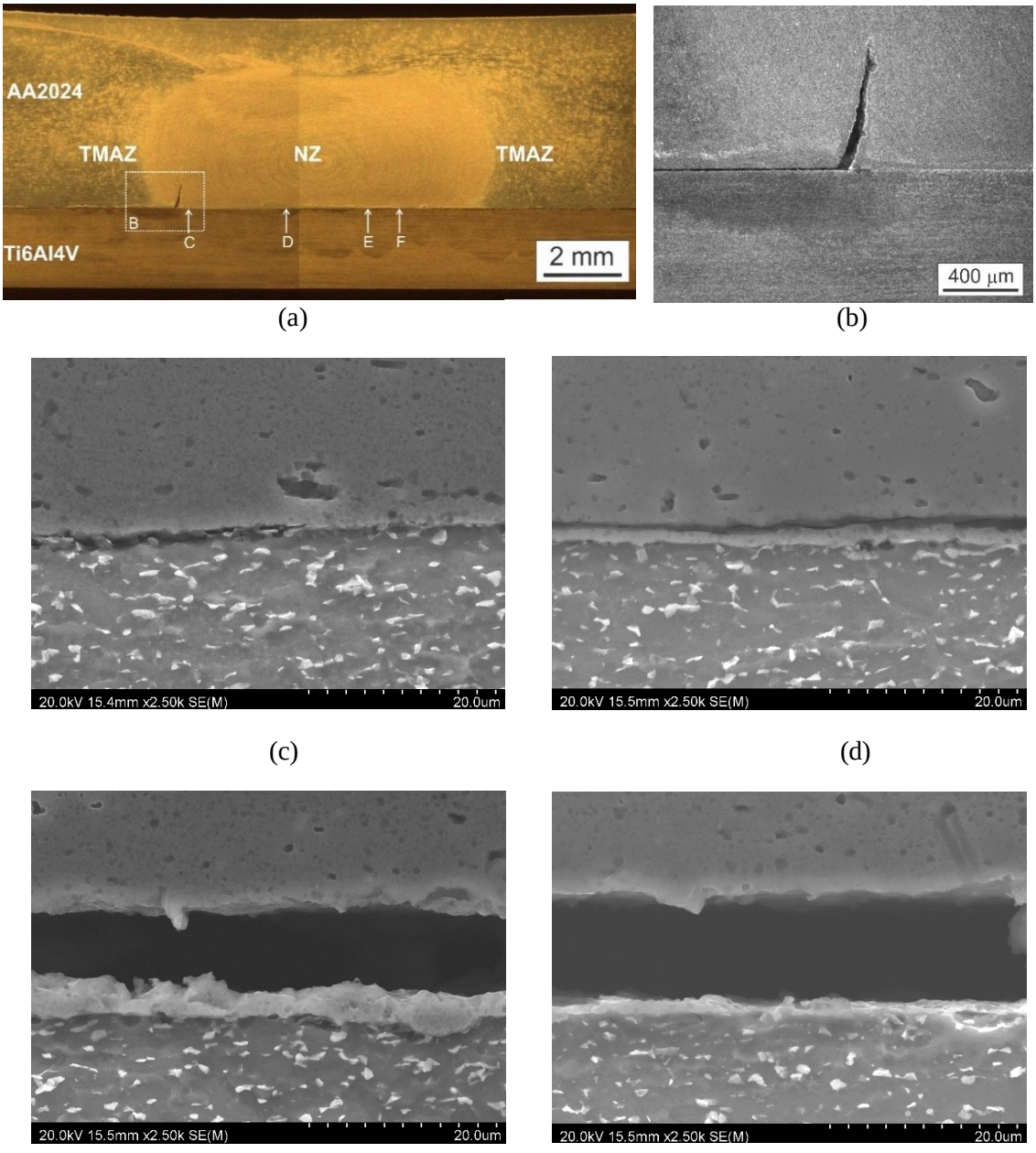

(a) (b)

(c) (d)

(e) (f)

Figure 3-5 Cross sectional images of the NP sample tested under 6 kN with the test interrupted at 10,560 cycles, (a) stereomicroscope image of the whole weld with area marked B for optical micrographs taken and shown in (b) and with locations pointed to as C to F for SEM micrographs taken and shown in (c) to (f), respectively.

As is shown in Figure 3-5a and is more clearly shown in Figure 3-5b, at the time when the test was interrupted, a crack has started to propagate in a path 2 manner and this path 2 crack was propagating inside NZ. Closer examination has revealed that while the path 2 crack has quite well propagated, path 1 cracking has actually well advanced at the time when the test was interrupted. As shown in Figure 3-5c, a crack has started propagating along path 1 from where the path 2 has started and the crack tip is seen in the mid location of the micrograph. The right half the

micrograph displays the well welded AA2024/Ti6Al4V interface which continues towards the right side from location C to location D (Figure 3-5a) where a crack has started to appear (Figure 3-5d). In fact, location D is the end of crack path 1 with the crack having propagated from other (right) side. As illustrated in Figure 3-5e and Figure 3-5f, the crack was more open from where it has propagated from (the right).

Although cracking along path 1 refers to the crack propagation along the AA2024/Ti6Al4V weld interface region, there are actually two pathways with path 1. As is seen in Figure 3-5c, the crack has largely propagated along the AA2024/Ti6Al4V interface (or interface intermetallic layer). On the other hand, as shown in Figure 3-5d and particularly clearly shown in Figure 3-5e, the crack has propagated inside AA2024 in a short distance from and largely parallel to the AA2024/Ti6Al4V interface. In Figure 3-5f, the crack has propagated slightly inside AA2024 on the left and largely along the interface on the right. Referring to fracture path of Al to Al alloy illustrated in Figure 3-5b, if the thickness of the Al plate was sufficiently thick, path 1 cracking would need to be added to the figure (of illustration). The competitive and mixed crack propagation, inside AA2024 or along the AA2024/Ti6Al4V interface (intermetallic layer) as shown in Figure 3-5, may have suggested that the diffusion AA2024/Ti6Al4V weld established during FSLW was comparable to friction stir AA2024 material in fatigue strength, at least under this mid loading range.

The second interrupted test sample is also a NP sample tested under 4kN for 174, 020 (high) cycles. This cycle number is approximately the same as that for sample “i” labeled in Figure 3-1. Figure 3-6 shows the cross-section of the whole weld and closely a number of locations along the AA2024/Ti6Al4V weld. As the weld was a NP weld, there was not a mixed stir zone. The mid-NZ width was 9.3 mm and the bottom NZ width was 7.4. In the location 2 mm distance outside the bottom NZ, as shown in Figure 3-6b, there was no welding between AA2024 and Ti6Al4V. In location C (Figure 3-6c), AA2024/Ti6Al4V was well welded. In the mid-right side of the low-magnification image, there are two cracks that were propagating upward in AA2024 before the interruption. On the left side of the low-magnification image, small cracks in AA2024 along the AA2024/Ti6Al4V interface can be identified, as pointed to by arrows. When the stress in a location became highly concentrated as the crack propagation reached that welded location, if the crack propagation along the AA2024/Ti6Al4V weld (interface) is difficult, crack initiation in AA2024 will take place.

The higher-magnification micrograph in Figure 3-6c (right) shows that the crack has not yet propagated further to the right when the sample testing was interrupted. No crack has been identified for the rest of the welded AA2024/Ti6Al4V in the rest of NZ and a typical interface region is shown in Figure 3-6d. The small crack from the right side has stopped in location E, just

outside of NZ, as shown in Figure 3-6e. In a short distance next (location F), it appears that the crack has propagated through the discontinuous AA2024/Ti6Al4V weld. Further away in location G, it is clear there was no welding between AA2024 and Ti6Al4V. Measurement has shown that the distance from the welded location of slightly more left of location C to location F is 8.8 mm. This means that under the friction stir heat and downforce during FSLW, diffusion welding has taken place with the effective width of the weld being at least 8.8 mm while the pin outside diameter is 6 mm.

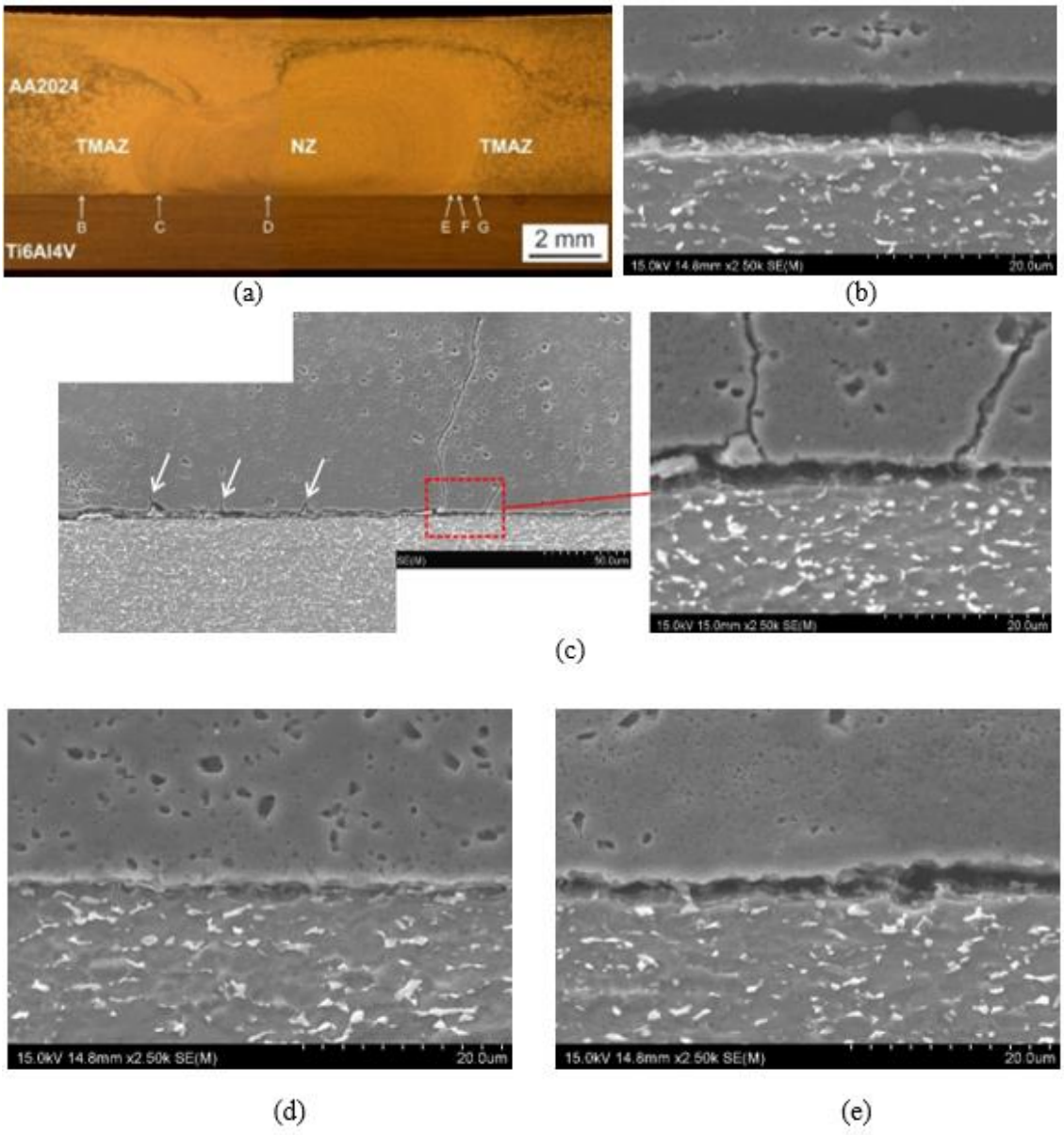

Figure 3-6 Cross sectional images of the NP sample tested under 4kN with the test interrupted at 174,020 cycles, (a) stereomicroscope image of the whole weld with locations pointed to as B to G for SEM micrographs taken and shown in (c) to (g), respectively. Area outline in (f) is for EDS elemental determination.

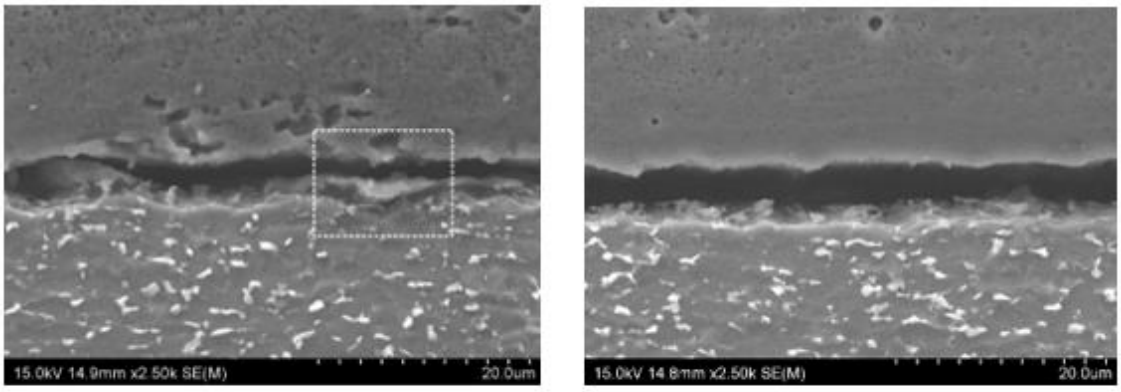

(f) (g)

Figure 3-6 cont.

A highly localised welded spot in the discontinuous welded location outlined in Figure 3-6f is further analysed. The outlined location suggests AA2024 has locally welded to Ti6Al4V but the crack has propagated through on the AA2024 side. A higher magnification micrograph and EDS spectra of points 1-3 marked in the micrograph are presented in Figure 3-7. Point 1 is titanium containing aluminium and thus Ti6Al4V material. Point 3 is clearly aluminium. Point 2 is basically aluminium with a trace of titanium having been included due to the EDS interaction volume to have included a little outside that small piece to be analysed. The small piece is thus aluminium welded onto Ti6Al4V. The crack has not propagated along the Al to Ti interface but has propagated through the aluminium away from the interface.

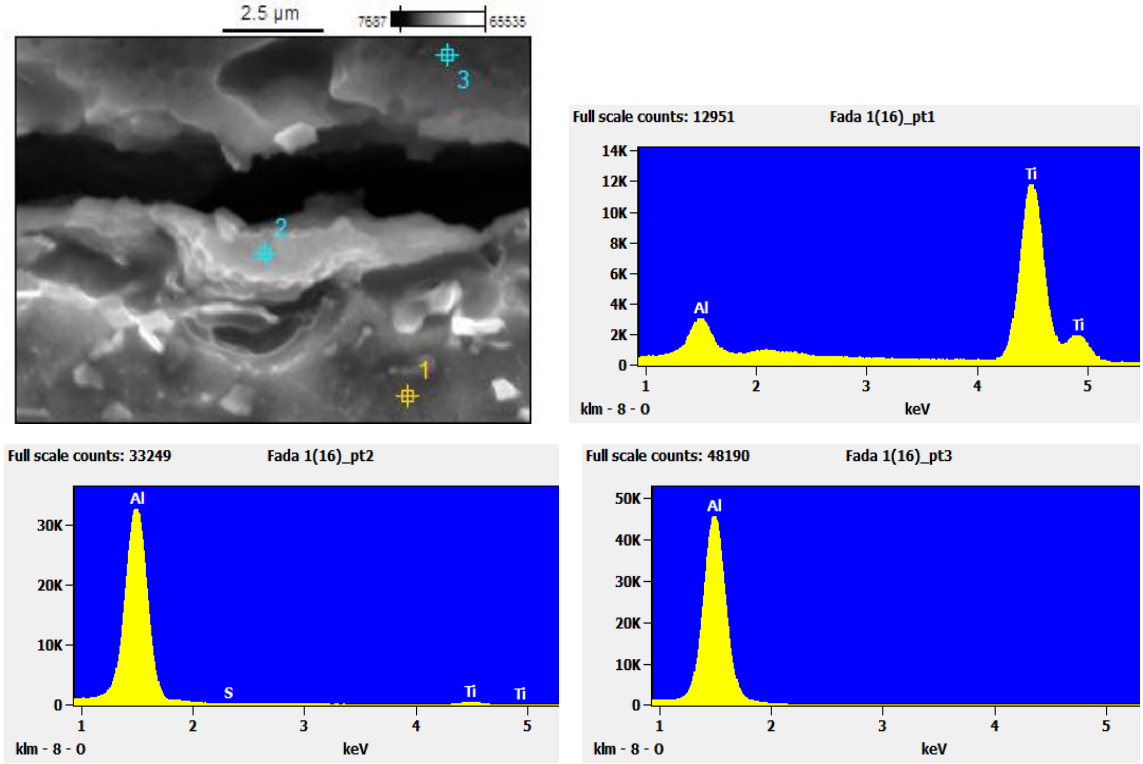

Figure 3-7 High magnification micrograph of the area outlined in Figure 3-6f and EDS spectra for points indicated in the micrograph: top right spectrum for point 1, bottom left spectrum for point 3, and bottom right spectrum for point 3.

The third interrupted test sample is a P sample tested also under 4 kN and the test was interrupted when 295, 100 cycles were reached. This (high) cycle number is close to that (174, 020) for the second interrupted sample, in a log scale. Figure 3-8a shows the cross-section of the whole weld. Different from the weld zones present in NP samples (Figure 3-5a and Figure 3-6a), there is a mix stir zone (MSZ), mixing Al, Ti, and brittle Ti-Al intermetallics, below the less regular NZ. Cracks in the upper region of MSZ can be identified although these cracks may not be associated with fatigue testing. In location B in Figure 3-8a, weld is not established, as shown in Figure 3-8b. Location C (Figure 3-8c) is where AA2024/Ti6Al4V has been welded and cracking may have just started but has not significantly propagated. From there on and to the right until location e, the AA2024/Ti6Al4V interface region is similar to that shown in Figure 3-8d, showing the interface being well welded without cracking. In location e (Figure 3-8e), the outflow from MSZ has also resulted in a well welded interface region between the MSZ material and Ti6Al4V.

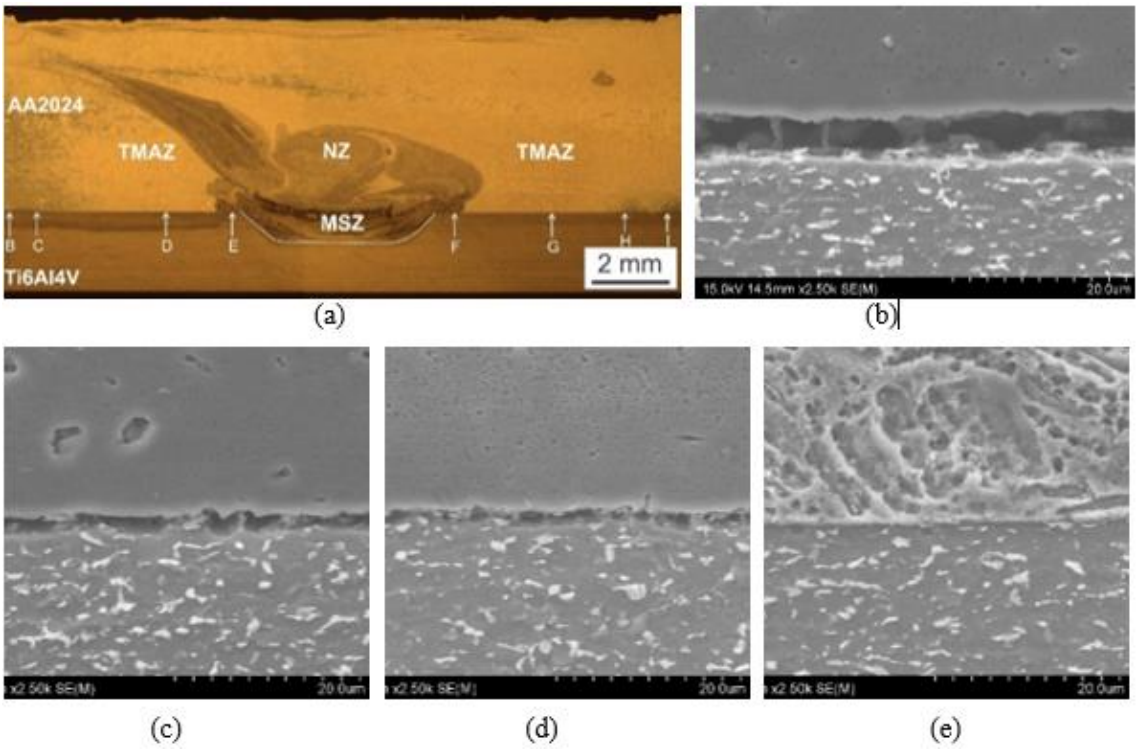

Figure 3-8 Cross sectional images of the P sample tested under 4 kN with the test interrupted at ~295,100 cycles, (a) stereomicroscope image of the whole weld with locations pointed to as B to I for SEM micrographs taken and shown in (b) to (i), respectively.

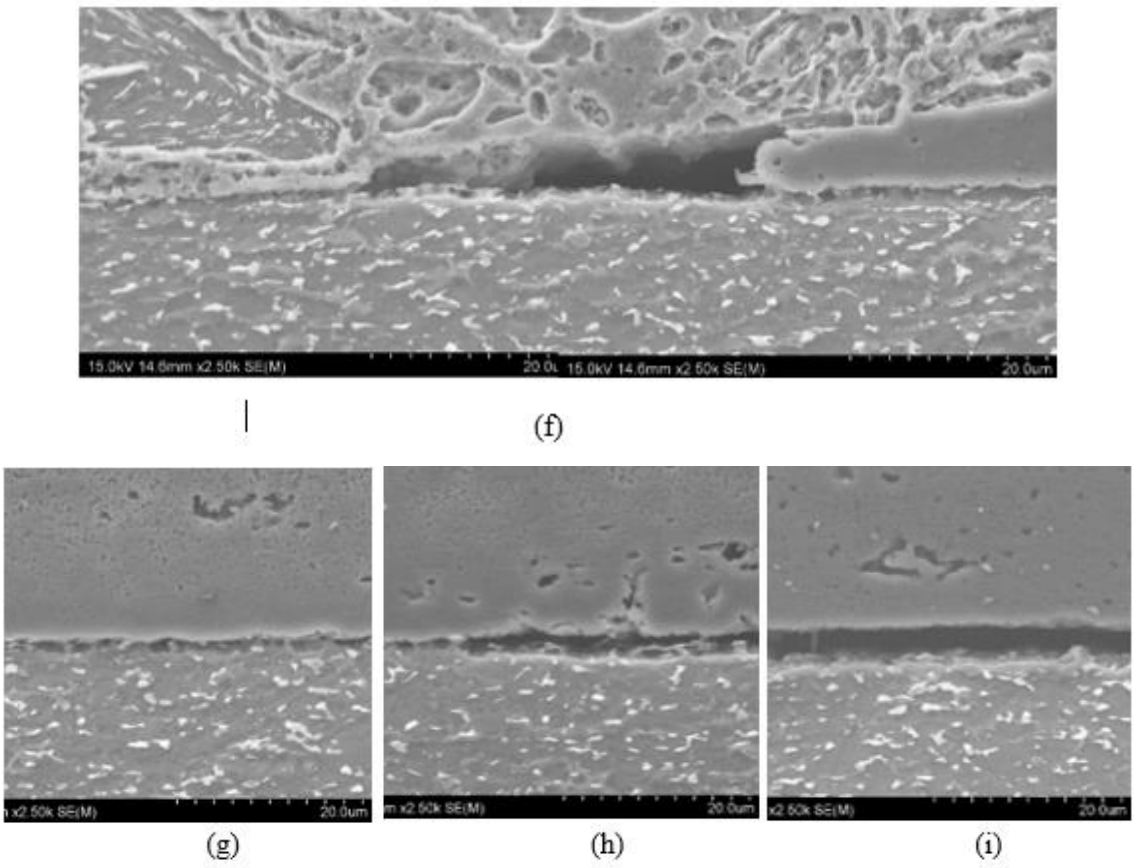

Figure 3-8 cont.

Location F (Figure 3-8f) is the other side of the weld where MSZ/TMAZ has met. A small cavity suggests the insufficient plastic flow during FS in that location. But on both side of the small cavity, AA2024/Ti6Al4V has been well diffusion welded. This is the same along AA2024/Ti6Al4V interface for a long distance of ~2.5mm and an example is shown in Figure 3-8g. In location H (Figure 3-8h), an interface crack can be seen. Further away, as shown in Figure 3-8i, no welding between AA2024/Ti6Al4V has taken place. The above explanation and measurement have shown that outside of width equal to bottom pin diameter, AA2024/Ti6Al4V has been diffusion welded for a distance of ~5 mm on each side and ~10 mm in total. Thus, the width of diffusion weld outside MSZ for P condition can be significantly larger than that of NP condition for which diffusion weld width is ~9 mm. This explains fatigue strength of P samples is not significantly lower than NP samples, despite of MSZ being a brittle zone.

The essence of diffusion welding of an aluminium alloy part to titanium alloy part is the formation of interface intermetallics and thus to metallurgically join the alloy couple. It has now been well understood [61] that, under the normal Al to Ti alloy friction stir condition where friction stir of aluminium alloy portion is dominant, excessive growth of the interface intermetallics does not occur. (Static) joint strength is then high. And thus, the primary importance of Ti-Al diffusion welding during friction stir is for the required Ti-Al intermetallic at the interface to form. Given a suitable contact at the interface between aluminium alloy and titanium alloy, the rate of

intermetallic formation should also follow Arrhenius type of relation and is thus strongly temperature dependent. For the present AA2024 to Ti6Al4V FSLW and for $d_P > 0$, the friction between the tool pin and Ti6Al4V must have generated a high amount of heat to have resulted in a high temperature weld zone outside the MSZ so that the condition for diffusion welding is favourable. An attempt is made to explain this, as described below.

3.4 Thermal Condition, Contact Condition and Diffusion Welding

Temperature histories at two points in the AA2024/Ti6Al4V interface region determined in the FSLW experiment by recording T and F_Z simultaneously are shown in Figure 3-9. Before 183s, the vertical location of the pin was aimed for $d_P \approx 0$, meaning no penetration. At 183s when the tool-pin had well passed the first thermocouple location in the zero d_P section, the tool pin was intentionally lowered to ascertain $d_P > 0$. The response to this pin penetrating to the bottom Ti6Al4V plate is the increase in F_Z. At that point (183s), the front of the pin was 13-14 mm to the second thermocouple location. After the initial pin penetration and rapid increase in F_Z, F_Z gradually decreased, due to pin wear. Then, further slightly lowering of the tool-pin was applied for a FSLW distance corresponding to the period 230-260s and during this period the average F_Z at ~20 kN is higher than the average F_Z at 16-17 kN before 183s. Thus, when the rotating pin was passing the second thermocouple location, $d_P > 0$.

Figure 3-9 shows that maximum temperature ($T_{Max} = 600$ °C) for $d_P > 0$ was significantly higher than T_{Max} (480°C) for $d_P \approx 0$. During friction stir, temperature increases in the weld zone due to frictional heat and deformation heat generated. It is well understood that T_{Max} should be lower than the solidus temperature and, for AA2024, T_{Max} should be lower than 502 °C during friction stir of the alloy [83]. Thus, $T_{Max} = 480$ °C detected is reasonable for $d_P \approx 0$. For $d_P > 0$, heat generation at pin bottom due to the friction stir of Ti6Al4V with a considerably higher solidus temperature (1605 °C) should thus result in $T_{Max} >> 502$ °C locally in the bottom mix stir zone. The more the pin bottom penetrates the higher the T_{Max} should be. Thus, $T_{Max} = 600$ °C as detected and shown in Figure 3-9 is also reasonable.

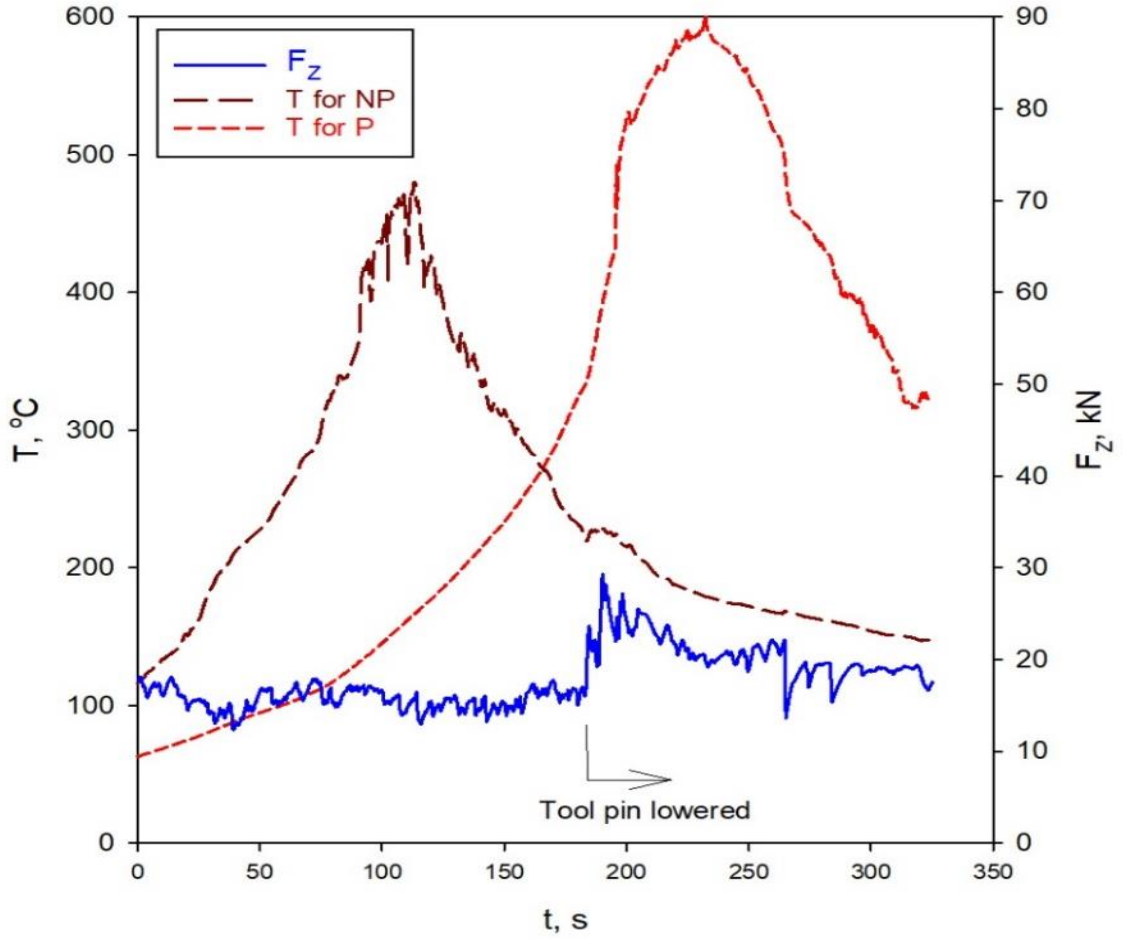

Figure 3-9 Temperature histories at two points, a NP point and a P point, of interface region together with down force data recorded simultaneously in the experiment. The moment (~183s) at which the tool-pin was lowered aiming for the pin to penetrate is indicated.

For a discussion of the significance of how T values may affect diffusion welding, we may consider the lengths of times during which the AA2024/Ti6Al4V interface region has remained at high temperatures. Taking two temperature ranges, > 500 °C (500-600 °C) and 400 – 500 °C, data estimated from Figure 3-9 are listed in Table 3-1. Clearly, for $d_P > 0$, the interface region remained at above 500 °C for a long time (67s). On the contrary, T_{Max} has not exceeded 500 °C for $d_P \approx 0$. A longer time recorded by the thermocouple should also mean a higher temperature field surrounding the pin bottom longer. A precise temperature field cannot be established but data in Table 3-1 may be used to suggest, for aiding the discussion, indicative isotherms travelling with the pin in the cross section normal to welding direction as shown in Figure 3-10. The figure is intended to suggest schematically that temperatures of the interface region outside the pin bottom are also significantly higher for $d_P > 0$ than for $d_P \approx 0$. In the figure, the NZ and NZ+MSZ have been drawn after tracing them in Figure 3-5a for $d_P \approx 0$ and in Figure 3-8a for $d_P > 0$, respectively. They are thus realistic sizes.

Table 3-2 Lengths of times recorded for spending at two high temperature ranges.

	$d_P \approx 0$	$d_P > 0$
$t_{T>500°C}$, s	0	67
$t_{T>400°C}$, s	23	93
$\Delta t(t_{T>400°C}$-$t_{T>500°C}$, s	23	26

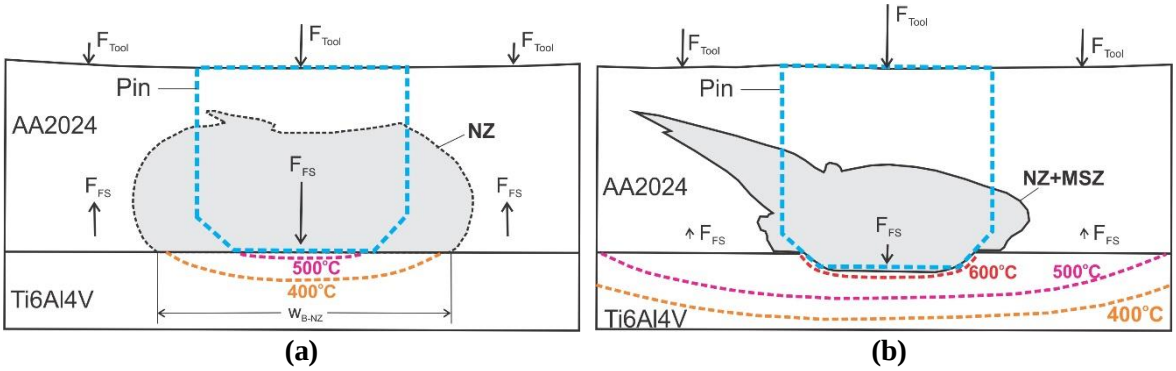

Figure 3-10 Schematic illustration of possible isotherms surrounding the pin (bottom) in the Ti6Al4V side and forces due to stir flow and friction stir tool for (a) $d_P \approx 0$ and (b) $d_P > 0$.

Although a more precise determination is not possible, data in Table 3-2 can provide useful estimated values. For $d_P \approx 0$, 23s means a forward distance 7.6 mm (= 23s × 20 mm / 60s) that the tool has travelled during FSLW. This is comparable to the width of the nugget zone bottom. Thus, considering sideway in the cross section normal to welding (forward) direction, 400-500 °C at interface region under the pin should be confined approximately within the width of the bottom NZ, as suggested by the isotherms in Figure 3-10a. For $d_P > 0$, 67s means a forward distance of 22 mm and 93s a forward distance 31 mm. Thus, even recognising that the width of the isotherm in direction normal to the welding direction should be smaller than that in welding direction, it is expected that outside of the pin bottom part, 6 -7 mm of the interface on both sides were at > 500 °C and further (3-4 mm) outside on both side at 400-500 °C. This is schematically illustrated in Figure 3-10b. However, after a number of seconds, as the pin have moved forward, the widths of the isotherms outside the pin should decrease.

For diffusion welding, not only the interface temperature is a determining factor, contact condition is also one. Compression stress at the interface clearly provides a favourable contact condition. For this, the force normal to the interface during FSLW needs to be considered. The force cannot be measured, but in Figure 3-10, two contributing sources have been schematically illustrated, based on friction stir principle. The first was the force due to stir flow. The downward flow (of AA2024) adjacent to the pin driven an upward flow next thus forming NZ, with the downward flow causing a force acting onto Ti6Al4V, indicated as F_{FS} in Figure 3-10, which resulted in

AA2024/Ti6Al4V interface under compression. Compression due to F_{FS} was however only within the area under NZ for $d_P = 0$ and MSZ for $d_P > 0$ thus the width ($W_{B\text{-}NZ}$ in Figure 3-10a, not given in Figure 3-10b for clarity of the drawing) is the width of NZ or MSZ bottom. The upward flow in the outer NZ drove the flow outside NZ, meaning in TMAZ, upward. Thus, beyond $w_{B\text{-}NZ}$, there was a smaller upward F_{FS}. The second source was the force (F_{Sh} in Figure 3-10) due to the tilted shoulder forging forward having a downforce component. This force should be the highest within $W_{B\text{-}NZ}$, decreasing as the distance increasing outward.

The force/stress distributions cannot be obtained but the reasoning above, as illustrated in Figure 3-10, can suggest whether the interface contact condition in a location was favourable or not for diffusion welding. For $d_P = 0$ and for location within $W_{B\text{-}NZ}$, F_{Sh} was downward and high and F_{Sh} was high, providing the best contact condition. For $d_P = 0$ and for location outside $w_{B\text{-}NZ}$, F_{Sh} was upward and F_{Sh} was low, providing a poor contact condition. For $d_P > 0$, MSZ has affected stir flow as reflected by the significantly smaller NZ, only comparable to the size of the pin. There was little (plastic) flow of Ti6Al4V due to the temperature was far below the solidus temperature of the alloy. This little stir flow inside NZ and MSZ means very low F_{FS} outside $W_{B\text{-}NZ}$. Thus, for $d_P > 0$ and for location outside $W_{B\text{-}MSZ}$, F_{Sh} should be very low but F_{Sh} should not be low, providing a downward force from AA2024 acting on the interface and thus providing a favourable contact condition.

Thus, there were four thermal and contact conditions for diffusion welding of AA2024 to Ti6Al4V, depending on the pin penetration condition, as summarised in Table 3.3. For $d_P \approx 0$, the interface within $W_{B\text{-}NZ}$ was 400 - 500 °C for probably a number of seconds and the combined (F_{FS}+F_{Sh}) force was very strong and acted downward to the interface. Thus, within $w_{B\text{-}NZ}$, AA2024 to Ti6Al4V has been completely diffusion welded, as has been shown in 3.3. Outside $W_{B\text{-}NZ}$, the combined (F_{FS}+F_{Sh}) force should be a weak one upward meaning no compression force at interface. Thus, there was little diffusion welding as has also been shown in 3.3. For $d_P > 0$, within $W_{B\text{-}MSZ}$, high temperatures and the region being sufficiently under compression resulted in excessive Al to Ti reaction and intermetallic growth forming a brittle MSZ. Outside, the interface reached 500-600°C for a number of seconds and experienced a net combined F_{FS}+F_{Sh} forcing down onto the interface. This was a favourable condition and thus sufficient AA2024 to Ti6Al4V diffusion welding forming a thin interface intermetallic layer has taken place, as has been demonstrated in section 3.3.

Table 3-3 Summary of contact force indications and temperatures at interface (within the distance covered by the shoulder size).

	$d_P = 0$		$d_P > 0$	
	Within $W_{B\text{-}NZ}$	Outside $W_{B\text{-}NZ}$	Within $W_{B\text{-}MSZ}$	Outside $W_{B\text{-}MSZ}$
F_{FS}	Strong ↓	Moderate ↑	Weak ↓	Weak- ↑
F_{Sh}	Moderate ↓	Weak ↓	Moderate+ ↓	Weak+ ↓
F_{FS}+F_{Sh}	Strong+ ↓	Weak ↑	Moderate+ ↓	Weak ↓
Temperature	400-500 °C	< 400 °C	600 °C	500-600 °C

Note: ↓ and ↑ indicates downward and upward force, respectively,

+ and - indicates slightly stronger and slightly weaker, respectively.

3.5 Further Examination of Fracture Surfaces and the Intermetallic Layer

How the diffusion welds of FSLW AA2024 to Ti6Al4V as described above have fractured during fatigue loading is now further examined. Figure 3-11a and Figure 3-11b show a fractured couple (Ti6Al4V side on the left and AA2024 side on the right) of a NP sample (sample "i" with the data point marked "i" in Figure 3-1) and a fractured couple of full P sample (sample "ii" with data point marked "ii" in Figure 3-1), respectively. In the NP sample (Fig. 3-11a), on the right, a large crack is clear corresponding to the cracks in NP samples in Figure 3-3b and Figure 3-3c. In the P sample (Fig. 3-11b), rough fracture surface in the fractured weld interface region can be inferred, corresponding to P samples in Figure 3-3d and Figure 3-3e. Note that, in Figure 3-1, data points for P samples are marked next to each data point with the percentage of P. This percentage has been estimated by gridding the photos of samples and counting the grids of P area. Detailed examination of the fracture surfaces, as will be presented below, has revealed the features of fracturing in the two samples having similar cycle numbers (~1.6×10^5, as shown in Figure 3-1) in the high cycle region and under similar and low cyclic loading condition (40 MPa) during fatigue testing.

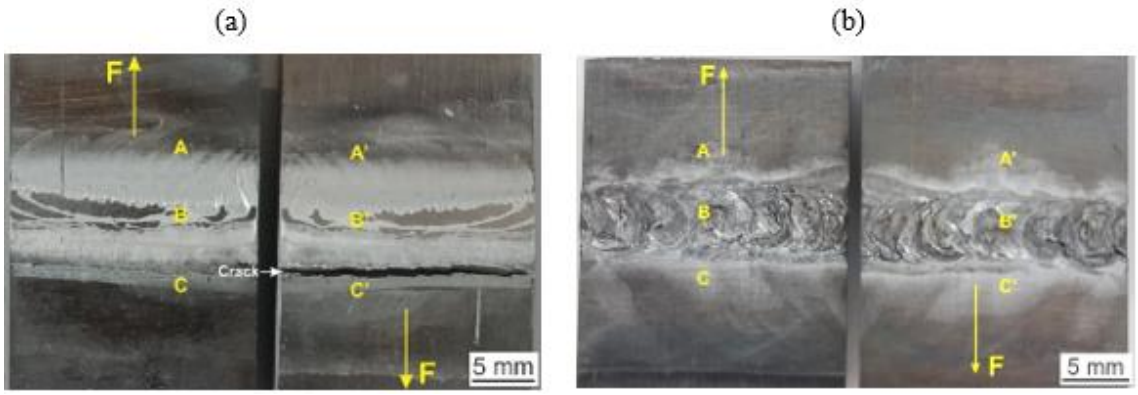

Figure 3-11 Photos of tested samples showing (a) a non-penetration weld marked "i" and (b) penetration marked "ii" in Fig.3-1. In each weld couple, the left is Ti6Al4V and the right is AA2024. Locations indicated A, B, C, A', B' and C' are where SEM images were taken. Arrows in yellow with F indicate force direction during testing. A while arrow points to a crack in AA2024.

Figure 3-12 displays SEM images for sample "i" (NP). The images were taken from locations indicated as A, B, C on the Ti6Al4V side and A', B', C' on AA2024 side, respectively, in Figure 3-11a. By comparing the SEM images in Figure 3-12a and Figure 3-12c to that of parent metal, the rolling and wire brushing marks on Ti6Al4V plate surface before FSLW have been obscured by the welded AA2024. This is consistent with the appearance indicating shear and tear fracture of AA2024 material on the Ti6Al4V (left) site matching the AA2024 site (right) in Figure 3-12a and Figure 3-12c. Thus, there must be a weld in these locations and fracturing has occurred with the crack having propagated through AA2024 but parallel and next to the interface, similar to that shown also in Figure 3-5e or Figure 3-5f. This means that the actual width of the weld ($W_{Lap\text{-}a}$) is larger than the width equivalent to the pin outside diameter ($W_{Lap\text{-}p}$). This is consistent with the observations on the Ti6Al4V/AA2024 interface region in Figure 3-5 to Figure 3-8 that, as has been explained, the diffusion welded width is larger than the pin diameter.

In the mid location of the NP sample (sample "i"), as shown in Figure 3-12b, about half of the area (of the image) shows the fatigue fracture being in a highly ductile mode with a dimple appearance and the other half displaying little deformation before fracture. The ductile area must have resulted from AA2024 ductile fracture, consistent with what has been observed in the cross section of the test interrupted sample shown in Figure 3-5e. The nature of fatigue fraction in the non-ductile area in Figure 3-12b cannot however be inferred in the image which is not sufficiently high in magnification. The non-ductile area is not very local and it represents a significant portion of the interface in the mid location of the NP sample. As shown in Figure 3-11a-left, in the mid location (location B and horizontally along), the brighter region represents AA2024 welded material thus fracture having occurred in AA2024 near the weld interface but then the dull area has basically not covered by AA2024 material. The images of Figure 3-12 cannot show what may have caused the non-ductile appearance although immediately under the pin during FSLW in NP condition a welded interface forming a thin intermetallic layer should be expected.

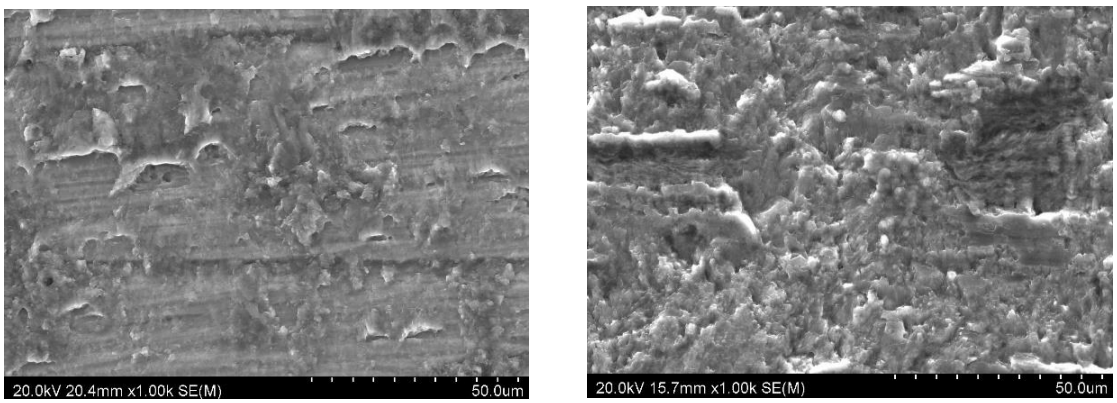

(a)

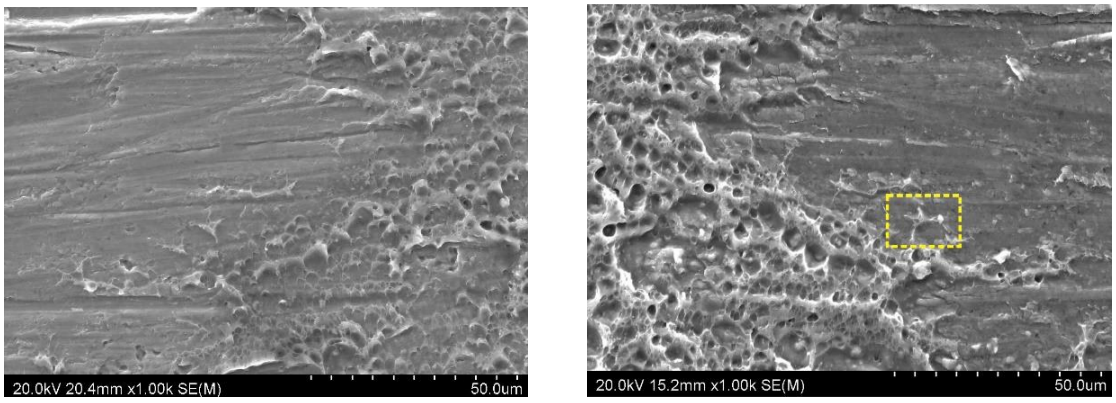

(b)

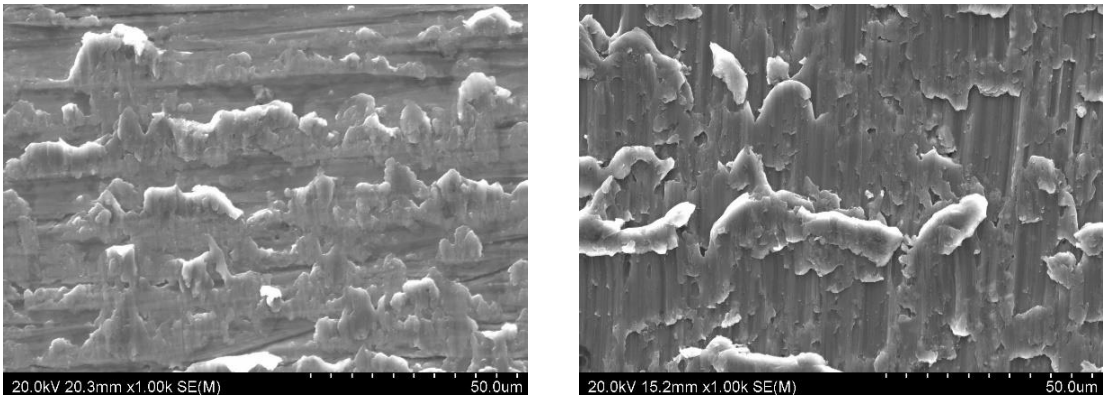

(c)

Figure 3-12 SEM fractographs taken in a non-penetrated tested sample, sample "i", (a), (b) and (c) left image and right image taken in locations A and A', B and B', and C and C' in Figure 3-11a, respectively. In the right image of (b), a small area has been outlined where a high magnification image has been taken, as will be shown.

A high magnification image in the area outlined in Figure 3-12b, on the right was taken and shown in Figure 3-13. The image includes ductile-dimple areas and the rest is rather smooth (deformation-free) with many cracks. EDS analysis has been carried out and two typical and representative spectra, one for the dimple area and the other for the smooth surface are also provided in Figure 3-13. Clearly, as shown in the spectrum for the dimple area, basically it is Al. This is the result of ductile fracture inside AA2024 away from the interface. In the other spectrum

that is for the smooth surface portion, a small Ti peak is also present. Thus, it can be suggested that the top smooth surface is a Ti-Al intermetallic thin layer and is the result of fracturing either inside the intermetallic layer of the weld interface or the interface between the intermetallic layer and Ti6Al4V. As shown in Figure 3-13, many cracks have formed during fatigue shear loading of the intermetallic layer although the main fracturing is along the lapping interface.

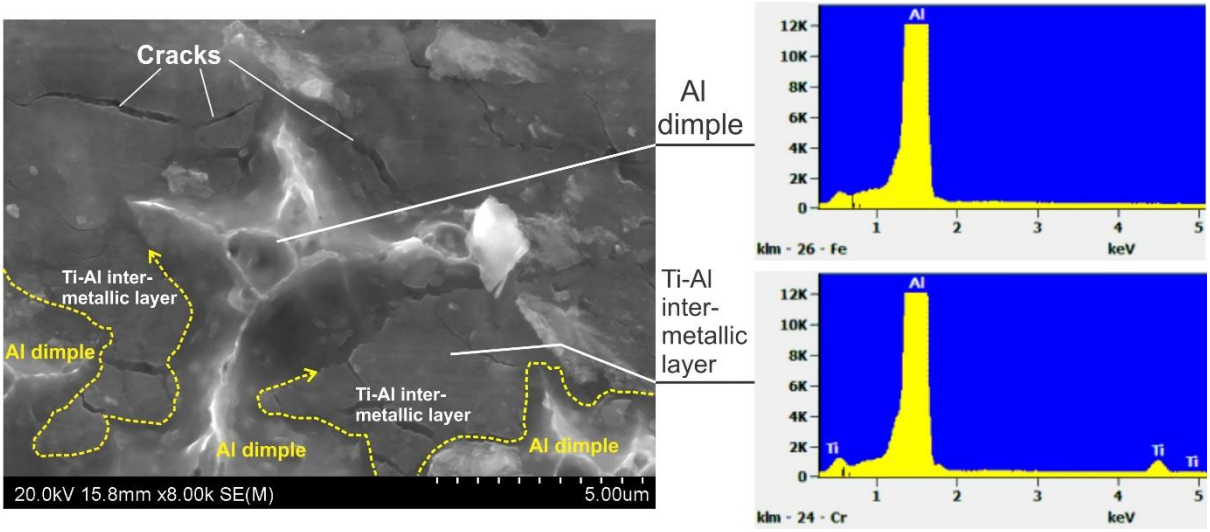

Figure 3-13 High magnification SEM fractography taken in the small area outlined in Fig. 12b-right showing ductile dimples and non-ductile smooth surface with cracks, together with two EDS spectra each analyzed in the spot as pointed to, one in a fracture dimple and the other in the smooth fracture surface spot. In the lower part of the SEM image, the boundaries of Al dimple areas and the smooth surface area have been traced and indicated.

In Figure 3-14, SEM images for sample "ii" (P) are shown and the images were taken from locations indicated as A, B, C on the Ti6Al4V side and A', B', C' on the AA2024 side, respectively, in Figure 3-11b. Features in Figure 3-14a and Figure 3-14c are similar to those shown in Figure 3-12a and Figure 3-12c and, as has already been explained, they are largely shear and tear fracturing inside AA2024 in locations outside the pin penetrated width. On the other hand, in the mid of the P sample (sample "ii") which is the MSZ, brittle fracture is dominant (Figure 3-14b). Despite of the brittle MSZ, as has already been demonstrated and explained (in the previous two sections), the wide diffusion weld area outside the pin bottom penetration and brittle MSZ area have supported the cyclic loading and have resulted in the high cycle life of the weld.

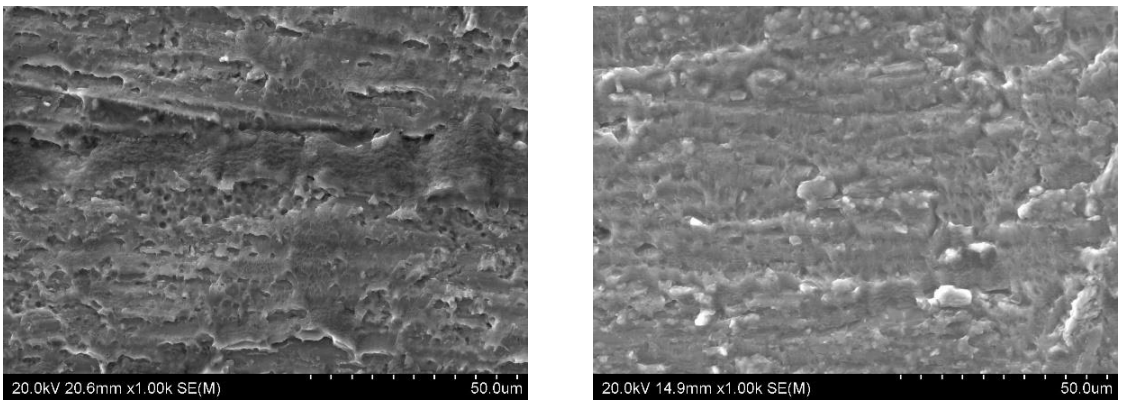

(a)

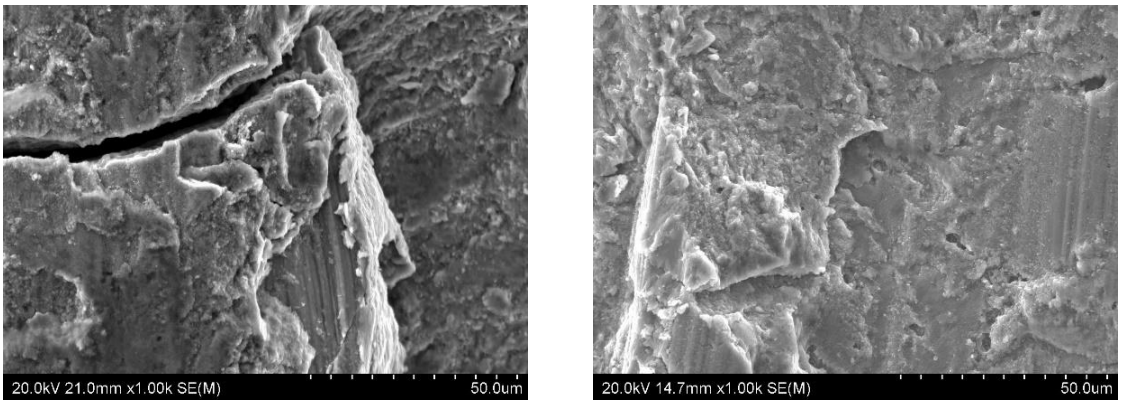

(b)

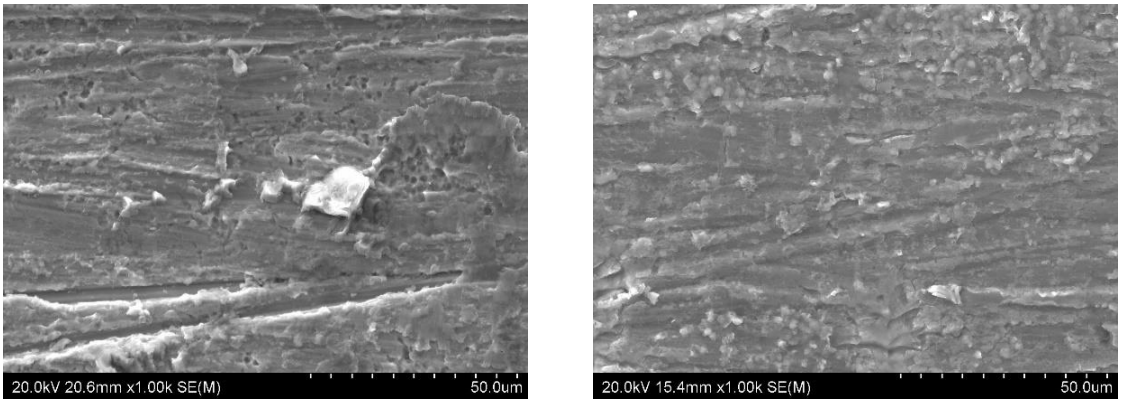

(c)

Figure 3-14 SEM fractographs taken in a penetrated tested sample, sample "ii", (a), (b) and (c) left image and right image was taken in locations A and A', B and B', and C and C' in Figure 3-11b, respectively.

3.6 Summary

Fatigue limit of AA2024/Ti6Al4V welds made using friction stir lap welding (FSLW) of 20 mm wide samples and tested with R = 0.1 have been found to be $F_{Max} \approx 3.5$ kN for fracture path propagating along the AA2024/Ti6Al4V interface region. This loading can be regarded equivalent to the high cycle fatigue loading to shear fracture a thick (> 5 mm) AA2024/AA2024

lap weld made using. Thus, AA2024/Ti6Al4V welds made using FSLW can be considered as high fatigue performing welds, resulting from the diffusion welding under the thermomechanical condition during FSLW. The strong AA2024/Ti6Al4V welded interface region has resulted in either fracturing inside AA2024 next to the interface or fracturing along with the thin interface intermetallic layer. The FSLW condition used has resulted in the diffusion welded width greater than the pin diameter, contributing to the good fatigue performance of the welds. Significantly higher peak temperatures have been detected and a higher downforce has likely acted at the interface during FSLW with the pin having slightly penetrated to the bottom plate, comparing to no pin penetration. This thermomechanical condition has resulted in a significantly larger diffusion weld width outside the pin bottom in pin penetration welds. Thus, despite having a brittle mix stir zone of Ti/Al and intermetallics, the fatigue strength of the pin penetration welds is comparable to the fatigue strength of non-penetration welds.

4. EFFECT OF INCREASING TOOL SIZE ON FATIGUE STRENGTH OF WELDS

The second part of this thesis research addresses the question of how increasing tool pin diameter may affect the weld area which in turn may affect the fatigue limit. A large pin diameter may increase the weld width and thus should be expected to increase the weld strength but the pin diameter effect even for static strength of Al to Cu, Al to steel, and Al to Ti have not been well studied. Thus, in this study, fatigue properties of AA2024 toTi6Al4V welds made by FSLW using a larger diameter tool pin has been determined and compared with the fatigue performance of welds made using the normal diameter tool pin. The comparison is aided by the use of stress concentration values predicted by simulation. The detailed results of experiments, analysis, simulation and discussions are presented in this chapter.

4.1 Fatigue Data

In last chapter (Chapter 3.1), fatigue data have been presented by plotting remote applied stress and maximum load against the cycle numbers of the weld samples. This plotting of fatigue data has been followed in this chapter for welds made using the larger pin and is presented in Figure 4-1. Each type data with their respective symbol which represent each type of fracture path. Further to fracture path 1 and path 2 as in normal pin samples, using the larger pin, a new fracture path meaning fracturing in the Ti6Al4V has been observed for two samples. The detail of this fracture path 3 will be explained further in the next section. From the data plotted in Fig. 4-1, the different fracture paths do not appear to have affected significantly the fatigue life from low cycle fatigue to high cycle fatigue.

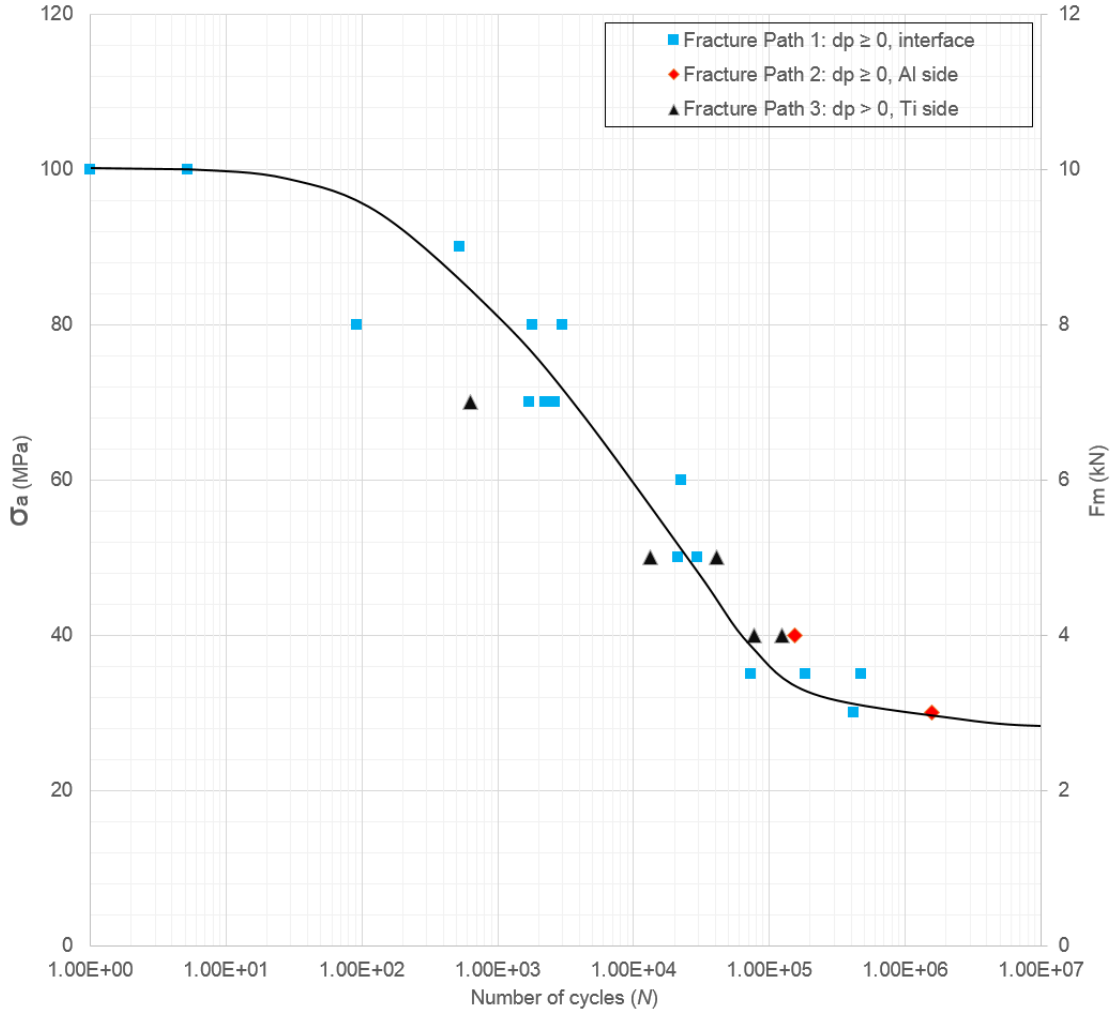

Figure 4-1 Maximum fracture load F_m (kN) and stress stress amplitude σ_a (MPa) plotted against the number of fatigue cycles in volving three fracture paths: Path 1; fracture at the interface ($d_p \geq 0$; Path 2, fracture on the AA2024 side ($d_p \geq 0$) and path 3 ($d_p > 0$), fracture on the Ti6Al4V side.

Note in Fig. 4-1 for the large pin samples, different from Fig. 3-1 for the normal pin samples, there is only $d_p > 0$ condition. This means all test samples were sectioned from welds made with pin having penetrated the bottom Ti6Al4V plate. The reason for this was the use of pin length of the larger pins same as the pin length of the normal pin. However, being a large diameter pin and using the same tilt angle for all the sample during FSLW operation, the pin length was in fact slightly larger and hence chances of a slight penetration is also high. For the welds made using the larger size pin, a slight pin penetration ($d_p > 0$) had resulted despite of having the same pin length as the normal pin. Thus, comparison to normal pin would be more suitably made only for samples with ($d_p > 0$). However, as has been well presented in the last chapter, the slight pin penetration has not resulted in a strong effect on fatigue properties, although the weld structures are different.

Fig. 4-2 presents all the fatigue test data for test samples of welds made using the normal size pin and larger size pin. The pin penetration conditions, already described and explained in Fig. 3-1 and Figure 4-1, have not specified in this figure (Fig. 4-2) for the purpose of comparison of fatigue properties using the different pin sizes. It is clear that in the low fatigue cycle range, fatigue strength values do not appear to differ. A closer viewing of data may suggest a slightly lower fatigue limit of welds made using the larger size pin (at ~ 3.0 kN), compared to the fatigue limit of ~ 3.5 kN for welds made using the normal size pin. It should be noted that, as has been explained in Chapter 2 (Experimental Procedures), the larger pin FSLW series differ from series 1 using the normal pin not only on pin size but also on rotational speed. The use of 1400 rpm had caused a tunnel defect and thus 1000 rpm was used. This may have cuased a different diffusion weld width as temperatures in weld region using a low rotational speed may result in a lower weld region temperature and thus less diffusional weld width. This will be explored later in this chapter when cross-sectional microstructure is examined and described.

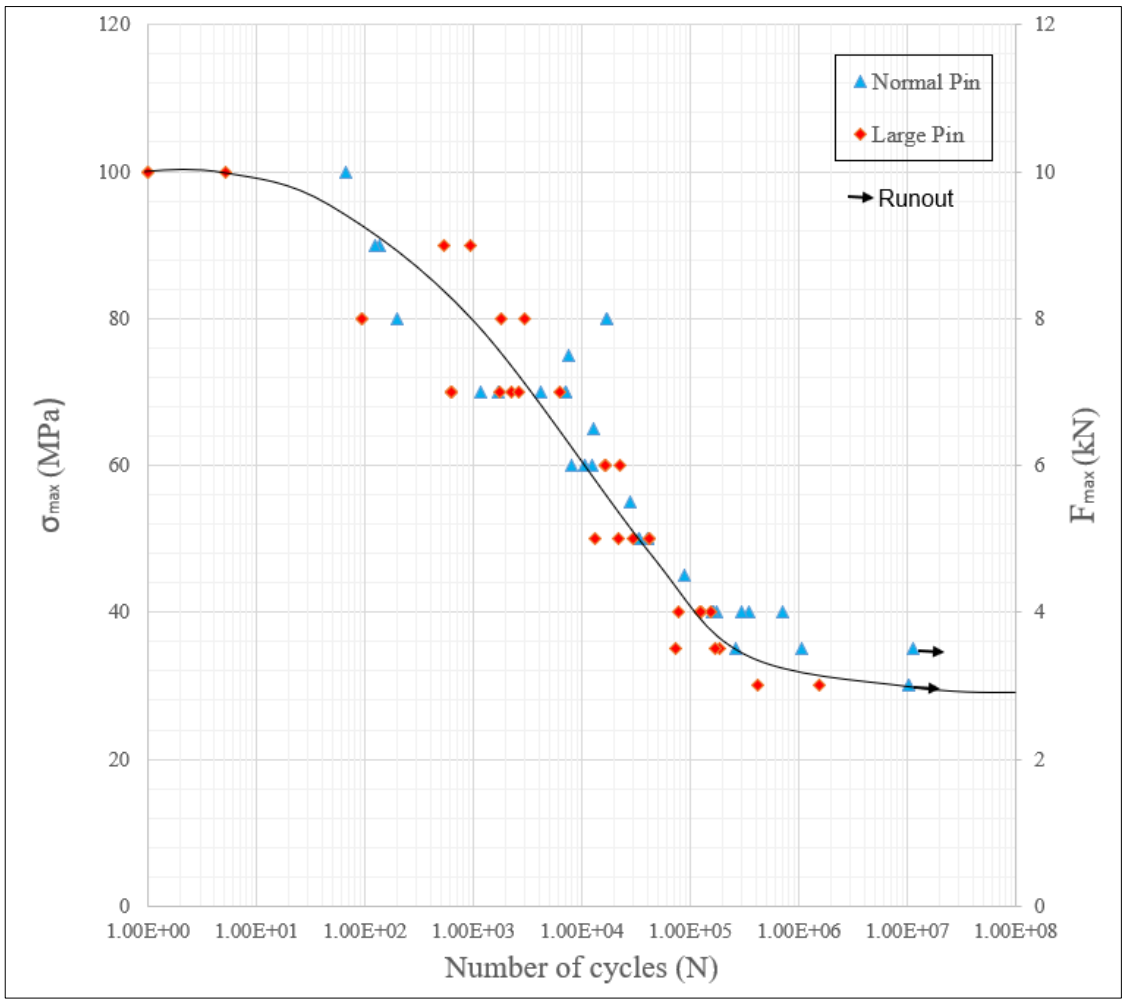

Figure 4-2 Comparisons of S-N data of normal against the larger pin expressed in both stress and applied load against cycle numbers (*N*).

4.2 Fracture Path 3

In this section, the effects of tool size on fatigue fracture and the stress distribution have been briefly discussed with the prior knowledge with the current literature [47-58], in which most of their work was devoted to improving the strength of the FSL welds. However, there are still areas to explore on the nature of fracture of welds with fatigue testing. A significant part of this section is to understand how a fracture initiates at various critical locations of the weld particularly on the bottom plate (TiAl64V) due to thinning effect.

A common type of fracture for a FSL weld of dissimilar AA2024/Ti6Al4V joint failing at the interface has been denoted as fracture path 1 in this study. It has shown that, the depth of penetration can be either a bit more or equal to zero ($d_P \geq 0$). The second type of fracture has been the fracture occurring at the Al side and herein described as fracture path 2. This type of fracture has been found to have resulted from material thinning at the top plate (Al side) or high fatigue resistance at the weld interface causing this type of failure. The third type of fracture has been the fracture on TiAl64V side and known as fracture path 3. The fracture on the Ti side has been mainly due to material thinning resulting in high-stress concentration at the location leading to failure on the bottom plate. It can be observed (see Figure 4-1) that fracture path 2 (Al side) is more fatigue resistant, however, when looking at fracture path 1 and fracture path 3, they are quite close to each other.

Fracture path 3 in Figure 4-3 has been only experienced with the use of a larger size pin but not with the normal pin. Figure 4-3 schematically illustrates fracture Path 3 which only eventuated with the use of a larger pin. With the use of a normal pin, a fracture may occur either at the weld interface or on the Al side because Ti has high stiffness and cannot easily fracture. However, with the use of the larger pin, fracture occurred on the Ti side which has been mostly due to material thinning proportional to the size of the tool while there has not been any change in the specimen width leading to an increase in stress concentration on the bottom (Ti) plate resulting in the fracture. Also, Figure 4-3 represents the FSL weld signifying both penetrated (a+b) in the bottom plate and non-penetrated (b) under their respective imaginary areas to better understand and demonstrate the three common fracture routes. Fracture path 1 is the fracture at the interface, path 2 is the fracture of the top plate (AA2024-T6) which has been already discussed (Chapter 3) and path 3 is the main theme of this section and is the fracture of the bottom (TiAl64V) plate. Fracture direction in each fracture path was determined by the nature of the weld sample produced where the crack could initiate at any of the critical locations at the weld region. The left side of AA2024 and the right side of TiAl64V are the respective loading ends of the tested samples. In all the samples tested, the top plate in each sample is AA2024 and the bottom plate is TiAl64V. A weld sample of the plate fractured on the Ti side is shown in Figure 4-4a as top view and Figure 4-4b as side view in which the fracture occurred right at the centre of the weld.

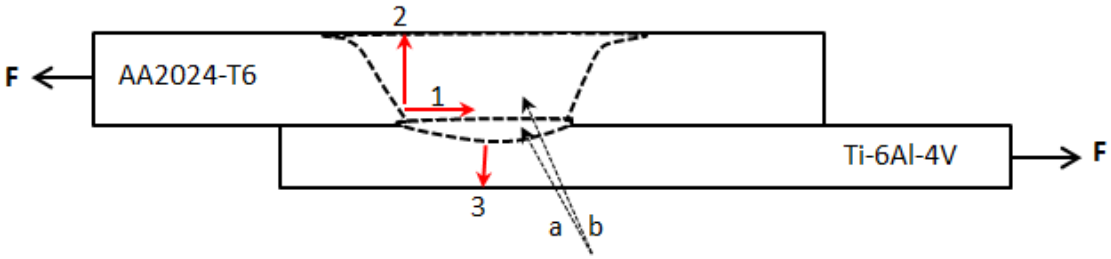

Figure 4-3 Schematic illustration of fracture paths during fatigue loading: (a) penetrated (d_P >0) weld area and (b) non-penetrated ($d_P \approx 0$)

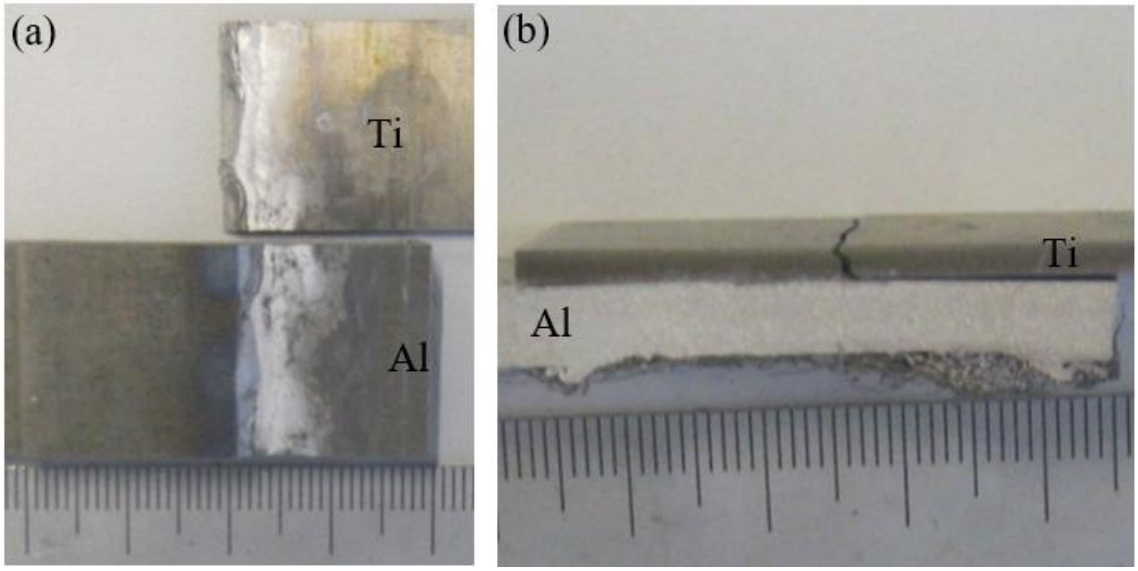

Figure 4-4 Actual photograph of a FSLW fatigue tested sample failed with fracture path 3: (a) top view and labelled, (b) side view with fractured TiAl64V plate on top with a centre fracture.

Figure 4-5 (a) is a sample fractured at the interface with fracture path 1, with a very little top plate flash. However, Figure 4-5b is fracture at the interface with fracture path1 and also crack propagated to the top plate at the edge of the pin on the loading end with a bit more material flash. Also, Figure 4-5c has more material flash on the top plate but with a complete fracture of the top plate with fracture path 2. Figure 4-5d has been found to have more material flash and also quite significantly penetrated to the bottom plate resulted in the fracture on the bottom plate (TiAl64V) ending up with fracture path 3. The fatigue fracture of weld samples that failed at the TiAl64V side has been observed to be affected mainly due to the amount of pin penetration ($d_P >> 0$) onto the bottom plate. It was also observed that with small amount of weld flash and more depth of pin penetration onto the lower lapping plate (TiAl64V) predominantly would trigger the lower plate to fracture. The bottom plate thinning could be avoided by careful downforce tool control for lesser penetration ($d_P \approx 0$) and also avoiding heavy top plate flash during welding. For instance, the shoulder eating more into the top plate creating more flash (see Figures 4-5b and 4-5c) paving ways for initiating fracture on the Al side.

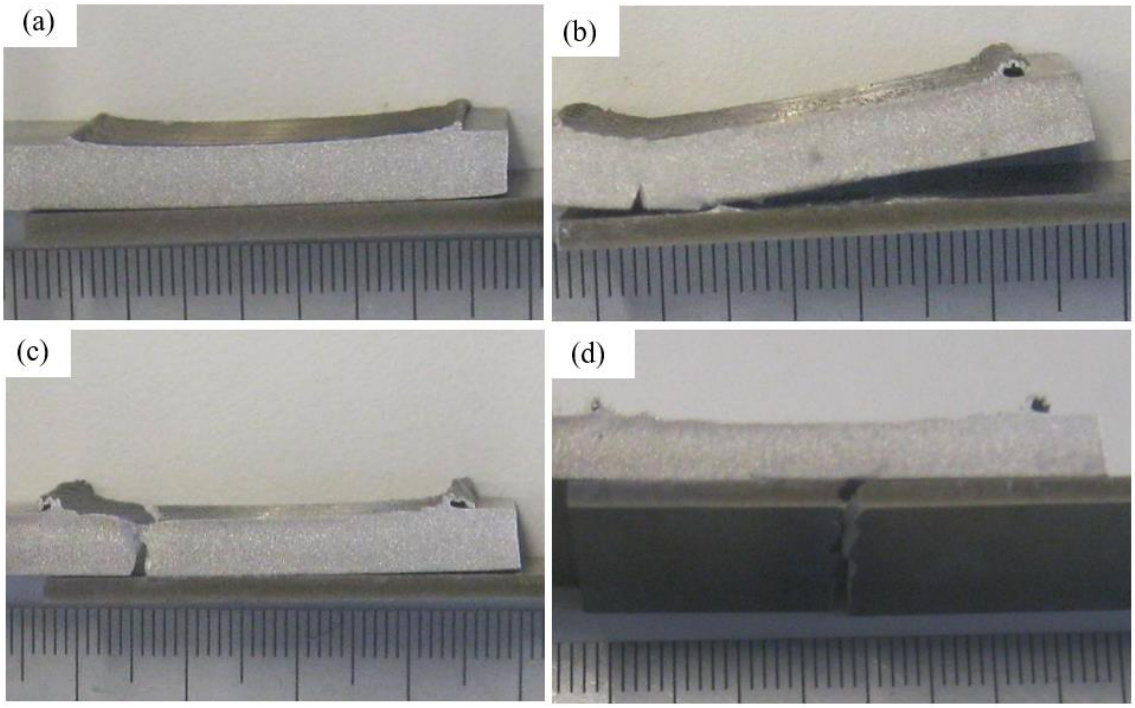

Figure 4-5 Actual photograph images of some selected FSL weld tested samples showing various fractures paths: (a) fracture path 1-fracture at the AA2024/Ti6Al4V interface, (b) fracture path 1 with crack initiated at AA2024 loading end, (c) fracture path 2- fracture in AA2024 at the loading side, (d) fracture path 3-fracture on Ti6Al4V side with fracture in the centre.

In Figure 4-6a, it is apparent that the weld sample has very few flashes on the top plate and it has fractured at the centre of the weld of the bottom plate (TiAl64V). In Figure 4-6b, it is also apparent that the dark patches left on the bottom surface of TiAl64V revealed that the pin had plunged more deeply into the bottom plate resulting in the fracture at the weld centre on the TiAl64V side. When the depth of penetration is zero ($d_P \approx 0$) with more weld flash on the top plate (AA2024) side thinning the plate during welding has resulted in the fracture of the top plate as shown in Figure 4-6c.

To further understand the importance of sample thickness in the fractures, a fracture on AA2024-T6 (topside) fracture is also discussed. As shown in Figure 4-6c that the side view of the weld sample fractured on the AA2024-T6 side of the weld and Figure 4-6d shows the top view of the fractured sample. Thinning of the top plate or more penetration on the lower plate with little weld flashing could result in weld samples fracturing on the parent materials. However, with less or zero penetration ($d_P \approx 0$) which is known to be a good weld [59] that could result in samples fracturing at the interface, giving optimum level of fatigue performance at various load conditions.

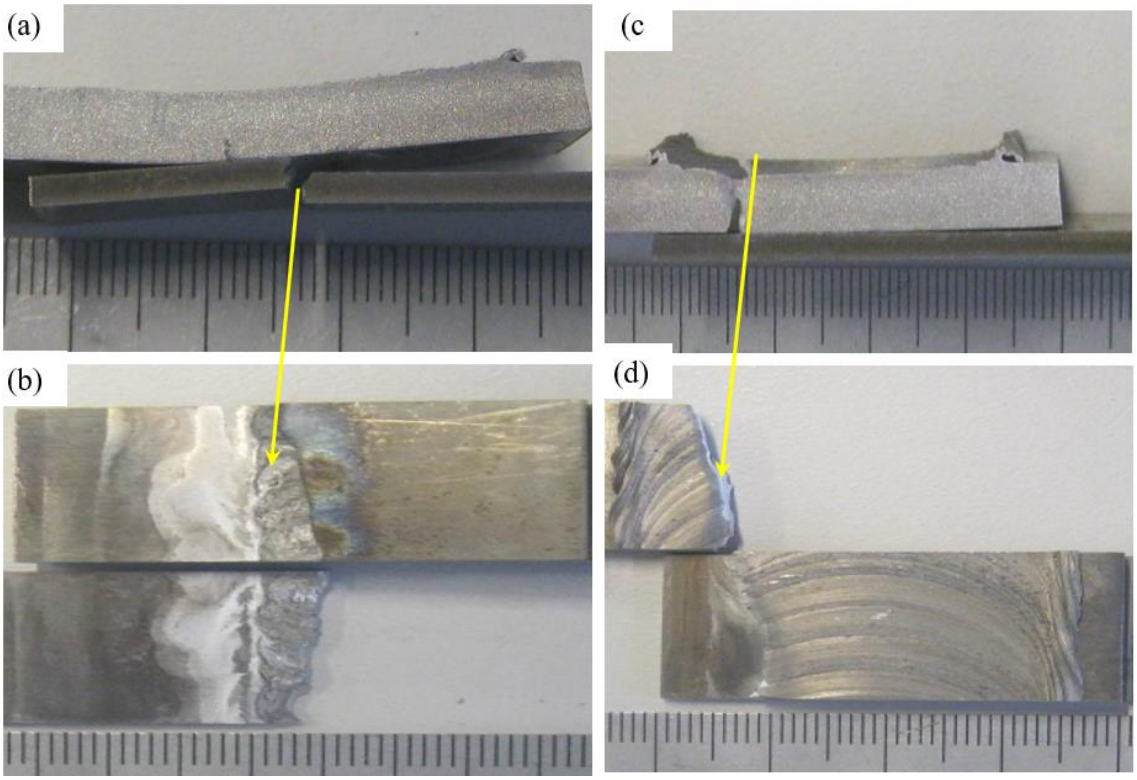

Figure 4-6 Fatigue fractured surfaces: (a) A side view of TiAl64V fractured weld sample, (b) A top view of TiAl64V fractured weld sample, (c) A side view of AA2024 fractured weld sample, (d) A top view of fractured AA2024 weld sample.

Figure 4-7a shows the schematic representation of penetrated "P" ($d_P > 0$) weld sample showing weld features such as mixed stir zone (MSZ), nugget zone (NZ), thermomechanical affected zone (TMAZ), and heat affected zone (HAZ). The effective weld width is the overall weld coverage area by the size of the pin width and the adjacent weld established outside of the pin through diffusion bonding. The size of the tool was found to play an important role in the FSL weld in achieving an optimum level of weld width. However, it can also be noted that an increase in depth of pin penetration ($d_P > 0$) would also reduce weld strength significantly by producing a large amount of MSZ and intermetallic layers which are responsible for the weakening of the weld strength.

For a P sample $W_{j\text{-}P1}$ and $W_{j\text{-}P2}$ (see Figure 4-7a) is the joint width outside the pin width of a weld produced for a 'P' weld sample. The measurement is taken a bit outside the pin width where the HAZ region has also seen to form weld bonds through interdiffusion [84, 85]. For a P weld sample, a mixed stir zone (MSZ) is considered as having a brittle region with low weld strength. Therefore, for a 'P' weld sample overall effective weld width is considered from the two measurements denoted as $W_{j\text{-}P1}$ and $W_{j\text{-}P2}$ as shown in Figure 4-7a. However, for a 'NP' weld sample, the effective weld width is just the weld joint for a non-penetrated ($W_{j\text{-}NP}$) which has sufficient weld approximately equal to pin width as shown in Figure 4-7b. The effective plate thickness is one of the major determining factors for a 'P' weld sample breaking on the Ti side.

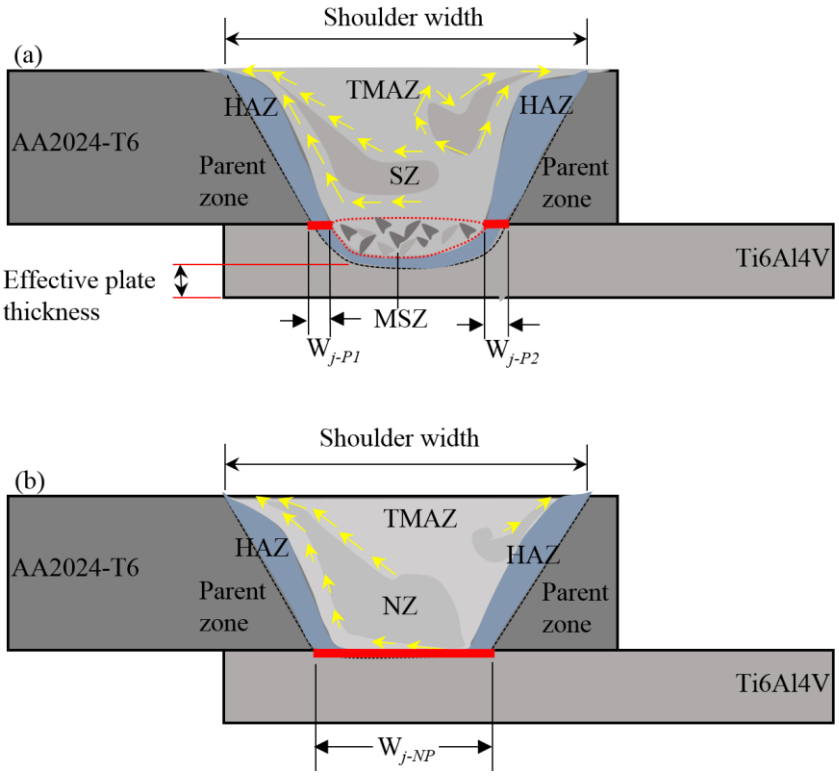

Figure 4-7 Schematic representation of weld distribution during FSL welding: a) penetrated sample with a mixed stir zone, b) non-penetrated sample with nugget zone.

To understand how the weld width has affected the joint strength, by increasing the size of the tool pin, and stress distribution of the welds with varying joint width were simulated. Figure 4-8 shows simulated equivalent stress distribution for the 4 welds varying joint width of 5-25 mm under an applied load of 40 MPa. The 25 mm joint width (green line) is the overall effective weld width which shows less than 200MPa from both ends of the weld. As the joint width reduces 15 mm, the stress level increases which is certainly expected but it shows that the stress level on the RS is higher (> 200 MPa) than AS side (< 200 MPa). The joint width having 8 mm is even further increased its stress concentration above 15 mm joint width. Furthermore, the stress concentration is even higher at 5 mm joint width which is certainly possible.

Besides, it can also be seen from Figure 4-8 that RS side has high stress concentration than on AS side as it is clearly displayed on the stress distribution based on each joint width, where from the weld centre on the left is a bit, more stress concentrated than on the right in each join width. Furthermore, it was observed that stress concentration had increased as the joint width was reduced as it is displayed as high-stress concentration on the centre of the joint width is mainly due to weld width reduction and may also have resulted from pin penetration onto the bottom plate creating brittle intermetallic growths such as thick IMCs and more MSZ.

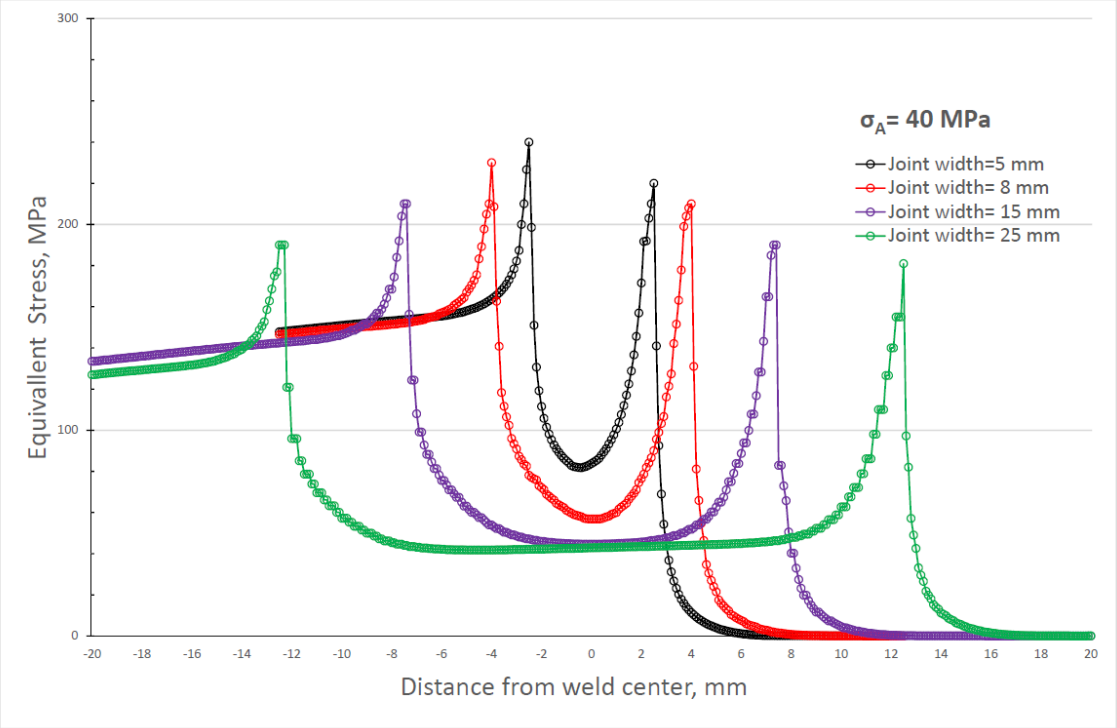

Figure 4-8 Schematic Stress distribution from weld widths of the two ends of a weld: AS on the right and RS on the left. Four different weld joint width at 40 MPa (4 kN).

The stress concentration on the Ti side will be discussed with an emphasis on the effects of material thinning. Figure 4-9a shows the schematic geometry of a weld having a pin penetrated on the Ti part. The depth of pin penetration, d_P = 0.5 mm and 1 mm width-wise (20 mm specimen width). Figure 4-9b shows the simulated effective stress (von misses stress) distribution for the above-mentioned weld under applied stress of 40 MPa (4 kN). The region (red) in Figure 4-9b is the stress concentration during the test with applied stress of only 40MPa (4 kN) indicating significant stress concentration at the bottom of pin penetration zone. Therefore, the high-stress concentration at the thinned region, initiated the fracture to occur at the location as indicated (in red color). This agrees with other tested samples observed during fatigue testing of AA2024 to Ti6Al4V FSL welds (see Fig. 4-5 and Fig. 4-6). However, for a 'NP' weld sample, as shown in Figure 4-9c, the stress level is low at the tip of the pin but because the bottom plate is thinner than the top it shows more stress on the Ti side. However, in actual situation Ti6Al4V is stiff so may not break easily on the bottom plate.

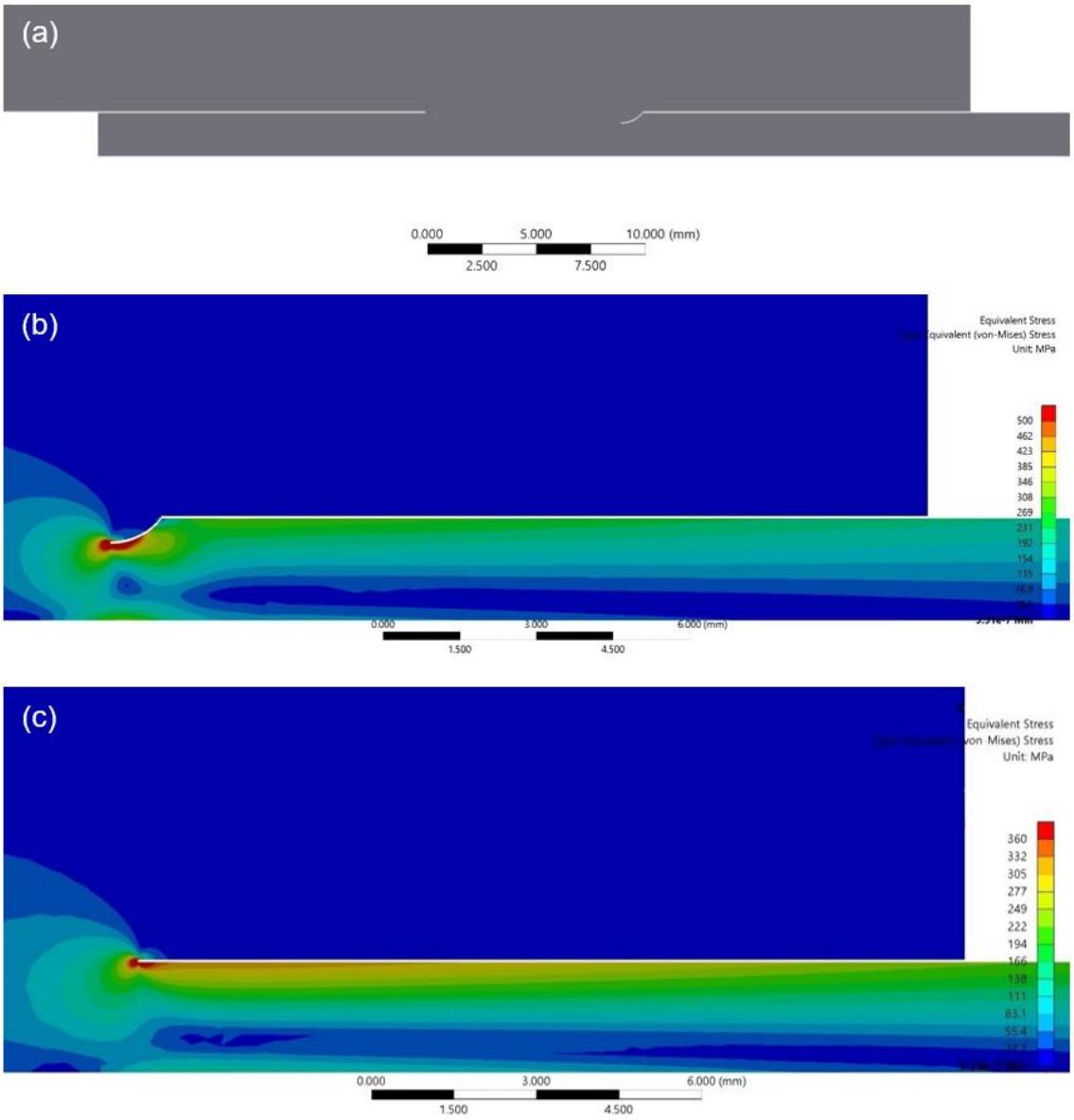

Figure 4-9 Stress distributions in Al-Ti FSL welds: (a) a schematic illustration of Al to Ti FSL weld geometry penetrated on Ti side, (b) Stress on Ti side with 0.5mm penetrated sample, and (c) Stress level on NP sample.

4.3 Detailed Examination of Fracture

4.3.1 Fracture Surface

Figure 4-10 (a-c) shows the fracture surfaces of the welds seen to have more penetration ($d_P > 0$), a little or less penetration ($d_P \geq 0$) while in some areas were non-penetrated ($d_P \leq 0$) but just touching ($d_P \approx 0$). A very narrow penetration at the centre of the pin is shown in Figure 4-10a as indicated by the arrow pointing in the direction of the weld. Some samples have more penetration ($d_P > 0$) while the others have less amount of penetration ($d_P \approx$ 0-0.1 mm) to approximately zero penetration ($d_P \approx 0$). A typical example of a less penetrated ($d_P < 0$) and penetrated ($d_P > 0$) weld sample is shown in Figure 4-10b and Figure 4-10c, respectively, with the most parts being more penetrated except towards the top end of the Al side. About 90 per cent more penetrated ($d_P > 0$) weld samples have a wide area of penetration on the TiAl64V plate as shown in Figure 4-10c.

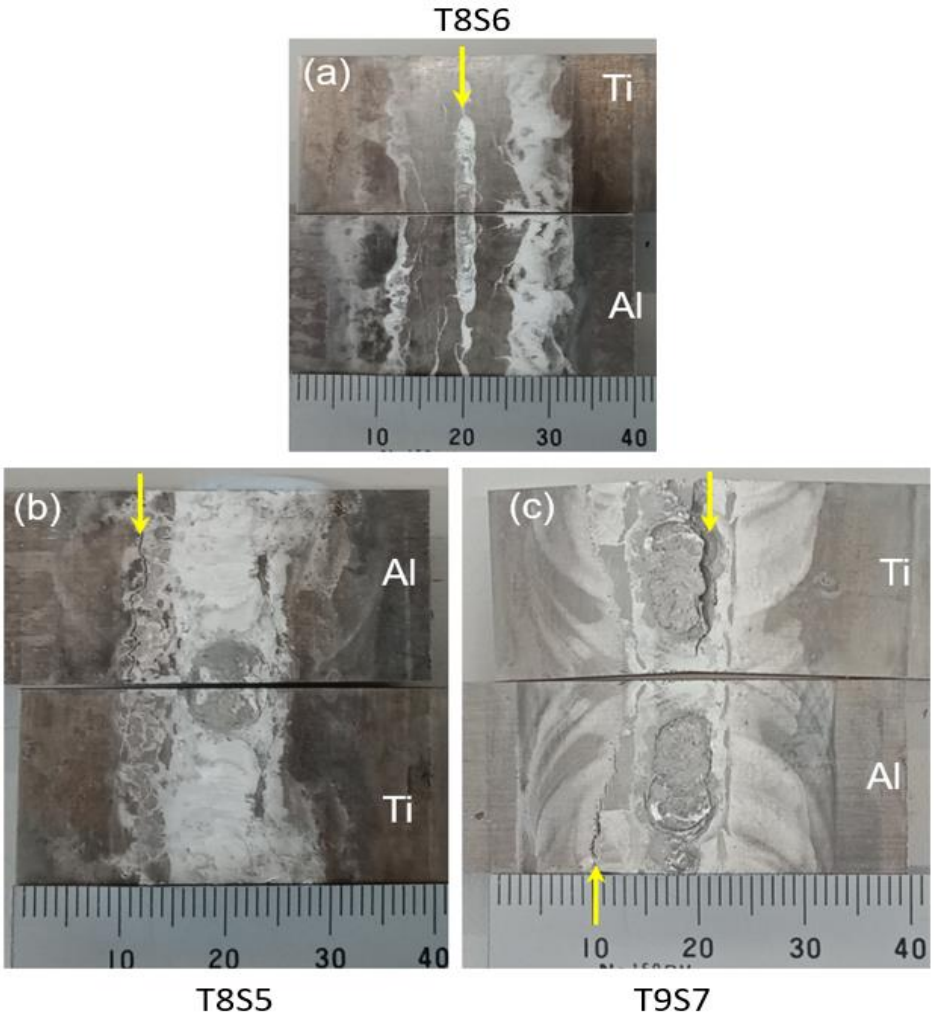

Figure 4-10 Fracture samples: (a) A long narrow penetration, (b) A less penetration with more penetration on one end of the weld sample, (c) More penetration and about 10 per cent non-penetrated at the other end of the weld sample.

The fractured weld samples in Figure 4-10b (T8S5) and Figure 4-10c (T9S7) were again used as representative weld samples to obtain scanning electron microscopy (SEM) micrographs to compare the quality of weld in terms of effective weld width. Figure 4-11a shows fracture surfaces

of a weld sample with AA2024 at the top and Ti6Al4V at the bottom. To further illustrate where two of the selected samples for fracture surface analysis conducted, a schematic illustration is shown in Figure 4-11b indicating the spots where SEM images were taken.

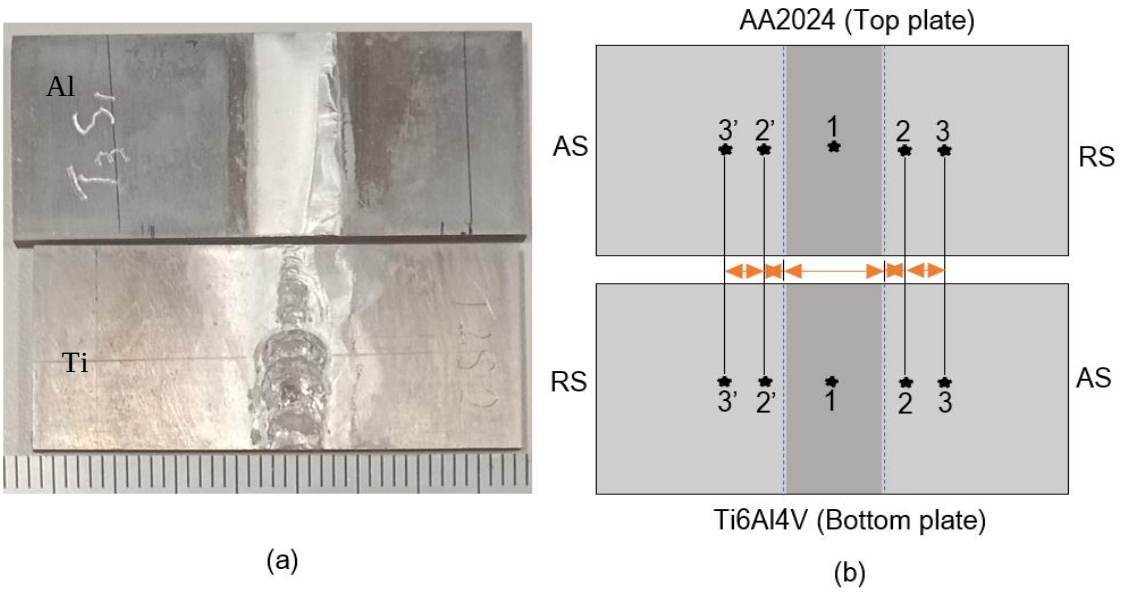

Figure 4-11 Fracture surface measurements: (a) pictorial view of an FSL weld sample displaying top and the bottom plate fracture surface and (b) schematic illustrations of Al and Ti fracture surfaces with locations where SEM images were taken (Locations 1-2 and 1-2' = 5.5 mm, Locations 1-3 and 1-3' = 8 mm).

Figure 4-12 to Figure 4-16 present the SEM images to constructively analyse the weld qualities at different weld spots (illustrated in Figure 4-11b) within the effective weld width on both sides of the weld ends, AS and RS. Also, in Figure 4-12 to Figure 4-16, the letters "a" and "b" in each figure represent the weld samples T8S5 and T9S7, respectively. The SEM images were taken at five different spots both on the Al and Ti sides of the fractured samples of each weld. First point is at the centre of each weld, the second point is at 5.5 mm from the weld centre on both AS and RS sides, and the last point is 8 mm farther away from the weld centre.

Figure 4-12 shows the comparison of the two welds (T8S5 and T9S7) samples for the SEM micrographs taken at the centre of their respective welds. Figure 4-12a (T8S5) clearly shows that there is a tough interface layer present which is exemplified by the ductile nature of the fracture on both sides of the SEM micrograph and there are further small regions in Figure 4-12a (right) that exhibits ductility with dimples on the bottom plate (TiAl64V). However, it is apparent that in Figure 4-12b there appears to show that the fracture surfaces have no sign of plastic deformation with a brittle fracture on both sides of the fracture surfaces. Also, the fracture surfaces of the top (AA2024) and bottom (TiAl64V) plates are different and seem to show lumps of friction-stirred particles on each of the visible base metals. This signifies that there was no effective bonding at the pin penetrated region along the weld line at the weld interface.

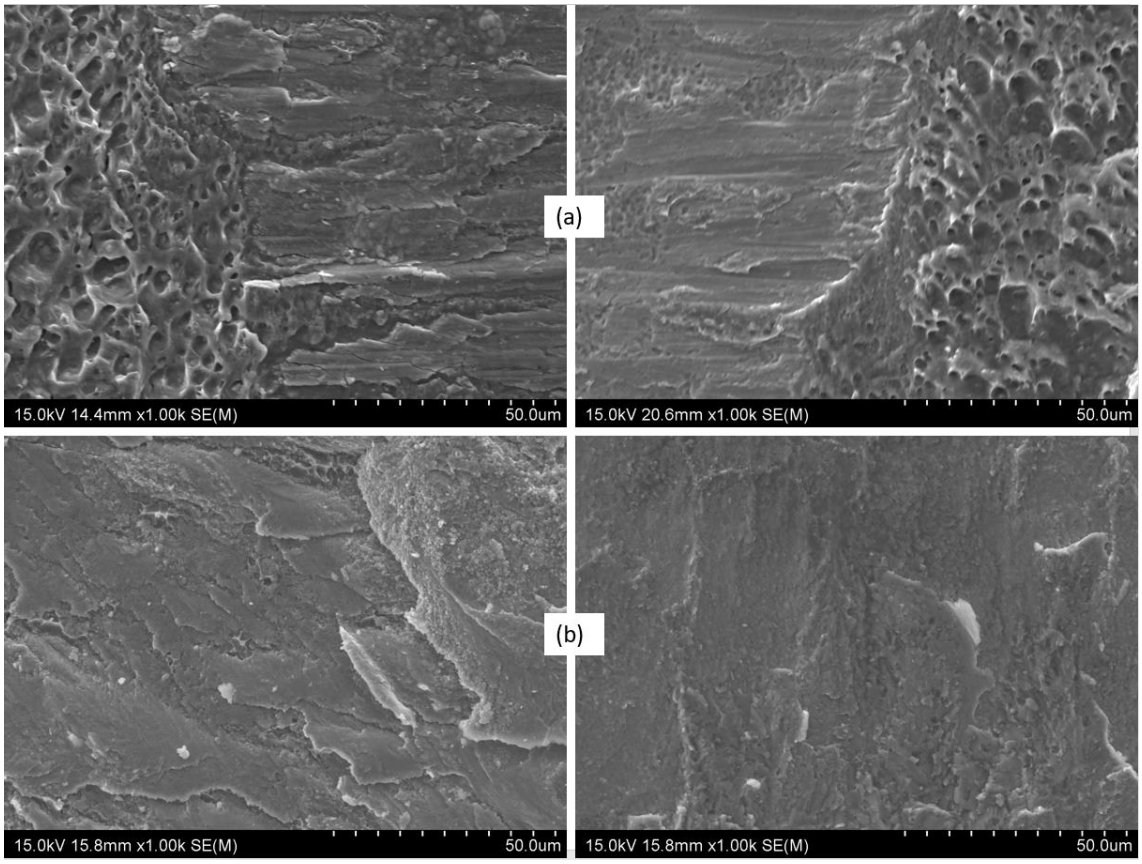

Figure 4-12 SEM images of two different welds at the centre of each weld (location 1 as indicated in Figure 4-11b): (a) T8S5 weld sample with Al on the left and Ti on the right side and (b) T9S7 weld sample with Al (left) and Ti (Right).

Unlike penetrated weld sample (See Figure 4-12b), Figure 4-13 compares SEM micrograph taken outside of the weld centre which is 5.5mm away from the weld centre on the AS side (location 2, 2' in Figure 4-11b). It is apparent that in Figure 4-13a the weld joint has been formed and shown by the dimple ductile fracture images on both sides. It is also obvious that the scratch marks left behind on the bottom plate (TiAl64V) during sanding with an 80-grit paper before welding. Figure 4-13b also shows that the joints have been formed in this region. This is 5.5 mm away from the tool centre. Therefore, in both welds, it is evident that joints can be accomplished during welding on the outside of pin width with a penetrated weld through diffusion bonding as described earlier in this section and in Chapter 3.

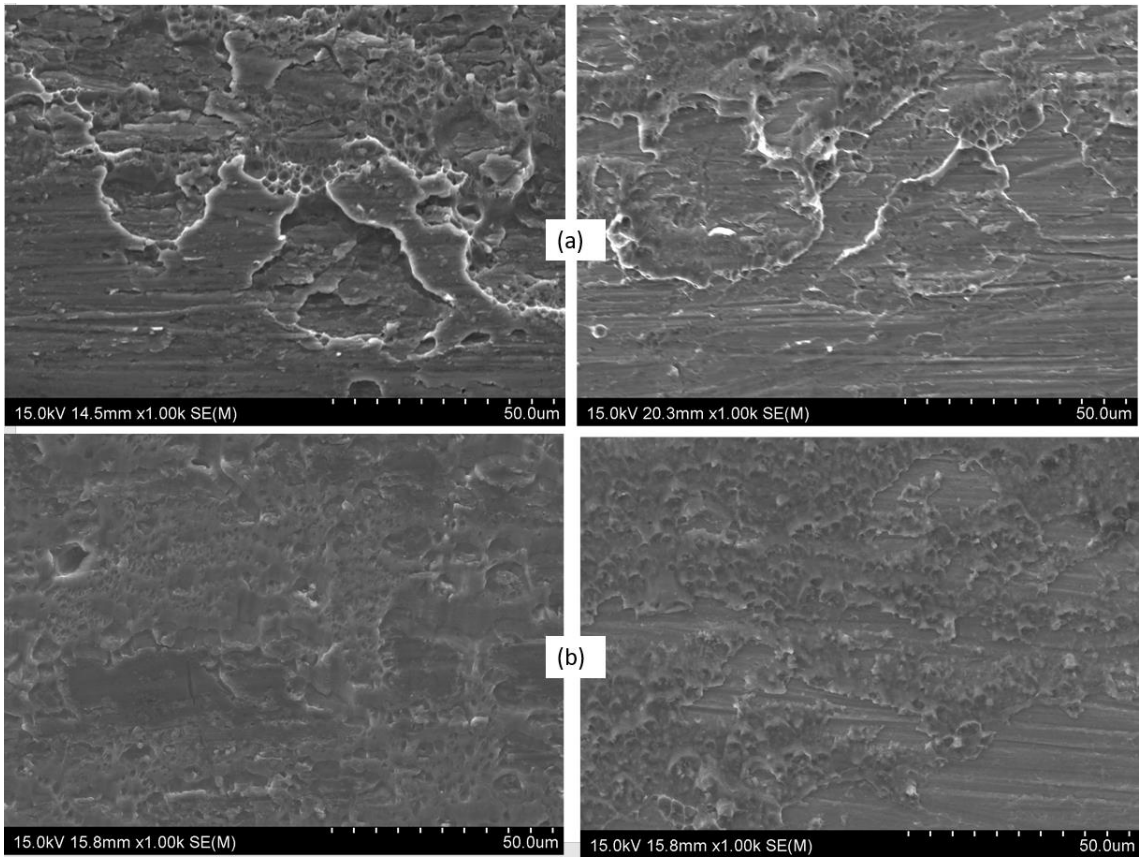

Figure 4-13 SEM images of two different welds at 5.5 mm from the weld centre on the advancing side (location 2 as indicated in Figure 4-11b): (a) T8S5: Al side (left) and Ti side (right), (b) T9S7: Al side (left) and Ti side (right).

Figure 4-14 presents the SEM micrographs taken further away from the weld centre which is about 8 mm from the weld centre. It can be seen that in Figure 4-14a (top-bottom micrographs) a sufficient bonding has been established from the weld sample as it has been revealed by high plastic deformation on both sides of the fracture surfaces. For the second weld sample in Figure 4-14b (top and bottom micrographs) it is also clear that the joints have been formed as revealed (right) with ductile features of fracture surfaces while behind it appears to show strips of lines left behind during sanding of the parent Ti6Al4V alloy.

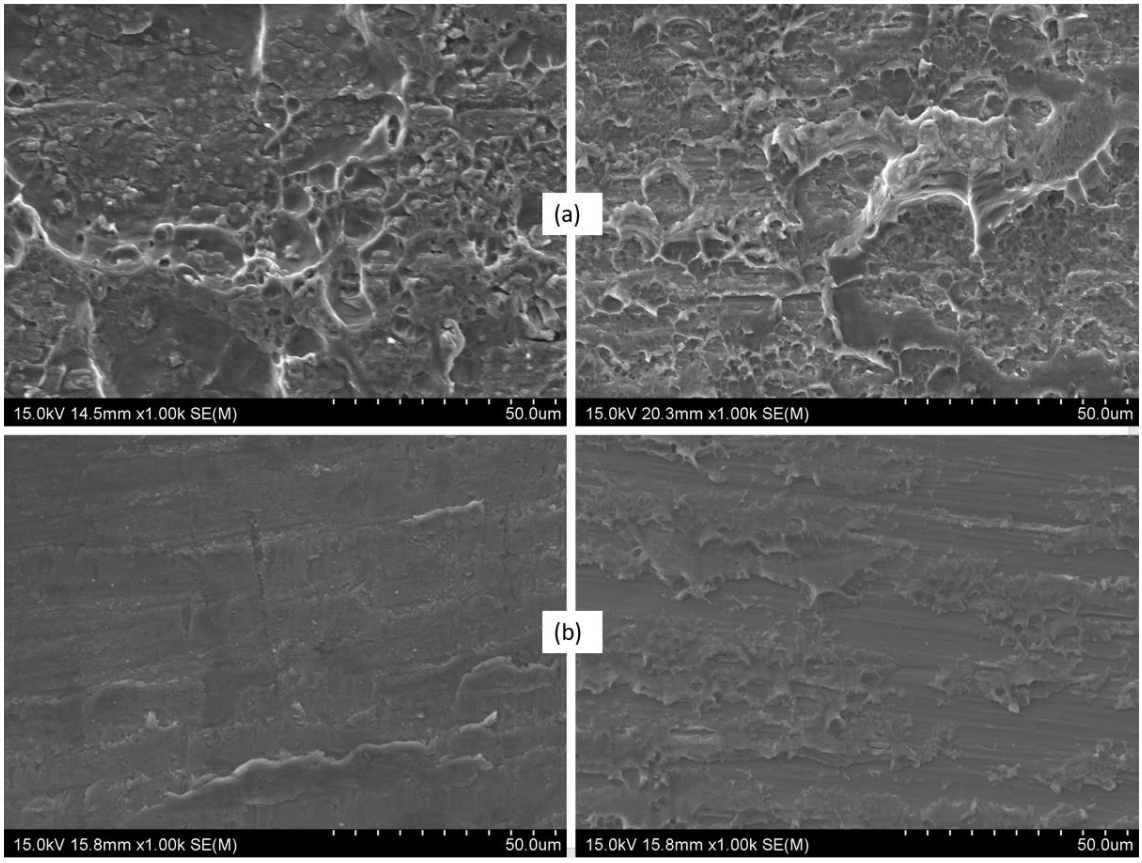

Figure 4-14 Compares SEM images of two different welds at 8 mm from the weld centre on the advancing side (location 3 as indicated in Figure 4-11b): (a) T8S5: Al side (left) and Ti side (right), (b) T9S7: Al side (left) and Ti side (right).

Figure 4-15 presents the SEM images of T8S5 and T9S7 on the RS side of their welds. The images were taken at 5.5 mm away from the tool centre. It is apparent that Figure 4-15a seems to have no visible features of bonding but marks left behind from Ti scrapping lines shown on both sides of the weld fracture surfaces. However, Figure 4-15b has a fracture surface on the Al side shows small dimples scattered which indicates that a weld joint has been formed. It is also apparent in Figure 4-15b that there is a joint formed but not as good as on the advancing side of the weld despite having an equal distance from the weld centre.

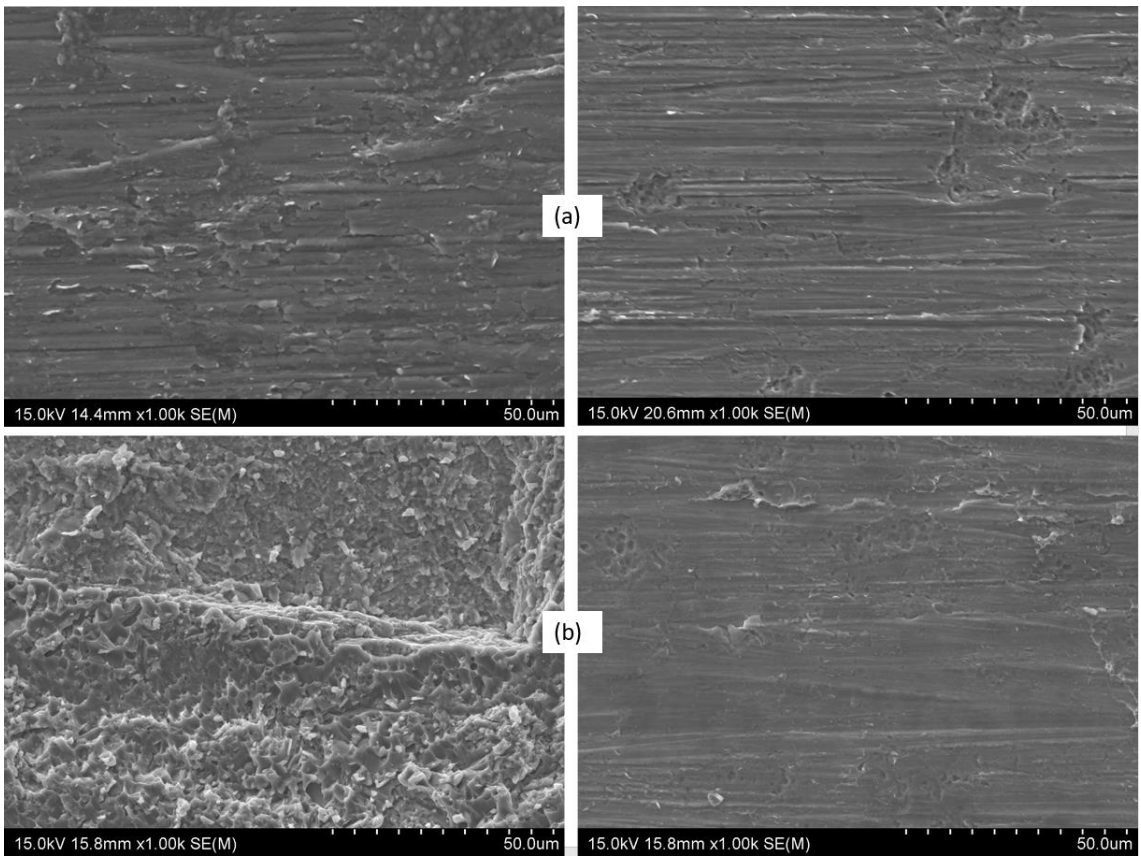

Figure 4-15 SEM images of two welds at 5.5 mm from the weld centre on the RS side (location 2' as indicated in Figure 4-11b): (a) Sample T8S5 Al (left) side and Ti (right) side, (b) Sample T9S7; Al (left) side and Ti (right) side.

Figure 4-16 shows T8S5 and T9S7 weld samples with their respective SEM images taken at 8 mm away from the weld centre on the RS side. Figure 4-16a shows a clear smear of Al on the Ti6Al4V (right) side which reveals that sufficient weld has been formed but low visibility to see on the Al (left) side. However, the weld joint is still strong outside of pin width. Figure 4-16b shows that weld joints have also been formed with many spots with dimples on the Ti (right) side. A large crack on fractured surface (Fig. 4-16b) on the AA2024 (left) side. It is now clear that welds are formed even further away from the edge of the pin as a result of diffusion bonding. The outside of the pin weld formation will be looked at in detail in section 4.3.2.

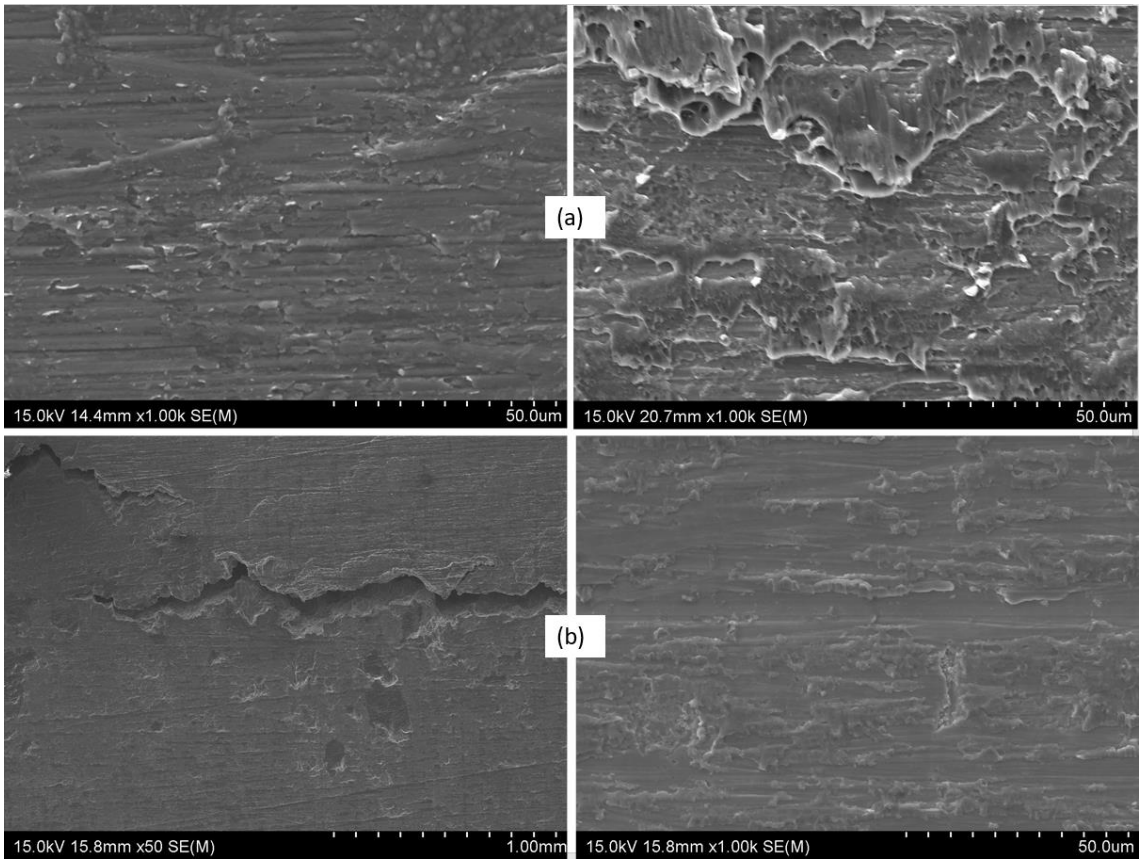

Figure 4-16 SEM images of two different welds at 8 mm from the weld centre on the RS (location 3' as indicated in Figure 4-11b), (a) Sample T8S5: Al (left) and Ti (right) and (b) Sample T9S7: Al (left) side and Ti (right) side.

4.3.2 Cross-sections

In some weld samples, fractures occurred at the interface but crack initiated outside the weld area as shown in Figure 4-17. The effective weld width is the approximate total width of the weld sample. To describe the weld width more precisely, the effective weld width is divided into three sections as shown in Figure 4-17b where 9 mm is the pin width, 5 mm on AS side, and 5 mm on the RS side shows some welds shown (white smears). A total of 19 mm is covered by the weld. It is just an estimate but total coverage could be more in some areas. It is apparent that the fracture has initiated away from the edge of the pin but within the tool shoulder and it is at the HAZ region. Figure 4-17a shows the side view of the fractured sample revealing the V-shape crack path on the advancing side of the weld while uplifting at the unloading end of the AA2024 side as this is normal. It is also apparent that fracture initiated at the edge of the weld close to the large pin penetrated end which has a high-stress concentration area owing to about 80 per cent weld is zero penetrated with a low-stress level at the weld centre. From Figure 4-17b, it is clear that an approximate crack area from the tool edge is about 8mm from the tool edge on the AS side. It is obvious that the crack path has followed the stress concentration region. The crack actually initiated about more than 5 mm outside of pin width and moved a bit into the edge of the pin and again advanced out of the 5 mm dash line drawn (Figure 4-17b). This signifies that between HAZ

and TMAZ regions is the weakest weld spot. Also, it shows that fracture outside the weld centre means high weld strength at the weld interface.

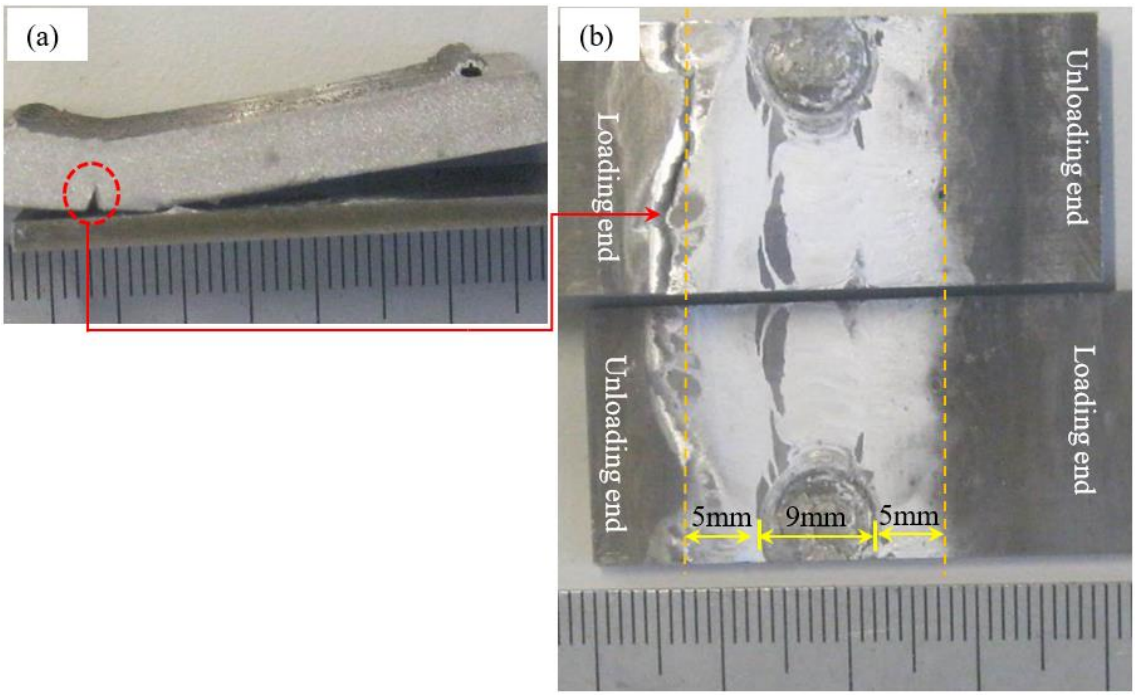

Figure 4-17 Actual photograph of fractured surfaces: (a) Side view of a fractured weld sample, (b) Top view of the fractured weld sample, showing crack outide the 5 mm away from the end of tool pin diameter (D_{pin} = 9 mm).

To further understand the effective weld width, cross-sections of two different weld samples will be examined for microstructural features and level of continuity of weld from the weld centre and further away from pin edge on both advancing and retreating sides. The first sample will be a weld with penetration 'P' and the discussions will be followed by a non-penetrated 'NP' weld sample.

Before, going into details it is worth understanding why MSZ is not considered a reliable weld region because it is hard and brittle which means it is unable to bear loads. FSL weld joint of a penetrated weld is primarily supported by a diffusion bonding [84] outside pin width as shown in Figure 4-18. This finding of diffusion welding outside the pin penetration area has never been considered in literature before. But as it has been demonstrated in weld samples of normal pin as described in the last chapter (chapter 3) now for the samples of larger pin, the major load bearing region is outside of the pin penetrated area. This finding is backed by microstructure analysis of the fracture weld samples and cross-sectional examination of metallography samples. The schematic illustration in Figure 4-18a shows the MSZ with diminishing diffusion bonding on both ends of the edges of the pin showing (in red) the intermetallic growth layers. Dimensions labelled 2.2, 3.2, and 4.2 on both ends from the 9 mm pin centre are the endpoints where SEM micrographs were taken and analysed for their weld strength. Figure 4-18b shows the 'NP' sample having weld

continuity on the weld centre which extends towards the opposite edges of the pin. From the two figures (Fig.4-18a & Fig. 4-18b), it can be argued that the 'NP' sample has provided much better weld coverage and hence strength than the "P" weld sample due to weld continuity combining the pin width size weld and a bit of weld from the outside of the pin weld. This diffusion weld from outside the pin coverage region has given additional weld strength than 'P' sample as it is also evident in fatigue life comparison (see Fig. 4-1). The difference is not much higher but gives a general view that weld with near penetration or none penetrated but joints formed with the right combination of well-controlled process parameters such as F_Z, υ, and ω could provide a better weld strength. Outside weld coverage may vary depending on the nature of pin control during welding. There can be some traces of intermetallic layers at the MSZ, however, they may not have weld continuity to give sufficient weld strength to support a load.

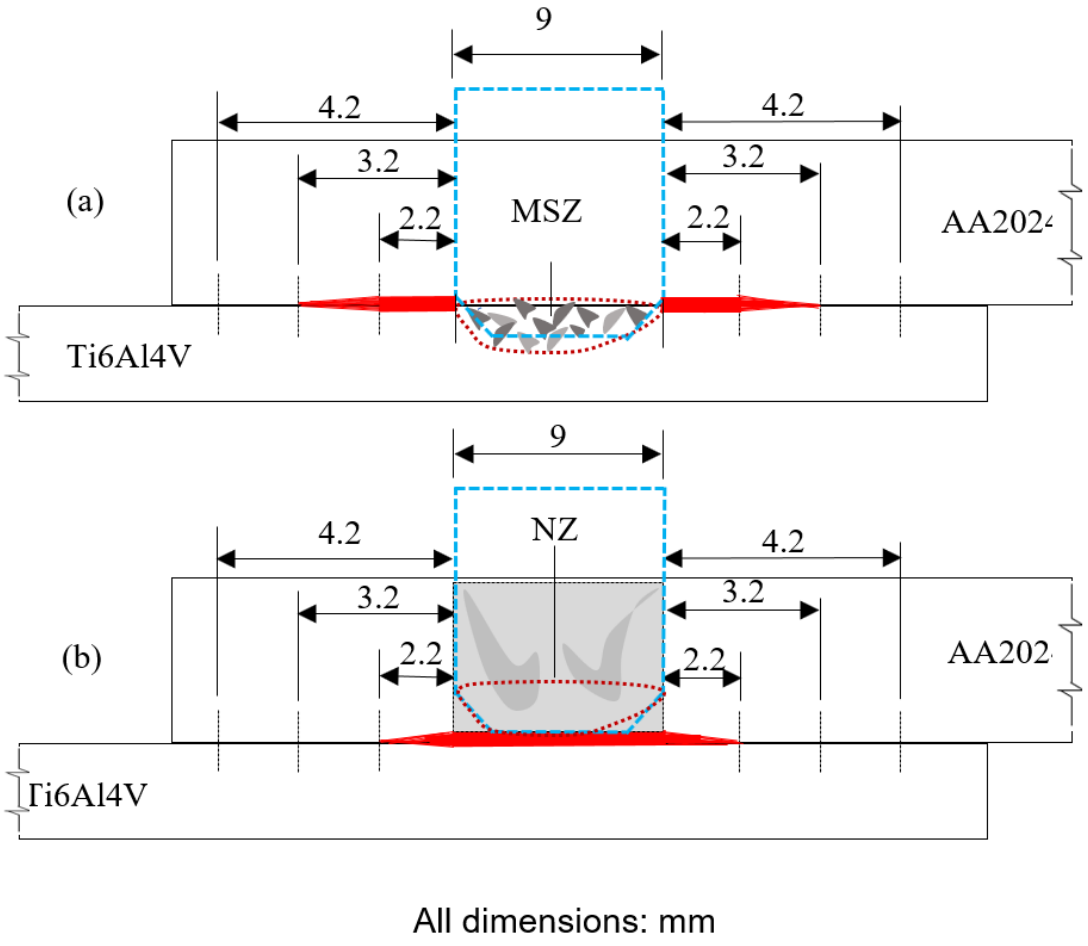

Figure 4-18 Schematic illustration of P and NP welds: (a) intermetallic growth outside of pin width for a penetrated weld sample, (b) NP weld sample with weld continuity consistent.

The measurements taken outside of the pin width of each weld sample from the weld centre are presented in Table 4-1. The amount of pin penetration for each weld sample in Table 4-1 was again measured by carefully analysing the optical micrographs as shown in Figure 4-19. The amount of penetration in percentage was determined and is presented in Table 4-1. The extent of

pin penetration has been measured and estimated with the aid of optical micrographs as shown in Figure 4-19 for the first weld sample (T9S1) is about 80 per cent ‘P’ while the second and the last specimen are 20 per cent ‘P’ and 10 per cent ‘P’, respectively. Figures 4-19a, Figure 4-19b and Figure 4-19c also correspond to “F” in Table 4-1 (weld center) and F in stereomicrograph in Figures 4-20, 4-22, and 4-23, respectively. These optical micrograph images have been taken to clearly show areas of penetration that have not been visible with stereomicrographs.

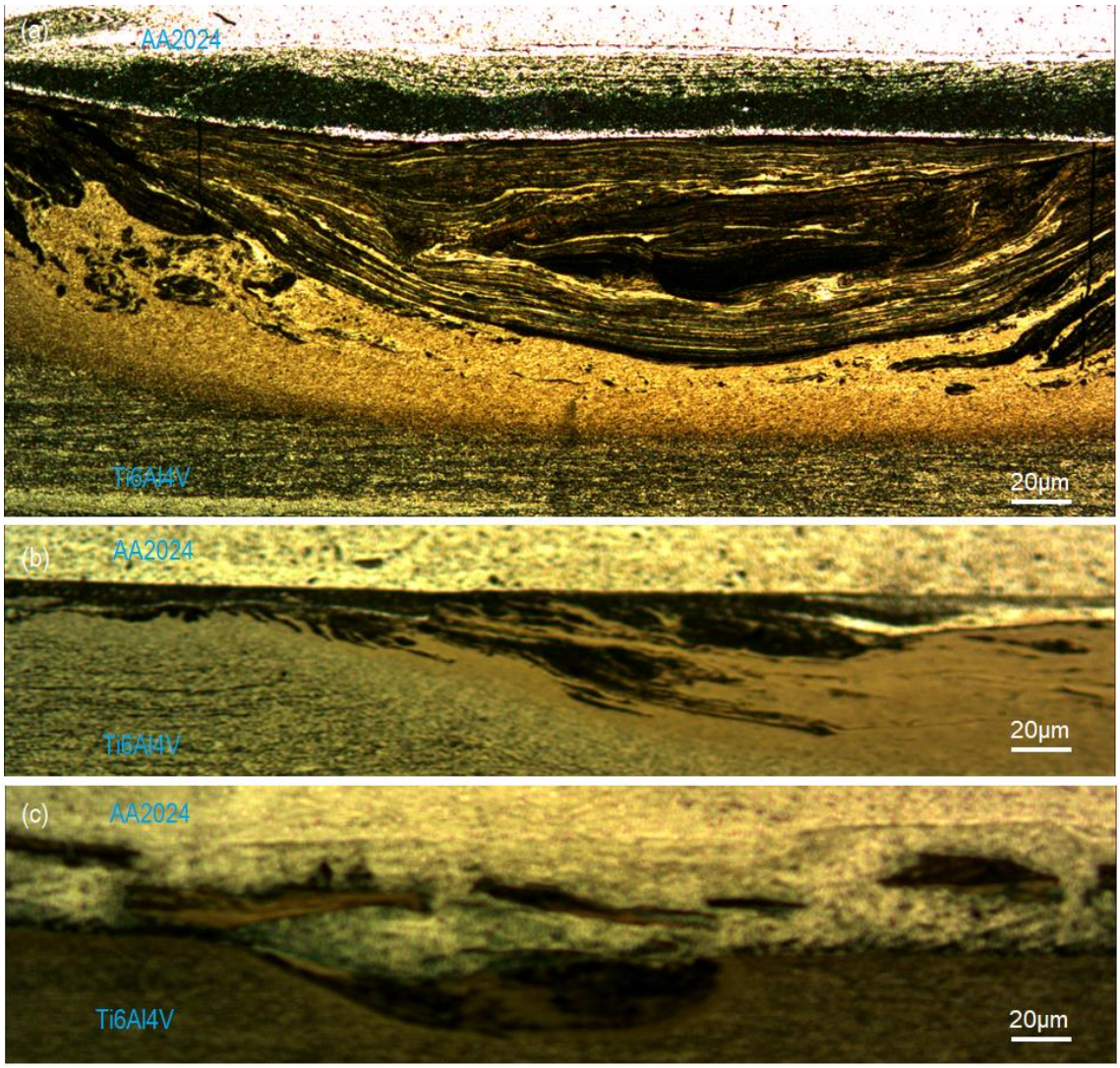

Figure 4-19 Optical micrograph of penetrated region of each weld: (a) 80 per cent ‘P’ weld (T9S1), (b) 20 per cent ‘P’ (T9S2) and (c) 10 per cent ‘P’ (T8S1).

Table 4-1 Cross-sectional SEM images from measurements taken from weld centre towards advancing and retreating sides of each type of weld sample.

Sample	Advancing side	Weld centre	Retreating Side

Type	D_{pin}	B	C	D	E	F	G	H	I	J
T9S1-P	60-80%	9.8^{1*}	7.8^{2*}	6.8^{3*}	5.8^{3*}	0	5.8^{3*}	6.7^{3*}	7.7^{2*}	8.7^{1*}
T9S2-NP	20%	-	7.8^{2*}	6.8^{3*}	5.8^{3*}	0	5.8^{3*}	6.8^{3*}	7.8^{2*}	-
T8S1-NP	10%	-	-	6.3^{2*}	5.3^{3*}	0	5.8^{3*}	6.8^{2*}	-	-

Note: 1*-No joining, 2*-Partially joined, 3*-Fully jointed.

The stereomicrograph in Figure 4-20, displays several weld features of a cross-section of the first sample (T9S1-P, Table 4-1) is shown in Figure 4-20a. The cross-section shows HAZ, TMAZ, NZ, MSZ, material flow out, and flow back directions. The material flow out is mainly on the advancing side of the weld and the retreating side is a material flow back due to the bottom plate stiffness and resistance against the pin pressure resulting in the backflow.

To look at the microstructure and interface bonding between the FSL weld joint, each letter from B to I (see Fig. 4-20a) also corresponds to the values tabulated in Table 4-1. The interface region at location B (Figure 4-20b) which is 4.3 mm (9.6 mm from centre) away from the tool edge shows a lack of bonding with an obvious interface gap between the two lapping plates. At location C (Figure 4-20c) is 1mm towards the end of pin width starts to narrow down the gap and, in some spots, bonding has already initiated. However, there are a few spots showing discontinuity. This means the interface intermetallic growth is low in that region. Moving further, location "D" (Fig. 4-20d) reveals a continuous weld at the interface. The location E (Fig. 4-20e) is also at the edge of the pin and material flow out region. The SEM image (Fig. 4-20e) shows completely continuous and the weld joint was fully established. Before looking into the opposite side (Fig. 4-20a, G to I, location F (Fig. 4-20f) is at the centre of the FSL weld. The weld continuity is also well established; however, it has been explained (Fig. 4-19a) earlier that the MSZ is highly brittle and hard which means the weld strength is poor in this zone. Besides, the intermetallic layer that is responsible for forming a strong bond is also discontinued by the aggressive stirring nature at MSZ. At the RS at location G (Fig. 4-20g) is a weld flow-back region that shows sufficiently weld joint established. However, 2 mm away (6.5 mm from weld centre) from the edge of the pin is location H (Fig. 4-20h) and it starts showing weld discontinuity. Unlike on the AS, the weld outside of the pin on RS is shorter and location I (Fig. 4-20i) further exposes more weld discontinuity. However, the difference is very small so it can be negligible in terms of weld strength. Location J is completely no joint formed which is the same as at location B from AS side.

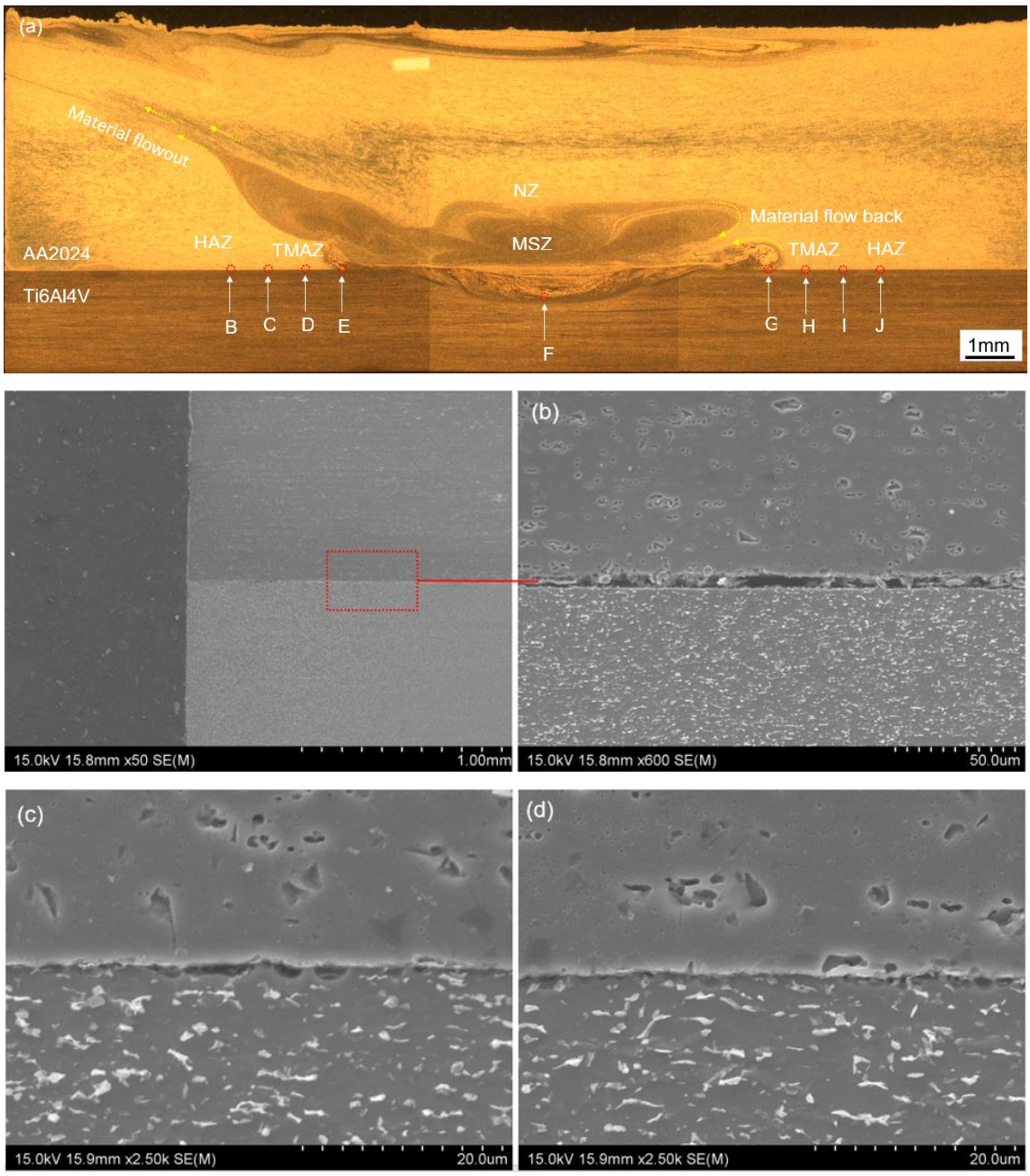

Figure 4-20 Cross-sectional images of the P sample (T9S1): (a) stereomicroscope image of the whole weld with locations pointed B to J for SEM micrographs taken and shown in (b) to (i), respectively.

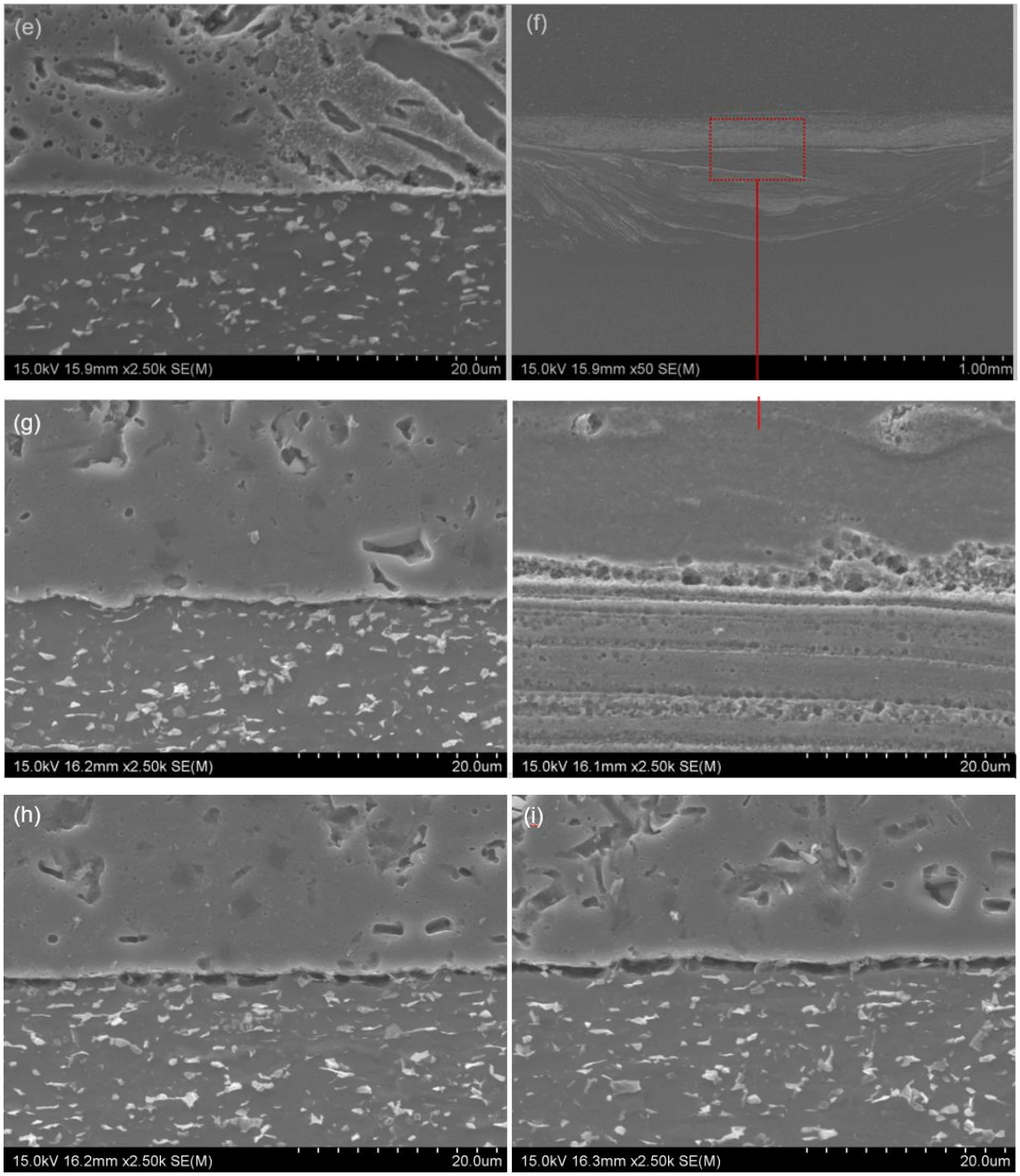

Figure 4-20 cont.

Figure 4-21a presents a higher magnification micrograph taken at MSZ (Figure 21a) and EDS spectra of points 1-3. Point 1 is largely AA2024 with a very little trace of Ti6Al4V. Point 2 is also AA2024 with some trace of Ti6Al4V. Point 3 is largely Ti6Al4V piece embedded into AA2024 matrix and also a small trace of other elements present.

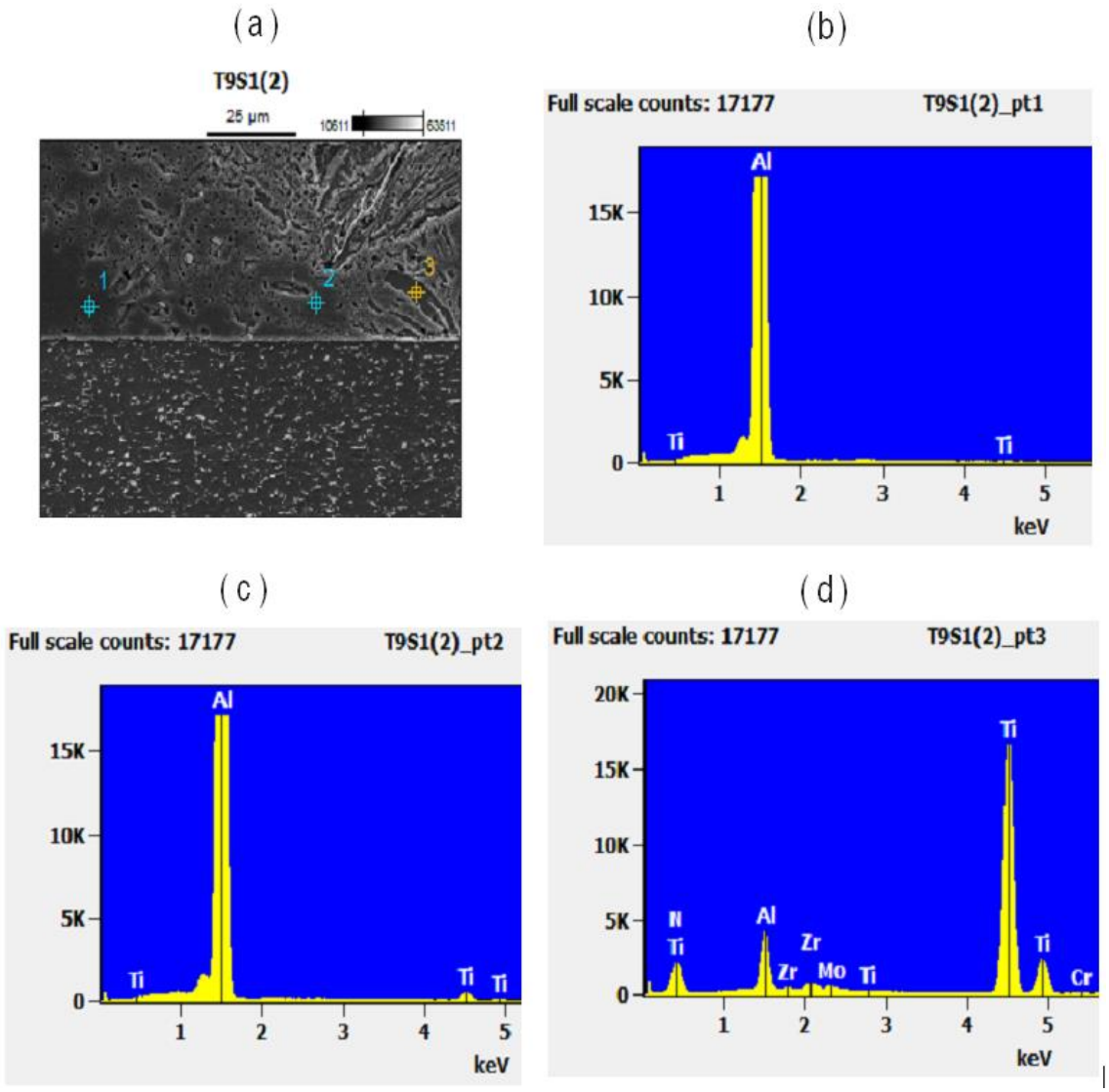

Figure 4-21 EDS for the flow out region on the advancing side: (a) EDS micrograph, (b) EDS spectra Pt1 Al-rich MSZ, (c) EDS spectra Pt2 Al-rich MSZ, and (d) EDS spectra Pt3 MSZ with Ti –Al.

Similarly, according to the stereomicrograph in Figure 4-22 displays, several weld features of a cross-section of the second weld sample (see Table 4-1: T9S2; 20 per cent P,) are shown in Figure 4-22a. The cross-section shows HAZ, TMAZ, NZ, MSZ, material flow out, and flow back directions. The material flow out is on the advancing side of the weld and the retreating side is a material flow back due to the bottom plate being stiff and resistant against the pin pressure resulting in the backflow. Figure 4-22a also shows a cross-sectional image of the 20 per cent NP weld sample of the whole weld and locations pointed D to H which correspond to SEM micrographs shown from (d) to (h) as shown in Figure 4-22, respectively. From AS side, it can be seen that Figure 4-22d (Fig. 4-22a, D) is 6.8 mm from the weld centre (2.3 mm from pin edge) and it is clear from the SEM image that a partial weld joint was formed. However, Figure 4-22e shows a full weld continuity without any gaps. Locations B and F (Fig. 4-22a) is about 2.3 mm (6.8 mm from weld centre) outside of the edge of the pin on advancing and retreating sides, respectively. The weld continuity is partially maintained with interdiffusion bonding, similarly

explained in article by Wei et al. [59] and gradually vanishes and the interface gap widens as shown in Figure 4-22d and Figure 4-22h. It is also evident that at locations E (Fig. 4-22e) and G (Fig. 4-22g) which is 1.3 mm (5.8 mm from weld centre), the weld is continuous and the gap narrows at both locations where the material flow out and flow back have been initiated, respectively. Discontinuity starts to widen further away from the tool edge on both AS and RS as pressure and heat dissipated further away from the weld centre.

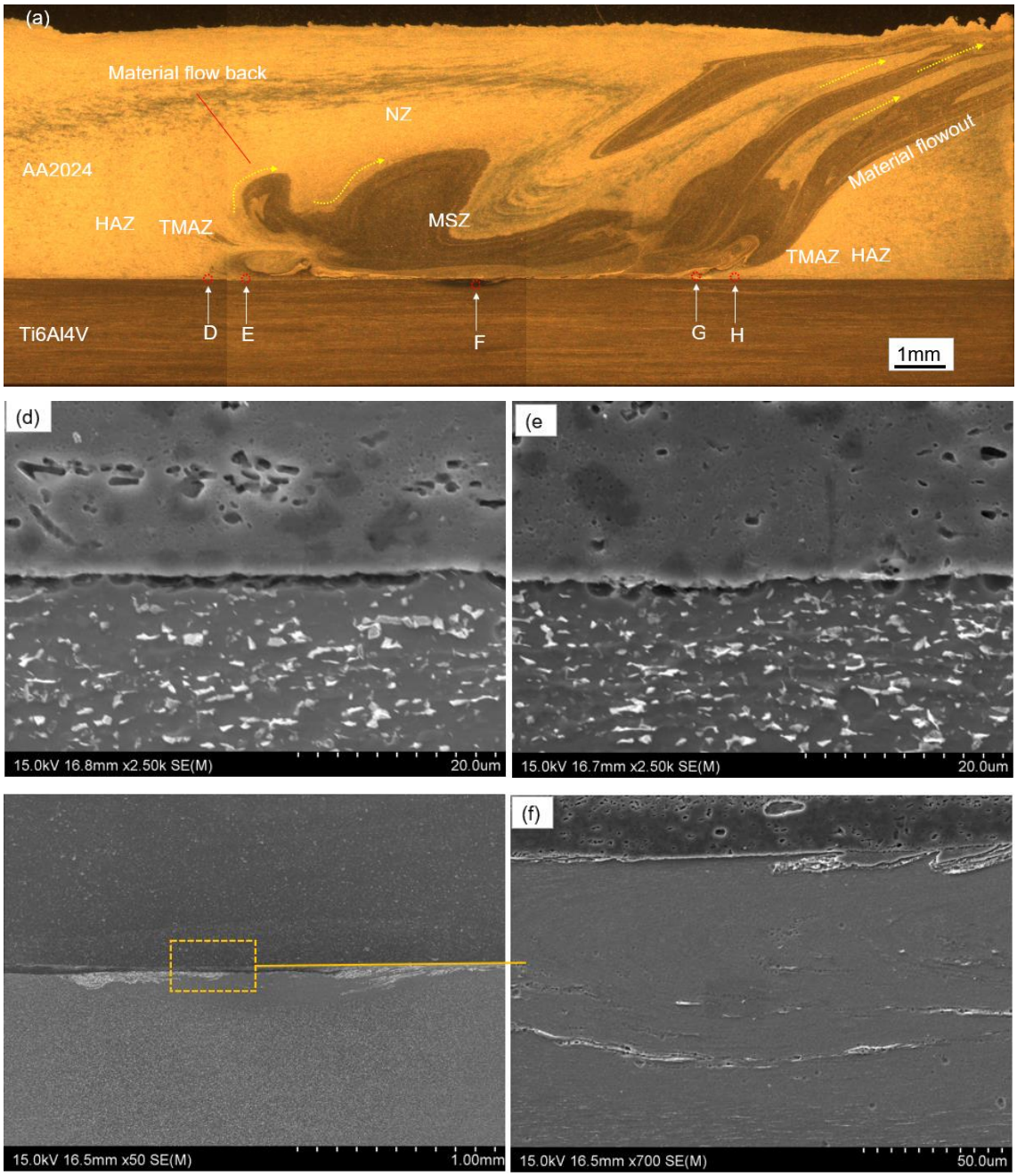

Figure 4-22 Cross-sectional images of slightly 80 per cent NP sample (T9S2), (a) stereomicroscopic image of the whole weld and locations pointed A to E for SEM micrographs taken and shown in (d) to (h), respectively.

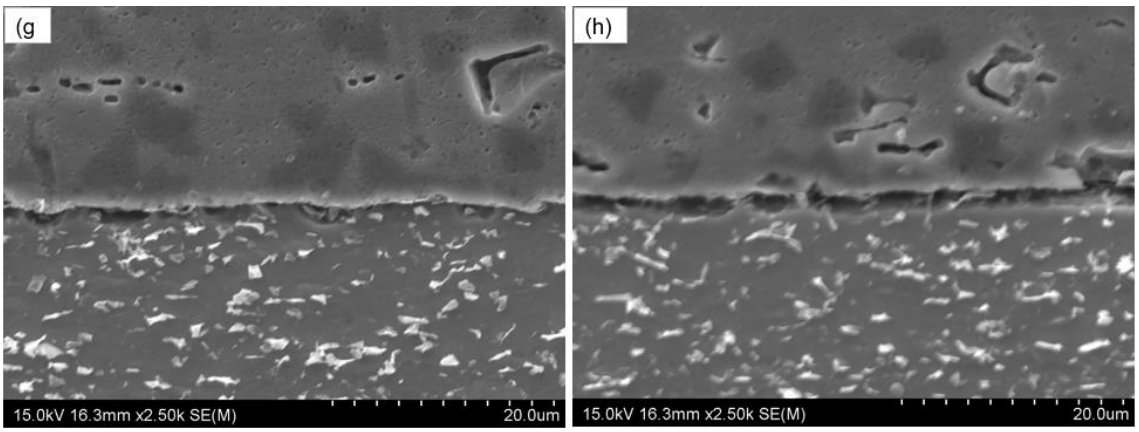

Figure 4-22 cont.

Further fracture surface analysis of the 10 per cent NP sample was done with a different weld to see any effects with a depth of pin penetration. The stereomicrograph shown in Figure 4-23a is the 10 per cent P weld sample showing macrograph of common weld features such as TMAZ areas, NZ, MSZ, and material flow out or flow back direction which is on the advancing side of the weld. Starting from AS side, Figure 4-23b the SEM image clearly shows no joint with discontinuity maintained throughout which is 9.8 mm away from the weld centre (5.3 mm from pin edge). Taking a step into the weld centre with 1 mm (8.8 mm from weld centre), the discontinuity gap only lessens but still no joint is formed as shown in Figure 4-23c. A further 1 mm into the weld centre (7.8 mm from weld centre), weld joint has been partially formed as shown in Figure 4-23d. Finally, at the flow out region (Fig. 4-23e) a full weld joint has been formed. At the centre of the weld is a complete weld joint established as shown in Fig. 4-23f (Fig. 4-23a, F). Similarly, on the RS side, Figure 4-23g (Fig. 4-24a, G) shows a fully joint weld and it is at the material flow back location. Figure 4-23h shows a partial weld joint with weld discontinuity halfway through while Figure 4-23h to 4-23i shows no weld and discontinuity gap has widened. It is now evident that for NP weld or a small percentage of P weld has its weld joint forms approximately equal to the size of the pin bottom width and is about 1-2 mm outside the pin width depending on the pin position control. Optimum amount of pin penetration and temperature distribution is required durinh FSW at the weld interface resulting in interdiffusion of atoms from the alloys in forming the high strength weld bonds.

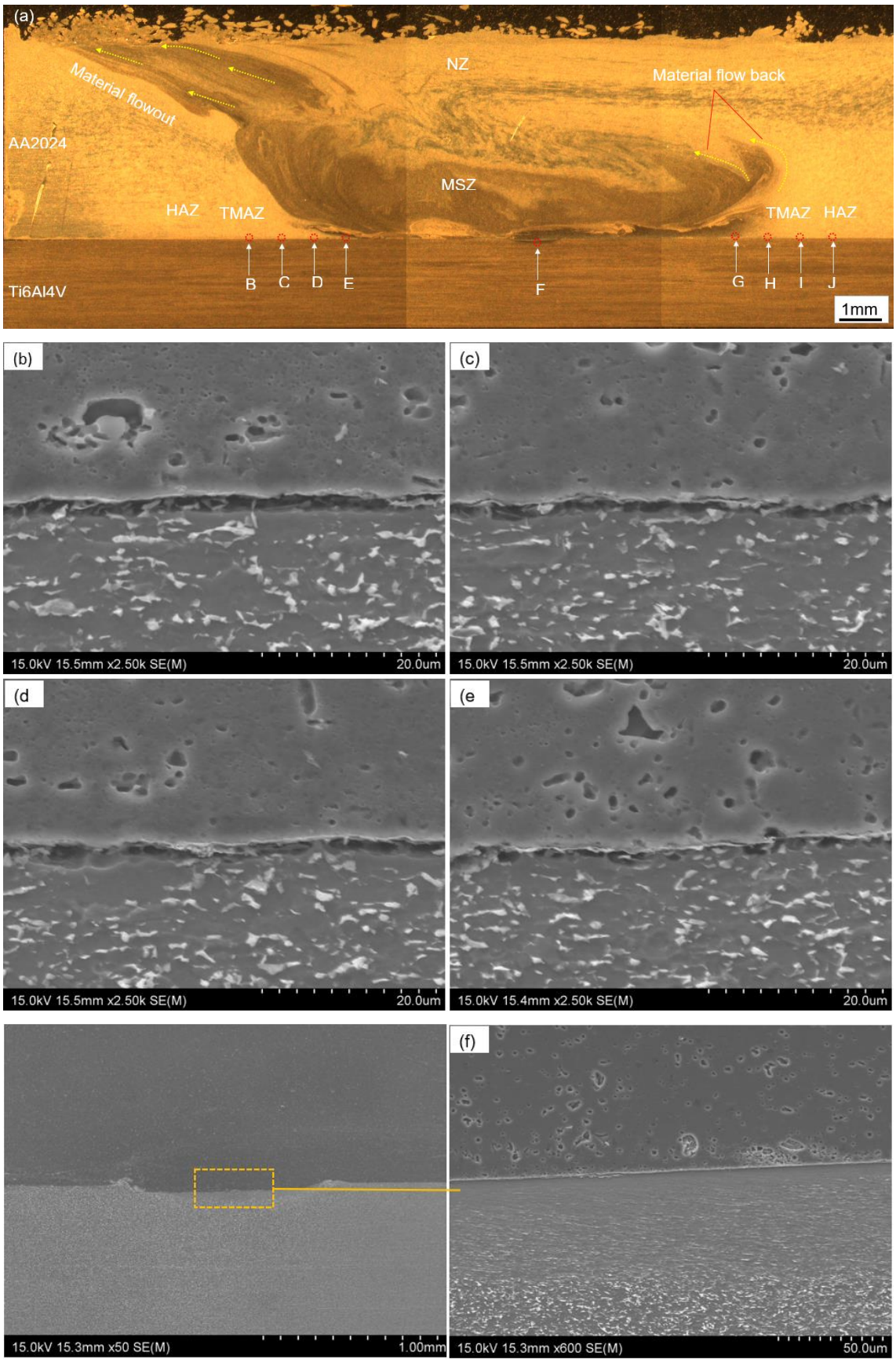

Figure 4-23 Cross-sectional images of 90 per cent NP sample (T8S1), (a) stereomicroscopic image of the whole weld and locations pointed A to E for SEM micrographs taken and shown in (b) to (j), respectively.

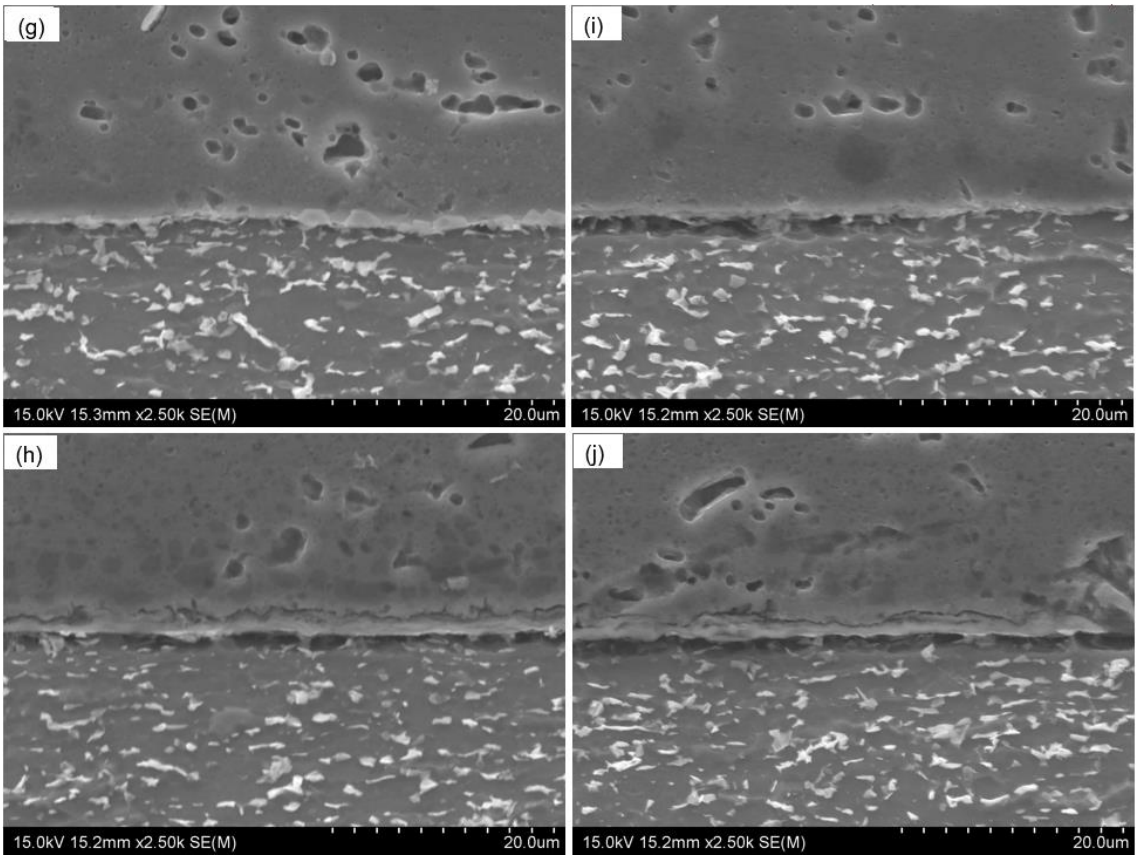

Figure 4-23 cont.

4.4 Summary

The use of the larger size pin has an insignificant effect on the fatigue strength of the FSL welds. This is despite the prediction by the simulation results which predict the higher strength for the weld made by bigger size pin. The growth of cracks in the bottom plate (TiAl4V), which leads to failure, has been discovered as a new fracture path. The reasons for the insignificant effects of the larger size pin on fatigue strength are; lower rotational speed was used during the welding and a possible lower temperature at the interface for the diffusion welding by the thermomechanical action of the rotating tool. The use of the larger size pin has resulted in local thinning of the bottom plate (Ti6Al4V). As a result, in some samples, creating fracture path 3 which has actually prevented the true strength of weld at the interface to be measured as the specimen failed at the base metal (Ti6Al4V), bottom plate.

The use of the larger size pin has increased the mix stir zone (MSZ) as the pin has in most weld locations penetrated partly or fully. The largest width of MSZ in AA2024/Ti6Al4V weld interface is 9 mm, equal to the pin diameter. This larger MSZ has contributed little to increase fatigue strength as the zone is a brittle one. The diffusion weld width outside the MSZ of the large pin samples are similar to that of the normal pin samples at 4-5 mm on both sides. Thus, fatigue strength of larger size pin samples are comparable to normal pin size samples.

For AA2024 top plate fracture occurred at three locations; fracture at weld centre, fracture at the end of bottom pin edge and fracture ~5 mm outside the pin contact regions on the advancing side. Fracture at the centre of the weld for the bottom plate and the top plate was mainly due to material thinning on the AA2024 side and excessive tool shoulder plunging during FSW resulting in more material flash. Fracture at the pin edge has been attributed to strong AA2024/Ti6Al4V interface intermetallic bonding causing the fracture at the high stress concentration region. The fracture location further away from the pin edge (~5 mm) may be the result of strong AA2024/Ti6Al4V interface weld bond reached via interdiffusion during FSW extending from the weld size that is equal to the pin size (pin tip diameter).

5. FRACTURE STRENGTH OF Al INTERLAYER AA2024 TO TI6AL4V FSL WELD

As has been explained in 1.5, the final part of this thesis research was an attempt to explore and test the novel idea of simply placing an interlayer instead of friction stir deposition before FSLW. As has already been reviewed, a predisposition of Al before FSLW of Al to Ti for preventing tool wear due to tool penetration has been reported in a recent study. The preposition procedure however adds manufacturing cost. Thus, the current study was made to evaluate the weld quality regarding the interface regions of the AA2024 to Ti6Al4V welds made by FSLW using a thin Al-layer, without an extra deposition procedure. Fatigue testing of the welds was conducted and whether the use of an inter-layer may affect the interface structure under the condition of non-penetration of pin and the corresponding fatigue performance of the welds has been studied. The details of results and discussion of these results are reported below in this chapter.

5.1 Friction Stir Flow and Weld Structures

FSL weld joints of using a pure Al interlayer and AA2024 to Ti6Al4V were developed using optimized process parameters (ω, υ, ∠) and tool profiles ($D_{shoulder}$, D_{pin}, L_{pin}) in Chapter 2 (See Table 2-3 and Table 2-4)**.** The photograph of a typical sound and defect-free A/Ti FSL weld joint is shown in Figure 5-1. Note pin was position controlled to more ascertain d_p being slightly negative but also for the pin to have penetrate the Al interlayer during FSLW experiments. As will be shown in cross sections of the welds soon, proper penetration and thus the normal friction nugget mixing the AA2024 and Al interlayer material were achieved.

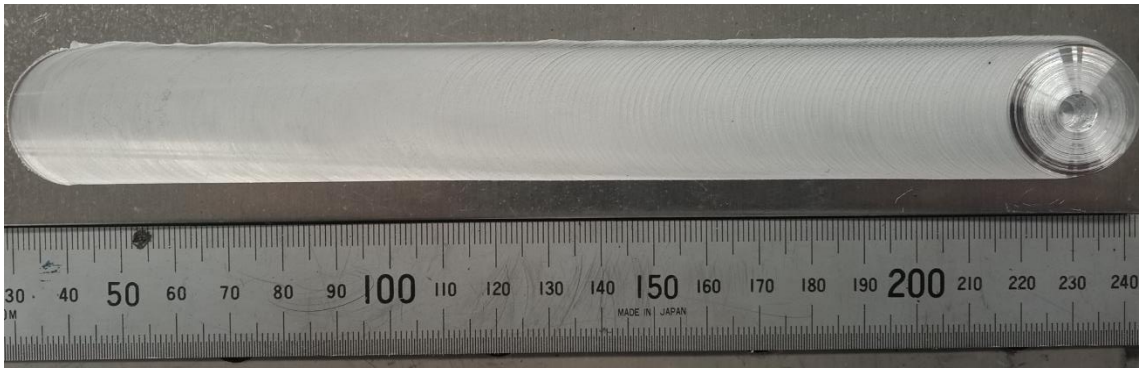

Figure 5-1 Photograph of defect-free FSL welded plate with little flash and characteristic hole or the weld end. AA2024 as top plate and the bottom plate as Ti6Al4V (veiled by the ruler).

A pure Al strip of dimensions 8 mm (or 10 mm) wide, 0.5 mm thick and 240 mm long, similar to the size of the machined groove on the bottom plate (Ti6Al4V) was mechanically fitted into the rectangular groove as shown in Figure 5-2a, shown in cross-sectional view before welding. Unlike normal material flow characteristics, FS flow between mechanically fitted Al interlayer and

AA2024 alloy as the top lapping plate was characterized by some degree of the shape of the rectangular groove on the bottom plate (Ti6Al4V) surface during welding. As the pin thrusted towards the Al interlayer without touching the bottom plate (Ti6Al4V), the plasticized Al interlayer was drawn out and rigorously mixed with the plasticized AA2024 material as schematically shown in Figure 5-2b. The Al interlayer has been clearly plasticized and drawn along with the tool pin edge but not stirred to create a MSZ.

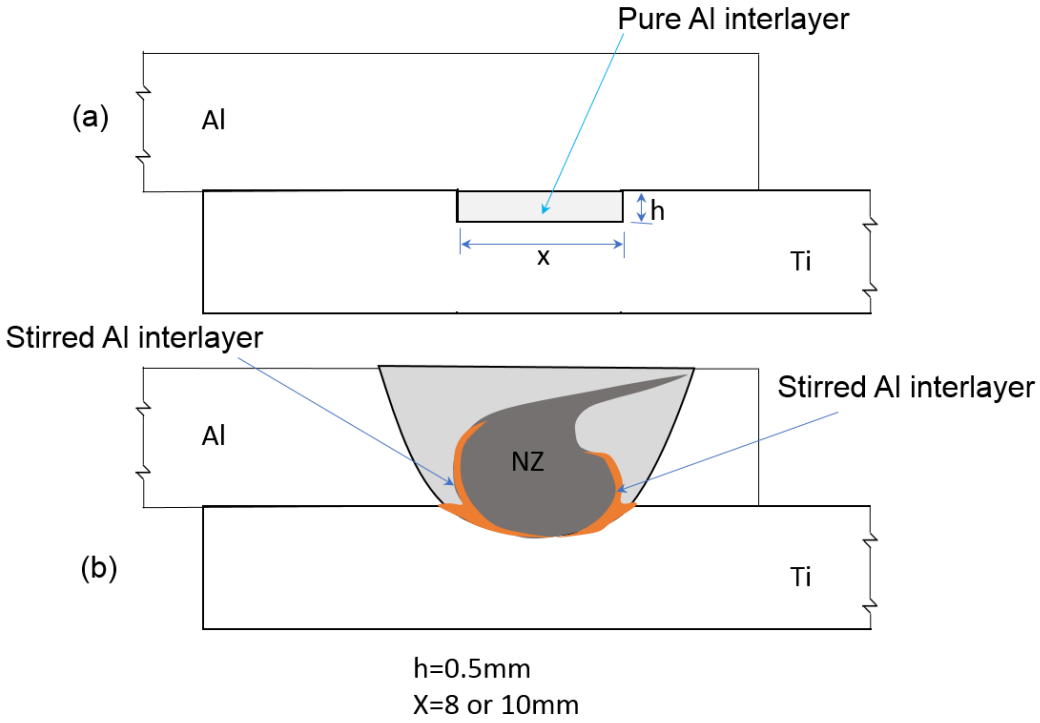

Figure 5-2 Schematic illustration of pure Al as an interlayer: (a) before welding, showing the placement of the Al interlayer fitted into the groove machined on Ti 6Al4V; (b) after welding showing the nugget zone (NZ) containing the stirred AA2024 and Al interlayer drawn around the edge of the tool pin during FSW.

The stereomicrograph in Figure 5-3a, displays several weld features of a cross-section of the first sample 1 (N5S3) with 10 mm groove size. The cross-section shows HAZ, TMAZ, SZ, MSZ, and material flow out directions. The Al interlayer has partially been pushed out of the rectangular groove by the down thrust exerted from the tool pin and has partially been stirred to mix with AA2024 material to become the nugget zone (NZ). The drawn-out Al interlayer coalesced in the AA2024 plasticized regime and vividly formed a hook-shaped structure inside the AA2024 matrix on both AS and RS (see Fig. 5-3). The Centre of the weld shows a clear formation of an onion-ring shape which is typical. To elaborate on the formation of onion-ring is basically the action of the tool shoulder and the pin as comprehensively explained and reported by Kumar and Kailas[86]. However, material flow out of the groove is also affected by the edges on both ends of the groove directing the material flow into the centre creating the onion ring as the tool traversed along the weld line. Further, it is obvious from Figure 5-3 that the Al interlayer was not

only plasticized and remained at the bottom surface but displaced by the flow of plasticized top plate (AA2024-T6).

To look at the weld structure at the interface and bonding between the FSL weld joint, each letter from “B” to “E” in Figure 5-3a corresponds to SEM images (b) to (e), respectively. The interface region at location “B” (Figure 5-3b) has a gap and it could be one of the weakest points of the weld. While location “C” (Figure 5-3c) shows a discontinuous interface with Al matrix taking the shape of the tiny grooves left behind during machining. The location “D” (Figure 5-3d) shows another gap which is at the corner of the groove is also another weakest point in the weld structure. Apparently, location “E” (Figure 5-3e) shows complete discontinuity and it is further away from the groove corner on the right. The 10 mm groove has shown largely plasticized Al interlayer has been drawn towards the left end of the groove as shown in Figure 5-3a because of wider distance between the tool and the groove corner.

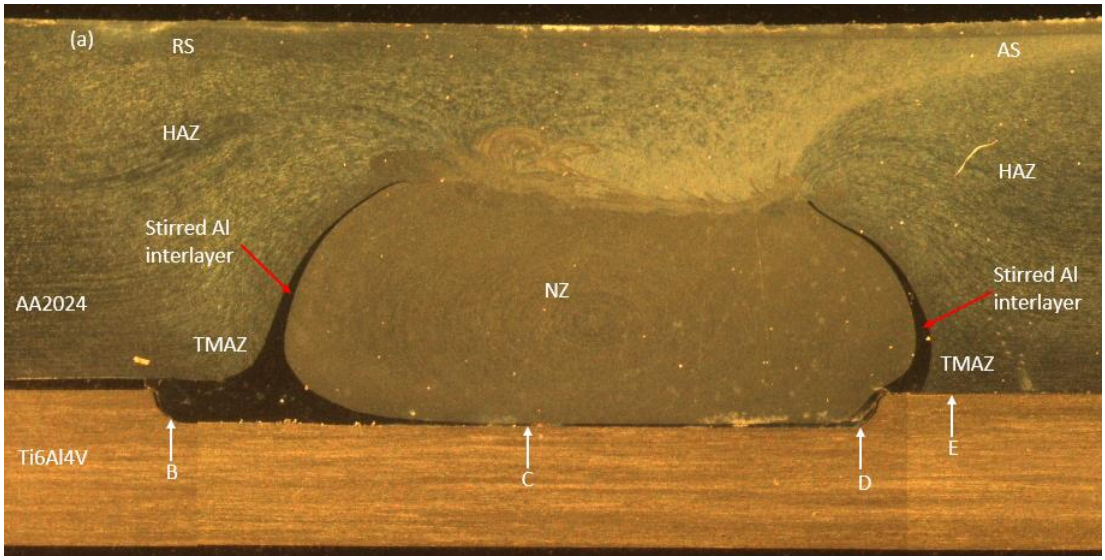

Figure 5-3 Cross sectional images of of Al interlayer-weld sample 1 (N5S3) with 10 mm groove size: (a) stereomicrograph of the whole weld with locations pointed to as B to E for SEM micrographs taken and shown in (b) to (e), respectively: (b) SEM micrograph of left corner of machined groove, (c) SEM micrograph of AA2024/Ti6Al4V weld interface, (d) SEM micrograph of right-side corner of the groove, (e) SEM micrograph taken outside of the groove.

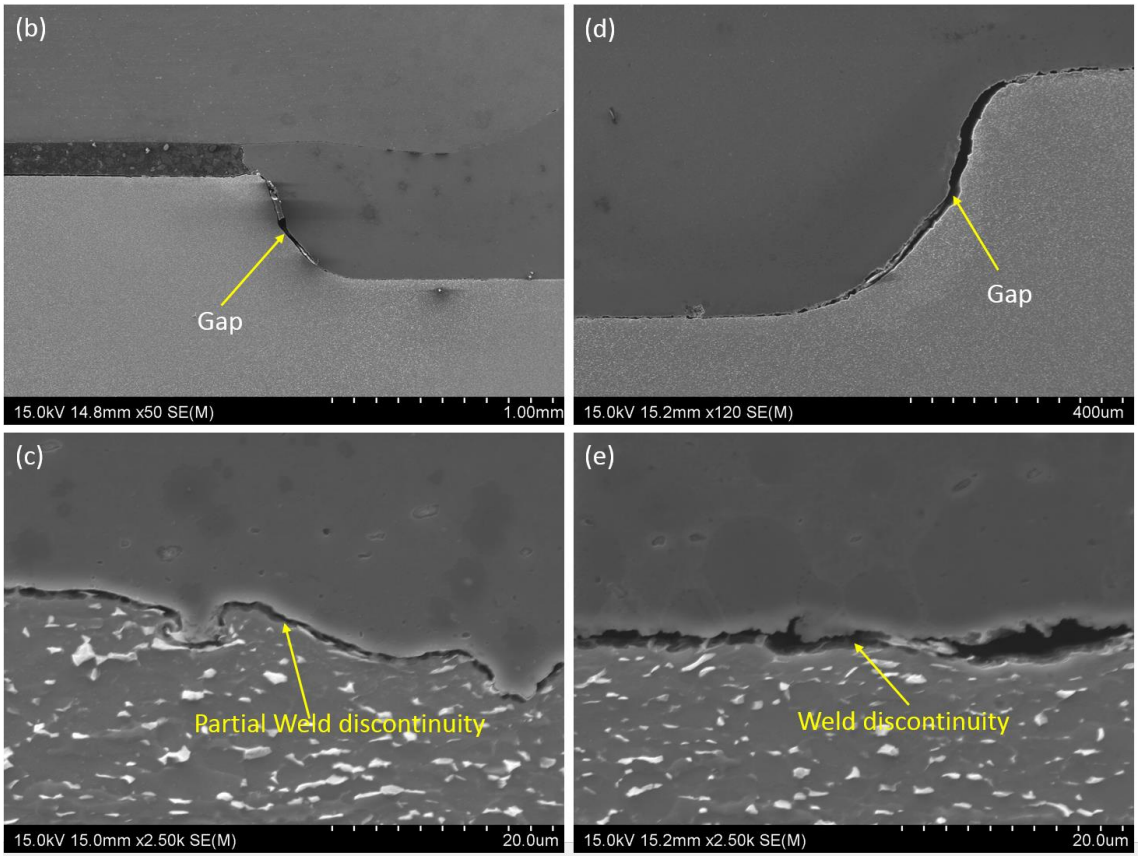

Figure 5-3 cont.

Figure 5-4a shows a stereomicrograph consisting of various weld features of sample 2 (N3S2) with 8 mm groove size. In this sample, the weld was performed after the groove was sanded with grit paper to thoroughly remove the rings of tool marks left behind after machining. Observing the cross-section, one apparent feature is the onion-ring formation at the MSZ which is common in most Al welds. However, there appears a new feature shaped like a sliced tomato just above the tip of the onion-ring. The plasticized pure Al layer was extruded along with the pin as clearly shown in dark curvy lines on both right and left from the weld centre. The material flow-out is mainly towards the AS from the pin extrusion. However, it also appears that material flow driven around the shoulder is pushed out as flash on both ends of the weld (AS and RS).

Again, to look at the weld structure at the interface and bonding between the FSL weld joint, each letter from “B” to “E” in Figure 5-4a corresponds to SEM micrographs (b) to (e), respectively. The interface region at location “B” (Figure 5-4b) has a complete weld discontinuity (gap) and the weakest spot of the weld. In location “C” (Figure 5-4c) shows a compl ete weld continuity at the interface. This means that the joint was established at the interface as a result of Ti surface being cleaned after sanding. Location “D” (Figure 5-4d) shows another gap with completely no joint that has been established and is also the weakest point in the weld structure while location “E” (Figure 5-3e) shows weld discontinuity which is further away from the end of the groove but within the tool shoulder. However, with the use of 8 mm Al interlayer, most of the Al thin sheet

has been plasticized due to the heat generated during the welding and the materials have been drawn out of the groove into the AA2024 matrix as shown in Figure 5-4a.

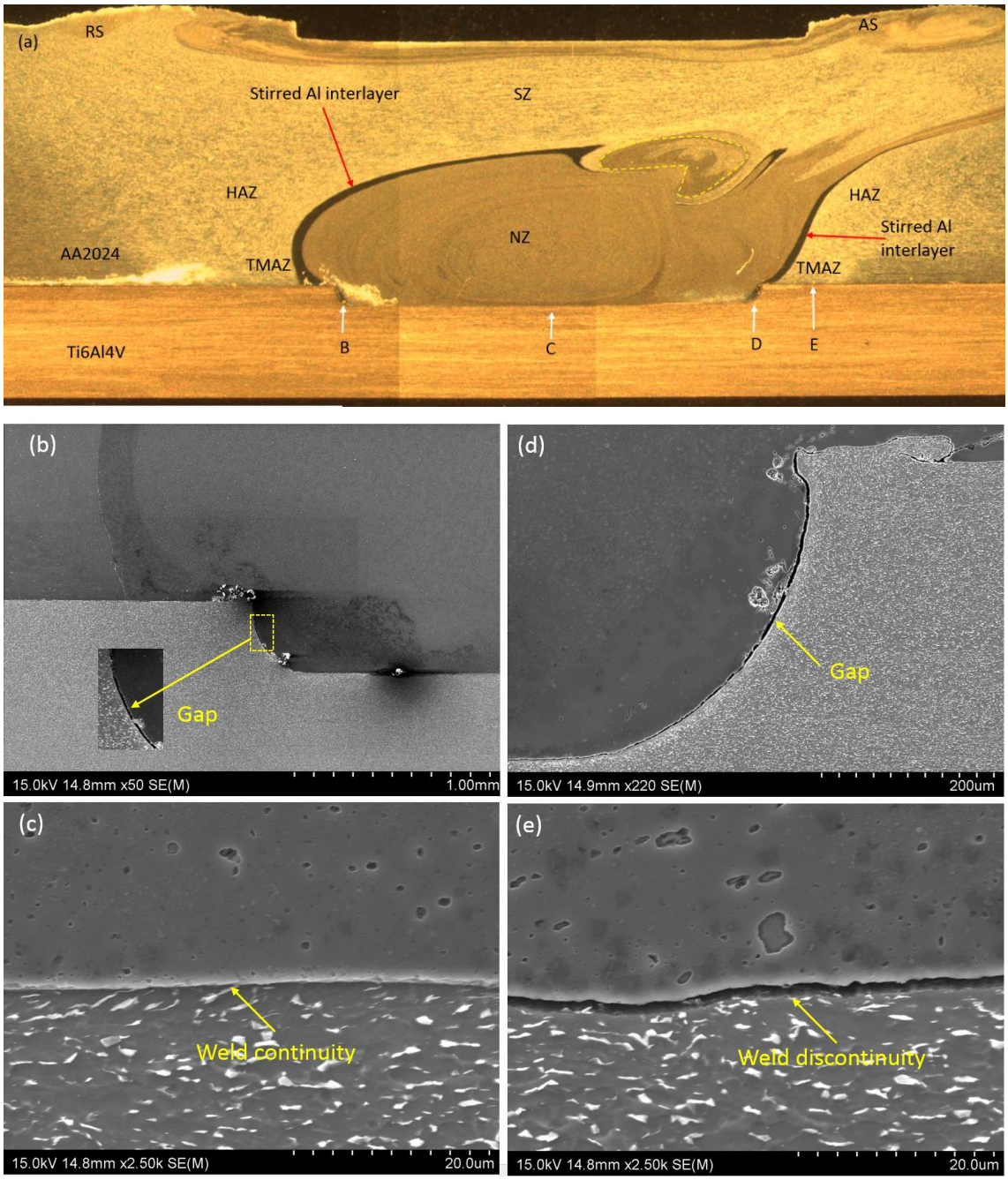

Figure 5-4 SEM micrographs of the cross-sectional view of Sample 2 (N3S2) with 8 mm groove: a) Cross-sectional optical micrograph with various weld features, (b) SEM micrograph at the left side of the machined groove corner, (c) SEM micrograph at the weld interface, (d) SEM micrograph of at the right side of the machined grooved corner, (e) SEM micrograph outside the tool pin edge.

5.2 S-N Data and Comparison to Data using Normal FSL Weld

Figure 5-5 shows a FSL welded fatigue test specimen, 20 mm width and 160 mm long with AA2024 as the top plate and Ti6Al4V as the bottom plate. All the tests were conducted in as-weld condition, as has been described in Chapter 2. The specimens for fatigue testing samples

were cut from the welded plates using an electron discharging machine (EDM). 20 mm x 40 mm spacer from each base metal was prepared to properly align the specimen before testing. This was done to avoid premature bending while the specimen was clamped in the fatigue machine during testing. All tests were carried out with a constant amplitude loading, load ratio R = 0.1, and frequency of 20 Hz. The number of cycles to failure was recorded at fracture while runout (10^7 cycles) was prematurely terminated. These testing conditions are consistent with those used for welds made with other FSLW conditions.

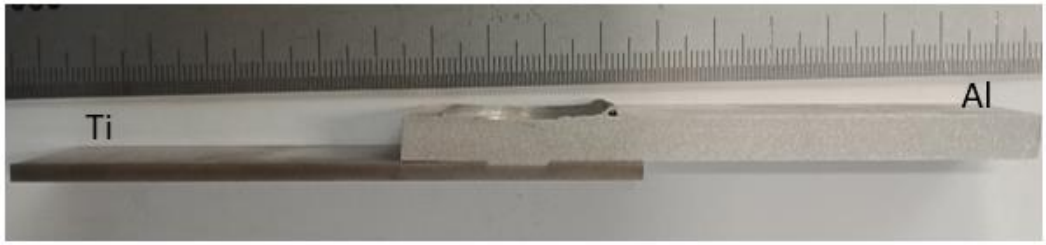

Figure 5-5 AA2024 (5mm thick)/Ti6Al4V (2 mm thick) FSL weld fatigue test specimen (20 mm x 160 mm).

Figure 5- 6 shows a comparative S-N curve of Al interlayer AA2024/Ti6Al4V FSL weld to that of the normal weld. A significant difference can be seen from Figure 5-6 from the fatigue life of normal weld to that of 8 mm and 10 mm width pure Al strips used as Al interlayers in AA2024/Ti6Al4V FSL welds (see Figure 5-2a). At fatigue stress of 40 MPa (4 kN), 10 mm Al interlayer with AA2024 to Ti6Al4V FSL weld tested fatigue life is 14,560 cycles, and for 8 mm is 60,240 cycles which is higher by 80 per cent in weld strength. However, the performance of the fatigue life of normal AA2024 to Ti6Al4V FSL welds stands at 348,440 cycles at the same loading conditions and proved a better fatigue strength than both sizes of Al strips used as an interlayer with AA2024 to Ti6Al4V FSL welds. Compared to the normal weld, the Al interlayer AA2024 to Ti6Al4V FSL weld fatigue life shows significantly low as shown in Figure 5-6. The low fatigue performance of Al interlayer AA2024 to Ti6Al4V FSL weld has been basically due to weld discontinuity in most parts of the corners of the grooves (see Fig.-5-3 and Fig.5-4). It has also been observed that the corners of the machined groove have gaps. These locations have been seen as the weakest zones during fatigue loading because of lack of weld formation in the areas. In both cases, the high load > 4 kN led to low fatigue strength (< 10^6 cycles).

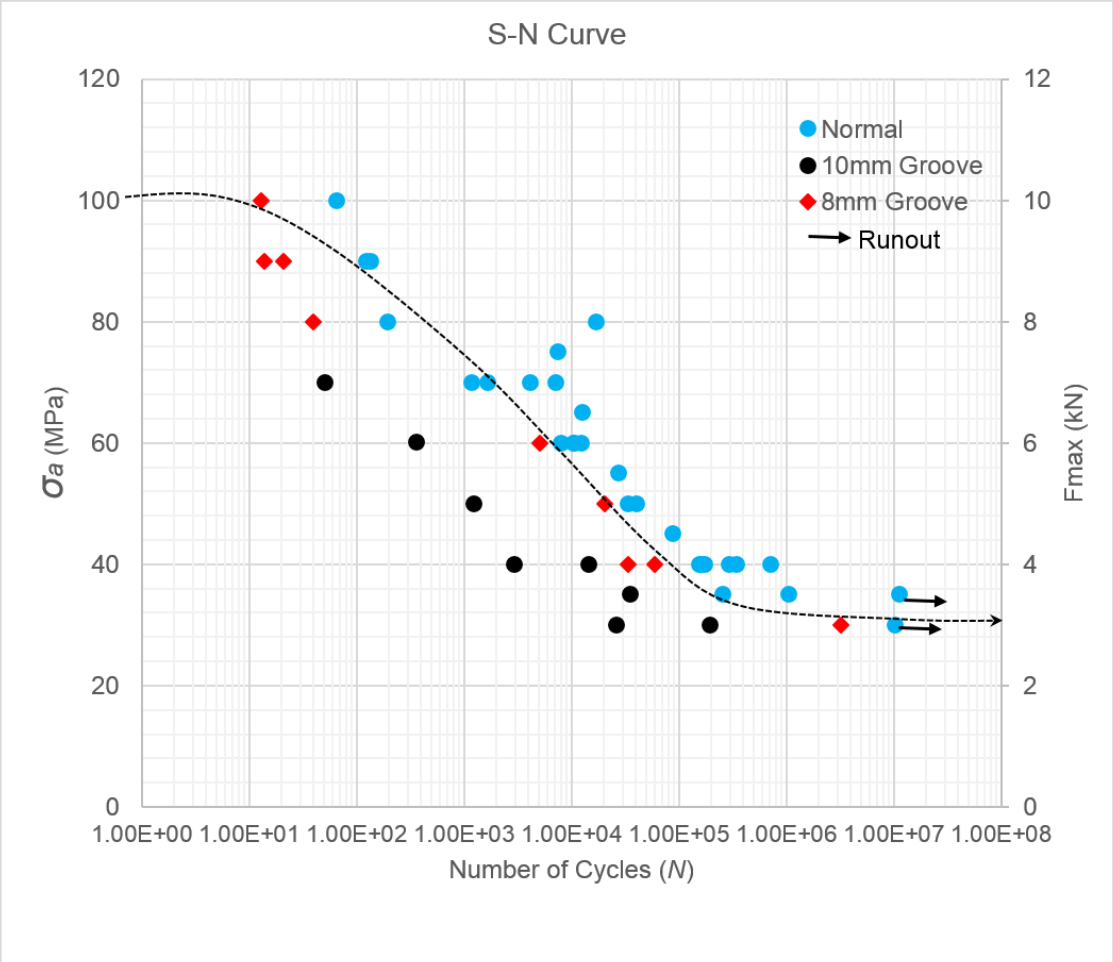

Figure 5-6 A comparative S-N curve for Al-Interlayer FSLW and normal weld. Maximum load and stress plotted against the fatigue cycle number. Groove sizes of 8 mm and 10 mm are labelled with their corresponding color as indicated with black arrow indicating a run out for the normal pin.

The lower fatigue strength values of welds using an interlayer in general, in comparison to those of welds made using the normal pin in series 1, may resulted in the intension of pin being not to penetrate to Ti6Al4V. In other words, it was intended that not only $d_p \approx 0$ but also $d_p < 0$. With position control, it is highly difficult to precisely control the pin position to significantly better than 0.1-0.2 mm. It is possible, when d_p = 0.3-0.4 mm, although the pin has penetrated to the interlayer, the temperature and force in the Ti6Al4V and Al interface may not be sufficiently high for a continuous diffusion weld, at least the diffusion weld width not sufficiently wide. Thus, overall, the fatigue strength values are lower.

5.3 Fracture Behaviour Comparing with Normal FSL Weld

Figure 5-7a shows a photograph of the FSL weld test specimen and Figure 5-7b shows a fractured specimen after it has been tested. The uplifting at the unloading end of the specimen is a common issue observed during the test for samples mainly at high loads (> 5 kN). The amount of lifting

depended on the strength of the weld at the interface i.e., more lifting is an indication a tough interface weld structure. All tested samples failed at the interface.

Figure 5-8a shows interface fracture with approximately 10 per cent weld coverage (only three spots) while the rest of the rectangular groove surface showing no welded deposition. However, crack initiated on the top plate (AA2024) away from the edge of the pin but is obviously within the TMAZ region as shown in Figure 5-9b. Also, Figure 5-8b shows enough weld coverage at the Al to Ti interface with a crack initiated on the Al part at the loading end of the weld. The crack path is obviously on the TMAZ/HAZ regions. The evidence of reasonable fatigue resistance of the weld is shown by fatigue life of 6 x 10^5 cycles at 40 MPa (4 kN) while the other three (see Figure 5-6) samples tested at the same loading condition have low cycle numbers as 34 x 10^3, 14 x 10^3 and 3 x10^3 cycles, respectively. However, compared to the fatigue life of a normal weld at the same loading condition (40MPa), the cycle number of 0.5 x 8 mm groove weld can reach as high as more than 7 x 10^5 (see Fig. 5-6) which is still low but quite reasonable as Al interlayer Al to Ti FSL welds generally have low fatigue life due to several contributing factors such as depth and width of the groove and lack of weld distribution at the two ends (corners) of the groove.

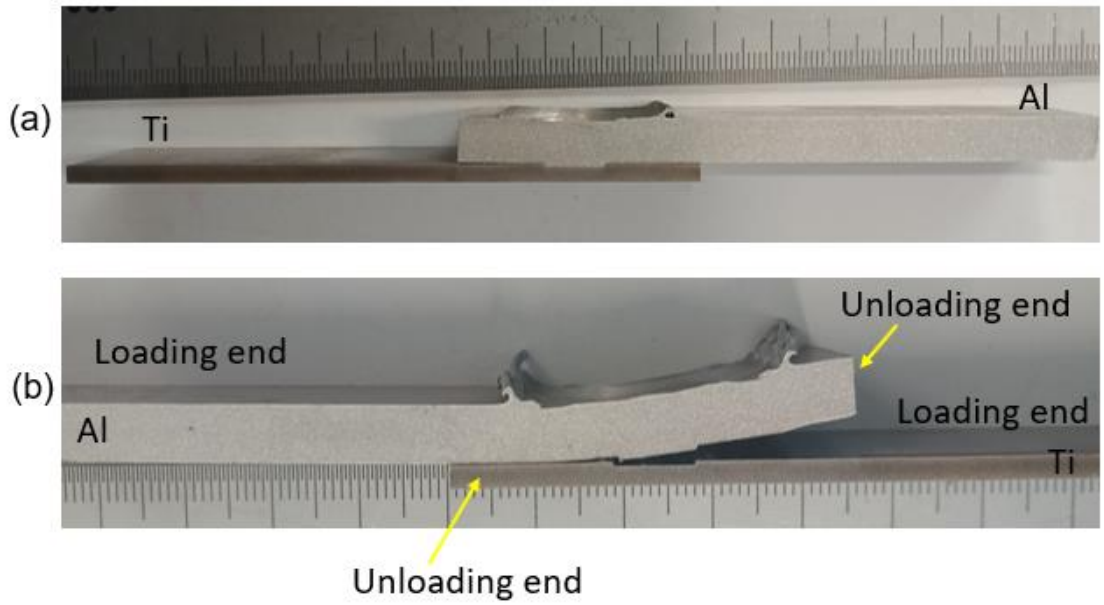

Figure 5-7 Photographs of fatigue test specimen; (a) before testing with AA2024/Ti6Al4V labelled (see Fig.5-5), (b) after the testing (different specimen) showing a fracture at the interface with lifting at the unloading end of AA2024

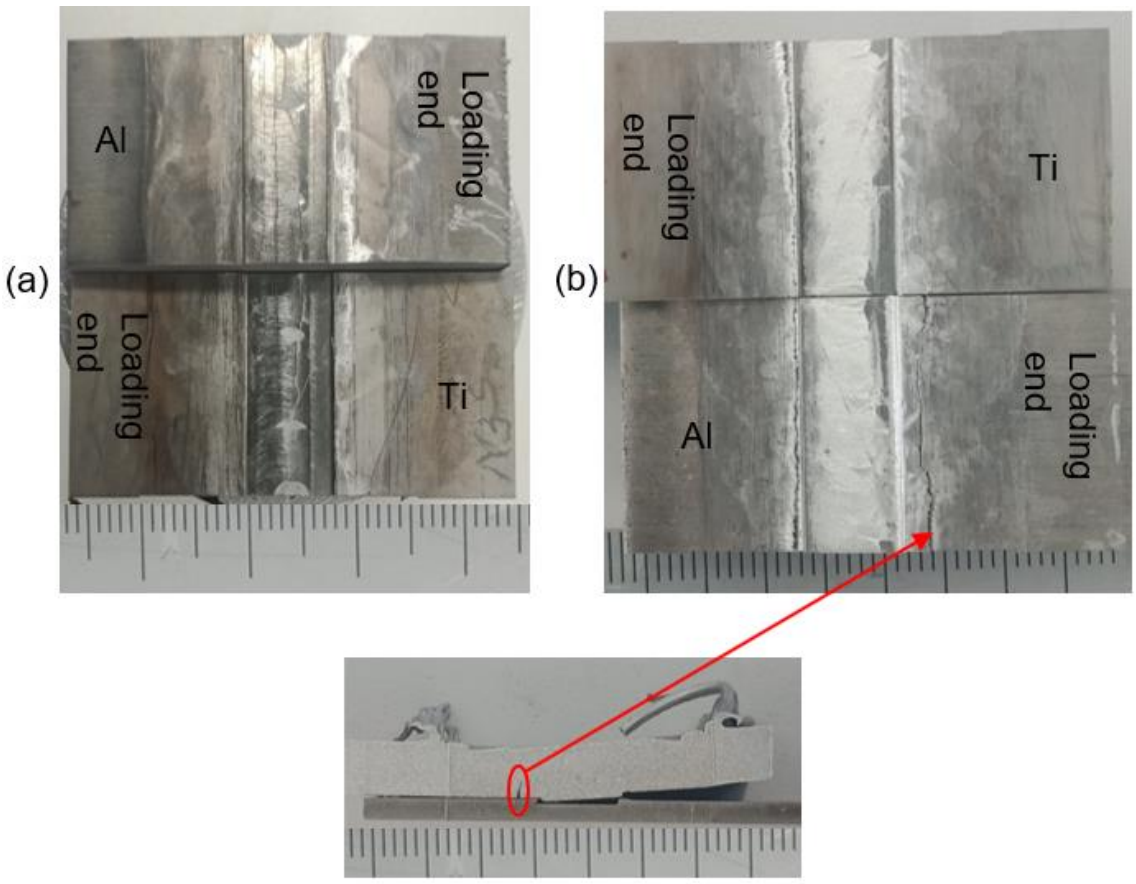

Figure 5-8 Al interlayer aided FSL weld fractured at the interface: (a) N3S6 approximately 10 per cent weld covered, (b) N2S5 approximately 90 per cent weld covered with crack initiation at the AA2024 loading end.

Figure 5-9 shows an SEM micrograph of sample identified as N3S6 taken at a spot on the Tide side of the fractured weld sample. Dimples with two types of fractures have been seen here as the main crack and secondary crack. The main crack is the crack progression from the initial crack. However, as the crack progressed over time, the main crack line diverged into one or more new crack directions which are known as secondary cracks as labelled on the bottom left micrograph of Figure 5-9.

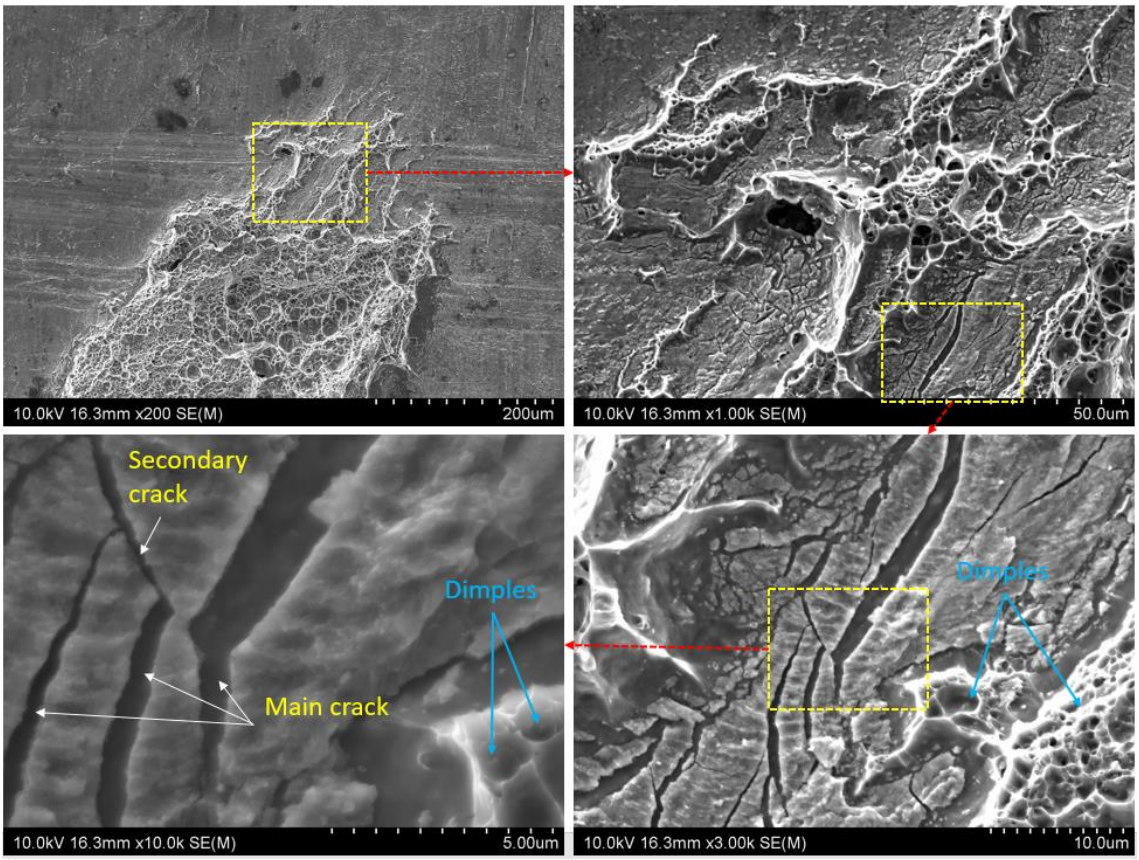

Figure 5-9 SEM micrograph of N3S6 weld sample fracture showing multiple cracks at the interface with ductile dimples.

Based on EDS spectra analysis on the three points considered in Figure 5-10a on Fig.5-9 micrograph, spectrum point 1 is an Al rich region as it is clearly revealed by high traces of aluminium in Figure 5-10b. The Al traces in Figure 5-10c is a bit lower and this may be due to the result of uneven migration of intermetallic diffusion of atoms during FSL welding. However, the EDS spectrum point 3 is apparent that aluminium has been bonded onto the Ti plate during welding which is a clear evidence of a strong weld bonding at the Al/Ti interface with complete aluminium without any other traces of elements detected at the spot which means interdiffusion welding has been accomplished similarly reported earlier in chapter 3.

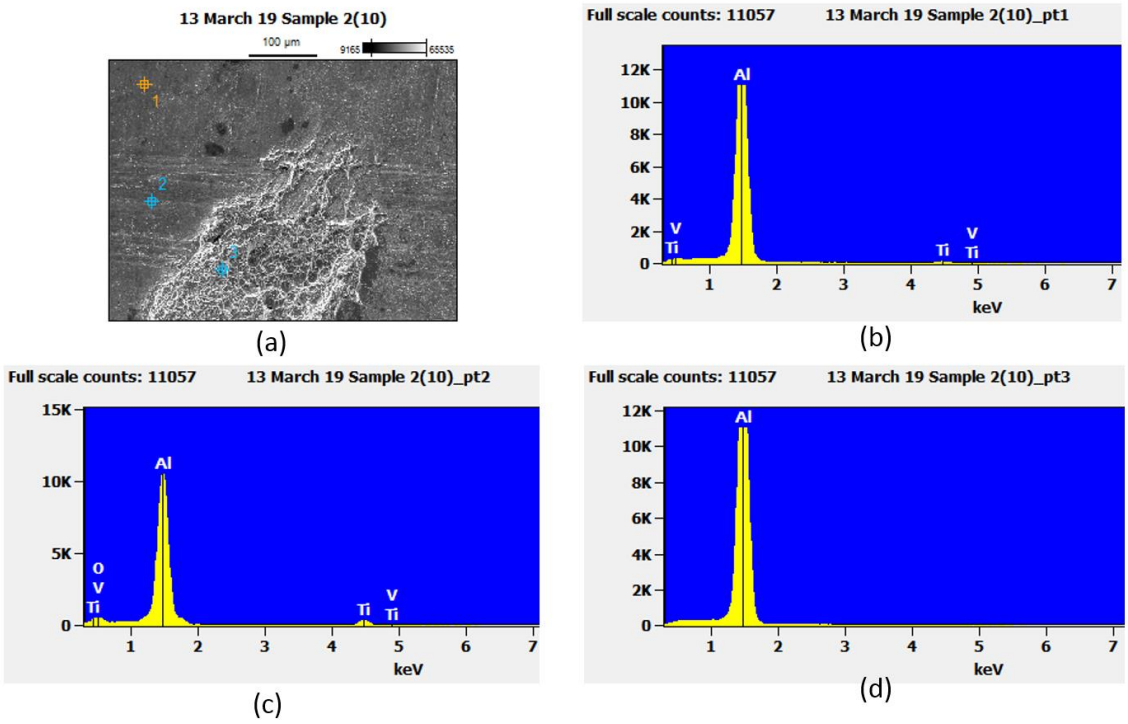

Figure 5-10 (a) SEM micrograph of interface fracture surface on Ti6Al4V side showing fractograph at Al/Ti interface with EDS spectra of intermetallic layer taken at three different spots for the SEM micrograph in Figure 5-9. (b) top right EDS spectrum for point 1, c) bottom left spectrum for point 2 and d) bottom right spectrum for point 3.

Apparently, Figure 5-11a shows EDS spectra analysis conducted at high magnification of Figure 5-9 micrograph in five different locations to investigate the presence of different elements. Figure 5-11 b to Figure 5-11f (EDS spectrum point 1 to EDS spectrum point 5) each presents a high amount of aluminium and other (Ti, Si, V, O) small traces of elements. These EDS spectra points have been taken near each other which have shown similar results displaying a large amount of aluminium which means interdiffusion bonding has been accomplished.

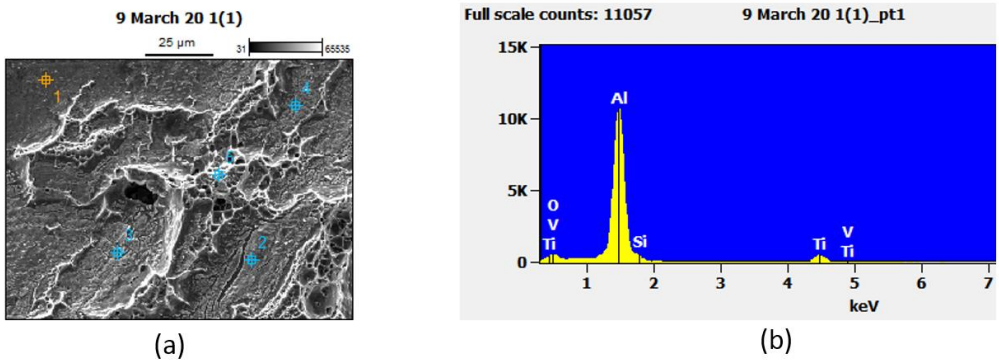

Figure 5-11 (a) High magnification SEM micrograph of Figure 5-10 top right with EDS spectra of intermetallic layer taken at five different spots adjacent to each other, (b) EDS spectrum for point 1, (c) EDS spectrum for point 2, (d) EDS spectrum for point 3, (e) EDS spectrum point 4 and (f) EDS spectrum point 5.

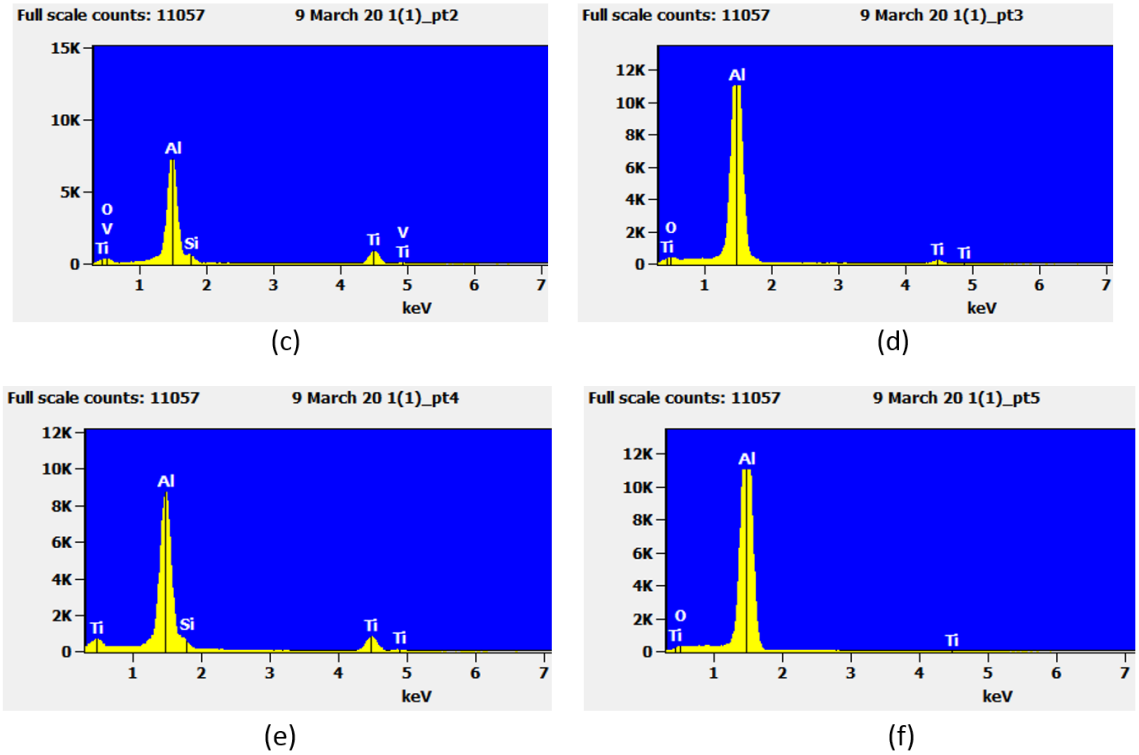

Figure 5-11 cont.

Figure 5-12a shows EDS spectra applied on the same FSL weld (N3S6) sample but at a different location. EDS spectra point 1 (Fig. 5-12b) and EDS spectra point 2 (Fig.5-12c) presents similar results having aluminium as a major element and small traces of Ti and O. Also, Figure 5-12d shows the presence of high amount of aluminium with small traces of Ti, O and Si. Similarly, as it has been shown in Figure 5-11, the presence of high amount of aluminium proves that weld joint has been established through diffusion bonding as the tool penetration on the base Ti6Al4V plate has been largely avoided with the insertion of Al interlayer onto the machined groove. (see Fig. 5-2a).

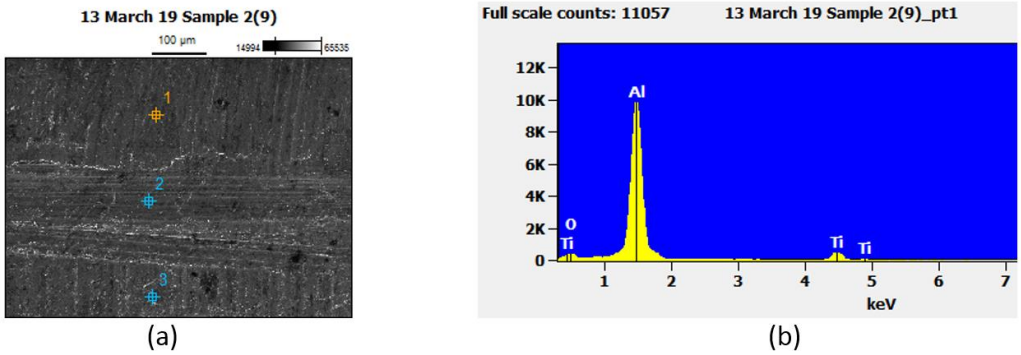

Figure 5-12 SEM micrograph of sample N3S6 fractograph taken at a region without showing any ductile dimples. Top right EDS spectrum point 1, bottom left EDS spectrum point 2 and bottom right EDS spectrum point 3.

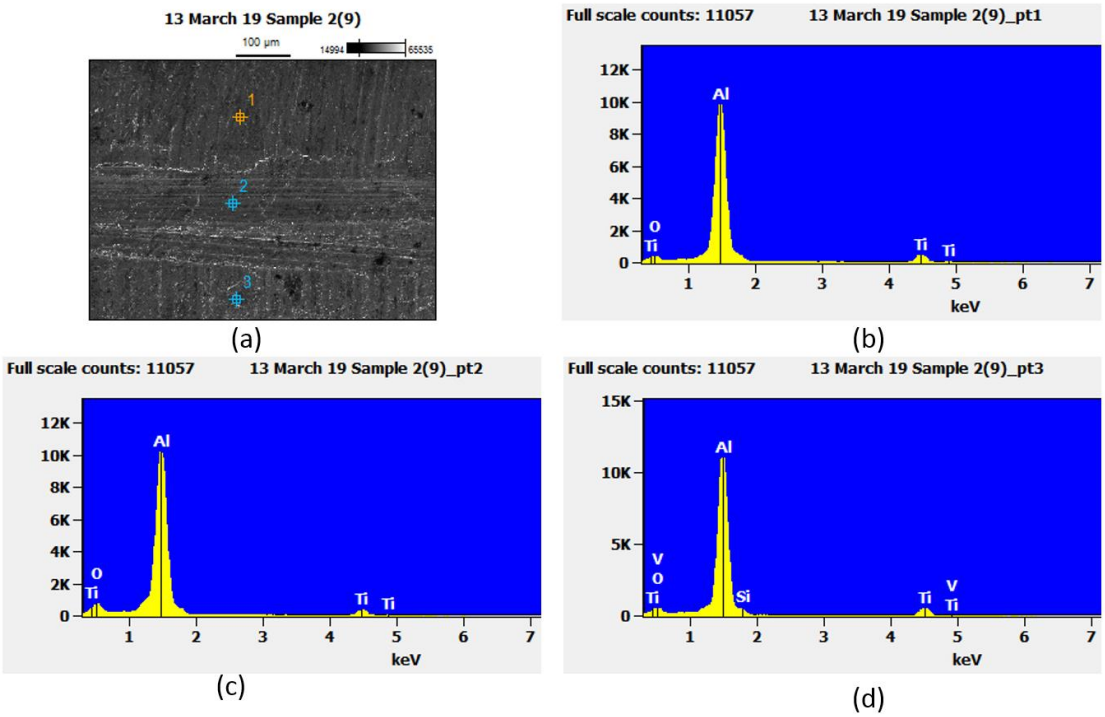

Figure 5-12 cont.

Figure 5-13 SEM micrograph of two different weld samples identified as N3S6 (see Fig.5-8a) and N2S5 (see Fig.5-10b). Their level of weld coverage can be seen differing from one another. some regions on the machined groove on Ti6Al4V plate has not shown sufficient Al to Ti bonding while the other areas on the same weld sample have shown smeared Al layers (see Fig. 5-8a) which is the indicative of the establishment of weld bonds through diffusion. However, joint strength may not be as good as areas shown with dimples (see Fig. 5-8b) which is an indication of high ductility and weld strength. However, the EDS spectra points (see Fig.5-11 and Fig.5-11) have proven that the weld joints have been established despite of showing varying fracture surface features. Besides, weld discontinuity has been found to be dominant mainly at the corners of the groove (see Fig.5-3 and Fig.5-4), showing lack of weld deposition due to the intricate nature of the setup of the parent alloys. These regions (corners) have been identified as potential areas for weld defects.

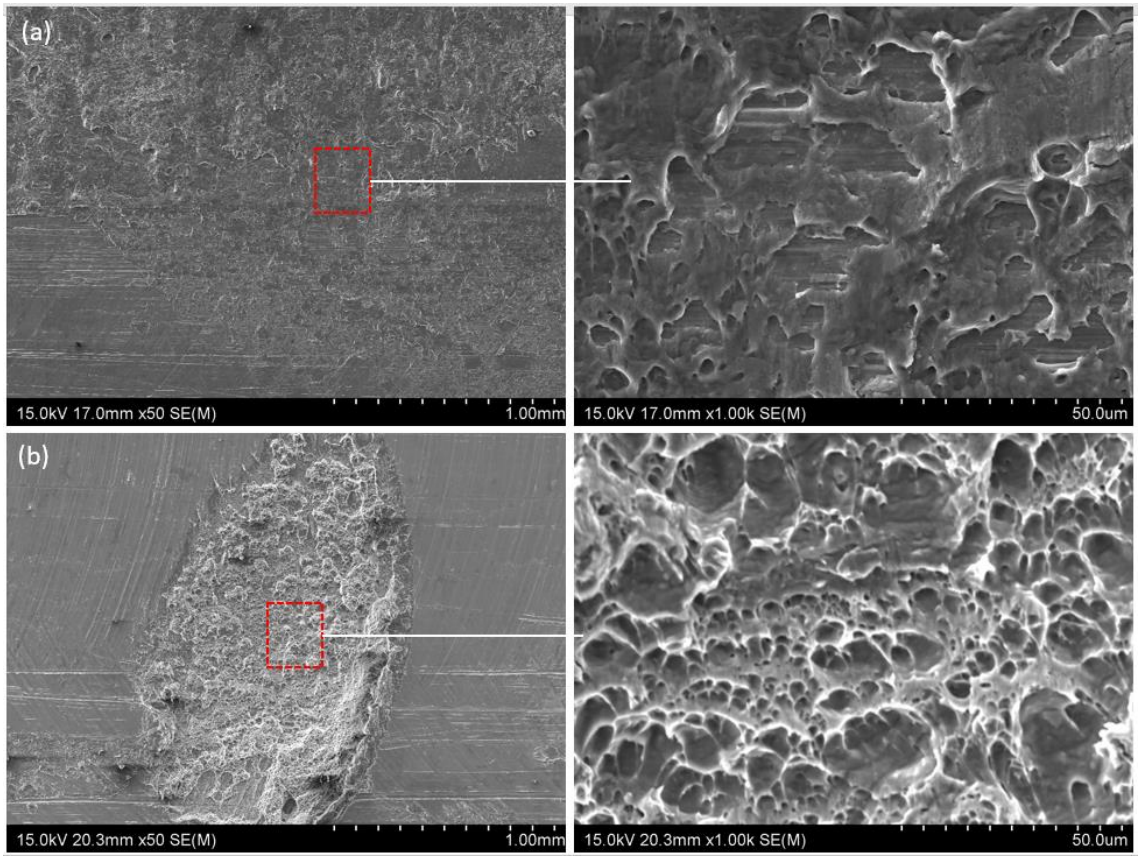

Figure 5-13 SEM micrograph of Al interlayer AA2024/Ti6Al4V FSLW fracture surfaces on Ti side: a) N2S5 (see Fig.5-8b), b) N3S6 (see Fig.5-8a).

5.4 Summary

The use of Al interlayer AA2024/Ti6Al4V FSLW has allowed position control ready made to ascertain not to have $d_p > 0$. However, FSLW position control with the use of interlayer also needs $d_p \approx 0$, as when the pin was 0.3-0.4 mm from the bottom Ti6Al4V, diffusion weld cannot be certain to be continued, adversely affect the joint strength and thus the fatigue strength of the welds. Observing *S-N* curve 10 mm Al interlayer showed a lower fatigue strength compared to that of 8 mm Al interlayer. This may likely the result of lacking depth control using the position control mechanism.

It was observed that there was a formation of a new feature of the weld at the nugget zone (NZ), a sliced tomato-like structure (of the interlayer material) on top of the conventional onion ring structure (NZ) as a second layer. This feature may be due to the plasticized Al interlayer being drawn towards the centre of NZ after the formation of the onion ring structure of the plasticized AA202024 as it was evident with optical micrograph. The diffusion welding mechanism has been well confirmed in the interface structure analysis of the samples in this series 3 study.

6. CONCLUSION

Friction stir lap welding (FSLW) experiments of AA2024-to-Ti6Al4V and fatigue life testing of the welds in 20 mm width have been conducted. FSLW experiments have included monitoring the temperatures in the weld interface region for later thermomechanical conditions for diffusion welding. Fatigue testing has included tests where the fatigue crack propagation could be frozen so that crack growth could "observed". Together with the subsequent metallographic and fractographic observations/analysis conducted in this research (and described in Chapter 2), the following conclusions can be made:

Using the normal size (6 mm outside diameter) tool pin

1. The fatigue limit of the welds has been found to be $F_{Max} \approx 3.5$ kN for fracture path propagating along the AA2024/Ti6Al4V interface region for welds made with zero pin penetration ($d_P \approx 0$). This loading can be regarded equivalent to the high cycle fatigue loading to fatigue shear fracture a thick (> 5 mm) AA2024/AA2024 lap weld made using FSLW. Thus, AA2024/Ti6Al4V lap welds made using FSLW can be considered as high fatigue performing welds.

2. The high fatigue strength values of $d_P \approx 0$ welds have resulted from the diffusion welding under the thermomechanical condition during FSLW, forming thin intermetallic layer strongly welding AA2024/AA2024 together. The width of the thin interface layer has been identified to be 8-9 mm, significantly larger than the width of the pin. Metallographic and fractographic evidence have shown that the strong AA2024/Ti6Al4V welded interface region has resulted in either fracturing inside AA2024 next to the interface or fracturing along the thin interface intermetallic layer of the FSL diffusion welds.

3. When $d_P > 0$, peak temperature of up to 600 °C have been detected in the weld interface region. This compares with the peak temperature of ~480 °C found for $d_P \approx 0$ welds. A higher downforce has also likely acted at the interface during FSLW with the pin having slightly penetrated to the bottom plate, comparing to no pin penetration. This thermomechanical condition has resulted in a significantly larger diffusion weld width, ~5 mm on both sides, outside the pin bottom in pin penetration welds. Thus, despite of having a brittle mix stir zone of Ti/Al and intermetallics, the fatigue strength of the pin penetrated welds were comparable to the fatigue strength of non-penetrated welds.

Using a larger size (9 mm outside diameter) tool pin

4. Fatigue strength (*S-N*) values of welds made using the larger size pin are comparable to that of standard tool pin, despite of having a 60 percent increase in the pin size. This is likely the result of lowering of the rotational tool speed (ω) from 1,400 rpm to 1,000 rpm that was purposely performed in order to avoid tunnel defects. The decrease of ω may have also lowered the temperature of the weld region, thus lowering the rate of the formation and growth rate of the interface intermetallic layer. As a result, the width (~9 mm) of interface Al to Ti intermetallic layer at the weld interface for the larger pin welds have been found to be similar to that of welds made using normal size pin for $d_P = 0$. For penetrating welds ($d_P > 0$), the diffusion weld distance (~5 mm for each side) outside the penetration area has also found to be similar to that in normal size pin welds. Thus, the fatigue strength values of the larger pin size welds were comparable to that of normal pin size welds.

5. Crack growth to fracture inside the Ti6Al4V bottom plate has also been identified for some weld samples of $d_P > 0$. This fracture at the bottom plate (Ti6Al4V) has been caused by the increase in penetration depth that is more readily resulted due to the geometry effect of a large pin with the same tilt angle more readily penetrating more for the same pin horizontal position. The deep penetration, meaning large d_P, caused more thining in the bottom Ti6Al4V plate and thus more readily to fracture in the plate. Simulation and calculation has confirmed this.

Using an Al Interlayer Aided FSL welds

6. Fatigue strength values of welds made using an Al interlayer, which allows for $d_P < 0$ and more easily avoiding $d_P > 0$, have been shown be comparable to the strength values of welds made using the normal pin without an interlayer. This is due to the same diffusion welding mechanism operating forming the thin interface intermetallic that is highly fatigue resistant. Fractographic examination has further confirmed and shown the presence of the thin interface layer and the fracture path being inside of AA2024 or the thin interface layer.

7. A lack of material flow reaching wide to the corners of the machined groove in the bottom base plate (Ti6Al4V) has shown complete lack of weld formation resulting in gaps at both ends of the bottom base plate. This confirms to the limited width of diffusion welding due to the thermomechanical condition for interface intermetallic to form and to weld the AA2024/Ti6Al4V couple.

REFERENCES

[1] P. Kah, M. Shrestha, and J. Martikainen, "Trends in Joining Dissimilar Metals by Welding," *Applied Mechanics and Materials,* vol. 440, pp. 269-276, 2014.

[2] Y. Fang, X. Jiang, D. Mo, D. Zhu, and Z. Luo, "A review on dissimilar metals' welding methods and mechanisms with interlayer," *The International Journal of Advanced Manufacturing Technology,* vol. 102, no. 9-12, pp. 2845-2863, 2019.

[3] W. M. T. E. D., b. o. H. J. C. Nicholas, S. W. M. G. Needham, H. P. T.-S. Murch, Cambridge; Christopher J. Dawes, and a. o. U. K. Cambs, "FRICTION WELDING," 1991.

[4] Z. W. Chen, T. Pasang, and Y. Qi, "Shear flow and formation of Nugget zone during friction stir welding of aluminium alloy 5083-O," *Materials Science and Engineering: A,* vol. 474, no. 1-2, pp. 312-316, 2008.

[5] S. H. Chowdhury, D. L. Chen, S. D. Bhole, X. Cao, and P. Wanjara, "Friction Stir Welded AZ31 Magnesium Alloy: Microstructure, Texture, and Tensile Properties," *Metallurgical and Materials Transactions A,* vol. 44, no. 1, pp. 323-336, 2012.

[6] F. Fadaeifard, K. Matori, S. Abd Aziz, L. Zolkarnain, and M. Abdul Rahim, "Effect of the Welding Speed on the Macrostructure, Microstructure and Mechanical Properties of AA6061-T6 Friction Stir Butt Welds," *Metals,* vol. 7, no. 2, 2017.

[7] N. Vulić and L. Roldo, "Friction Stir Welding for Marine Applications: Mechanical Behaviour and Microstructural Characteristics of Al-Mg-Si-Cu Plates," *Transactions on Maritime Science,* vol. 8, no. 1, pp. 75-83, 2019.

[8] M. C. Grzegorz Gesella, "The Application of Friction Stir Welding (FSW) of Aluminium Alloys in Shipbuilding and Railway Industry," 2019.

[9] V. Msomi and N. Mbana, 2019.

[10] A. G. Boitsov, D. N. Kuritsyn, M. V. Siluyanova, and V. V. Kuritsyna, "Friction Stir Welding in the Aerospace Industry," *Russian Engineering Research,* vol. 38, no. 12, pp. 1029-1033, 2019.

[11] D. Burford, C. Widener, and B. Tweedy, "Advances in Friction Stir Welding for Aerospace Applications," presented at the 6th AIAA Aviation Technology, Integration and Operations Conference (ATIO), 2006.

[12] M. Haghshenas and A. P. Gerlich, "Joining of automotive sheet materials by friction-based welding methods: A review," *Engineering Science and Technology, an International Journal,* vol. 21, no. 1, pp. 130-148, 2018.

[13] a. M. Z. Y. Mishra R.S., "Friction Stir Welding and Processing," *Materials Science and Engineering: A,* vol. 50, pp. 1-78., 2005.

[14] J. William D. Callister and D. G. Rethwisch, "Materials Science and Engineering - Edition 9," pp. 252-280, 2009.

[15] A. Simar and M.-N. Avettand-Fènoël, "State of the art about dissimilar metal friction stir welding," *Science and Technology of Welding and Joining,* vol. 22, no. 5, pp. 389-403, 2016.

[16] S. Celik and R. Cakir, "Effect of Friction Stir Welding Parameters on the Mechanical and Microstructure Properties of the Al-Cu Butt Joint," *Metals,* vol. 6, no. 6, 2016.

[17] S. Shankar, P. Vilaça, P. Dash, S. Chattopadhyaya, and S. Hloch, "Joint strength evaluation of friction stir welded Al-Cu dissimilar alloys," *Measurement,* vol. 146, pp. 892-902, 2019.

[18] S. Shankar and S. Chattopadhyaya, "Friction stir welding of commercially pure copper and 1050 aluminum alloys," *Materials Today: Proceedings,* 2019.

[19] S. K. Sahu, N. Haldar, S. Datta, and R. Kumar, "Experimental studies on AA6063-Cu dissimilar friction stir welding using Inconel 601 tool," *Materials Today: Proceedings,* 2019.

[20] W. Hou, L. H. Ahmad Shah, G. Huang, Y. Shen, and A. Gerlich, "The role of tool offset on the microstructure and mechanical properties of Al/Cu friction stir welded joints," *Journal of Alloys and Compounds,* vol. 825, 2020.

[21] M. V. N. Srujan Manohar and K. Mahadevan, "Prediction on mechanical and microstructural behaviour of friction stir welded thin gauge aluminium-copper sheets," *Materials Today: Proceedings,* 2020.

[22] V. M. Khojastehnezhad and H. H. Pourasl, "Microstructural characterization and mechanical properties of aluminum 6061-T6 plates welded with copper insert plate (Al/Cu/Al) using friction stir welding," *Transactions of Nonferrous Metals Society of China,* vol. 28, no. 3, pp. 415-426, 2018.

[23] N. P. Patel, P. Parlikar, R. Singh Dhari, K. Mehta, and M. Pandya, "Numerical modelling on cooling assisted friction stir welding of dissimilar Al-Cu joint," *Journal of Manufacturing Processes,* vol. 47, pp. 98-109, 2019.

[24] S. K. Sahu, N. Haldar, S. Datta, and R. Kumar, "Experimental studies on AA6063-Cu dissimilar friction stir welding using Inconel 601 tool," *Materials Today: Proceedings,* vol. 26, pp. 180-188, 2020.

[25] S. Shankar and S. Chattopadhyaya, "Friction stir welding of commercially pure copper and 1050 aluminum alloys," *Materials Today: Proceedings,* vol. 25, pp. 664-667, 2020.

[26] M. r. n. N. Ponweiser, "Investigation of phase equilibria and structural analysis in the systems Al-Cu, Cu-Si, Al-Cu-Si and Al-Mo-Si," Dissertation 2011.

[27] P. Xue, B. L. Xiao, D. R. Ni, and Z. Y. Ma, "Enhanced mechanical properties of friction stir welded dissimilar Al–Cu joint by intermetallic compounds," *Materials Science and Engineering: A,* vol. 527, no. 21-22, pp. 5723-5727, 2010.

[28] K. K. Ramachandran, N. Murugan, and S. Shashi Kumar, "Effect of tool axis offset and geometry of tool pin profile on the characteristics of friction stir welded dissimilar joints

of aluminum alloy AA5052 and HSLA steel," *Materials Science and Engineering: A*, vol. 639, pp. 219-233, 2015.

[29] R. S. Coelho, A. Kostka, J. F. dos Santos, and A. Kaysser-Pyzalla, "Friction-stir dissimilar welding of aluminium alloy to high strength steels: Mechanical properties and their relation to microstructure," *Materials Science and Engineering: A*, vol. 556, pp. 175-183, 2012.

[30] S. Kundu, D. Roy, R. Bhola, D. Bhattacharjee, B. Mishra, and S. Chatterjee, "Microstructure and tensile strength of friction stir welded joints between interstitial free steel and commercially pure aluminium," *Materials & Design*, vol. 50, pp. 370-375, 2013.

[31] H. Springer, A. Kostka, J. F. dos Santos, and D. Raabe, "Influence of intermetallic phases and Kirkendall-porosity on the mechanical properties of joints between steel and aluminium alloys," *Materials Science and Engineering: A*, vol. 528, no. 13-14, pp. 4630-4642, 2011.

[32] K. Kimapong, "Friction stir welding of aluminum alloy to steel," *WELDING JOURNAL*, p. 277, 2004.

[33] S. Y. Anaman, H.-H. Cho, H. Das, J.-S. Lee, and S.-T. Hong, "Microstructure and mechanical/electrochemical properties of friction stir butt welded joint of dissimilar aluminum and steel alloys," *Materials Characterization*, vol. 154, pp. 67-79, 2019.

[34] H. Sina, J. Corneliusson, K. Turba, and S. Iyengar, "A study on the formation of iron aluminide (FeAl) from elemental powders," *Journal of Alloys and Compounds*, vol. 636, pp. 261-269, 2015.

[35] V. Raghavan, "Al-Ti (Aluminum-Titanium)," *Journal of Phase Equilibria & Diffusion*, vol. 26, no. 2, pp. 171-172, 2005.

[36] U. Dressler, G. Biallas, and U. Alfaro Mercado, "Friction stir welding of titanium alloy TiAl6V4 to aluminium alloy AA2024-T3," *Materials Science and Engineering: A*, vol. 526, no. 1-2, pp. 113-117, 2009.

[37] C. L. Yuhua Chen, Geping Liu, "Study on the Joining of Titanium and Aluminum Dissimilar Alloys by Friction Stir Welding," *The Open Material Science Journal*, vol. 5, pp. 256-261, 2011.

[38] Z. Song, K. Nakata, A. Wu, J. Liao, and L. Zhou, "Influence of probe offset distance on interfacial microstructure and mechanical properties of friction stir butt welded joint of Ti6Al4V and A6061 dissimilar alloys," *Materials & Design*, vol. 57, pp. 269-278, 2014.

[39] B. Li, Z. Zhang, Y. Shen, W. Hu, and L. Luo, "Dissimilar friction stir welding of Ti–6Al–4V alloy and aluminum alloy employing a modified butt joint configuration: Influences of process variables on the weld interfaces and tensile properties," *Materials & Design*, vol. 53, pp. 838-848, 2014.

[40] A. Wu, Z. Song, K. Nakata, J. Liao, and L. Zhou, "Interface and properties of the friction stir welded joints of titanium alloy Ti6Al4V with aluminum alloy 6061," *Materials & Design,* vol. 71, pp. 85-92, 2015.

[41] Y. Chen, W. Cao, S. Li, C. Chen, and J. Xie, "Microstructure and Mechanical Properties of Friction Stir Weld of Dissimilar Ti6Al4V Titanium Alloy to AA2024 Aluminum Alloy," in *Transactions on Intelligent Welding Manufacturing*(Transactions on Intelligent Welding Manufacturing, 2018, pp. 153-162.

[42] J.-W. Choi, H. Liu, and H. Fujii, "Dissimilar friction stir welding of pure Ti and pure Al," *Materials Science and Engineering: A,* vol. 730, pp. 168-176, 2018.

[43] M. S. GopalVanga1, G. Narendra Santosh kumar3, "Evaluation of Tensile Properties and Microstructural Properties of Friction stirwelded AL-CU Lap Joints," *International Journal of Innovative Research in Science, Engineering and Technology,* vol. 5, no. 5, 2016.

[44] T. Choudhury, A. Ghorai, T. Medhi, U. Acharya, B. S. Roy, and S. C. Saha, "Study of microstructure and mechanical properties in friction stir welded aluminum copper lap joint," *Materials Today: Proceedings,* 2020.

[45] Q. Guan, H. Zhang, H. Liu, Q. Gao, M. Gong, and F. Qu, "Structure-property characteristics of Al-Cu joint formed by high-rotation-speed friction stir lap welding without tool penetration into lower Cu sheet," *Journal of Manufacturing Processes,* vol. 57, pp. 363-369, 2020.

[46] H. Bisadi, A. Tavakoli, M. Tour Sangsaraki, and K. Tour Sangsaraki, "The influences of rotational and welding speeds on microstructures and mechanical properties of friction stir welded Al5083 and commercially pure copper sheets lap joints," *Materials & Design,* vol. 43, pp. 80-88, 2013.

[47] V. Firouzdor and S. Kou, "Al-to-Cu Friction Stir Lap Welding," *Metallurgical and Materials Transactions A,* vol. 43, no. 1, pp. 303-315, 2011.

[48] Z. W. Chen, S. Yazdanian, and G. Littlefair, "Effects of tool positioning on joint interface microstructure and fracture strength of friction stir lap Al-to-steel welds," *Journal of Materials Science,* vol. 48, no. 6, pp. 2624-2634, 2012.

[49] M. Movahedi, A. H. Kokabi, S. M. Seyed Reihani, W. J. Cheng, and C. J. Wang, "Effect of annealing treatment on joint strength of aluminum/steel friction stir lap weld," *Materials & Design,* vol. 44, pp. 487-492, 2013.

[50] Z. B. Yazid Helal, Lahcene Fellah, "Microstructural evolution and mechanical properties of dissimilar friction stir lap welding aluminum alloy 6061-T6 to ultra low carbon steel," *Enenergy Procedia* vol. 157, pp. 208-215, 2019.

[51] L. Zhou *et al.*, "Microstructure and mechanical properties of Al/steel dissimilar welds fabricated by friction surfacing assisted friction stir lap welding," *Journal of Materials Research and Technology,* vol. 9, no. 1, pp. 212-221, 2020.

[52] M. Movahedi, A. H. Kokabi, S. M. S. Reihani, and H. Najafi, "Mechanical and Microstructural Characterization of Al-5083/St-12 lap joints made by friction stir welding," *Procedia Engineering*, vol. 10, pp. 3297-3303, 2011.

[53] Z. B. Yazid Helal, "PIN DIAMETER EFFECT ON MICROSTRUCTURE AND MECHANICAL PROPERTIES OF DISSIMILAR FRICTION STIR LAP WELDING ALUMINUM ALLOY 6061-T6 TO DUAL PHASE STEEL," *Acta Metallurgica Slovaca,*, vol. 24, no. 2, pp. 163-173, 2018.

[54] L. F. M. d. S. A. O. c. R. D. Adams, "Book_Handbook Of Adhesion Technology," vol. 2, pp. 465-467, 2011.

[55] M. Haghshenas, A. Abdel-Gwad, A. M. Omran, B. Gökçe, S. Sahraeinejad, and A. P. Gerlich, "Friction stir weld assisted diffusion bonding of 5754 aluminum alloy to coated high strength steels," *Materials & Design*, vol. 55, pp. 442-449, 2014.

[56] Y. C. Chen and K. Nakata, "Microstructural characterization and mechanical properties in friction stir welding of aluminum and titanium dissimilar alloys," *Materials & Design*, vol. 30, no. 3, pp. 469-474, 2009.

[57] Y.-h. Chen, Q. Ni, and L.-m. Ke, "Interface characteristic of friction stir welding lap joints of Ti/Al dissimilar alloys," *Transactions of Nonferrous Metals Society of China*, vol. 22, no. 2, pp. 299-304, 2012.

[58] Y. Wei, J. Li, J. Xiong, F. Huang, F. Zhang, and S. H. Raza, "Joining aluminum to titanium alloy by friction stir lap welding with cutting pin," *Materials Characterization*, vol. 71, pp. 1-5, 2012.

[59] Z. W. Chen and S. Yazdanian, "Microstructures in interface region and mechanical behaviours of friction stir lap Al6060 to Ti–6Al–4V welds," *Materials Science and Engineering: A*, vol. 634, pp. 37-45, 2015.

[60] B. Li, Y. Shen, L. Luo, and W. Hu, "Effects of processing variables and heat treatments on Al/Ti-6Al-4V interface microstructure of bimetal clad-plate fabricated via a novel route employing friction stir lap welding," *Journal of Alloys and Compounds*, vol. 658, pp. 904-913, 2016.

[61] Y. Huang, Z. Lv, L. Wan, J. Shen, and J. F. dos Santos, "A new method of hybrid friction stir welding assisted by friction surfacing for joining dissimilar Ti/Al alloy," *Materials Letters*, vol. 207, pp. 172-175, 2017.

[62] Y. Yue, Z. Zhang, S. Ji, Z. Li, and D. Yan, "Friction stir lap welding of 6061-T6 Al to Ti-6Al-4V using low rotating speed," *The International Journal of Advanced Manufacturing Technology*, vol. 96, no. 5-8, pp. 2285-2291, 2018.

[63] L. Zhou *et al.*, "Influence of Rotation Speed on Microstructure and Mechanical Properties of Friction Stir Lap Welded Joints of AA 6061 and Ti6Al4V Alloys," *Metallurgical and Materials Transactions A*, vol. 50, no. 2, pp. 733-745, 2019.

[64] H. Zhao, M. Yu, Z. Jiang, L. Zhou, and X. Song, "Interfacial microstructure and mechanical properties of Al/Ti dissimilar joints fabricated via friction stir welding," *Journal of Alloys and Compounds*, vol. 789, pp. 139-149, 2019.

[65] M. Yu, H. Zhao, Z. Jiang, F. Guo, L. Zhou, and X. Song, "Microstructure and mechanical properties of friction stir lap AA6061-Ti6Al4V welds," *Journal of Materials Processing Technology*, vol. 270, pp. 274-284, 2019.

[66] L. Zhou, M. Yu, H. Zhao, Z. Jiang, F. Guo, and X. Song, "Dissimilar friction stir welding of AA6061 and Ti6Al4V alloys: A study on microstructure and mechanical properties," *Journal of Manufacturing Processes*, vol. 48, pp. 119-126, 2019.

[67] M. Yu *et al.*, "Influence of welding parameters on interface evolution and mechanical properties of FSW Al/Ti lap joints," *Journal of Materials Science & Technology*, vol. 35, no. 8, pp. 1543-1554, 2019.

[68] P. Myler, *Fatigue of Aerospace Materials*. 2012.

[69] J. William D. Callister, *Materials Science and Engineering: An Introduction*, 8 ed. 2007, pp. 225-230.

[70] D. Fersini and A. Pirondi, "Fatigue behaviour of Al2024-T3 friction stir welded lap joints," *Engineering Fracture Mechanics*, vol. 74, no. 4, pp. 468-480, 2007.

[71] D. Fersini and A. Pirondi, "Analysis and modelling of fatigue failure of friction stir welded aluminum alloy single-lap joints," *Engineering Fracture Mechanics*, vol. 75, no. 3-4, pp. 790-803, 2008.

[72] X. Xu, X. Yang, G. Zhou, and J. Tong, "Microstructures and fatigue properties of friction stir lap welds in aluminum alloy AA6061-T6," *Materials & Design*, vol. 35, pp. 175-183, 2012.

[73] V. Infante, D. F. O. Braga, F. Duarte, P. M. G. Moreira, M. de Freitas, and P. M. S. T. de Castro, "Study of the fatigue behaviour of dissimilar aluminium joints produced by friction stir welding," *International Journal of Fatigue*, vol. 82, pp. 310-316, 2016.

[74] Z. N. Haji, "LOW CYCLE FATIGUE BEHAVIOR OF ALUMINUM ALLOYS AA2024-T6 AND AA7020-T6," *Diyala Journal of Engineering Sciences*, pp. 127-137, 2010.

[75] U. S. T. I. Inc. (2002). *Titanium-Alloys-Ti6Al4V-Grade-5*. Available: https://usa-titanium.com/

[76] D. T. LLC, "aluminium-alloy-1100-data-sheet," 2010.

[77] A. E. a. S. S. Kathryn Beamish, "Development of a low cost Friction Stir Welding Monitoring System - TWI," Paper presented at 6th International Symposium, Friction Stir Welding, Saint-Sauveur, Canada, 10-13 Oct.2006. 2006.

[78] M. Corporation, "User manual | MTS Series 793™ Control Software," 2015.

[79] H. H. T. Corporation, "SEM-Hitachi-S-4800-Instruction-Manual," pp. 3-8, 2002.

[80] Z. H. Zhang, W. Y. Li, Y. Feng, J. L. Li, and Y. J. Chao, "Global anisotropic response of friction stir welded 2024 aluminum sheets," *Acta Materialia*, vol. 92, pp. 117-125, 2015.

[81] Z. Zhang, W. Li, F. Wang, and J. Li, "Sample geometry and size effects on tensile properties of friction stir welded AA2024 joints," *Materials Letters*, vol. 162, pp. 94-96, 2016.

[82] D. F. O. Braga *et al.*, "Fatigue performance of hybrid overlap friction stir welding and adhesive bonding of an Al-Mg-Cu alloy," *Fatigue & Fracture of Engineering Materials & Structures*, https://doi.org/10.1111/ffe.12933 vol. 42, no. 6, pp. 1262-1270, 2019/06/01 2019.

[83] A. Gerlich, P. Su, M. Yamamoto, and T. H. North, "Effect of welding parameters on the strain rate and microstructure of friction stir spot welded 2024 aluminum alloy," *Journal of Materials Science*, vol. 42, no. 14, pp. 5589-5601, 2007.

[84] S. Rajakumar and V. Balasubramanian, "Diffusion bonding of titanium and AA 7075 aluminum alloy dissimilar joints—process modeling and optimization using desirability approach," *The International Journal of Advanced Manufacturing Technology*, vol. 86, no. 1-4, pp. 1095-1112, 2016.

[85] N. Thiyaneshwaran, K. Sivaprasad, and B. Ravisankar, "Nucleation and growth of TiAl3 intermetallic phase in diffusion bonded Ti/Al Metal Intermetallic Laminate," *Sci Rep*, vol. 8, no. 1, p. 16797, Nov 14 2018.

[86] K. Kumar and S. V. Kailas, "The role of friction stir welding tool on material flow and weld formation," *Materials Science and Engineering: A*, vol. 485, no. 1-2, pp. 367-374, 2008.